

Development and Application of a Paediatric OPM-MEG System

by

Natalie Rhodes, M.Sci.

Thesis submitted to the University of Nottingham

for the degree of *Doctor of Philosophy*

January 2024

Contents

Abstract vi

Acknowledgements viii

1 Introduction 1

1.1 Functional neuroimaging 2

1.2 Paediatric MEG 4

1.2.1 An example application for paediatric MEG 4

1.2.2 Paediatric MEG systems 5

1.3 A new generation of MEG 7

1.4 Thesis aims 9

1.5 Thesis outline 9

2 Magnetoencephalography 11

2.1 Chapter overview 11

2.2 Origin of the MEG signal 11

2.2.1 The neuron 11

2.2.2 Resting potential 13

2.2.3 Neurotransmission 13

2.3 MEG signals 17

2.3.1 Evoked responses 17

2.3.2 Spontaneous rhythms 17

2.3.3 Induced responses 18

2.3.4 Functional connectivity 19

2.4 Collecting MEG data 21

2.4.1 A brief history of MEG 21

2.4.2 Superconductivity 22

2.4.3 Josephson junctions 23

2.4.4 Magnetometer vs. gradiometer 24

2.4.5 Conventional MEG data acquisition 25

2.5 Mathematical modelling of MEG signals 27

2.5.1 The forward problem 27

2.5.2 The inverse problem 33
2.5.3 Functional connectivity 36
2.6 Chapter summary 38
3 Optically pumped magnetometer-based MEG 39
3.1 Chapter overview 39
3.2 Introduction 39
3.2.1 OPM-MEG system overview 39
3.2.2 A brief history of OPMs 40
3.2.3 The QuSpin OPM 41
3.2.4 QZFM operation 42
3.3 The quantum origin 43
3.3.1 Principle of operation 43
3.3.2 Quantum mechanical explanation 43
3.3.3 The SERF regime 47
3.4 Signal equations 48
3.4.1 Cross-axis projection error 51
3.5 Triaxial Measurement 52
3.6 Magnetically shielded environments 55
3.6.1 DC fields 56
3.6.2 AC Fields 57
3.6.3 Degaussing 57
3.7 Active magnetic shielding 58
3.7.1 Nulling static magnetic fields with bi-planar electromagnetic coils 58
3.7.2 Dynamic magnetic field compensation 60
3.8 OPM-MEG subject interface 61
3.8.1 OPM-MEG helmet design 61
3.9 Coregistration 64
3.10 Chapter summary 65
4 Measuring theta band activity with OPM-MEG 66
4.1 Chapter overview 66
4.2 Introduction 66
4.3 Methods 68
4.3.1 Participants 68

4.3.2 Paradigms 69
4.3.3 OPM-MEG data collection 69
4.3.4 SQUID-MEG data collection 73
4.3.5 Data analysis 74
4.4 Results 77
4.4.1 System comparison 77
4.4.2 Magnetic field nulling 78
4.4.3 Visual experiment 79
4.4.4 Working memory (2-back) experiment 80
4.4.5 OPM-MEG artefact reduction 83
4.5 Discussion 85
4.6 Conclusion 90
5 MEG without MRI: a template warping method 91
5.1 Chapter overview 91
5.2 Introduction 91
5.3 Methods 93
5.3.1 Template warping 93
5.3.2 MEG participants and paradigm 95
5.3.3 OPM-MEG data acquisition 96
5.3.4 Coregistration 97
5.3.5 Geometric comparison 97
5.3.6 Data pre-processing 97
5.3.7 MEG analysis 98
5.4 Results 99
5.4.1 Geometric comparison 99
5.4.2 Peak beta modulation 100
5.4.3 Connectivity 103
5.4.4 Contribution of forward errors 104
5.5 Discussion 105
5.6 Conclusion 108
Appendix A 110
6 The neurodevelopmental trajectory of beta band oscillations 111
6.1 Chapter overview 111
6.2 Introduction 111

6.3 Methods 114
6.3.1 Participants and experiment 114
6.3.2 Data collection and coregistration 114
6.3.3 MEG data pre-processing 115
6.3.4 Source reconstruction and beta modulation 116
6.3.5 Functional connectivity analyses 117
6.3.6 Beta bursts and Hidden Markov Modelling 117
6.4 Results 118
6.4.1 Beta modulation with age 118
6.4.2 Functional connectivity in the beta band 122
6.4.3 Burst interpretation of beta dynamics 124
6.5 Discussion 128
6.6 Conclusion 131
7 The development of visual gamma oscillations: a cross-site collaborative study 133
7.1 Chapter overview 133
7.2 Introduction 133
7.3 Methods 136
7.3.1 Paradigm 136
7.3.2 Participants 137
7.3.3 UoN system 138
7.3.4 SickKids system 139
7.3.5 Pseudo-MRI generation 141
7.3.6 Pre-processing 141
7.3.7 Source reconstruction 142
7.3.8 Spectral analyses 143
7.4 Results 143
7.4.1 Cross-site comparison in a single adult 143
7.4.2 Cross-site comparison in a group of adults 144
7.4.3 Developmental analyses 145
7.4.4 Age-related spectral content changes 149
7.5 Discussion 151
7.5.1 Cross-site comparison 152
7.5.2 Development of visual gamma 153
7.5.3 Heterogeneity in the gamma response 154
7.5.4 Limitations 155

7.6 Conclusion 156

8 Concluding remarks 158

8.1 Summary 158

8.2 Future work 158

8.2.1 Technical development: towards integrated OPM-MEG systems 158

8.2.2 Going younger: baby OPM-MEG 159

8.2.3 Paediatric OPM-MEG in the clinic 160

8.3 Final thoughts 161

References 162

Abstract

The first few years of life see rapid changes in brain function, as we grow and learn, yet the developing brain remains poorly understood. This is in part due to instrumentational constraints. Magnetoencephalography (MEG) is a non-invasive neuroimaging technique that assesses human brain function through the detection of magnetic fields generated by neural currents. As a direct measure of electrophysiology, MEG can detect changes in brain activity with a high temporal resolution. Further, by measuring across the whole head, MEG is able to probe the dynamics of brain networks as they evolve in support of cognition. MEG is therefore, in principle, the ideal tool to understand how the brain changes in the first years of life. However, conventional MEG systems are based on sensors that must be cryogenically cooled to reach the sensitivities required to detect the neuromagnetic field. As such, sensors are held in one-size-fits-all systems that require participants to remain still during data acquisition, which is not ideal for scanning young participants. MEG systems are also built for adults and therefore lack sensitivity for scanning infants and children. Recently, optically pumped magnetometers (OPMs) have emerged as a potential replacement for cryogenic sensors in MEG. OPMs are lightweight, flexible and operate without the requirement for cryogenic cooling. As such, OPMs can be placed close to the scalp surface, enabling the development of wearable MEG systems that can conform to different head sizes and allow naturalistic movement.

This thesis aims to develop and implement the first whole-head paediatric OPM-MEG system for studying neurodevelopment. We first test a whole-head adult system for sensitivity to neural activity in the theta band in comparison to conventional MEG instrumentation, assessing whether OPM-MEG is sensitive to low frequency signals. This is particularly important in neurodevelopment, where previous studies have found elevated low frequency activity in younger participants. Next, we propose and demonstrate a method of warping template anatomical MRI scans to 3D structure scans of the participant's head shape to generate "pseudo-MRIs", enabling the analysis of OPM-MEG data without the acquisition of an individual's brain structure. This is important for children who may find the MRI scanning environment challenging.

Following this, we describe two of the first neurodevelopmental studies using OPM-MEG. We first investigate the developmental trajectory of cortical beta-band oscillations using a simple sensory task across a group of healthy children and adults. We use data-driven analysis approaches to investigate how beta band activity arises and analyse the evolution of the spectral properties of MEG signals with age. Finally, we use data collected from two systems at different sites to form (to our knowledge) the largest (to date) OPM-MEG study of 102 participants aged from 2 years to adulthood. We analyse data during a visual task to investigate how visual gamma oscillations change with age. Overall, the thesis demonstrates how OPM-MEG can be used as a new, viable platform for the study of neurodevelopment.

Acknowledgements

The work in this thesis would not have been possible without the support of so many amazing people. I would like to first thank my supervisors, Matt, and Elena (*Gracias*), for their patience, kindness, inspiration, and time (including all those evenings reading this thesis, Matt!). You have both pioneered this technology and made all this work possible. I would like to thank my examiners Matias and Krish for an enjoyable viva experience. It was an absolute pleasure to have the opportunity to discuss my work with you both.

Thank you to Margot and her incredible team at SickKids. The time spent working with you has already taught me so much and motivated me to finish this thesis faster so I could come back sooner! I can't wait to work with you all for the next stage of my career.

To the Nottingham MEG/OPM-MEG group, I feel so fortunate to have worked with you over the past few years. A huge shoutout to Niall, Ryan and Lukas, the fountains of all knowledge. You have never made any question I have asked (and there have been many) feel dumb. Thank you. Molly, I don't know how I would have survived these years without you. Thank you for always providing the most sensible (dare I say moral) advice, all with a gin in hand on a Friday night (4 pm).

To everyone at the SPMIC, thank you for the best years I could have hoped for. Thank you, Dan and Alex, for always keeping me grounded. Caitlin for showing me what a real work ethic is (hospitality + PhD, what!?), and providing me with unfailing support in both my work and personal life. Abi, my rock. Thank you for the stressed-out car trips, the therapy dog sessions (I love you Penny) and the amazing friendship throughout. Seb, we started this journey back in undergraduate together and I can't believe you're following me to Toronto. I'll never get rid of you! Thank you for all our neuroscience chats, morning coffee meetings, many pub trips and dinner parties (cheers Mike).

Cara, Ed, Ely, Hamish and Heather, no matter where we are in the world, we are always one group chat message away. Laszlo and Six, thanks for being mum and dad. Lewis, you dealt with living with me, plus my first year of PhD, plus COVID, and survived. Thank you.

I want to dedicate this work to my uncle Mike and granny Barbara, who we lost during this time. You are with me, always. Dad, you are the reason I got interested in this field. From the first MS society stall at Brighouse gala to a neuroimaging PhD, I will never tire of trying to find a way to help you. Thank you, Nana, Jenny, Katie and Tom, our Monday evening calls have been a weekly respite when things got tough. Thank you for reading through this thesis for grammar (especially Nana who went through around 40,000 words!) it has been a family effort!

Finally, mum. From the day I left, when you insisted on embarrassing me by telling the waiter that I was going to start a PhD, you have been my biggest supporter. Everything you gave up helping me, Katie and Tom flourish has not gone unnoticed. Every day I feel so lucky and grateful to have the world's best mum.

This is for (and because of) you.

1 Introduction

"Our brains are the most boundless equation, and once humanity solves it it'll be more powerful than when we went to the moon. There's no greater mystery in the universe than a human."

– Fredrick Backman in And Every Morning the Way Home Gets Longer

The human brain has been an object of scientific intrigue since the origin of the scientific method. Our understanding of the functional organisation of the brain before the advent of functional neuroimaging was almost entirely based on traumatic brain injury. Famous head injury cases, such as that of Phineas Gage (Harlow, 1848) or those described by Broca (Broca, 1861), provided insights into functional specialisation, collecting evidence that different human functions can be related to different regions of the brain. The twentieth century saw rapid advances in medical technology, allowing us to 'see' inside the brains of healthy, living humans. Neuroimaging enables us to take detailed images of the inner structures using tools such as X-ray computed tomography (Hounsfield, 1973) and magnetic resonance imaging (MRI) (Lauterbur, 1973; Mansfield and Grannell, 1973) and detect signals that can be related to brain function with the development of electroencephalography (Berger, 1929) or functional MRI (Ogawa et al., 1990).

However, these imaging modalities are not always practical for imaging brains during infancy and early childhood. Human brains change rapidly in the first few years of life; we learn to walk, talk and gain cognitive function within a few years. However, very little is understood about the function of the developing brain, and this is (in part) due to limitations of instrumentation. One tool that could offer insight into the developmental trajectories of brain function is magnetoencephalography (MEG) (Cohen, 1968). In this thesis, we will investigate the potential of a new generation of MEG system, which can be worn on the head and allows natural movement, for paediatric neuroimaging.

This introductory chapter provides an overview of functional neuroimaging, and the range of tools used to measure brain activity. We review an example of existing paediatric MEG literature, placing the relevance of the work in this thesis within the

context of current research. Finally, the thesis aims are described, and an overview of each chapter is provided. Some of this work is in submission as a review article for the British Journal of Radiology.

1.1 Functional neuroimaging

Functional neuroimaging refers to the application of imaging techniques to observe brain activity. Such signals play a pivotal role in furthering our understanding of the functional organisation of the brain.

Functional neuroimaging methods can broadly be split into two groups: direct and indirect measures. Direct measures assess electrophysiological activity in the brain. Such activity contributes to the passage of information between brain regions. Indirect measures detect the physiological changes associated with electrophysiological activity. There are five non-invasive techniques typically used in clinical and research environments:

Direct measures:

- **Electroencephalography (EEG)** – Current flow in active neurons generates a potential difference in the extracellular space. These signals can be measured using **intracranial EEG (iEEG)** or **Electrocorticography (ECoG)** via implanted electrodes or surface electrode grids, respectively. Invasive electrode recordings are considered the gold standard and have provided substantial insight from both animal studies (Renshaw et al., 1940) and patient recordings (Parvizi and Kastner, 2018) but are unsuitable for studying healthy human participants. However, due to the conduction of electrical signals through tissue, this potential difference can be detected at the scalp surface using electrodes placed in contact with the skin (Berger, 1929). EEG is cheap and accessible and has become a routine clinical tool for assessing brain function. EEG has excellent temporal resolution but suffers from poor spatial resolution due to the smearing of electrical signals by the high resistivity of the skull.
- **Magnetoencephalography (MEG)** – MEG, the magnetic counterpart of EEG, measures magnetic fields generated by (mostly) the same electrical activity that gives rise to EEG (Cohen, 1968). MEG also has excellent temporal resolution, but in addition, benefits from higher spatial resolution than EEG, as magnetic signals pass through the skull mostly undisturbed. However, as the magnetic fields at the scalp surface are very small, very sensitive

magnetometers are required. In conventional MEG systems, cryogenically cooled sensors (superconducting quantum interference devices or SQUIDs) must be held in a rigid helmet in a bath of liquid helium. This makes MEG cumbersome and expensive and has therefore had limited clinical uptake.

Indirect measures:

- **Functional Magnetic Resonance Imaging (fMRI)** – The oxygen content of blood provides contrast in MRI signals (Ogawa et al., 1990). As brain activity necessitates the consumption of oxygen to provide energy, the local blood oxygen level can be related to function. This can be accessed via the Blood Oxygen Level Dependence (BOLD) effect. This technique benefits from excellent spatial resolution but suffers from intrinsically poor temporal resolution due to the time delay (typically a couple of seconds) associated with the indirect metabolic response. Nevertheless, fMRI is extensively employed in research because of its capacity to delineate functionally relevant brain regions and networks that are functionally interconnected.
- **Positron Emission Tomography (PET)** – Brain function can be inferred using a radioactively labelled isotope that accumulates in active brain tissue and decays via positron emission, emitting gamma radiation upon collision with an electron (Raichle et al., 1983). The gamma radiation is measured by detectors surrounding the participant and back-projection is used to infer the location of the source. Using Oxygen-15 as the isotope provides a measure of blood oxygenation, and therefore indicates active brain regions. PET is again temporally limited by the time delay associated with indirect blood oxygenation measures. In addition, the use of radioactive isotopes prevents multiple recordings on a single participant due to exposure to ionising radiation and for this same reason, is not approved for paediatric research.
- **Functional Near Infra-Red Spectroscopy (fNIRS)** – Near infra-red light is shone through the scalp surface and reflected light is measured using detectors also located around the scalp surface. Haemoglobin absorbs a varied amount of light depending on blood volume, flow and oxygenation, and so the light intensity detected can be related to haemodynamic activity in the brain, and therefore indirectly brain function (Villringer et al., 1993). fNIRS benefits from a low-cost wearable system and has therefore been applied to a wide range of participant groups. However, it also suffers from poor temporal and spatial resolution and can only detect signals from the outermost cortex.

In this thesis, we focus on MEG and its potential for studying neurodevelopment. MEG combines the excellent temporal resolution from the direct measurement of electrophysiology with a high spatial resolution, enabling the detection of transient neural networks as they evolve. This combination of high spatial and temporal precision is unique, and for this reason, MEG is (arguably) the most attractive means to study neurodevelopment. However, the main limitation of MEG is the instrumentation used to detect the signals, and it is this problem we aim to address in this work. Conventional MEG systems use rigid helmets that are typically designed around the adult head (see Figure 1.1), meaning children with smaller head sizes have a greater separation between the brain and the MEG sensors. Due to the inverse square relationship between magnetic field amplitude and distance from the source, this results in substantially lower signal-to-noise ratio (SNR) when scanning young children (Gaetz et al., 2008; Hamalainen et al., 1993). In addition, with smaller heads there is more space in the MEG helmet, allowing for more head motion, which further degrades data quality (Messaritaki et al., 2017). Despite this, there is a growing body of research into MEG signals from early life.



***Figure 1.1. Conventional MEG**. A conventional MEG system (CTF Systems, Canada).*

1.2 Paediatric MEG

1.2.1 An example application for paediatric MEG

Despite its limitations, MEG has been instrumental in studying brain development and the disorders that affect it in both clinical and research settings. Here, we consider an example of such research by providing a brief literature review on the application of MEG for the study of auditory processing in autism spectrum disorder (ASD). ASD is

one of the most prevalent neurodevelopmental conditions, with 1 to 1.5 % of children diagnosed globally (Zeidan et al., 2022), and is marked by difficulties in social functioning. Consequently, there have been a range of studies examining auditory processing in children with ASD, particularly its relation to language abilities (Cardy et al., 2005; Roberts et al., 2011; T. P. Roberts et al., 2019). These studies have generally shown that the primary auditory evoked field components (known as the M50 [~50ms latency] and M100 [~100ms latency]) are delayed in those with ASD (T. P. Roberts et al., 2019). These effects are seen from young children to adults (Matsuzaki et al., 2020), and are associated with language proficiency. Importantly, these MEG studies only involve children listening passively to auditory tones and therefore can, with training, usually be completed even in minimally verbal children (Kuschner et al., 2021).

Studies have further suggested that the slower auditory responses in ASD may be related to lower gamma-aminobutyric acid (GABA) concentration (an inhibitory neurotransmitter) measured using magnetic resonance spectroscopy (MRS), suggesting altered neurotransmission in ASD (Roberts et al., 2020). These studies suggest that MEG is a key modality to derive putative biomarkers for a diagnosis of neurodevelopmental disorders (see Roberts et al., 2021 for an extensive review). However, measurement of such biomarkers in very young children (e.g., to enable the early diagnosis and possible intervention) remains challenging due to limitations of current systems. Consequently, if MEG is to achieve its true potential in ASD (and other neurodevelopmental conditions), new types of hardware will be needed.

1.2.2 Paediatric MEG systems

Most paediatric MEG studies have been conducted using adult-sized MEG systems (Kikuchi et al., 2016). Whilst possible, these studies must address the confound that – on average – younger children will have smaller heads and therefore lower SNR. Consequently, there are far fewer MEG studies with very young children (< 5 years) and most studies concentrate on school-age children – whilst extremely valuable, these studies miss the most dramatic neurodevelopmental changes that occur in the first few years of life. To scan infants (i.e., under 1 year old) using an adult MEG typically involves separate measurements for each hemisphere, with participants laid on one side, and then the other, to attain whole brain coverage over two independent experiments (Kujala et al., 2004). Such studies typically have a very low data retention rate, with many studies rejecting more than half of the recruited infant participants due to unsuccessful scans or insufficient data quality (Bosseler et al., 2013; Kuhl et al.,

2014). In addition, they preclude measurement of brain-wide networks, where one requires simultaneous data from all brain regions to measure relations between signals from different hemispheres.

There have been several attempts to address this instrumentation gap, with the introduction of child- or infant-sized MEG systems, designed around smaller head sizes. This reduces the brain-to-sensor distance and therefore increases signal sensitivity, while still using the same (cryogenic) sensing technology.

The first of such systems was the Squid Array for Reproductive Assessment (SARA), a system designed for foetal, neonate and infant recordings, shown in Figure 1.2. The device used 151 SQUID-based gradiometers in a concave array to conform to the pregnant abdomen or an infant's head using an attached cradle (Holst et al., 2005). Due to the wide array design, infant recordings still required three separate sessions to gain whole-head coverage. This system was followed by the BabySQUID, which housed 76 first-order gradiometers in an ellipsoid-shaped helmet, designed to cover approximately half the head (again precluding whole brain coverage) (Okada et al., 2006).

The first whole-head paediatric MEG system became available in 2010, with the development of the KIT system (Johnson et al., 2010; Yoshimura et al., 2013, 2012), initially comprising 64 channels (later upgraded to 151 channels), and designed to fit >90 % 5-year-old children. For younger infants, the Artemis 123 was designed to be compatible from birth to 3 years old (designed around the median 3-year-old head in the USA) (Roberts et al., 2014). The most recent of such cryogenic SQUID-based infant systems is the BabyMEG, which has a dense array of 375 magnetometers in a helmet designed to fit up to 4 years of age (Okada et al., 2016).

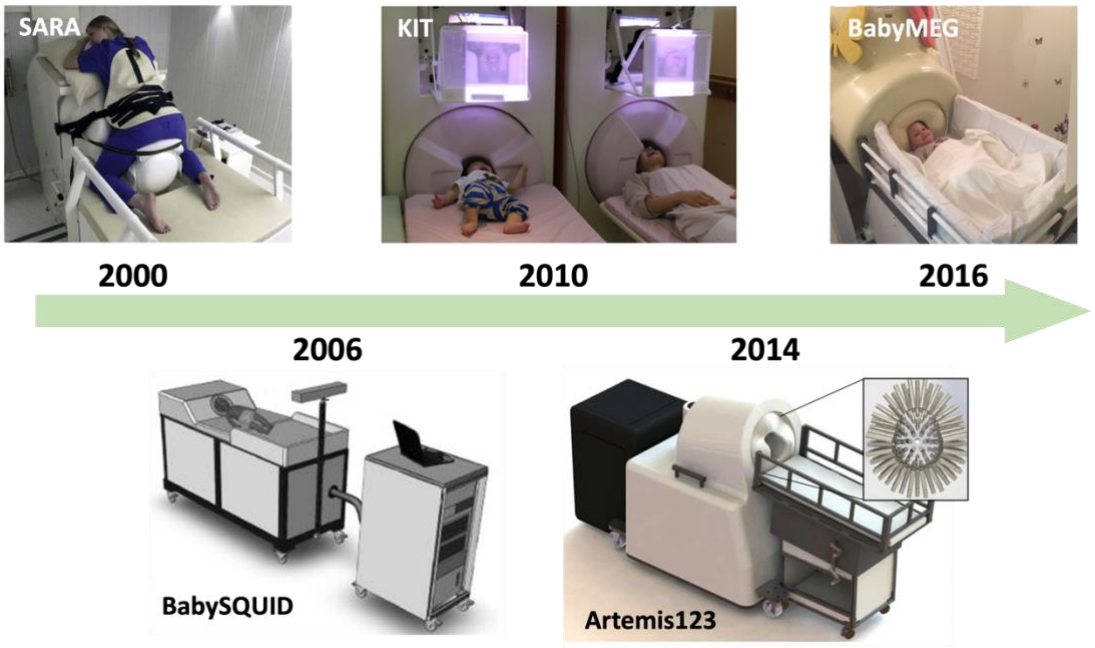


***Figure 1.2. Paediatric MEG systems**. By date, the SARA system with a pregnant participant (Vasung et al., 2019); a schematic of the BabySQUID system (Okada et al., 2006); the KIT infant system (left) next to the adult system (Hirata et al., 2014); the Artemis123 (Roberts et al., 2014) and the BabyMEG (Okada et al., 2016).*

These systems (Figure 1.2) all help to address the problem of small heads. However, for neurodevelopmental studies, where the aim is to scan large numbers of individuals at different ages and look for changes in brain function, there remains a significant confound. Younger participants have to be scanned in a different system to older children or adults, and even with paediatric systems, a new-born baby's head remains much smaller than that of a 4-year-old, meaning the same limitations of changing SNR apply.

1.3 A new generation of MEG

It is clear that there is a demand for a more viable and adaptable MEG system suitable for investigating electrophysiology from birth to adulthood. However, it requires sensitive sensors to detect the minute magnetic field changes at the scalp surface. Previously, this has only been obtainable with cryogenically cooled superconducting technologies. However, in recent years, several promising alternatives to SQUIDs for MEG have been introduced.

- **High-Tc SQUIDs** benefit from a higher critical temperature, allowing a superconductive state (and hence operation) at liquid nitrogen temperatures (77 K), rather than liquid helium temperatures (4 K). This reduces the required size of the insulating gap between the sensor and scalp to less than 1 mm

(Faley et al., 2017), resulting in greater signal magnitude. Unfortunately, high-Tc SQUIDs still require nitrogen cooling and are therefore difficult to deploy in a wearable system.

- **Nitrogen Vacancy (NV) magnetometers** offer a promising flexible alternative. By isolating the electronic spin of an NV centre, these systems become sensitive to very weak magnetic fields, which could be exploited to measure brain activity (Hahl et al., 2022; Rondin et al., 2014). NV magnetometers function at room temperature and can be miniaturised to be housed in casings that can sit on the scalp. However, at the time of writing, the sensitivity at room temperature remains lower than that of SQUIDs, achieving multiple $pT/\sqrt{Hz}$ noise floors, compared to <10 $fT/\sqrt{Hz}$ for a SQUID.
- **Solid-state fluxgate magnetometers** have been developed by a group in Moscow, that can detect MEG signals. They were able to detect alpha oscillations from a single channel (Koshev et al., 2021) and have simulated multi-channel arrays of such sensors (Skidchenko et al., 2023). However, these remain in very early development and the current prototypes suffer from a noise floor that is approximately ten times larger than SQUIDs.
- **Optically pumped magnetometers (OPMs)** manipulate the quantum properties of alkali metal atoms to induce a magnetically sensitive state within an ensemble. OPMs successfully achieve comparable sensitivity to SQUIDs (commercial sensors have a noise floor of ~15 $fT/\sqrt{Hz}$) while maintaining an external temperature closer to body temperature, and so can be held much closer to the scalp surface. Theoretically, the sensitivity of an OPM could exceed that of SQUIDs to achieve sub $fT/\sqrt{Hz}$ (Dang et al., 2010). Additionally, they have already been miniaturised to enable wearability (Sander et al., 2012), and commercialised (Alem et al., 2023; Gutteling et al., 2023; Osborne et al., 2018). Multi-channel, whole-head OPM-based MEG systems have been demonstrated (Boto et al., 2018) and already cost less than conventional SQUID-MEG systems. The bandwidth of OPMs is typically 0 – 150 Hz, which, while lower than that of SQUIDs still covers the range of frequencies of interest in most MEG studies. The dynamic range of the current commercially available sensors is approximately $\pm$1.5 nT. While this is limited, additional methods of background magnetic field control (Holmes et al., 2018) allow sensors to operate without exceeding this range (see Chapter 3). For

these reasons, OPMs have emerged as the stand-out alternative to SQUIDs for the next generation of MEG instrumentation (Brookes et al., 2022).

1.4 Thesis aims

The overarching aim of this thesis is ***to develop and test the first whole-head paediatric OPM-MEG system***. To achieve this, we will address four key areas:

1. We will evaluate the performance of an OPM-MEG system in comparison to a conventional cryogenic MEG system, when detecting signals that oscillate at a low frequency. Low frequencies are a particular challenge for OPMs but are important in the early years of development.
2. We will design and test a method of generating "pseudo-MRIs" using age-matched templates MRIs for MEG analyses. This is particularly important for enabling source-level processing of MEG data from healthy child participants, who may find the MRI scanning environment a challenge.
3. We will construct and demonstrate an OPM-MEG system by scanning a cohort of healthy preschool and school-aged children and healthy adults during a simple sensory task. We acquire whole-head recordings to analyse connectivity and look at developmental trajectories from childhood to adulthood.
4. We will conduct the first multi-centre OPM-MEG study, enabling the collection of (to our knowledge) the largest OPM-MEG dataset to date. We will generate evidence that multi-site data can be analysed collectively, using a visual paradigm in a large group of children aged 2-13 years and adults, to assess the developmental trajectory of gamma-band activity.

1.5 Thesis outline

In what follows,

Chapter 2 introduces the basic idea of neurophysiology and electrical signalling in the brain, describing the signals measured by MEG. Conventional MEG systems are then described, including the principle of operation for SQUID sensors. The analysis techniques typically used with MEG data are covered, including the forward and inverse problem solutions and functional connectivity.

Chapter 3 describes OPMs, from the quantum mechanical principles of optical pumping to the construction of wearable MEG systems. We discuss in detail the commercial QuSpin magnetometers, used for all OPM-MEG data collection described

in this thesis. We then describe the principles of magnetic shielding and consider the evolution of helmet and system design.

Chapters 4 – 7 are experimental chapters that address aims 1-4, respectively.

Chapter 8 provides a summary of our findings and offers concluding remarks on the future of OPM-MEG technology.

2 Magnetoencephalography

2.1 Chapter overview

Magnetoencephalography (MEG) is a non-invasive, direct measure of human electrophysiology that characterises the changes in the magnetic field at the scalp surface that are generated by neural current flow in the brain. This chapter first covers the theory underlying the cellular origins of the MEG signal and describes the types of signals measured. The instrumentation used to collect MEG data is then described, and a typical scanning procedure outlined. Finally, the methods by which data are typically processed are explained, detailing how signals at the scalp surface can be mathematically reconstructed as maps of brain function and source-level time courses. Some of this theory has been published in a contributed textbook chapter, Rhodes et al., Springer Nature (Rhodes et al., 2022).

2.2 Origin of the MEG signal

The human brain is made up of a network of more than 100 billion individual electrically active cells (neurons), interconnected in complex circuits. It is through these cells and circuits that we gain our senses, our perception, and our ability to learn, to move, and to hold memories. These fundamental building blocks of the nervous system facilitate the generation and transportation of electrical signals across the brain. Neurons are supported by a second class of cell, glia. While there are many more glial cells than neurons (2-10 times more (Kandel et al., 2000)), they provide metabolic support and so are not directly involved in passing electrical signals, and are unlikely to contribute to the MEG signal. We will therefore concentrate on the signalling unit of the nervous system, the neuron.

2.2.1 The neuron

While neurons can be separated into many different classes, each with a slightly different morphology, they typically have four main regions:

1. The cell body (or soma) - the metabolic centre. This region contains the cell nucleus, and therefore the cell's genetic information.

2. Dendrites – the signal receivers. Dendrites branch out from the cell body, forming synaptic connections with other neurons, through which they receive signals and transport these to the cell body.
3. The axon – the signal transmitter. A long protrusion from the cell body that carries signals to other neurons. The axon is connected to the cell body via the axon hillock.
4. Presynaptic terminal – the connector. This enlarged region at the end of axon branches forms the connection between the transmitting neuron's axon and the receiving neuron's dendrites, as seen in the boxes in Figure 2.1a.

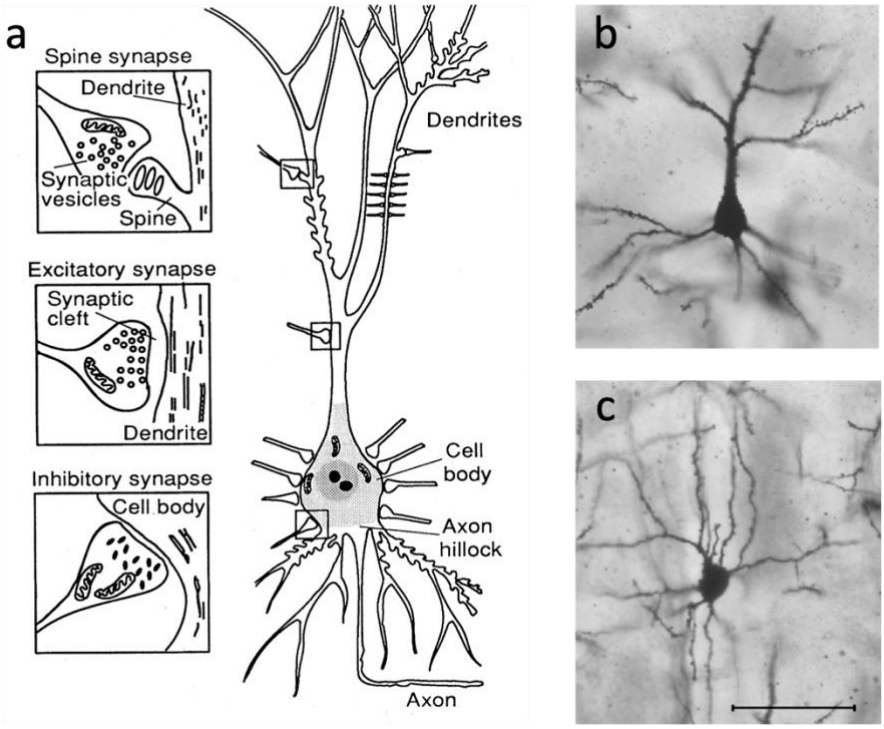


***Figure 2.1. The neuron**. a) The structure of a human neuron (adapted from Hamalainen et al., 1993); b) a pyramidal neuron and c) a stellate neuron (adapted from Churchill et al., 2004)*

Neurons are broadly separated into two categories, principal (pyramidal) cells and interneurons. These cells differ in distribution of dendrites around the cell body. For example, stellate interneurons (Figure 2.1c) have dendrites arranged symmetrically around the cell body; pyramidal neurons (Figure 2.1b) have an asymmetric distribution of dendrites around the cell body. This is important as the orientation of the current-carrying dendrites influences the ability to measure magnetic fields. The spherically symmetric stellate dendritic currents generate fields that effectively cancel one another out, producing little measurable MEG signal. The directionally biased pyramidal dendritic current flow generates magnetic fields that interfere

constructively, and therefore it is pyramidal neurons that likely contribute most to the measured MEG signal.

Neurons are interconnected in a massively complex system of networks, with simple functions requiring electrical impulses to be passed between thousands, if not millions, of cells. How these electrical impulses are generated, and then transmitted, is based on the balance of potential difference across cell membranes.

2.2.2 Resting potential

Resting neurons have a stable membrane potential that is actively maintained by ion transport mechanisms. Cell membrane "pumps" transport ions against concentration gradients using chemical energy (via adenosine triphosphate or ATP), coinciding with ions leaking out along the concentration gradients through "ion channels". At rest, permeability is larger for potassium K^+, causing an excess within the cell interior and an abundance of sodium Na^+ and chloride Cl^- outside the cell membrane, resulting in a negative potential difference of approximately -70 mV across the cell wall. The cell membrane potential, ΔE, is given by the Goldman Equation,

$$\Delta E = \frac{RT}{F} ln \frac{P_K[K^+]_o + P_{Na}[Na^+]_o + P_{Cl}[Cl^-]_i}{P_K[K^+]_i + P_{Na}[Na^+]_i + P_{Cl}[Cl^-]_o} \tag{2.1}$$

where R is the gas constant, T is the absolute temperature, F is the Faraday constant, P_K etc. are the relative permeabilities, $[K^+]_o$ are the extracellular concentrations and $[K^+]_i$ are the intracellular concentrations (Goldman, 1943). The net concentration of these ions always remains largely the same. It is instead the membrane permeability that changes due to impeding electrical impulses.

2.2.3 Neurotransmission

Information is transmitted along neurons to other neurons by action potentials that trigger post-synaptic potentials via the emission of chemical neurotransmitters across synapses (the connections between neurons).

2.2.3.1 Action potentials

If the membrane permeability changes, this can cause the potential difference across the cell wall to decrease beyond a threshold of approximately -55 mV, causing sodium ions to rapidly flow into the cell, while potassium ions flow out. The rapid influx of the positively charged sodium ions briefly increases the potential to approximately +40 mV (depolarisation). At this point, the sodium influx ceases, and potassium ions

continue to flow out of the cell, briefly reaching a point of hyperpolarisation (membrane potential of less than -70 mV) before returning to the resting potential difference of -70 mV by ion channels actively pumping against the concentration gradient (repolarisation). This is shown in Figure 2.2a. This process is typically initiated at the axon hillock (Figure 2.1) and then repeats at adjacent points along the length of the axon, producing a pulse of current, known as an action potential.

The magnetic field produced by an action potential can be described by a quadrupolar field. The amplitude of a magnetic field produced by a quadrupole diminishes rapidly with distance from the source, following an inverse cube law $\left({}^{1}/_{r^3}\right)$. Action potentials are short in duration, typically lasting 1 – 2 ms, meaning that there is a low likelihood for many thousands of action potentials to fire synchronously to allow constructive interference and a large measurable signal. Due to a combination of these two features, action potentials are not likely to be the main contributor to the MEG signal.

2.2.3.2 Post-synaptic potentials

When an action potential reaches the presynaptic terminal (Figure 2.1a), neurotransmitters are released across the synapse, causing a change in permeability at the dendrite wall of the receiving cell. The polarisation of the receiving cell changes, known as the post-synaptic potential, resulting in an intracellular flow of ions, known as the primary current. To restore the resting potential difference, ions are pumped against the concentration gradient, resulting in a secondary extracellular (volume) current between the ion pump and synapse in the opposite direction to the primary current (Figure 2.2b). Post-synaptic signals can be either excitatory or inhibitory. Whether a signal is excitatory or inhibitory depends upon the ion channels opened by neurotransmission. An increase in permeability to sodium and potassium ions leads to depolarization and therefore an excitatory signal, whereas an increase in permeability to chloride results in hyperpolarization and an inhibitory signal. The role of the neuron is to integrate these signals; if a sufficient number of excitatory post-synaptic potentials are received by the neuron, it will become more likely to generate an action potential. Likewise, more inhibitory post-synaptic potentials result in a decrease in the probability of a neuron generating an action potential.

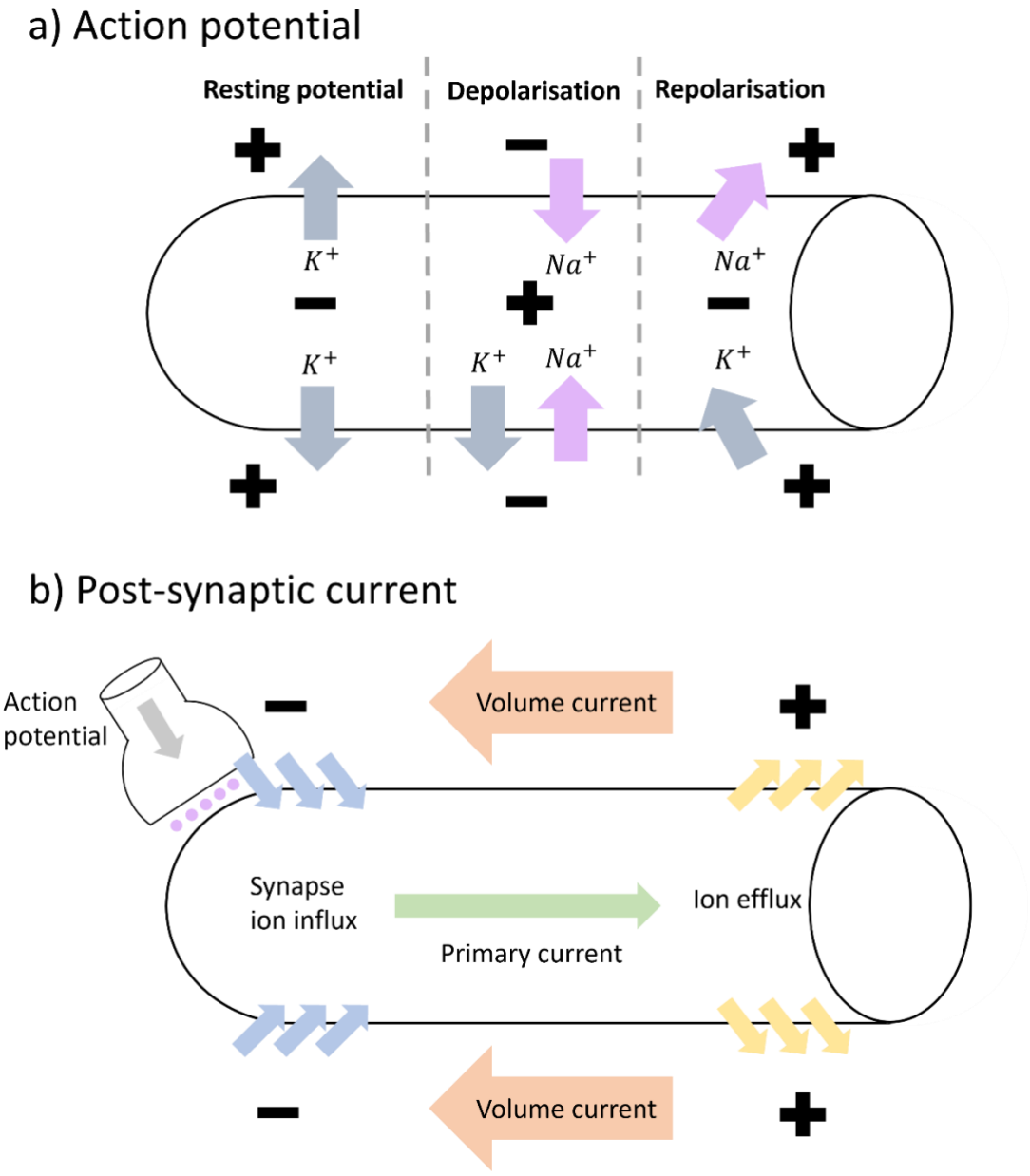


Figure 2.2. Action potential and post-synaptic current. *a) A diagram showing the flow of ions during the resting potential, depolarisation, and repolarisation phases of an action potential. b) A post-synaptic current diagram. At the left, we see the influx of ions from the synapse, and at the right we see the ion pumps, pumping positive ions against the concentration gradient, producing the volume currents in opposing direction to the primary current.*

The post-synaptic current typically lasts in the order of tens of milliseconds (Hamalainen et al., 1993), meaning that there is a greater likelihood of synchronisation of post-synaptic currents than action potentials. Further, the primary post-synaptic current can be modelled as a current dipole, meaning the induced magnetic field from such activity decays with the inverse square of distance $\left({}^{1}/_{r^2}\right)$. Therefore, post-synaptic potentials both produce larger amplitude magnetic fields at distance and are more likely to fire synchronously, meaning they consequently provide the largest contribution to the measured MEG signal.

2.2.3.3 A measurable MEG signal

Mathematically, if a post-synaptic current can be modelled as a current dipole, strength Q, is given by,

$$Q = \lambda I, \tag{2.2}$$

where $\lambda = \sqrt{r_m/r_i}$ is the characteristic decay length, which for the post-synaptic current is dependent on the resistivities of the membrane (r_m) and intracellular fluid (r_i), respectively, and I is the current. The post-synaptic current can be rewritten using Ohm's law to give,

$$Q = \frac{\Delta V \lambda}{R}, \tag{2.3}$$

where R is the cells' internal resistance $R = r_i\lambda$ and ΔV is the change in voltage. However, the resistivity of the intracellular fluid can be expressed in terms of the diameter of the dendrite d and the intracellular conductivity σ_i, such that,

$$r_i = \frac{4}{\sigma_i \pi d^2}, \tag{2.4}$$

and therefore Equation 2.3 can be re-written as,

$$Q = \frac{\Delta V \sigma_i \pi d^2}{4}. \tag{2.5}$$

Typical values for these terms have been determined experimentally ($d = 1\ \mu m, \sigma_i = 1\ \Omega^{-1}m^{-1}, \Delta V = 25\ mV$), yielding $Q \approx 20\ fAm$ for the current from a single unit post-synaptic event (Hamalainen et al., 1993).

Measurable MEG signals are typically of order ~10 fT, which, for a conventional sensor geometry and realistic source depth, requires a source amplitude of approximately 1 nAm. Therefore, a MEG signal requires around 10^4-10^5 synchronised post-synaptic events.

2.2.3.4 Summary

The above theoretical analysis shows that MEG signals, detected outside the head, originate mostly from the constructive interference of the magnetic fields produced by the primary current from post-synaptic potentials of many thousands of synchronously firing pyramidal neurons.

2.3 MEG signals

MEG measures a range of brain signals, from stimulus responses to oscillations that occur without stimuli. We broadly separate these into evoked responses, spontaneous rhythms, and induced responses.

2.3.1 Evoked responses

Evoked responses occur when a participant is exposed to an external stimulus and neural currents in relevant brain regions are time and phase-locked to the onset of the stimulus. Typically, a stimulus is presented over multiple trials, and the signals are averaged, which attenuates noise by the square root of the number of trials and proportionally “enhances” time and phase-locked signals related to the stimuli (see Figure 2.3). Evoked activity from healthy brains typically has relatively consistent morphology, meaning deviation from the norm in terms of timing or temporal morphology is often associated with abnormal function. Repeated stimuli in short succession can drive a steady-state evoked response, which describes evoked activity that mirrors either the driving frequency of the stimuli or its harmonics.

2.3.2 Spontaneous rhythms

Spontaneously occurring rhythmic activity dominates the MEG signal. Spontaneous rhythms are always present, even in the absence of stimuli, and are typically grouped into the following frequency bands based on associated functions and spatiotemporal relationships:

- **Delta (1 – 3 Hz)**: slow delta oscillations are typically associated with deep sleep (Cajochen et al., 1999; Steriade et al., 1993), some cognitive processes involving attention (Harmony, 2013), and may be impaired in multiple pathologies, including traumatic brain injury (Huang et al., 2014).
- **Theta (4 – 8 Hz)**: theta oscillations are associated with memory and cognition, with the hippocampus centrally involved in theta networks (Karakaş, 2020). They are implicated (similarly to delta) in multiple cognitive disorders, including Alzheimer’s (Jeong, 2004) and Parkinson’s (Stoffers et al., 2007). Further, in early life, we see greater power in these low frequency oscillations (Miskovic et al., 2015). Chapter 4 will focus on theta oscillations.
- **Alpha (8 – 12 Hz)**: the first spontaneous rhythms to be detected by EEG in 1929 (Berger, 1929), alpha oscillations are high amplitude, particularly in the occipital cortex. They are thought to gate inhibition and information transfer

(Jensen and Mazaheri, 2010), and are also implicated in pathological function, such as in Alzheimer's Disease (Başar, 2012). The peak frequency of alpha is age-dependent, with a lower frequency in early life (Miskovic et al., 2015).

- **Beta (13 – 30 Hz)**: often associated with sensorimotor function, beta oscillations reduce in amplitude during sensory or motor tasks, and then rebound above baseline following task cessation (Barone and Rossiter, 2021; Pfurtscheller and Lopes da Silva, 1999). However they are not only implicated in sensorimotor tasks and are found across the wider brain (Michalareas et al., 2016; Siegel et al., 2009), and are associated with top-down processing and inhibition (Bastos et al., 2015; Engel and Fries, 2010). Abnormalities in beta are associated with a variety of disorders, including Autism Spectrum Disorder (ASD) (Ronconi et al., 2020), and by pharmaceuticals (Muthukumaraswamy et al., 2013). Chapter 6 focuses on the development of sensorimotor beta oscillations.
- **Gamma (> 30 Hz)**: gamma oscillations are thought to be critical in cognition and information processing. As they are induced by interactions between inhibitory and excitatory neurons, they are thought to provide a metric of cortical inhibitory-excitatory balance (Sohal and Rubenstein, 2019). This is believed to be impaired in a range of neuropathologies, including ASD and schizophrenia. Chapter 7 will focus on gamma oscillations.

These canonical frequency bands do not encompass the entire range of measurable electrophysiological signals; we neglect here the high frequency ripples (80 – 250 Hz) (Kuhnke et al., 2018), or even fast ripples (>250 Hz) (Pizzo et al., 2016), which are typical markers of epileptiform activity. However, it is the above-described frequency bands that are present in healthy brain function that we will focus on. We typically transform MEG signals into the frequency domain to investigate the spectral content of spontaneous rhythms, as shown in Figure 2.3. Often, we focus on how tasks can affect these spontaneous rhythms.

2.3.3 Induced responses

When an external stimulus causes a spontaneous rhythm to change, we describe these as induced responses. These manifest as time-locked but not phase-locked changes in oscillatory signals. This means that averaging signals in the time domain, as we would with evoked activity, attenuates the induced response rather than providing relative amplification. Therefore, to study induced response effects, we typically filter data to a frequency range of interest and calculate the amplitude

envelope of such signals before averaging, as shown in Figure 2.3. Visualising induced responses can be done either by a single frequency band amplitude or across all frequencies using a time-frequency spectrogram (TFS). This provides a way to investigate the change in spectral content over time across a range of frequencies, enabling observation of induced activity across a trial. An example of this is shown in the TFS in Figure 2.3, where a visual task is shown to elicit an increase in amplitude in the gamma band (> 30 Hz) relative to a baseline period, signified by yellow.

2.3.4 Functional connectivity

While different brain regions have been independently associated with different functions, it is the communication between brain regions through complex networks of connections that enables healthy brain function. Such networks are investigated through functional connectivity, whereby signals from different spatial locations are related to one another to measure interdependency and thus infer connectivity. The premise of such measures is that brain regions that are active at the same time, or in the same way, are likely to be "connected" to one another. This was first introduced through fMRI, whereby brain regions which showed a synchronised increase in demand for oxygenated blood were suggested to be connected (Biswal et al., 1995). In electrophysiology, functional connectivity is typically investigated via one of two metrics: phase coherence and amplitude envelope correlation (Figure 2.3).

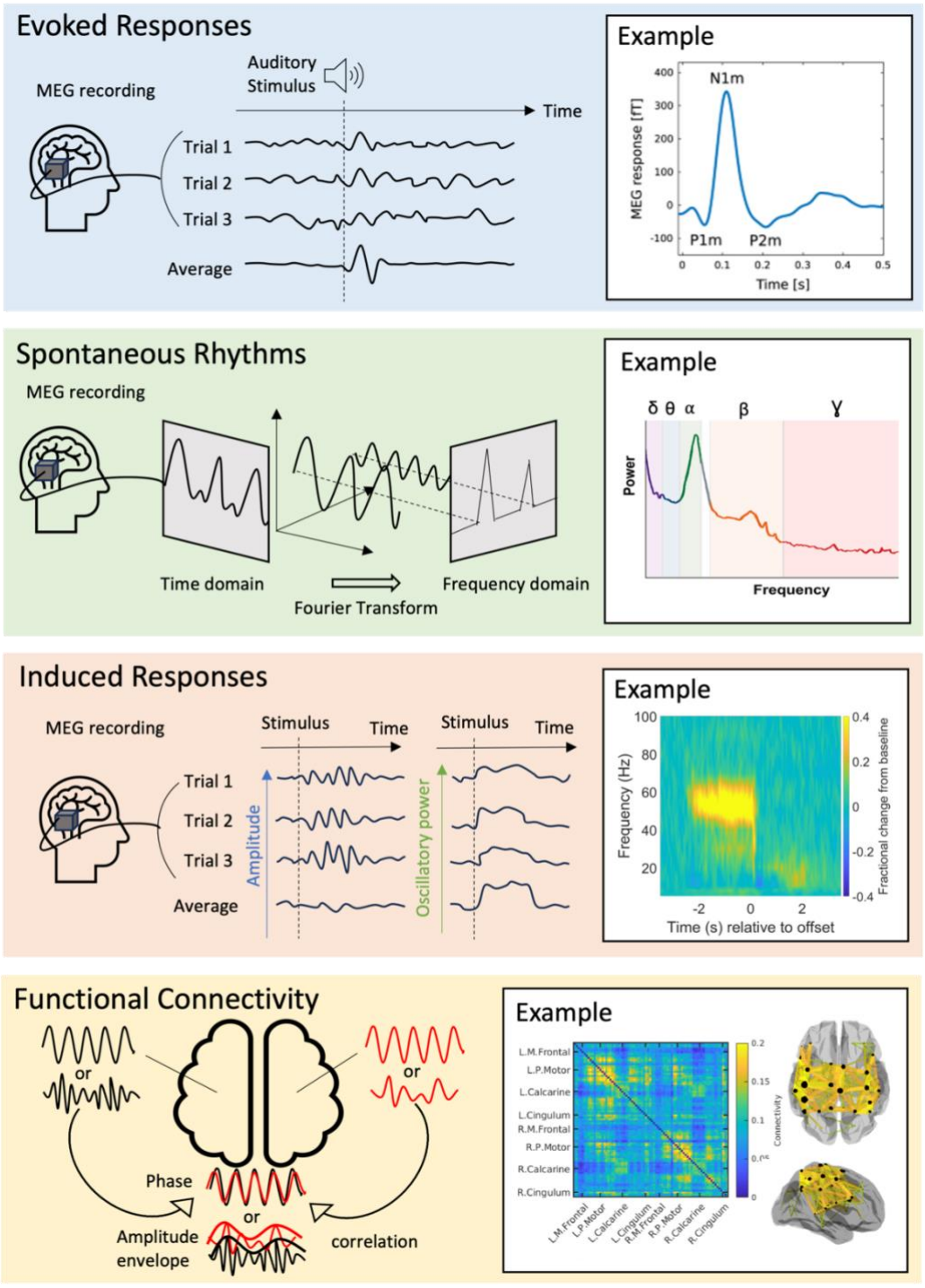


Figure 2.3. MEG Signals. *The top panel shows evoked activity, with a diagram of an auditory evoked activity (left), showing time-locked responses and trial averaging to reduce noise, and an example auditory evoked response (right) (adapted from Hajizadeh et al., 2019). The second panel shows spontaneous rhythms of neural oscillations. The diagram on the left shows how these signals are transformed into the frequency domain to analyse the spectral content. The example (right) shows an average power spectrum from MEG recordings from 434 participants, with separate frequency bands highlighted in different colours (adapted from Rempe et al., 2023). The third panel shows induced responses. The diagram (left) shows how averaging in the time domain diminishes the signals as they are out of phase, but taking the oscillatory amplitude allows averaging to attenuate noise. The example (right) shows an increase in gamma-band amplitude during a visual task (adapted from Hill et al., 2022). The bottom panel shows functional connectivity. The diagram on the left shows how functional connectivity can be measured via phase coherence or amplitude envelope correlation. The example on the right shows a functional connectome showing the amplitude envelope correlation across the beta band during resting state (Boto et al., 2021).*

Phase coherence follows the hypothesis of “communication by coherence”, suggesting that neurons that fire in phase are best placed to receive signals from one another, and so it follows that regions that oscillate in phase are most likely to be functionally connected (Fries, 2005). Amplitude envelope correlation (AEC) instead assumes that synchronised changes in amplitude across specific frequencies of neural oscillations from spatially distinct brain regions suggest connectedness (Engel et al., 2013). It has been shown that networks revealed by AEC analysis of MEG data show high similarity to those observed by fMRI (Brookes et al., 2011c). It has also been shown that (unlike fMRI) the high temporal resolution of MEG offers time-resolved assessment of network dynamics (G.C. O’Neill et al., 2015). A methodological description of AEC analysis is provided in Chapter 2.5.3.

2.4 Collecting MEG data

The amplitude of the MEG signal is tens to hundreds of femtotesla. To put this into perspective, the Earth’s magnetic field is approximately fifty microtesla, and so the neuromagnetic signal is approximately a billion times smaller. Further, interfering magnetic sources in the environment, such as vehicles and the many sources of electrical power present in urban areas, are many orders of magnitude larger than the signals of interest. As such, MEG requires highly sensitive instrumentation to capture the small neuromagnetic signals and analysis techniques are used to disentangle them from environmental magnetic noise. In this section, we will describe the conventional instrumentation used detect the MEG signal.

2.4.1 A brief history of MEG

The first instance of a recording of human neuromagnetic signals used a single sensor comprising a copper pick-up coil of one million turns of wire, housed inside a pod-like magnetically shielded room (Cohen, 1968). Such coils, however, could not be practically made into a multi-channel array to sample magnetic field patterns at multiple spatial locations, and so take advantage of the spatial specificity theoretically provided by MEG. In the years following the first MEG recording, multi-channel arrays were constructed using superconducting quantum interference devices (SQUIDs) (Silver and Zimmerman, 1965). First demonstrated for neuromagnetic recording in the early 1970s (Cohen, 1972), SQUIDs operate through a combination of superconductivity and the Josephson effect (Josephson, 1974, 1962).

2.4.2 Superconductivity

Superconductivity describes the phenomenon whereby a material shows a complete lack of electrical resistance when taken below a critical temperature, T_c. This allows materials to form a perfect conductor (Onnes, 1911). In this superconducting state, materials behave like ideal diamagnets, which expel any magnetic field from within their bulk (Meissner and Ochsenfeld, 1933). However, this effect is destroyed by certain magnetic conditions. In type-I superconducting materials (typically elemental metals), this condition is above a critical magnetic field, B_C. Type-II superconductors, however, have two critical magnetic fields B_{C1} and B_{C2} (where B_{C1}<<B_{C2}), between which magnetic flux can penetrate the material and the density of magnetic flux rises with field strength up to B_{C2}, whereby superconductivity is destroyed (Rjabinin and Shubnikow, 1935).

A theory to explain superconductivity was proposed by Bardeen, Cooper and Schrieffer in 1957 (known as BCS theory - Bardeen et al., 1957). The theory states that an electron passing through a lattice causes the lattice to distort towards it, causing a build-up of positive charge around the electron. If a second electron passes nearby, it is attracted to the positive charge, binding to the first electron, creating a structure known as a Cooper pair that can move around the lattice without friction. The bond between the electrons in the Cooper pair is weak, requiring very little thermal energy to be broken, and hence why superconductivity typically requires very low temperatures.

Critically, Cooper pairs act like bosons and can therefore occupy the same quantum state. BCS theory explains that the binding energy between Cooper pairs increases as more pairs exist in the same state. Consequently, this favours a state where the motion of all Cooper pairs is equivalent, giving rise to the observed supercurrents. We can also describe the ensemble of Cooper pairs by a single wave function of the form,

$$\varphi(r) = \varphi_0 e^{i\boldsymbol{q}\cdot\boldsymbol{r}}, \tag{2.6}$$

where φ_0 is the ground-state wave function of the Cooper pair, $\boldsymbol{r}$ is the centre of mass common to all Cooper pairs and their momentum is $\hbar\boldsymbol{q}$. Therefore, the wave function propagates as an oscillator, with phase dependent on $\boldsymbol{q}\cdot\boldsymbol{r}$. If we consider a superconducting loop, magnetic flux that passes through the loop is quantised and induces a “shielding current” in the loop, which can be manipulated through the Josephson effect to provide a measure of the magnetic field.

2.4.3 Josephson junctions

The Josephson effect dictates that superconductivity remains when introducing an insulating barrier – a Josephson junction – between two superconducting materials (Josephson, 1962). Cooper pairs can tunnel across the barrier without resistance up to a critical current, beyond which, the insulating barrier has resistive properties. If we apply a bias current across the junction that is larger than the critical current, a change in magnetic field will no longer induce a change in current, but rather a change in potential difference. A SQUID typically incorporates two Josephson junctions on either side of a superconducting loop, as shown in Figure 2.4a. The potential difference across the SQUID varies periodically with the flux through the superconducting loop,

$$V \propto A cos\left(\frac{e}{\hbar}\boldsymbol{\Phi}\right), \tag{2.7}$$

where A is the effective area of the SQUID loop, e is the electron charge, $\hbar$ is the reduced Planck's constant and the period is the flux quantum $\boldsymbol{\Phi_0} = 2.7 \times 10^{-1} Wb$. Because the flux quantum is so small, SQUIDs are highly sensitive to the tiny neuromagnetic fields.

However, due to the periodicity of Equation 2.7, a potential difference does not correspond to a unique amount of flux. Therefore, feedback circuitry with lock-in detection enables measurement of the flux as an approximately linear function of potential difference by applying equal and opposite magnetic flux to maintain constant flux. The applied potential therefore provides the measurement of flux.

Figure 2.4 shows a diagram of SQUID circuitry, including a flux transformer that is coupled to the SQUID. This allows the SQUID to be held distal from the scalp surface, shielding it from external interference.

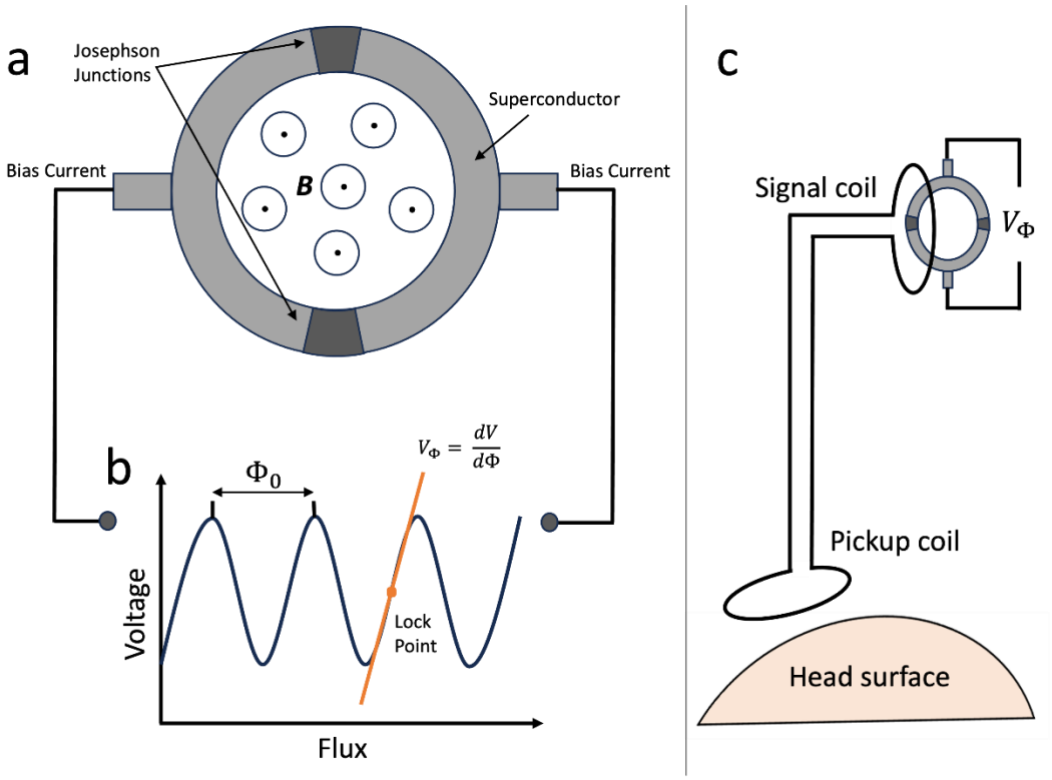


***Figure 2.4. SQUID Circuitry**. a) A diagram of a SQUID, showing two Josephson junctions around a superconducting ring, through which there is a magnetic field, B, and b) the voltage output from a SQUID and how feedback circuitry enables measurement of flux. c) A flux transformer to shield the SQUID from external interference.*

2.4.4 Magnetometer vs. gradiometer

SQUID magnetometers comprise a single superconducting wire-wound loop placed close to the head, which is magnetically coupled to the SQUID; gradiometers comprise two loops, separated by some baseline distance and also coupled to the SQUID. Gradiometers can be planar, or axial, depending on the orientation of the separation between the coils, shown in Figure 2.5.

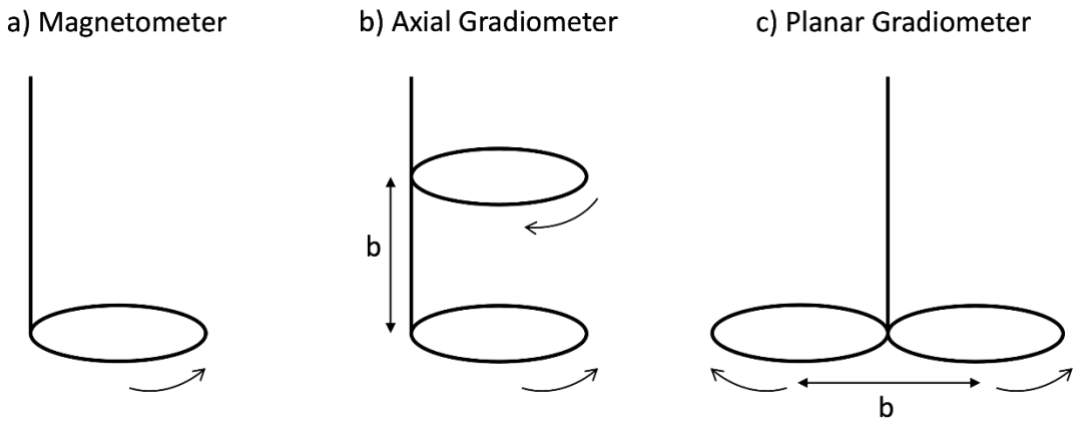


***Figure 2.5. Gradiometry**. a) A SQUID magnetometer comprising a single loop, b) an axial gradiometer, with the baseline labelled as b, and c) a planar gradiometer with baseline b.*

The principle of gradiometry is to enhance sensitivity to nearby sources of magnetic field (i.e., sources from within the head) and reject common-mode interference (i.e., distal sources whose field does that vary rapidly in space) by measuring the magnetic field gradient rather than the absolute magnetic field. However, this comes at a cost of some depth resolution in the brain, meaning that gradiometers are less sensitive to deep brain sources than magnetometers. Conventional MEG systems have been based on magnetometers, gradiometers, or a mixture of the two.

The gradiometer layouts shown in Figure 2.5 are classed as first-order gradiometers. It is possible to improve interference rejection further by introducing higher-order field gradients, however, building physical high-order gradiometers is impractical. Instead, we can form synthetic higher-order gradiometers by using a combination of the first-order gradiometers and reference sensors distal to the head. The CTF MEG system used in the work described in this thesis employs synthetic 3rd-order gradiometry using distal pickup coils that measure three orthogonal field components to characterize external interference for rejection (Vrba, 2002).

2.4.5 Conventional MEG data acquisition

Conventional MEG systems comprise multiple elements. The work described in this thesis uses a CTF MEG system (CTF, Canada), and so here we focus on this system for the following description. The system is housed within a magnetically shielded room (see Chapter 3.6 for a description of passive magnetic shielding). Waveguides in the walls of the shielded room provide the ability to feed connections from within the room to the control room, enabling data acquisition and control of stimulus equipment. Typically, visual stimuli are presented via back projection onto a screen in front of the participant. Stimulus equipment can include (but is not limited to) button

response boxes, earphones for auditory stimuli, eye tracking systems or nerve stimulation devices.

A participant is positioned on the patient support, which can be held in either a seated position or supine, with their head held inside a helmet that sits at the bottom of the gantry containing the Dewar of SQUIDs and liquid helium. Padding holds the participant's head in place to provide comfort and reduce head motion relative to sensors within the helmet. A video camera and intercom system allow the experimenter to monitor and communicate with the participant during acquisition.

The CTF system uses a dedicated electronics rack to read out SQUID measurements and perform analogue to digital conversion before transfer to the acquisition PC, which allows real-time visualisation and data recording. Stimuli are controlled by a separate stimulus PC, which sends timing information in the form of triggers to the acquisition PC to align stimuli and MEG data recording.

2.4.5.1 Safety

SQUID sensors are housed in a Dewar of liquid helium, which is held at approximately 4 K. There are risks associated with the use of cryogens, including cryogenic burns and asphyxiation by oxygen displacement from helium gas, should large volumes of liquid helium evaporate. Participant safety is ensured by continuous monitoring and communication during MEG recordings, oxygen sensors in the shielded room to monitor the oxygen levels throughout, and flow rate meters to warn of excess helium evaporation.

2.4.5.2 Quality control

Before running a MEG experiment, a recording is typically taken without any participant in the room. This "empty room noise recording" is inspected to ensure that the noise floor is within a suitable range for MEG acquisition (< 10 $fT/\sqrt{Hz}$), and to identify sources of interference. Once the participant is inside the room, with their head held in the helmet, tests are run to ensure that artefacts are not excessively large that would suggest the presence of magnetic materials (typically asking the participant to blink, take a deep breath and clench their jaw).

2.4.5.3 Coregistration

Coregistration is the process by which the locations of the MEG sensors are determined relative to a participant's anatomy. For conventional MEG systems, the positions and orientations of each sensor are well-known relative to one another, and so the position of the array must only be determined relative to the brain structure. Fiducial coils are attached to the nasion and preauricular points before data collection

and are energised throughout the scan to track head position relative to MEG sensors. Either prior to, or following MEG data acquisition, the locations of the fiducial coils are determined relative to the participant's head/face shape using 3D digitisation, typically with a Polhemus system (Polhemus FASTRAK 3D digitiser). The head shape from the 3D digitisation is aligned to an anatomical MR image (typically T1 MPRAGE). First, the scalp is extracted from the MRI using edge detection via software tools such as FieldTrip (Oostenveld et al., 2011). An iterative closest point (ICP) algorithm is then used to match 3D digitisation points to the MRI scalp. This yields the location of the fiducial markers relative to the participant's MRI anatomy, and therefore the sensor array relative to brain structure.

2.5 Mathematical modelling of MEG signals

While MEG signals can be analysed in sensor space, to take advantage of the high spatial resolution afforded by measuring magnetic fields (rather than electric potentials), we most often analyse data in source space. This process involves estimating the currents within the brain that would generate the magnetic field measured at the scalp surface. This is known as the inverse problem solution and is ill-posed (Hadamard, 1902), meaning that a single magnetic field measured by the MEG sensors could be generated by an infinite number of different current distributions within the brain. To estimate a solution, we must first construct a model that describes the magnetic field generated by a known current source in the brain (known as the forward model). We then apply a set of assumptions in order to infer a solution to the inverse problem.

2.5.1 The forward problem

The forward problem involves the calculation of the magnetic field distribution outside the head produced by a known current distribution inside the head. This is a well-posed problem, but we must still make approximations to solve it analytically. First, we assume that, when viewed from a distance, the magnetic field from the synchronous firing of a large number of post-synaptic currents looks like a magnetic field that would result from a single current dipole. Next, we make an approximation that describes the conductivity of the tissues between the current source and the MEG detector. There are multiple ways to do this, ranging in complexity.

2.5.1.1 Single sphere model

The simplest forward model was developed by Sarvas (1987) and describes the head as a single conducting spherical volume, G, with homogeneous conductivity.

We can use Maxwell's equations to describe the current density, $\boldsymbol{J}$, in terms of the electric field $\boldsymbol{E}$ and local magnetic field $\boldsymbol{B}$, such that,

$$\begin{aligned} \boldsymbol{\nabla} \cdot \boldsymbol{E} &= \frac{\rho}{\epsilon} \\ \boldsymbol{\nabla} \times \boldsymbol{E} &= \frac{-\partial \boldsymbol{B}}{\partial t} \\ \boldsymbol{\nabla} \cdot \boldsymbol{B} &= 0 \\ \boldsymbol{\nabla} \times \boldsymbol{B} &= \mu_0 \left(\boldsymbol{J} + \epsilon \frac{\partial \boldsymbol{E}}{dt} \right), \end{aligned} \tag{2.8}$$

where ρ is the charge density, ϵ is the permittivity and μ_0 is the permeability of free space. Typically, as the neuromagnetic fields we measure vary at less than 100 Hz, we can make a quasi-static approximation (Hamalainen et al., 1993), removing the time dependence to modify two of Maxwell's equations to,

$$\begin{aligned} \boldsymbol{\nabla} \times \boldsymbol{E} &= 0 \\ \boldsymbol{\nabla} \times \boldsymbol{B} &= \mu_0 \boldsymbol{J}. \end{aligned} \tag{2.9}$$

The magnetic field at a location $\boldsymbol{r}$ outside the spherical conductor due to a current density at $\boldsymbol{r'}$ inside the conductor is described by the Ampère-Laplace law, the continuous counterpart of the Biot-Savart law that applies to closed wire loops (Hamalainen et al., 1993) such that,

$$\boldsymbol{B}(\boldsymbol{r}) = \frac{\mu_0}{4\pi} \int_G \mathrm{J}(\boldsymbol{r'}) \times \frac{\boldsymbol{r} - \boldsymbol{r'}}{|\boldsymbol{r} - \boldsymbol{r'}|^3} dv, \tag{2.10}$$

where dv is a volume element of the volume G. Recall from Figure 2.2 that post-synaptic potentials provide two types of current that contribute to the MEG signal: the primary current, $\boldsymbol{J^P}(\boldsymbol{r'})$, and the volume current $\boldsymbol{J^V}(\boldsymbol{r'})$. The total current density at $\boldsymbol{r'}$ is therefore the sum of the primary and volume currents,

$$\boldsymbol{J}(\boldsymbol{r'}) = \boldsymbol{J^P}(\boldsymbol{r'}) + \boldsymbol{J^V}(\boldsymbol{r'}). \tag{2.11}$$

As the volume currents are from the electrical field generated outside the cell by the ion pumps, we can rewrite this as

$$\boldsymbol{J}(\boldsymbol{r'}) = \boldsymbol{J^P}(\boldsymbol{r'}) + \sigma \boldsymbol{E}(\boldsymbol{r'}), \tag{2.12}$$

where σ represents the local conductivity at $\boldsymbol{r}'$, which we have approximated as homogeneous throughout G. We can rewrite the electrical field as the negative of the gradient of the electrical scalar potential, V, and so

$$\boldsymbol{J}(\boldsymbol{r}') = \boldsymbol{J}^{\boldsymbol{P}}(\boldsymbol{r}') - \sigma\nabla V(\boldsymbol{r}'). \tag{2.13}$$

If we now substitute Equation 2.13 into Equation 2.10, we find that,

$$\boldsymbol{B}(\boldsymbol{r}) = \frac{\mu_0}{4\pi}\int_G \boldsymbol{J}^{\boldsymbol{P}}(\boldsymbol{r}') \times \frac{\boldsymbol{r}-\boldsymbol{r}'}{|\boldsymbol{r}-\boldsymbol{r}'|^3}\,dv - \frac{\mu_0\sigma}{4\pi}\int_G \nabla V(\boldsymbol{r}') \times \frac{\boldsymbol{r}-\boldsymbol{r}'}{|\boldsymbol{r}-\boldsymbol{r}'|^3}\,dv. \tag{2.14}$$

Note that the first term represents the contribution to the magnetic field from the primary current, and the second term represents the contribution from the volume currents. Concentrating on the second term and using the vector identity $\nabla a \times \nabla b = \nabla \times (a\nabla b)$, letting $\nabla a = \nabla V$ and $\nabla b = \frac{\boldsymbol{r}-\boldsymbol{r}'}{|\boldsymbol{r}-\boldsymbol{r}'|^3}$ so that,

$$\boldsymbol{B}^{\boldsymbol{V}}(\boldsymbol{r}) = -\frac{\mu_0\sigma}{4\pi}\int_G \nabla \times V(\boldsymbol{r}')\frac{\boldsymbol{r}-\boldsymbol{r}'}{|\boldsymbol{r}-\boldsymbol{r}'|^3}\,dv. \tag{2.15}$$

We can then apply the generalised Stokes theorem, $\int_G \boldsymbol{\nabla} \times \boldsymbol{X}dv' = \int_S \hat{\boldsymbol{n}} \times \boldsymbol{X}ds$, where $\hat{\boldsymbol{n}}$ represents a vector normal to the surface element ds, rewriting Equation 2.15 as,

$$\boldsymbol{B}^{\boldsymbol{V}}(\boldsymbol{r}) = -\frac{\mu_0\sigma}{4\pi}\int_S \hat{\boldsymbol{n}}(\mathbf{r}') \times V(\boldsymbol{r}')\frac{\boldsymbol{r}-\boldsymbol{r}'}{|\boldsymbol{r}-\boldsymbol{r}'|^3}\,ds, \tag{2.16}$$

where $\hat{\boldsymbol{n}}(\mathbf{r}')$ is the vector normal at location $\mathbf{r}'$. If we re-write Equation 2.14 with the modified volume current term, we get a simplified form of the Geselowitz equation (Geselowitz, 1970),

$$\boldsymbol{B}(\boldsymbol{r}) = \frac{\mu_0}{4\pi}\int_G \boldsymbol{J}^{\boldsymbol{P}}(\boldsymbol{r}') \times \frac{\boldsymbol{r}-\boldsymbol{r}'}{|\boldsymbol{r}-\boldsymbol{r}'|^3}\,dv - \frac{\mu_0\sigma}{4\pi}\int_S \hat{\boldsymbol{n}}(\mathbf{r}') \times V(\boldsymbol{r}')\frac{\boldsymbol{r}-\boldsymbol{r}'}{|\boldsymbol{r}-\boldsymbol{r}'|^3}\,ds. \tag{2.17}$$

This formula states that the volume current can be represented by a set of fictitious currents on the surface of the conductor. If we place a MEG sensor at location $\boldsymbol{r}$ with sensitivity to the magnetic field component oriented radially from the conductor surface, $\hat{\boldsymbol{e}}_{\boldsymbol{r}}$, such that $B_r(\boldsymbol{r}) = \boldsymbol{B}(\boldsymbol{r}) \cdot \hat{\boldsymbol{e}}_{\boldsymbol{r}}$, we find,

$$B_r(\boldsymbol{r}) = \frac{\mu_0}{4\pi}\int_G \boldsymbol{J}^{\boldsymbol{P}}(\boldsymbol{r}') \times \frac{\boldsymbol{r}-\boldsymbol{r}'}{|\boldsymbol{r}-\boldsymbol{r}'|^3} \cdot \hat{\boldsymbol{e}}_{\boldsymbol{r}}\,dv - \frac{\mu_0\sigma}{4\pi}\int_S \hat{\boldsymbol{n}}(\mathbf{r}') \times V(\boldsymbol{r}')\frac{\boldsymbol{r}-\boldsymbol{r}'}{|\boldsymbol{r}-\boldsymbol{r}'|^3} \cdot \hat{\boldsymbol{e}}_{\boldsymbol{r}}\,ds. \tag{2.18}$$

Looking at the second term we see that,

$$\hat{\boldsymbol{n}}(\mathbf{r}') \times (\boldsymbol{r} - \boldsymbol{r}') \cdot \hat{\boldsymbol{e}}_{\boldsymbol{r}} = (\hat{\boldsymbol{n}}(\mathbf{r}') \times \mathbf{r} - \hat{\boldsymbol{n}}(\mathbf{r}') \times \mathbf{r}') \cdot \hat{\boldsymbol{e}}_{\boldsymbol{r}}, \tag{2.19}$$

and for a spherical conductor, as shown in Figure 2.6, we find that $\hat{\boldsymbol{n}}(\mathbf{r}') \times \mathbf{r}' = 0$ as they are parallel, and $\hat{\boldsymbol{n}}(\mathbf{r}') \times \mathbf{r} \cdot \hat{\boldsymbol{e}}_{\boldsymbol{r}} = 0$, as the cross product of $\hat{\boldsymbol{n}}(\mathbf{r}') \times \mathbf{r}$ is perpendicular to $\hat{\boldsymbol{e}}_{\boldsymbol{r}}$. Therefore, the second term of Equation 2.18 is zero in the case of the spherical model, giving,

$$B_r(\boldsymbol{r}) = \frac{\mu_0}{4\pi} \int_G \boldsymbol{J}^{\boldsymbol{P}}(\boldsymbol{r}') \times \frac{\boldsymbol{r} - \boldsymbol{r}'}{|\boldsymbol{r} - \boldsymbol{r}'|^3} \cdot \hat{\boldsymbol{e}}_{\boldsymbol{r}} dv. \tag{2.20}$$

The resulting radial magnetic field then only depends on the primary current. The volume current (and therefore the conductivity of the medium) has no effect. The single sphere is thus an attractive model to use due to its simplicity.

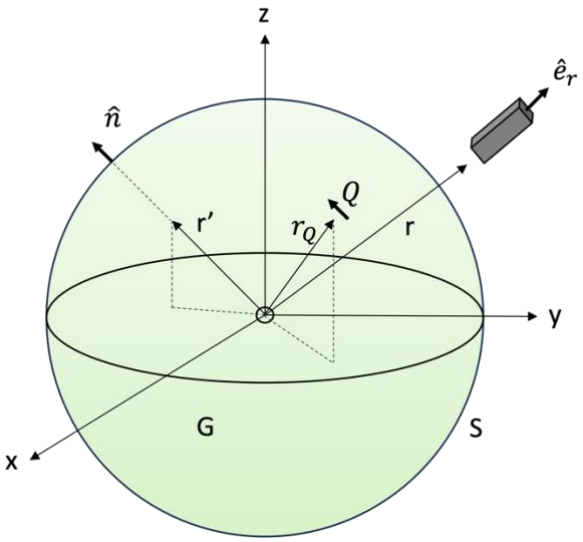


Figure 2.6. Single Sphere Model. *A schematic describing the single sphere forward model. We approximate the head as a spherical volume G bound by surface S. A current dipole Q is at location* $\boldsymbol{r}_{\boldsymbol{Q}}$*. r' is a location inside the volume conductor generating a magnetic signal at the detector at r.*

If we now introduce the dipole model, which states that the primary current is approximated as a unidirectional current at a point, $\boldsymbol{r}_{\boldsymbol{Q}}$ (shown in Figure 2.6). Mathematically,

$$\boldsymbol{J}^{\boldsymbol{P}}(\boldsymbol{r}') = \boldsymbol{Q}\delta(\boldsymbol{r}' - \boldsymbol{r}_{\boldsymbol{Q}}), \tag{2.21}$$

Where $\boldsymbol{Q}$ represents the magnitude and direction of the dipole and the Dirac delta function, δ, means that the current is zero at all locations in the conductor except from at $\boldsymbol{r}_{\boldsymbol{Q}}$. Equation 2.20 now becomes,

$$B_r(\boldsymbol{r}) = \frac{\mu_0}{4\pi}\int_G \boldsymbol{Q}\delta(\boldsymbol{r}' - \boldsymbol{r_Q}) \times \frac{\boldsymbol{r} - \boldsymbol{r}'}{|\boldsymbol{r} - \boldsymbol{r}'|^3} \cdot \hat{\boldsymbol{e}}_{\boldsymbol{r}} dv. \tag{2.22}$$

Here, the δ function allows us to remove the volume integral, giving,

$$B_r(\boldsymbol{r}) = -\frac{\mu_0}{4\pi}\frac{\boldsymbol{Q} \times (\boldsymbol{r} - \boldsymbol{r_Q})}{|\boldsymbol{r} - \boldsymbol{r_Q}|^3} \cdot \hat{\boldsymbol{e}}_{\boldsymbol{r}}. \tag{2.23}$$

This provides us with the radial component of the magnetic field. To take the entire magnetic field vector, we first assume that there are no currents outside the head ($\boldsymbol{J} = 0$ outside G). If we then consider Maxwell's equation $\boldsymbol{\nabla} \times \boldsymbol{B} = \mu_0 \boldsymbol{J} = \boldsymbol{0}$, we can describe the magnetic field vector in terms of the magnetic scalar potential, $U(\boldsymbol{r})$, such that,

$$\boldsymbol{B}(\boldsymbol{r}) = -\mu_0 \nabla U(\boldsymbol{r}). \tag{2.24}$$

Consider a line integral of $\nabla U(r)$ along the radius $\boldsymbol{r} + t\hat{\boldsymbol{e}}_{\boldsymbol{r}}$, $0 \leq t \leq \infty$.

$$\begin{aligned} U(\boldsymbol{r}) &= -\int_0^\infty \nabla U(\boldsymbol{r} + t\hat{\boldsymbol{e}}_{\boldsymbol{r}}) \cdot \hat{\boldsymbol{e}}_{\boldsymbol{r}} dt \\ &= \frac{1}{\mu_0}\int_0^\infty \boldsymbol{B}(\boldsymbol{r} + t\hat{\boldsymbol{e}}_{\boldsymbol{r}}) \cdot \hat{\boldsymbol{e}}_{\boldsymbol{r}}\, dt \end{aligned} \tag{2.25}$$

Recall that $B_r(\boldsymbol{r}) = \boldsymbol{B}(\boldsymbol{r}) \cdot \hat{\boldsymbol{e}}_{\boldsymbol{r}}$,

$$U(\boldsymbol{r}) = \frac{1}{\mu_0}\int_0^\infty B_r(\boldsymbol{r} + t\hat{\boldsymbol{e}}_{\boldsymbol{r}}) dt, \tag{2.26}$$

and that our radial component is described by the magnetic field due to the primary current, $\boldsymbol{B}_P(\boldsymbol{r})$ in the radial direction,

$$U(\boldsymbol{r}) = \frac{1}{\mu_0}\int_0^\infty \boldsymbol{B}_P(\boldsymbol{r} + t\hat{\boldsymbol{e}}_{\boldsymbol{r}}) \cdot \hat{\boldsymbol{e}}_{\boldsymbol{r}} dt. \tag{2.27}$$

Now substituting in Equation 2.23,

$$U(\boldsymbol{r}) = \frac{\boldsymbol{Q}}{4\pi} \times (\boldsymbol{r} - \boldsymbol{r_Q}) \cdot \hat{\boldsymbol{e}}_{\boldsymbol{r}} \int_0^\infty \frac{\boldsymbol{dt}}{|\boldsymbol{r} + t\hat{\boldsymbol{e}}_{\boldsymbol{r}} - \boldsymbol{r_Q}|^3}. \tag{2.28}$$

which has a solution described by Sarvas (1987),

$$U(\boldsymbol{r}) = \frac{1}{4\pi}\frac{\boldsymbol{Q} \times \boldsymbol{r_Q} \cdot \boldsymbol{r}}{F}, \tag{2.29}$$

where $F = a(ra + \boldsymbol{r}^2 - \boldsymbol{r_Q} \cdot \boldsymbol{r})$, $\boldsymbol{a} = \boldsymbol{r} - \boldsymbol{r_Q}$, $a = |\boldsymbol{a}|$ and $r = |\boldsymbol{r}|$.

Finally, the total magnetic field outside the conductor is obtained by substituting Equation 2.29 into 2.24 yielding

$$\boldsymbol{B}(\boldsymbol{r}) = -\frac{\mu_0}{4\pi F^2}\left(F\boldsymbol{Q} \times \boldsymbol{r_Q} - \boldsymbol{Q} \times \boldsymbol{r_Q} \cdot \boldsymbol{r}\nabla F\right), \tag{2.30}$$

with $\nabla F = (r^{-1}a^2 + a^{-1}\boldsymbol{a} \cdot \boldsymbol{r} + 2a + 2r)\boldsymbol{r} - (a + 2r + a^{-1}\boldsymbol{a} \cdot \boldsymbol{r})\boldsymbol{r_Q}$.

The single sphere model is the simplest approximation for the forward model. However, it suffers from oversimplification, neglecting the inhomogeneity in conductivity of different tissues in the head and poorly representing the shape of the head. This has nonuniform effects across different brain regions. Specifically, frontal and frontotemporal regions are particularly poorly modelled by a sphere (Hämäläinen and Sarvas, 1989).

2.5.1.2 Multiple spheres model

The multiple spheres model provides an improved approximation for the geometry of the head by generating a single (best-fitting) sphere for each MEG sensor (Huang et al., 1999). Each sphere is placed within the vicinity of the sensor but such that it fits within the skull geometry. This results in a series of homogeneous overlapping spheres that better fit the geometry of the brain than a single sphere. The forward solution is then computed independently for each sphere, and a combination of all spheres is used for subsequent source modelling. This has particular advantages for areas of the brain that deviate from spherical geometry (Lalancette et al., 2011).

2.5.1.3 BEM

A boundary element model (BEM) is a method of estimating the forward field by representing the head anatomy as a set of nested compartments with different conductivities (typically separating into the brain, skull, and scalp). This method most accurately models the individual brain geometry, however, this comes at a high computational cost. This would also likely lead to errors in combination with template anatomy (see Chapter 5).

2.5.1.4 Single shell model

A practical alternative to BEM forward solutions is the single shell model, which assumes that the head is a homogeneous single volume with an isotropic conductivity profile (Nolte, 2003). The single shell model uses a spherical harmonic basis to approximate the head, such that a lead field (the forward model solution a sensor) at position $\boldsymbol{r}$ is,

$$\boldsymbol{L}(\boldsymbol{r}) = \boldsymbol{L}(\boldsymbol{r})_{sphere} - \nabla U(\boldsymbol{r}), \tag{2.31}$$

where $\boldsymbol{L}(\boldsymbol{r})_{sphere}$ is the lead field based on the single sphere approximation, and $U(\boldsymbol{r})$ is a spherical harmonic basis set, such that lead fields will be tangential to the surface of the volume conductor. For MEG recordings, Stenroos et al. (2014) found that the single shell model performed comparably to a BEM, and so the work described in this thesis uses a single shell forward model.

2.5.2 The inverse problem

To trace MEG signals back to their cortical origin, we must generate a solution to the MEG inverse problem. This states: given a measured magnetic field distribution outside the head, can we reconstruct the underlying current distribution in the brain? Mathematically, this problem is ill-posed, but a range of processes to approximate the solution have been described.

2.5.2.1 Lead fields and the generative model

A key principle in MEG analysis is the generative model. This describes the magnetic field, $m_i(t)$, measured by a sensor, i, at time t given a current dipole of strength q at some location $\boldsymbol{r}'$ in the brain at time t. The generative model is written,

$$m_i(t) = \int_V L_i(\boldsymbol{r}') \cdot q(\boldsymbol{r}', t) dV', \tag{2.32}$$

where $L_i(\boldsymbol{r}')$ describes the magnetic field that would be measured at sensor i if there were a unit current at location $\boldsymbol{r}'$. The integral sums all possible volume elements in the brain and thus all possible current sources. We simplify this expression by discretising the brain volume into M cubic voxels ($j = 1,2,3, \ldots M$), each containing a single unit current dipole. We can then rewrite (2.32) as a sum across voxels,

$$m_i(t) = \sum_{j=1}^{M} L_{i,j} \cdot q_j(t), \tag{2.33}$$

or in matrix form,

$$\boldsymbol{m}(t) = \boldsymbol{L}\boldsymbol{q}(t), \tag{2.34}$$

where $\boldsymbol{L}$ is the lead field matrix with dimensions of $N \times M$, where N is the number of channels and $\boldsymbol{q}(t)$ is a vector length M describing the current dipole strengths at each voxel location. Each column of $\boldsymbol{L}$ indicates how a single dipole (one of M possible dipoles) affects all N sensors (the forward field), whilst each row shows the dipoles that affect field at a single sensor (the lead field). In principle, the inverse problem is simply the process of inverting Equation 2.34. However, as $\boldsymbol{L}$ is both non-square

(there are many more voxels in the brain than MEG sensors) and singular, it is not possible to find $\boldsymbol{L}^{-1}$ to determine $\boldsymbol{q}(t)$. Instead, we must make some assumptions to estimate a solution.

2.5.2.2 Beamforming

Whilst there are other methods to solve the inverse problem (e.g., equivalent current dipoles (Cohen, 1968) or minimum norm estimation (Hämäläinen and Ilmoniemi, 1994)), in this thesis we concentrate on a method called beamforming. First developed for radar technology (Van Veen and Buckley, 1988), a beamformer is a spatial filter that gives a weighting to each MEG sensor, such that the weighted combination of the sensor measurements produces an estimation of source strength for each location in the brain (see Figure 2.7). Mathematically,

$$\hat{q}_{\boldsymbol{\theta}}(t) = \boldsymbol{w}_{\boldsymbol{\theta}}^{\boldsymbol{T}}\boldsymbol{m}(t), \tag{2.35}$$

where $\hat{q}_{\boldsymbol{\theta}}(t)$ is the beamformer estimate of the true source strength at $\boldsymbol{\theta}$, a given voxel position and current orientation and $\boldsymbol{w}_{\boldsymbol{\theta}}$ are the weighting parameters.

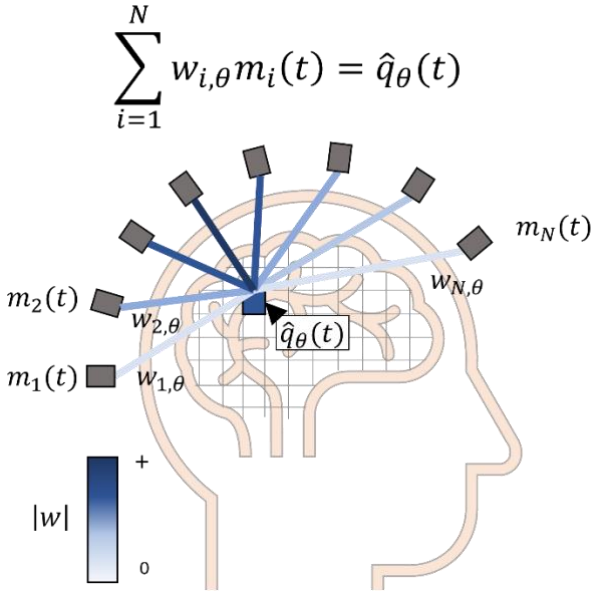


Figure 2.7. Beamforming method. *A schematic describing how the combination of the weights and sensor measurements provides the estimated source strength.*

Almost all (linear) inverse problem solutions can be cast in this way (Sekihara and Nagarajan, 2008) and differ by how we calculate the weights. In beamforming, we derive the weights by variance minimisation, such that the weights ensure unit gain at $\boldsymbol{\theta}$ while minimising signals from all other locations, including interfering non-brain signals. We can express this mathematically as,

$$\min_{\boldsymbol{w}_\theta} \left| \langle \hat{q}_{\boldsymbol{\theta}}{}^2(t) \rangle \right| \text{ subject to } \boldsymbol{w}_{\boldsymbol{\theta}}^{\boldsymbol{T}}\boldsymbol{L}_{\boldsymbol{\theta}} = 1, \tag{2.36}$$

where $\boldsymbol{L_\theta}$ is the forward field for $\boldsymbol{\theta}$ and $\langle \hat{q}_{\boldsymbol{\theta}}{}^2(t)\rangle$ describes the variance in the estimated source signal. Using Equation 2.35, we can evaluate the variance such that,

$$\begin{aligned}\langle \hat{q}_{\boldsymbol{\theta}}{}^2(t)\rangle &= \langle \boldsymbol{w_\theta^T m}(t)\rangle\langle \boldsymbol{w_\theta^T m}(t)\rangle \\ &= \boldsymbol{w_\theta^T}\langle \boldsymbol{m}(t)\boldsymbol{m^T}(t)\rangle \boldsymbol{w_\theta} \\ &\approx \boldsymbol{w_\theta^T C w_\theta},\end{aligned} \tag{2.37}$$

where $\boldsymbol{C}$ is an estimation of the covariance matrix of the MEG sensor data (and so has dimensions of $N \times N$). The covariance of data recorded at channels i and j is usually calculated as,

$$C_{ij} = \frac{1}{P}\sum_{p=1}^{P} m_i(t_p)\, m_j(t_p), \tag{2.38}$$

for P timepoints.

A solution to this constrained minimisation problem is analytically derived using Lagrange multipliers (Van Veen et al., 1997), resulting in the beamformer equation,

$$\boldsymbol{w_\theta^T} = \frac{\boldsymbol{L_\theta^T C^{-1}}}{\boldsymbol{L_\theta^T C^{-1} L_\theta}}. \tag{2.39}$$

In the case where $\boldsymbol{C}$ is close to singular (which can arise due to various reasons including too few samples with respect to dimensions, data with very high signal-to-noise or highly correlated sensor outputs), regularisation can be implemented using methods such as the Tikhonov method to enable inversion (Backus and Gilbert, 1968; Brookes et al., 2008). This involves calculating the regularised covariance such that, $\boldsymbol{C}_r = \boldsymbol{C} + \mu\boldsymbol{I}$, where μ is the regularisation parameter added to the diagonal ($\boldsymbol{I}$ is the identity matrix).

We have assumed that the orientation of the current source is known and represented within $\boldsymbol{\theta}$, however in practice this is not the case. We must therefore calculate the orientation of the current dipole. While there are multiple methods to achieve this, one such method calculates the orientation for which the maximum signal-to-noise ratio is given. For a spherical volume conductor, radial sources do not contribute to the MEG signal and even for realistic models, radial components are small, and so we constrain the search for the optimal dipole orientation by computing weights for different azimuthal angles ϕ from 0 to π. From this, the maximum SNR can be calculated using a pseudo-Z statistical approach, which for each angle is,

$$\mathrm{Z}_{\boldsymbol{r},\phi} = \frac{\boldsymbol{w}_{r,\phi}^{T} \boldsymbol{C} \boldsymbol{w}_{r,\phi}}{\boldsymbol{w}_{r,\phi}^{T} \boldsymbol{\Sigma} \boldsymbol{w}_{r,\phi}}, \tag{2.40}$$

where $\boldsymbol{\Sigma}$ is the noise covariance matrix, which can be approximated as the identity matrix. The source orientation angle can be determined by iterating through all possible angles to find the maximum pseudo-Z statistic. However, this is computationally expensive. An alternative method (used in this thesis) is proposed by Sekihara et al. (2004) and instead determines the optimal orientation using generalised eigenvalue decomposition. This effectively produces the same result but with less computational expense. Once the weights are calculated, MEG sensor data can be transformed into source space for subsequent analysis.

It is useful to generate images that provide spatial information about which regions of the brain are active during a task. This is commonly done by first computing beamformer weights for all brain locations and then contrasting stimulus and rest periods using the pseudo-T statistic, which is calculated by,

$$\mathrm{T} = \frac{\boldsymbol{w}_{\boldsymbol{\theta}}^{T} \boldsymbol{C}_{ON} \boldsymbol{w}_{\boldsymbol{\theta}} - \boldsymbol{w}_{\boldsymbol{\theta}}^{T} \boldsymbol{C}_{OFF} \boldsymbol{w}_{\boldsymbol{\theta}}}{2\left(\boldsymbol{w}_{\boldsymbol{\theta}}^{T} \boldsymbol{C}_{OFF} \boldsymbol{w}_{\boldsymbol{\theta}}\right)}, \tag{2.41}$$

where $\boldsymbol{w}_{\boldsymbol{\theta}}$ are the beamformer weights tuned to the location/orientation $\boldsymbol{\theta}$, and $\boldsymbol{C}_{ON}$ and $\boldsymbol{C}_{OFF}$ are the data covariance matrices computed during the stimulus and rest windows, respectively. This can be repeated for a grid of voxels across the entire brain, or for voxels in particular regions of interest as defined by a functional atlas.

Finally, we can use beamforming to extract "virtual electrode" time courses as follows,

$$VE = \widehat{\boldsymbol{q}}(t) = \boldsymbol{w}^{T} \boldsymbol{m}(t). \tag{2.42}$$

This describes a signal as if an electrode were placed in a specific location in the brain, giving spatial information in combination with temporal information. This process is used for all experimental chapters in this thesis (Chapters 4 – 7).

2.5.3 Functional connectivity

Beamforming offers a means to estimate electrophysiological signals in different brain regions. Functional connectivity extends this concept by looking for statistical interdependencies between signals at spatially distinct locations. If the signals from two or more distinct regions are related, that implies that these regions are in communication (see Figure 2.3). There are multiple metrics for calculating the statistical relationship between two signals, the work in this thesis focuses on

amplitude envelope correlation (AEC). AEC assesses the relationship of fluctuating oscillatory amplitude across two band-limited signals, typically filtered to one of the canonical frequency bands (see section 2.3.2). The most popular method (and the one used in this thesis) to generate the amplitude envelope is through the Hilbert transform. The complex analytic signal, $\hat{\boldsymbol{z}}(t)$, can be derived from the band-limited signal, $\widehat{\boldsymbol{q}}(t)$, and the Hilbert transform H, such that,

$$\hat{\boldsymbol{z}}(t) = \widehat{\boldsymbol{q}}(t) + iH[\widehat{\boldsymbol{q}}(t)]. \tag{2.43}$$

The Hilbert transform describes the convolution of the band-limited signal with the function $h = 1/\pi t$ such that,

$$H[\widehat{\boldsymbol{q}}(t)] = \frac{1}{\pi} P\left[\int_{-\infty}^{\infty} \frac{\widehat{\boldsymbol{q}}(\tau)}{t-\tau} d\tau\right], \tag{2.44}$$

where $P[\ ]$ describes the Cauchy principal value of the integral, avoiding the singularity at $t = \tau$.

The amplitude information can be extracted from Equation 2.43 as,

$$Envelope = \|\hat{\boldsymbol{z}}\| = \sqrt{\left(\widehat{\boldsymbol{q}}(t)\right)^2 + (H[\widehat{\boldsymbol{q}}(t)])^2}. \tag{2.45}$$

For each pair of regions, the Pearson's correlation coefficient is computed as a measure of the strength of the connection, which can be represented as

$$r_{E_1E_2} = \frac{\sum_{i=1}^{n}\left(E_{1_i} - \overline{E_1}\right)\left(E_{2_i} - \overline{E_2}\right)}{\sqrt{\sum_{i=1}^{n}\left(E_{1_i} - \overline{E_1}\right)^2}\sqrt{\sum_{i=1}^{n}\left(E_{2_i} - \overline{E_2}\right)^2}}, \tag{2.46}$$

where $\boldsymbol{E_1}$ and $\boldsymbol{E_2}$ are the amplitude envelope time courses for any two regions, with $\overline{E_1}$ and $\overline{E_2}$ signifying the corresponding mean values. This can be repeated across many pairs of locations, typically from parcellated functionally related brain regions, to evaluate whole-brain connectivity matrices.

2.5.3.1 Source leakage

Due to the ill-posed nature of the inverse problem, it is inevitable that a signal from a single brain region will be contaminated by signals from other brain regions. This can impact functional connectivity measures, and so must be accounted for. In this thesis we use pairwise orthogonalization to reduce the source leakage (Brookes et al., 2012). If we consider our two amplitude envelope time courses $\boldsymbol{E_1}(t)$ and $\boldsymbol{E_2}(t)$, we can create new orthogonal signals $\boldsymbol{a}(t)$ and $\boldsymbol{b}(t)$ by the linear projection of one signal to the other,

$$\boldsymbol{a}(t) = \boldsymbol{E_1}(t) \qquad (2.47)$$
$$\boldsymbol{b}(t) = \boldsymbol{E_2}(t) - \boldsymbol{E_1}\beta,$$

where $\beta = \boldsymbol{E_1}^{\dagger}\boldsymbol{E_2}$ and $\boldsymbol{E_1}^{\dagger}$ is the pseudo-inverse of $\boldsymbol{E_1}$. This is repeated across all pairs of signals. An alternative method for reducing leakage between signals from other sources is symmetric orthogonalization (Colclough et al., 2015), whereby all signals are orthogonalised simultaneously. While this typically has better performance in conventional MEG systems (Colclough et al., 2015), it requires the number of time courses to be less than or equal to the rank of the data, and so is not suitable for smaller MEG sensor arrays such as those used in this thesis.

2.6 Chapter summary

In this chapter, we have introduced the theory of MEG. We first described the origin and types of MEG signals and how these are measured by conventional MEG hardware. We then explained the maths behind how extracranial magnetic field signals can be related to brain activity and outlined typical MEG analyses. In the next chapter, we will introduce the next generation of MEG using optically pumped magnetometers.

3 Optically pumped magnetometer-based MEG

3.1 Chapter overview

This chapter discusses magnetoencephalography based upon the optically pumped magnetometer (OPM); the highly sensitive magnetic field sensor that forms the basis of the work described in this thesis. We will first provide an overview of the OPM-MEG system, outlining the separate components that make MEG measurements possible. We will then describe each component in detail. First, we will cover a brief history of OPMs and the physics behind how they operate, detailing the quantum mechanics that facilitate the sensitive measurement of biomagnetic signals. Following this, we discuss the benefits of OPM sensors that can measure in all three axes (triaxial), and how triaxial OPMs are constructed. We then describe how the system is shielded from external magnetic fields using both passive and active magnetic shielding. Finally, we consider the subject interface, and how we combine these components to design a system appropriate for human scanning. Some of this theory has been published in a contributed textbook chapter, Rhodes et al., Springer Nature (Rhodes et al., 2022).

3.2 Introduction

3.2.1 OPM-MEG system overview

Optically pumped magnetometers form the basis of a new generation of MEG systems. However, a complete OPM-MEG system comprises multiple components to enable measurement of the neuromagnetic field. A system typically comprises:

- Multiple OPM sensors
- A sensor array design that has optimum cortical coverage across regions of interest (or the whole brain) and assists in noise rejection
- Magnetic shielding (passively through magnetically shielded rooms and active shielding through electromagnetic coils)
- A subject interface (i.e., a way to position the participant within the shielded environment and a helmet/method to hold the sensor array close to the participant's head)

- A means to coregister the sensor array to the participant's anatomy

In this chapter, we will discuss each element of the OPM-MEG system. We start first with the principle of optical pumping and the evolution of the optically pumped magnetometer.

3.2.2 A brief history of OPMs

Optical pumping describes the method by which a light source (i.e., a laser) is used to manipulate the property of atomic spin, thereby changing the quantum state, or energy level, via absorption or emission of energy (Kastler, 1951). As spin governs interactions with magnetic fields, optical pumping can be used to induce a state in which an ensemble of atoms can become highly sensitive to small changes in magnetic field, thereby forming the foundation of a magnetic field sensor or magnetometer. Optically pumped magnetometers were first realised in the late 1950s and early 1960s (Bell and Bloom, 1957; Bloom, 1962). Sensitivities suitable for MEG measurements were reached in the 2000s (Dang et al., 2010; Kominis et al., 2003), and showcased in 2006 by the first single-channel recording of an auditory evoked response (Xia et al., 2006). However, at this stage, OPMs were large benchtop systems, mostly due to cumbersome optical instruments. Following advances in microfabrication and miniaturization techniques, OPMs were reduced from the bench top towards lightweight sensor heads (Johnson et al., 2013; Knappe et al., 2010; Mhaskar et al., 2012; Sander et al., 2012; Schwindt et al., 2007; Shah et al., 2007; Shah and Wakai, 2013; Sheng et al., 2017), capable of forming MEG arrays (see prototype OPMs in Figure 3.1).

The work described in this thesis was undertaken using QuSpin Zero-Field Magnetometers (QZFM), which were the first commercially available MEG-viable OPM sensors. More recently, two other companies have begun selling OPMs for MEG measurements, FieldLine and Mag4Health. The FieldLine OPM sensors have a similar design to the QuSpin magnetometers, with both OPMs based on optically pumping Rubidium-87 atoms. The Mag4Health OPMs are instead built around the manipulation of Helium-4 atoms to induce magnetic sensitivity, benefitting from cooler operational temperatures but suffering from poorer sensitivity and a larger sensor footprint. The three commercial OPMs are shown in Figure 3.1g-i. We will focus on the QZFM (g) for the following discussion.

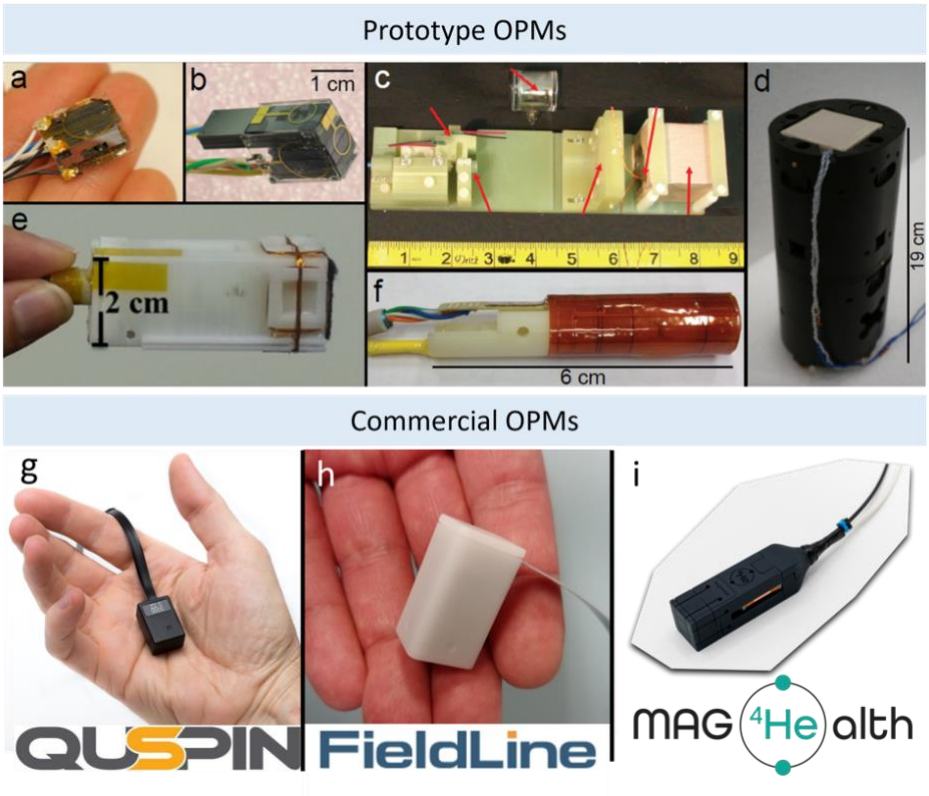


Figure 3.1. OPM sensors for MEG. *Prototype OPMs adapted from Boto, 2019. a) Sander et al., 2012, b) (Mhaskar et al., 2012), c) (Johnson et al., 2013), d) (Kamada et al., 2015) e) (Shah and Wakai, 2013), f) (Sheng et al., 2017). Below are the three commercial OPMs for MEG at the time of writing from g) QuSpin Inc., Louisville, CO, USA h) Fieldline Inc., Boulder, CO, USA, i) Mag4Health, Grenoble, France.*

3.2.3 The QuSpin OPM

At the time of writing, there are three generations of QZFM. All three generations share four key elements:

- A circularly polarised 795 nm wavelength laser tuned to the D1 transition of Rubidium-87 (^{87}Rb)
- A glass cell containing a vapour of ^{87}Rb heated to 150 °C using resistive coils
- Electromagnetic coils surrounding the glass cell to offset background magnetic fields and enable the generation of a modulation field (see below)
- A photodetector to measure light intensity transmitted through the glass cell

A simple diagram of the key components in the QZFM is shown in Figure 3.2a. The first generation (Gen-1) became commercially available in 2016 and is shown in Figure 3.2b. Gen-1 QZFM has casing dimensions of 13×19×110 mm^3 and contains a 3×3×3 mm^3 glass cell of ^{87}Rb offset 6 mm from the end of the sensor casing. Gen-1 QZFM is dual-axis and so is sensitive to two orthogonal axes, one oriented radially along the sensor's length and one tangential axis. The sensor head is connected to

an electronics box via 6.5 m of heavy cabling. While these sensors were used for initial MEG measurements (Barry et al., 2019; Boto et al., 2018, 2017; Hill et al., 2019; G. Roberts et al., 2019; Sander et al., 2020; Vivekananda et al., 2020), the size and weight made them difficult to implement in whole-head arrays. In the work described in this thesis, they are instead used to measure changes in the background magnetic field as reference sensors in Chapter 4.

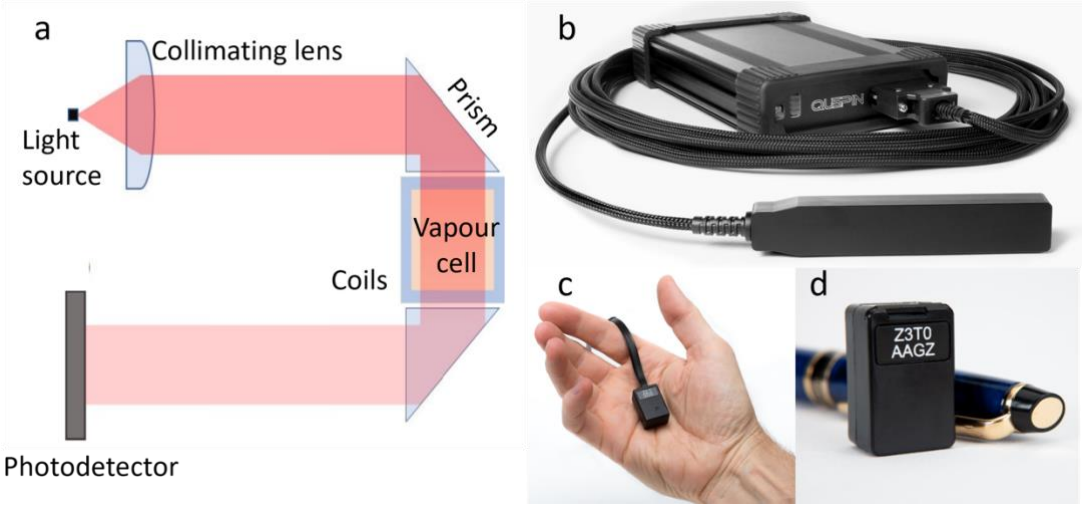


Figure 3.2. QZFM. *a) Basic schematic of components inside QZFM (adapted from (Osborne et al., 2018), b) Gen-1 QZFM with cable and electronics, c) Gen-2 QZFM with flex cable, d) Gen-3 triaxial sensor head detached from removable cabling (adapted from QuSpin)*

In 2018, a second generation of QZFM was made available (Figure 3.2c). Gen-2 QZFM has a smaller casing dimension of 12.4×16.6×24.4 mm^3, a cell stand-off of 6.5 mm^3 and a more lightweight cable design, with 60 cm of flex cable between the sensor head and the thicker cabling, reducing weight across a wearable array. This smaller and lightweight design enabled the first whole-head measurements (Hill et al., 2020), however as the cable was directly attached to the internal components in the OPM sensor head, Gen-2 sensors were susceptible to damage.

The third generation QZFM (Gen-3, Figure 3.2d) addressed this issue with a detachable sensor head in 2021. This generation saw the development of triaxial sensitivity. The work described in Chapters 4, 5 and 6 uses the triaxial Gen-3 QZFM, while the work described in Chapter 7 uses a combination of dual-axis Gen-3 and triaxial QZFM.

3.2.4 QZFM operation

Each QZFM is attached to an individual electronics unit, which controls and measures from its individual sensor head via proprietary software, interfaced via a USB

connection. Before measurement can be made, the environment required for optical pumping must be prepared. First, current is applied to the coils surrounding the vapour cell to resistively heat the vapour to 150 °C for operation within the SERF regime (Section 3.3.3). The laser is then tuned to the appropriate frequency for the D1 transition of ^{87}Rb for optical pumping and a modulation signal is applied via the on-board coils to facilitate measurement via lock-in detection. Finally, a zero-field environment within the vapour cell is induced by the application of current to the on-board coils to cancel any remnant magnetisation. In the “open-loop” mode of operation, the “field-zeroing” currents are determined prior to the MEG recording and are fixed throughout. In this mode, the voltage from the photodetector gives a measure of the external magnetic field and is multiplied by a conversion factor to obtain magnetic field measurements in Tesla (standard is 2.7 V nT^{-1}).

3.3 The quantum origin

3.3.1 Principle of operation

A classical interpretation of the working principle of an OPM can be described in three steps:

1. **Preparation**: atoms are prepared in a well-defined spin state, classically interpreted as a specific orientation with respect to a circularly polarised laser beam. The atomic ensemble becomes coherently aligned, and therefore spin polarised.
2. **Interaction**: atomic spins interact with an impinging magnetic field, causing a change in state (or orientation) via the absorption of laser light, with the amount of light absorption proportional to the size of the magnetic field.
3. **Detection**: detection of the laser light passing through the atomic ensemble provides an indirect measure of the magnetic field.

3.3.2 Quantum mechanical explanation

To better understand why an ensemble of Rubidium-87 atoms can become sensitive to small perturbations in magnetic fields, we must consider quantum mechanics. ^{87}Rb is an alkali metal, meaning it has a single valence electron in the outermost shell. This outermost electron can exist in several discrete quantum states and must absorb or emit energy to transition between them. Consider the intrinsic properties of such a

system. The total angular momentum of an atom F is the sum of the angular momentum of the nucleus I and electron J. Mathematically,

$$F = J + I. \tag{3.1}$$

The electron angular momentum is a product of the orbital angular momentum L and a spin angular momentum S,

$$J = L + S. \tag{3.2}$$

For ^{87}Rb, the nuclear spin quantum number is $I = {}^{3}/_{2}$ and the electron spin quantum number is $S = {}^{1}/_{2}$. The orbital angular momentum quantum number is $L = 0$ for the ground state and $L = 1$ for the first excited state.

A difference in energy levels arises due to interactions between the electron's orbital angular momentum L and its spin angular momentum S, known as fine structure splitting, shown in Figure 3.3. The energy difference between levels is described by the quantum number J, which can take values $|L - S| \leq J \leq |L + S|$. Therefore, the ground state (with $L = 0$) has a single fine structure level with $J = {}^{1}/_{2}$, while the first excited state has two possible energy levels, with $J = {}^{1}/_{2}$ and $J = {}^{3}/_{2}$. The first of these transitions is labelled the D1 transition and occurs when the electron absorbs photon energy equal to the difference in energy between the two states, where photon energy is described by,

$$E = hv = \frac{hc}{\lambda}, \tag{3.3}$$

where h is Planck's constant, c is the speed of light (in a vacuum), v is the frequency of the laser light and λ is the wavelength of the laser light. A transition can therefore be driven by tuning the frequency of the incident light. For the D1 transition of ^{87}Rb, 795 nm wavelength laser light is required.

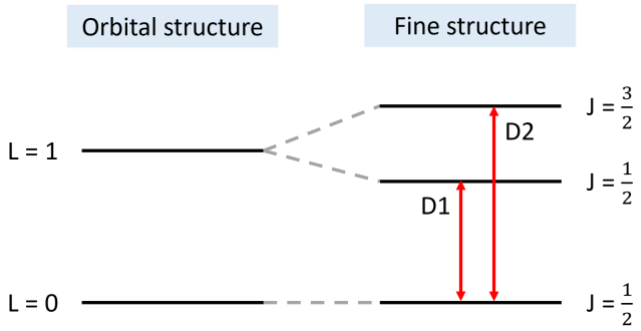


***Figure 3.3. Fine structure**. Interaction between the electron's orbital angular momentum and spin angular momentum splits the first excited state into two possible energy levels. Transitions from the ground state to these energy levels are labelled D1 and D2.*

A further splitting in energy levels arises from the interaction between the electron's total angular momentum J and the nuclear angular momentum I, as shown in Figure 3.4. The possible hyperfine states are described by the total angular momentum F, which can take values $|I - J| \leq F \leq |I + J|$. For the D1 transition, this splits the ground and first excited state into two further energy levels, where $F = 1$ or $F = 2$.

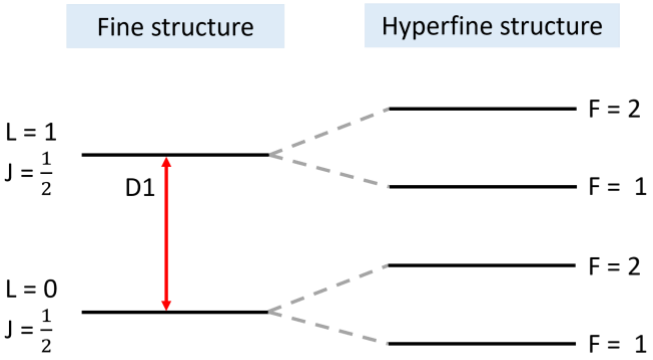


***Figure 3.4. Hyperfine structure**. Interaction between the electron's total angular momentum and nucleus angular momentum causes further splitting from the ground and first excited states in the D1 transition into two energy levels with F = 1 and F = 2.*

Finally, the presence of a magnetic field splits the hyperfine energy levels further, known as Zeeman splitting, shown in Figure 3.5. We introduce a final quantum number, m_f, which is related to the component of the angular momentum along the laser beam axis and has allowed values of integer steps between $-F$ and F, leading to an additional three energy levels for the $F = 1$ and five energy levels for the $F = 2$ hyperfine states.

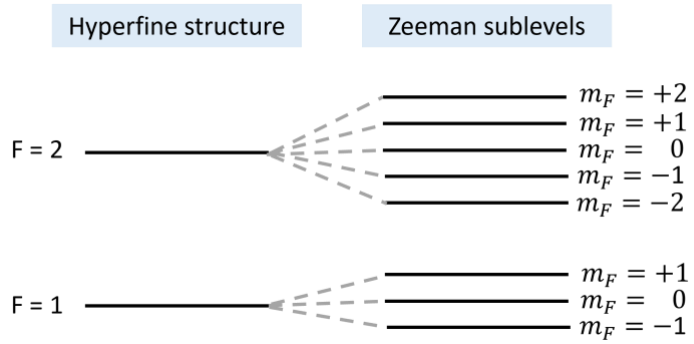


***Figure 3.5. Zeeman structure**. Interaction with a magnetic field causes further splitting of the hyperfine energy levels of the ground state.*

The energy difference between Zeeman levels is given by,

$$\Delta E = g_F \mu_B B, \tag{3.4}$$

where g_F is the hyperfine Lande g-factor, μ_B is the Bohr magneton and B is the magnetic field. The magnetic moment of an electron in this magnetic field precesses at the Larmor frequency,

$$\omega = \gamma B, \tag{3.5}$$

where γ is the gyromagnetic ratio, which for the valence electron in ^{87}Rb is given by,

$$\frac{\gamma}{2\pi} = \frac{g_F \mu_B}{\hbar}, \tag{3.6}$$

where $\hbar$ is the reduced Planck's constant. For the $F = 1$ hyperfine state $g_F = -\frac{1}{2}$, and for $F = 2$, $g_F = +\frac{1}{2}$. The electron spins therefore precess in opposite directions depending on the state they occupy.

Two mechanisms influence the energy level occupied by an electron: the absorption of laser light to move up to higher energy levels and the spontaneous emission of energy to move to lower energy levels. The rules that govern these two effects are known as the selection rules. Specifically, the laser causes two effects: the D1 transition and an increase in m_f, which arises when the laser light is positively circularly polarised. Spontaneous emission transitions the atom from the excited $L = 1$ to the ground $L = 0$ state by emitting a photon. This reverses the laser's effect on the D1 transition but does not entirely reverse the laser's effect on m_f as spontaneous emission is equally likely to produce changes of $m_f = -1,0,1$. Therefore, a third of the atoms retain their polarisation, a third gain an increment of polarisation and only a third lose the same increment, resulting in a net effect of "pumping" atoms into the highest Zeeman sublevel ($m_f = 2$) of the ground state, shown in Figure 3.6.

In this state, atoms can no longer make any energy transitions as there are no energy levels greater than $m_f = 2$ for the electrons to occupy. Therefore, if the atom exists in the $L = 0, F = 2, m_f = 2$ state, the laser transfers no energy to the ensemble, the vapour becomes effectively transparent, and light simply passes through unaffected. In this state, the vapour becomes highly polarised, where many atoms occupy the same state (classically interpreted as aligning with the laser beam) and collectively produce a strong net magnetisation aligned along the laser axis. This strongly polarised gas is highly sensitive to magnetic fields, as any perpendicular components of impinging magnetic fields produce a torque on the net magnetisation. This allows a transition between energy states, which requires the absorption of laser light and a resulting dip in the measured intensity of light at the photodetector.

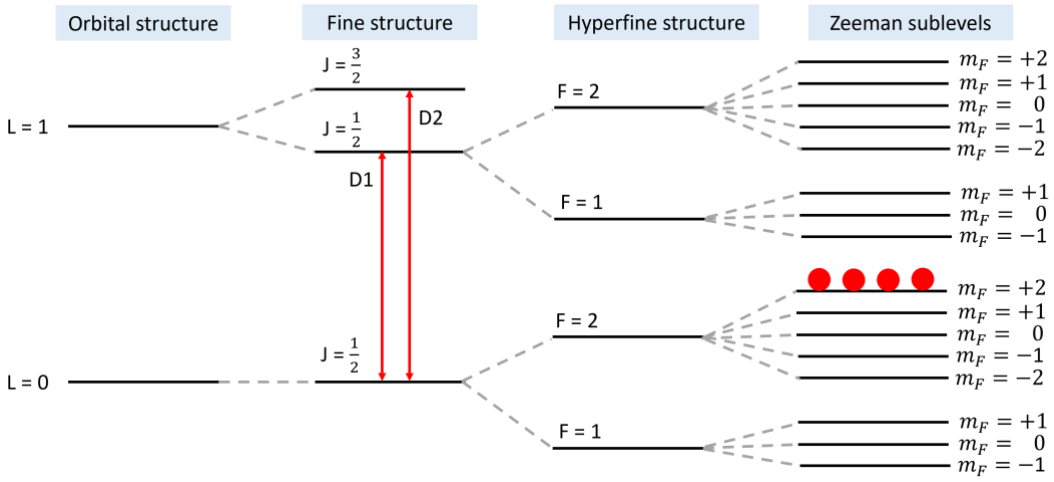


Figure 3.6. Optical pumping. *Optical pumping of ^{87}Rb using circularly polarised light tuned to the D1 transition. Spontaneous emission is equally likely to be in each of the $\mathbf{m_f = 0, -1, 1}$ states, resulting in a net effect of optical pumping to the highest Zeeman sublevel, shown by the red dots (Tierney et al., 2019).*

3.3.3 The SERF regime

The coherence of the atomic spins must be maintained over sufficient timescales for magnetic sensitivity to be used for measurement. However, atoms can be depolarised via multiple processes, including diffusion of atoms, spin-exchange and spin-destruction collisions, collisions with cell walls and interactions with the pumping laser (Happer, 1972). These effects are known as relaxation and are reduced by tuning experimental parameters. Coherence loss via wall collision can be reduced using an anti-relaxation coating (Robinson et al., 1958) or by including buffer gases (Brossel et al., 1955). However, in high density alkali vapours, spin-exchange is the dominant source of relaxation (Purcell and Field, 1956), whereby collisions between atoms allow the exchange of electron spin, as shown in Figure 3.7a. The rate at which such

collisions occur is the spin-exchange relaxation rate (R_{SE}) and is dependent on the time between collisions (T_{SE}) such that,

$$R_{SE} = \frac{1}{T_{SE}}. \tag{3.7}$$

To obtain the femto-Tesla sensitivities required to measure the neuromagnetic field, magnetometers must be designed to eliminate relaxation due to spin-exchange collisions (Seltzer, 2008), known as spin-exchange relaxation-free (SERF) magnetometers (Allred et al., 2002). Briefly, at high atomic densities and within a very low magnetic field environment, the spin-exchange rate will exceed the precession frequency ($R_{SE} \gg \gamma B$), meaning individual atoms precess by only a small angle between spin-exchange collisions (Figure 3.7b). As each atom samples the different energy sublevels in a short period of time, and there are more Zeeman sublevels for $F = 2$, the atomic ensemble precesses coherently in a slower net positive rate described by

$$\omega_0 = \frac{\gamma B}{Q}, \tag{3.8}$$

where Q is the nuclear slowing-down factor, a function of the polarization (Appelt et al., 1999) that describes the slowing of precession due to the SERF regime. Through this effect, SERF magnetometers can maintain coherence over long enough timescales to make sensitive magnetic field measurement.

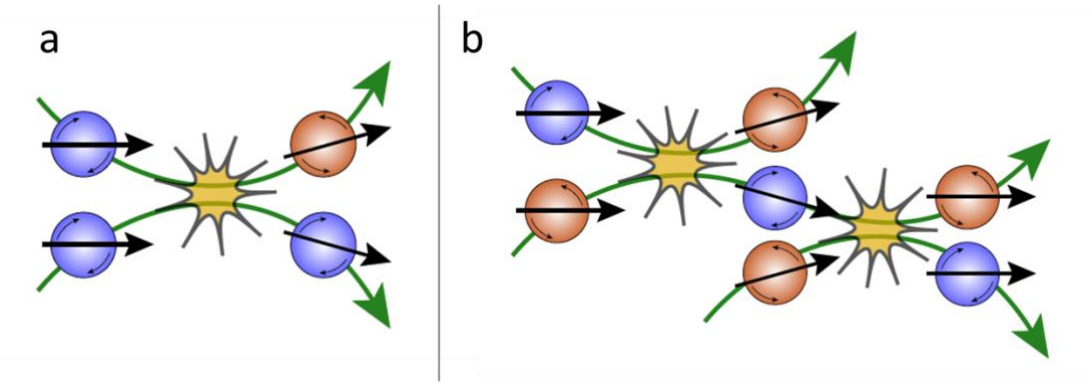


Figure 3.7. Spin-exchange relaxation and the SERF regime. *a) A spin-exchange collision alters the direction precession of the spin by change of hyperfine energy level, indicated by the colour of the sphere b) a high rate of spin-exchange collisions gives rise to a net positive polarisation at a slower frequency of precession, known as the SERF regime (adapted from Seltzer, 2008).*

3.4 Signal equations

The behaviour of the net polarisation, $\boldsymbol{P}$, of the optically pumped atomic ensemble can be described by the Bloch equation,

$$\frac{d\boldsymbol{P}}{dt} = \frac{1}{Q}\left[\boldsymbol{P} \times \gamma \boldsymbol{B} - (\boldsymbol{P} - P_0 \hat{\boldsymbol{z}})\frac{1}{T}\right], \tag{3.9}$$

where P_0 describes the equilibrium polarisation at zero field, T is the atomic spin coherence time constant that incorporates the optical pumping rate, R and relaxation time constant T_2, such that $T = \left(R + \frac{1}{T_2}\right)^{-1}$.

In the steady state, where $d\boldsymbol{P}/dT = 0$, the Bloch equation solutions become,

$$\begin{aligned} P_x &= \frac{\frac{B_y}{(\gamma T)} + B_x B_z}{\frac{1}{(\gamma T)^2} + {B_x}^2 + {B_y}^2 + {B_z}^2} P_0' \\ P_y &= \frac{\frac{-B_x}{(\gamma T)} + B_y B_z}{\frac{1}{(\gamma T)^2} + {B_x}^2 + {B_y}^2 + {B_z}^2} P_0' \\ P_z &= \frac{\frac{1}{(\gamma T)} + {B_z}^2}{\frac{1}{(\gamma T)^2} + {B_x}^2 + {B_y}^2 + {B_z}^2} P_0' \end{aligned} \tag{3.10}$$

where $P_0' = P_0 RT$. For measurement of magnetic fields that are oriented perpendicular to the laser propagation axis, which is given by B_x here, the terms that describe the magnetic fields in the other two axes, B_y and B_z, become zero, simplifying the Equations 3.10 to,

$$\begin{aligned} P_x &= 0 \\ P_y &= \frac{-\gamma T B_x}{1 + (\gamma T B_x)^2} P_0' \\ P_z &= \frac{1}{1 + (\gamma T B_x)^2} P_0'. \end{aligned} \tag{3.11}$$

Example curves in this case are plotted in Figure 3.8. The polarisation along the laser direction here (P_z) is a Lorentzian, and is described as the zero-field resonance or Hanle resonance (Hanle, 1925). For a QZFM, the full-width half-maximum is $\frac{2}{\gamma T} \sim 30$ nT. The polarisation along the y-axis here follows a dispersion curve shape. Both profiles could be used as magnetometers but are sensitive to $1/f$ noise. However, a Lorentzian magnetometer output would not allow discrimination between positive and negative changes in magnetic field. Signal modulation via an applied

oscillating magnetic field is therefore applied in the sensitive direction (here that would be B_x) to enable this discrimination.

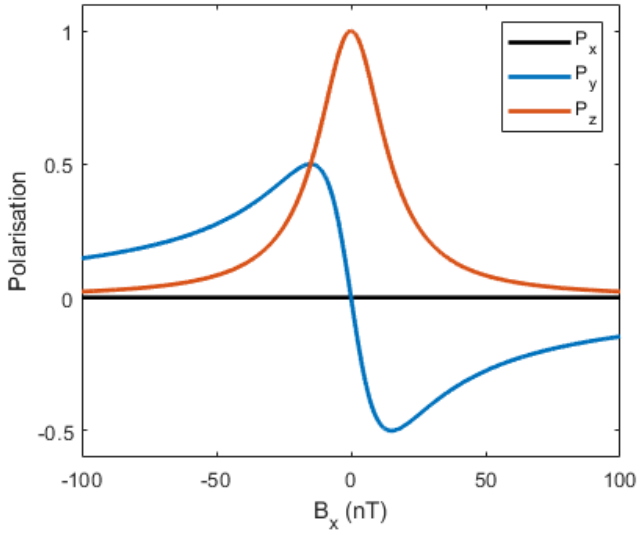


Figure 3.8. Solutions to the Bloch Equation in zero field. *In the direction of laser propagation (x), the polarisation is zero, in the y-direction the polarisation follows a dispersion curve, and in the z-direction it follows a Lorentzian shape, known as the zero-field resonance. Here, 2/* $\boldsymbol{\gamma T}$ *= 30 nT to represent QZFM.*

The modulation signal is at a frequency that is much higher than most neuronal signals of interest and a greater frequency than the relaxation rate of the atomic ensemble. For the QZFM this is 932 Hz, which is larger than the QZFM relaxation rate of ~ 100 Hz. The oscillating magnetic field b_x is applied via a modulating current in the coils surrounding the glass cell within the sensor head, changing the signal equation by the addition of a modulation term $b_x \cos(\omega t)$,

$$\frac{dP}{dt} = \frac{1}{Q}\left[p \times \gamma[B + b_x \cos(\omega t)\,\hat{x}] - (P - P_0\hat{z})\frac{1}{T}\right]. \tag{3.12}$$

Now that the modulation term varies in time, steady state solutions no longer apply and we must re-evaluate for P_z, assuming $B_y = B_z = 0$ to get,

$$P_z = \left(\frac{\gamma T B_x}{1 + (\gamma T B_x)^2}\right) J_0\left(\frac{\gamma b_x}{Q\omega}\right) J_1 P_0' \sin(\omega t)\,, \tag{3.13}$$

where J_n are Bessel functions of the first kind (Shah and Romalis, 2009; Tierney et al., 2019). These functions can be evaluated to reach a constant term that is dependent on the ratio of $\frac{\gamma b_x}{Q}$ and then subsequently combined to yield a constant of proportionality,

$$P_z \propto \frac{\gamma T B_x}{1 + (\gamma T B_x)^2} P_0'. \tag{3.14}$$

Therefore, after demodulation via lock-in detection, the output signal becomes a dispersion curve rather than a Lorentzian line shape, and so positive and negative magnetic field changes can be discriminated. This also reduces sensitivity to the $1/f$ noise that a Lorentzian output is susceptible to. Note that the sensor output is approximately linear around the zero field, and therefore a linear approximation can only be made for very small field changes (see Figure 3.9).

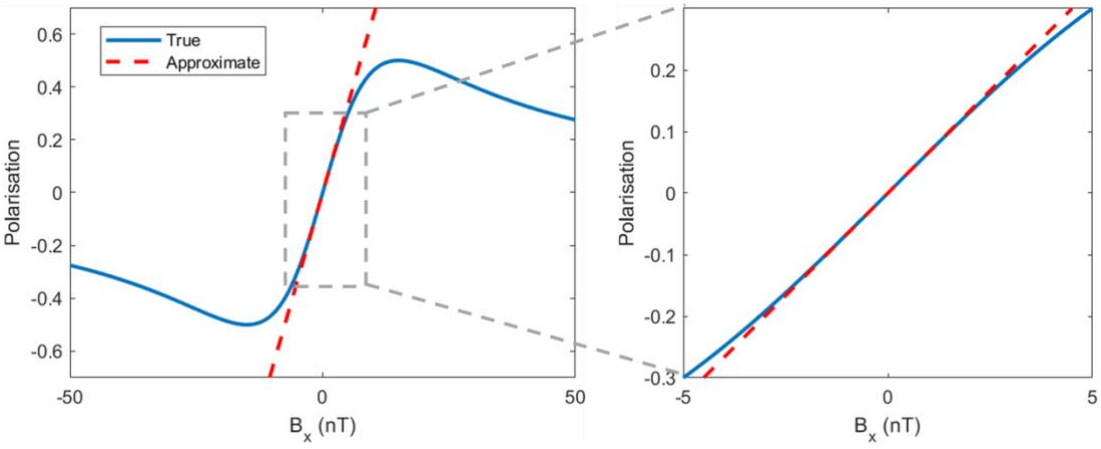


Figure 3.9. OPM voltage output. *Modulating the signal and using lock-in detection enables discrimination between positive and negative field changes from the dispersion curve. At very small field changes (shown here as ±5 nT in QZFM), the relationship is approximately linear.*

3.4.1 Cross-axis projection error

When deriving the signal equations previously, we assumed the magnetic field components in the y and z-direction (orthogonal to the laser beam direction) were zero. This is unlikely to be the case, with non-zero cross-axis terms changing the full signal equation to,

$$V \propto -J_0\left(\frac{\gamma b_x}{Q\omega}\right)J_1\left(\frac{\gamma b_x}{Q\omega}\right)\frac{\frac{1}{T}\gamma B_x + \gamma^2 {J_0}^2\left(\frac{\gamma b_x}{Q\omega}\right)B_y B_z}{\frac{1}{T^2} + \gamma^2 {B_x}^2 + {J_0}^2\left(\frac{\gamma b_x}{Q\omega}\right)\gamma^2 {B_y}^2 + {J_0}^2\left(\frac{\gamma b_x}{Q\omega}\right)\gamma^2 {B_z}^2}, \qquad (3.15)$$

where V is the voltage output from the sensor and B_x is the magnetic field direction we wish to measure. The sensor gain is dependent on the gradient of the response curve, which is related to B_x, B_y and B_z. Therefore, the magnetic field environment in all axes will alter the sensor gain and the measured output. This effect is known as cross-axis projection errors (CAPE) (Borna et al., 2022), and is shown for increasing cross-axis magnetic fields in Figure 3.10.

Not only can this change the amplitude of the measured signals but can introduce phase errors and therefore time delays in MEG signals. There are several strategies

for mitigating CAPE, including most obviously background magnetic field control, either just passively using magnetically shielding materials or in combination with active shielding via electromagnetic coils (Sections 3.6 and 3.7). Additionally, sensors can be designed to be operated within a 'closed loop' set-up, using feedback via internal coils to maintain a 'zero-field' environment throughout acquisition, even in the presence of field changes. As CAPE affects all three axes, 'closed loop' methods only work if all three axes can be nulled, and so requires triaxial sensors.

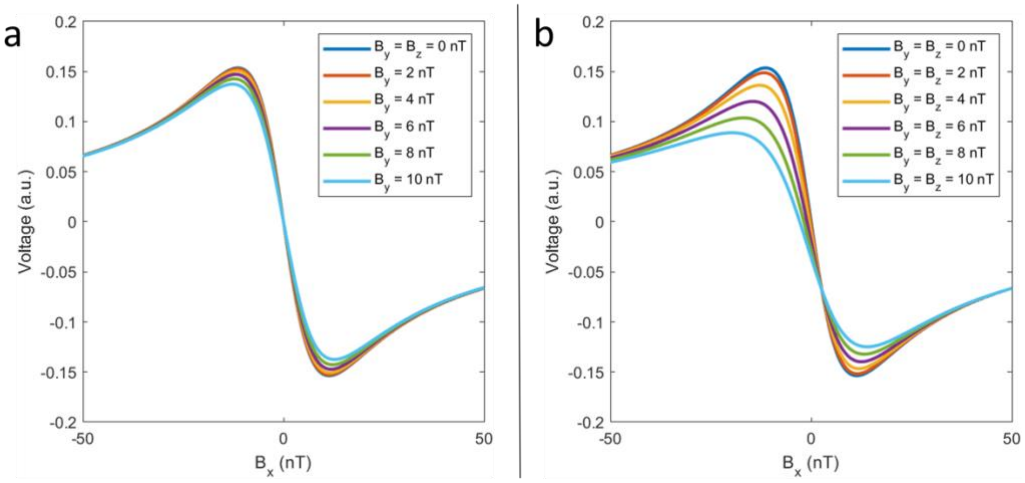


***Figure 3.10. Cross-axis projection error**. Simulation of the OPM signal equation describing how magnetic fields orthogonal to measurement direction alter the slope of the output. a) shows how a magnetic field in the y-direction up to 10nT alters the voltage response to magnetic fields in the x-direction. b) shows further changes with an additional field in the z-direction. These are calculated using* $\boldsymbol{\gamma/2\pi = 28\ rad\ s^{-1}nT^{-1}}$, $\boldsymbol{b_x = 200\ nT}$, $\boldsymbol{Q = 4}$, $\boldsymbol{\frac{\omega}{2\pi} = 1000\ rad\ s^{-1}}$ *and* $\boldsymbol{T = 5 \times 10^{-4}\ s}$.

3.5 Triaxial Measurement

In conventional MEG, sensors typically measure a single vector component of the neuromagnetic field, oriented (approximately) radially with respect to the scalp surface. This is mostly out of necessity, as it is challenging to orient bulky pick-up coils to measure the complete field vector. It is also sensible since the radial component of the neuromagnetic field has been shown to be the largest in amplitude, and tangential components are more susceptible to errors and approximations in forward modelling due to a greater effect from volume currents in the extracellular space (Iivanainen et al., 2017; Sarvas, 1987). This said, SQUID-MEG systems have been built that measure the full vector magnetic field at multiple locations or across the whole head (Haueisen et al., 2012; Nurminen et al., 2013). However, these triaxial sensors have not been widely adopted, potentially due to their complexity.

As OPMs do not rely on pick-up coils, sensors can be adapted to make triaxial measurements without significantly increasing their overall size. As the directional

sensitivity of an OPM is provided by a known oscillating magnetic field applied along a direction orthogonal to the laser axis as it passes through the vapour, even with a single laser beam, two independent field measurements can be made in two orientations orthogonal to the beam direction. Therefore, to make triaxial measurements, the laser beam can be split to direct two perpendicular beams through the same cell (see Figure 3.11), enabling triaxial field characterisation.

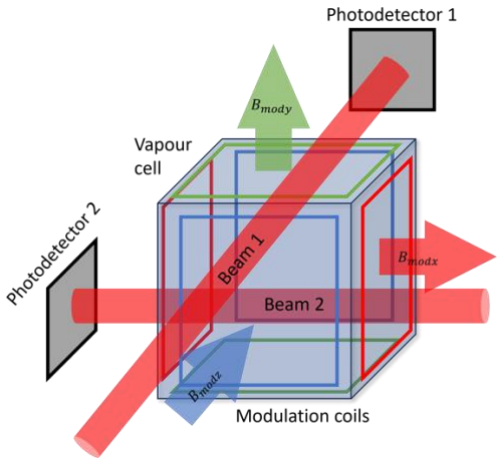


***Figure 3.11. Triaxial measurement**. Schematic diagram of a triaxial QZFM. A beam splitter separates the laser beam, allowing two beams to be directed through the vapour cell for independent optical pumping. The vapour cell is surrounded by modulation coils on all faces.(adapted from Boto et al., 2022)*

Measuring all three axes of the neuromagnetic field does not provide a three-fold improvement in sensitivity. However, measuring tangential components can improve data quality by three mechanisms: rejecting external interference, improving coverage across the cortex, and enabling “closed loop” sensor operation. For sensor data, additional components of the magnetic field improve the rejection abilities of methods such as homogeneous field correction (Tierney et al., 2021a) and signal space separation (Holmes et al., 2023a). The tangential components also reduce the correlation of the forward fields between the source of interest from within the brain and an external interfering source (see Figure 3.12a), which can be exploited when reconstructing sensor space data into source space (Brookes et al., 2021). Secondly, in simulation, triaxial sensors have shown a marked improvement on homogeneity of coverage (Figure 3.12b), which is particularly important in paediatric measurements, where the proximity of the brain to the scalp surface creates “hot spots” in coverage (Boto et al., 2022). Finally, at the time of writing, OPMs are being designed in a “closed loop” form, as in SQUID operation (see Chapter 2.4.4), using feedback to take magnetic field measurements while maintaining zero field across the vapour cell. This should reduce measurement error that arises due to operation beyond the linear regime of the sensor output (Figure 3.9). However, due to CAPE (Chapter 3.4.1), the

compensation towards zero-field must be applied in all three axes, to prevent magnetic fields orthogonal to the measurement axes causing changes in the output gain (the gradient of the lines in Figure 3.10).

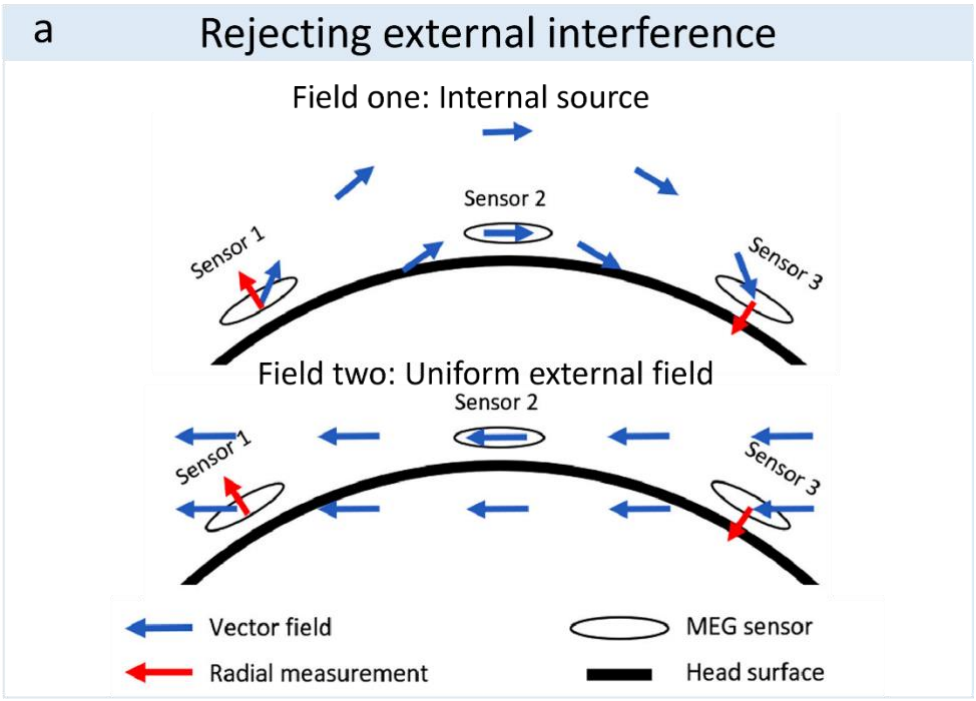


Figure 3.12. Triaxial advantages. *a) Shows a diagram demonstrating how triaxial measurements assist in the discrimination between magnetic sources originating from within and outside the head (adapted from (Brookes et al., 2021)). b) Shows simulated coverage across the cortex using an array of radial-only QZFM in comparison to triaxial QZFM. This is demonstrated for an adult template MRI, a 4-year-old and a 2-year-old (adapted from (Boto et al., 2022)).*

3.6 Magnetically shielded environments

As described in Chapter 3.4 and Figure 3.9, for operation in the SERF regime, OPMs suffer from a low dynamic range, with QZFM unable to cope with field changes above a few nT without either saturating sensor outputs or inducing gain errors (Borna et al., 2022; Boto et al., 2018). Consequently, a low magnetic field environment is required for MEG measurement with such sensors. Where conventional MEG systems require magnetic shielding to reduce dynamic changes in the environmental magnetic field, OPM-MEG systems require greater shielding to produce a sufficiently low static magnetic field (and minimal dynamic changes) for 'zero-field' operation. This is particularly important in wearable systems, where the translation of OPMs through any residual static magnetic field causes a measured change over time seen by the magnetometer.

Unshielded, the Earth's magnetic field is ~50 μT and environmental sources (e.g. electronic equipment) produce temporally varying magnetic fields, both of which are many orders of magnitude larger than brain signals of interest. MEG experiments, both conventional and OPM, are therefore conducted in magnetically shielded rooms (MSRs), which employ layers of materials chosen for their properties to shield from static (DC) and temporally varying (AC) magnetic fields. Shielding materials change the structure of the magnetic field from interfering sources; diverting lines of magnetic flux away from the area where a low magnetic field is intended (Hoburg, 1995). Shields are characterised by the shielding factor,

$$SF = \frac{|B_0|}{|B_S|}, \tag{3.16}$$

where B_0 is the unshielded field, and B_S is the shielded field. A larger shielding factor therefore corresponds to better shielding. There are two physical mechanisms (Figure 3.13) that require two different material properties and shielding factors used in the construction of MSRs.

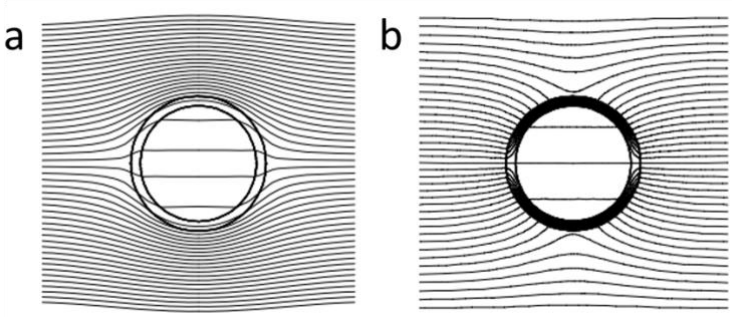


Figure 3.13. Magnetic shielding mechanisms. *a) A diagram demonstrating the process of flux shunting, where lines represent magnetic flux and a cross section of a cylindrical shield of high permeability material is shown in the centre, and b) a diagram describing eddy current cancellation, where a cross section of a material with high electrical conductivity generates magnetic flux that opposes incident flux (diagrams taken from Celozzi et al., 2008).*

3.6.1 DC fields

Low frequency or DC magnetic fields require a material with a high magnetic permeability μ_r to divert flux away from the shielded region using a mechanism known as flux shunting. This effect arises due to the boundary between materials of different relative magnetic permeability. Ampere's law dictates that the tangential component of the magnetic field $\mathbf{H}$ must be continuous across the surface of the material, and Gauss's law states that the normal component of $\mathbf{B}$ must also be continuous. Inside the material, $\mathbf{B}$ takes the form $\mathbf{B} = \mu_0\mu_r\mathbf{H}$, whereas $\mathbf{B}{\sim}\mu_0\mathbf{H}$ in the air. For high permeability materials, the magnetic field rapidly changes at the interface between the materials to satisfy the boundary conditions. This results in magnetic flux lines being 'pulled in' perpendicular to the material and then 'shunted' along the material surface before being released back into air, as shown in the diagram in Figure 3.13a. The shielding factor of such material is dependent on its magnetic permeability, the dimensions of the shield constructed from it and the area enclosed by such shield. For example, for a spherical shield with inner radius a and outer radius b, the shielding factor across the shielded volume will be (Hoburg, 1995)

$$SF = \frac{(\mu_r + 2)(2\mu_r + 1) - 2\frac{a^3}{b^3}(\mu_r - 1)^2}{9\mu_r}. \tag{3.17}$$

For a material with high magnetic permeability, Equation 3.17 can be simplified when the thickness of the shield, $\Delta = b - a$, is small compared to the inner radius, and $\mu_r\frac{\Delta}{a} \gg 1$, to (Cohen, 1970)

$$SF \approx \frac{2}{3}\mu_r\frac{\Delta}{a} + 1. \tag{3.18}$$

This approximation reveals a decrease in shielding factor for DC magnetic fields with larger shields if the thickness remains constant. Consequently, multiple layers of high permeability materials can be used with spaces between layers to improve the shielding factor.

3.6.2 AC Fields

Higher frequency or AC magnetic fields (~> 10 Hz) require a material with high electrical conductivity (e.g., copper) for shielding via eddy current cancellation. The time-varying magnetic flux density, $\mathbf{B}$, induces an electric field, $\mathbf{E}$, within the material due to Faraday's Law,

$$\nabla \times \mathbf{E} = -\left(\frac{\partial \mathbf{B}}{\partial t}\right). \tag{3.19}$$

For materials with high electrical conductivity, σ, this electric field induces a current density within the material, inducing magnetic flux that opposes the change in the imposed magnetic flux. The imposed and induced magnetic flux superimpose and cancel, expelling the total flux out of the conducting material and shielded region, shown in Figure 3.13b. For an AC field with angular frequency $\omega = 2\pi f$, the induced current density and total flux density decay exponentially into the material and shielded region with a characteristic decay length, or "skin depth",

$$\delta = \sqrt{\frac{2}{\omega \mu_0 \mu_r \sigma}}, \tag{3.20}$$

where μ_r is the relative magnetic permeability of the material. For time-varying magnetic fields, the shielding factor is complex, showing a frequency dependent phase variation, and can be expressed as,

$$SF = 1 + i\omega \frac{\mu_0 \sigma a \Delta}{3}, \tag{3.21}$$

for a spherical enclosure, when $\mu_r = 1$, $\delta \gg \Delta$ and $\Delta \ll a$. The shielding improvement here contrasts with the DC case, as it increases with radius for a fixed shield thickness.

3.6.3 Degaussing

While MSRs efficiently reduce the magnetic field inside the enclosure, the residual field inside many MSRs remains too high for OPM operation. Specifically, without

degaussing, even in a highly efficient shielded room (SF ~ 2,000), the background field would be on the order of 25 nT (Boto et al., 2018), and consequently, just a 4-degree rotation of an OPM would cause a field shift large enough to take the OPM outside its dynamic range. As such, additional tools are used to produce the low magnetic field environment required for OPM-MEG. One such method is degaussing. The materials used in MSRs (e.g., mu-metal) are typically alloys of ferromagnetic metals such as iron or nickel. Therefore, when exposed to magnetic fields they can become magnetised; a remnant magnetic field can be left in the shielded region. To reduce this, a process of degaussing is employed; large coils are wrapped around the room, through which a decaying oscillatory current is applied. This drives the ferromagnetic material around hysteresis loops of diminishing area, suppressing the remnant magnetic field, and improving the performance of the magnetic shielding.

3.7 Active magnetic shielding

With passive magnetic shielding in combination with degaussing (SF ~ 20,000), background magnetic fields can reach closer to 2 nT. However, even in this ultra-low field environment, magnetic artefacts from small movements will be larger than brain activity and large field measurements may cause CAPE (Chapter 3.4.1). For these reasons, further shielding (beyond passive) is required to achieve a sufficiently low residual field. This has been achieved with field nulling techniques based on the use of electromagnetic coils.

3.7.1 Nulling static magnetic fields with bi-planar electromagnetic coils

The basic scheme is to measure the residual field inside a magnetically shielded enclosure and then use coils to generate a field equal and opposite to that measured, thus cancelling it out. However, a challenge in coil design is to find a way to generate magnetic fields in all three Cartesian orientations. Conventionally this would be done using a Helmholtz-like set-up (Iivanainen et al., 2019). However, this involves enclosing the participant since the coils must be mounted on six planes surrounding the nulling volume. An elegant solution to this is a bi-planar coil system, which provides a more open scanning environment. Here, the coil design is based upon a harmonic minimisation method (Carlson et al., 1992), which has been used previously in MRI. This approach was adapted to compensate all three Cartesian components of the uniform background field and the spatial gradients in the MSR whilst restricting coils to two planes placed on either side of the participant.

From Maxwell's equations for magnetostatics, in a current-free region the magnetic field obeys,

$$\nabla . \mathbf{B} = 0, \tag{3.22}$$

and

$$\nabla \times \mathbf{H} = \mathbf{J}, \tag{3.23}$$

where J is a current density. In the air enclosed by the shield, $B = \mu_0 H$ and no current density exists, consequently,

$$\nabla \times \mathbf{B} = 0. \tag{3.24}$$

Evaluating these equations, the magnetic field can therefore be expressed as three vector components, B_x, B_y, B_z. In the absence of magnetic monopoles, these each obey Laplace's equation, so they can be represented as a series of spherical harmonics, with the lowest order terms corresponding to spatially uniform magnetic fields and magnetic field gradients. Due to a high degree of symmetry between the lowest-order gradient terms,

$$\begin{gathered} \frac{dB_z}{dx} = \frac{dB_x}{dz} \\ \frac{dB_z}{dy} = \frac{dB_y}{dz} \\ \frac{dB_x}{dy} = \frac{dB_y}{dx} \\ \frac{dB_x}{dx} + \frac{dB_y}{dy} + \frac{dB_z}{dz} = 0 \end{gathered} \tag{3.25}$$

a series of just eight components are required to fully describe the uniform magnetic fields and linear magnetic field gradients, rather than the expected twelve (Holmes et al., 2018). Therefore, three coils can be designed to produce the uniform field vector components and a further five coils designed to generate the independent field gradients. Each coil produces a homogenous magnetic field or field gradient (within 5%) inside a 40 cm length cube, shown in Figure 3.14a.

In Holmes et al. 2018, a reference array with four Gen-1 QZFM OPMs was set up around the participant to measure the remnant magnetic field inside the MSR, as shown in Figure 3.14b. Using the two sensitive axes, four OPMs can measure the three vector field components at two separate spatial locations, 30 cm apart. From

this, a linear combination of the uniform components and five field gradients that best model the measured field can be determined. Feedback controllers modulate the currents in the bi-planar coils. The remnant magnetic field is cancelled out by applying an equal and opposite magnetic field based on a known value of the coil field per unit of applied current. More specifically, the measured field and field gradients are passed to proportional integral derivative (PID) control loops for more precise control, meaning the current applied depends not only on the latest measurement but also on the history of the system. A desired “setpoint” value is required, which for nulling magnetic fields is close to zero. The error is computed as the difference between the setpoint and the measurement. The current applied to the coils is then given as the sum of three terms: the first proportional to the error; the second varies with the integral of the error over time; and the third with the derivative of the error. To null the static remnant magnetic field, once the error is minimised, the PIDs are switched off and a stable current is applied to the coils to maintain the low magnetic field volume. With this method, remnant fields inside the MSR reach as low as 250 pT.

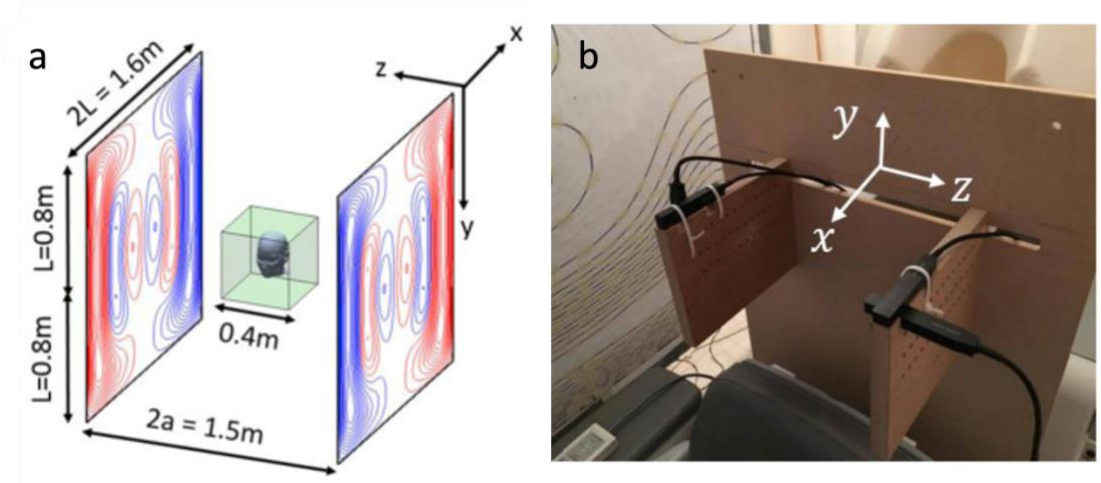


Figure 3.14. Active magnetic shielding using biplanar coils. *a) A diagram of the biplanar coils, demonstrating the nulled region by the green box surrounding the participant’s head, b) the reference array with four Gen-1 QZFM, held around the participant’s head (figure adapted from Holmes et al., 2018)*

3.7.2 Dynamic magnetic field compensation

In hostile magnetic environments, such as a city-centre site, the magnetic field within an MSR can vary unpredictably e.g., at a site in downtown Toronto, passing underground trains and vehicles caused large temporally varying magnetic fields. An example recording from a fluxgate magnetometer of such a site is shown in Figure 3.15.

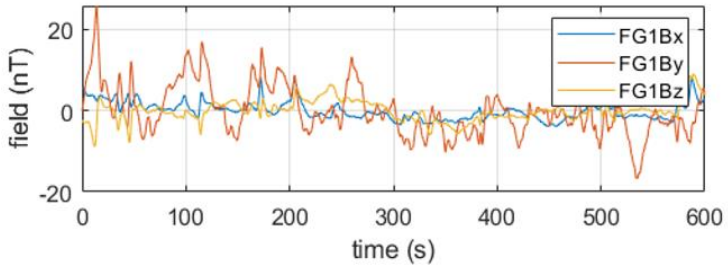


Figure 3.15. Temporally varying magnetic fields. *A graph showing magnetic field changes from within a repurposed Vacuumschmeltz shielded room at the Hospital for Sick Children (SickKids) in downtown Toronto, Canada. The measurements are made with fluxgate magnetometers (measuring in x,y and z), that have a larger dynamic range than commercial OPMs, allowing them to measure the magnetic field changes of over* $\pm \mathbf{20}\ \boldsymbol{nT}$.

This can cause OPMs to experience field changes beyond their dynamic range, sometimes just moments after nulling, making even short OPM-MEG scans unfeasible (Holmes et al., 2019). To counter this, a dynamic nulling system can be employed to account for the low frequency time-varying fields or drifts (Iivanainen et al., 2019). This can be achieved via a high-speed dynamic PID controller to regulate currents in the coils in accordance with measured field variation.

3.8 OPM-MEG subject interface

3.8.1 OPM-MEG helmet design

MEG requires the measurement of magnetic field signals from an array of sensors distributed across the head to enable source reconstruction. Wearable OPM arrays therefore require a method of mounting sensors close to the scalp while enabling free movement and a comfortable scanning environment. When designing such a system, there are five key considerations to balance:

- The sensors must be held rigidly (limiting relative movement)
- Sensors must be held close to the scalp to maximise the measured signal
- Sensor locations and orientations relative to the participant's head must be known to enable high-fidelity modelling and, consequently, source localisation
- The system must be ergonomic and practical – particularly for participant groups such as infants or patients
- As most OPMs are heated to operate in the SERF regime, heat must be able to dissipate

There have been a range of approaches taken to address this requirement. Here I will describe those approaches in reference to the evolution of the system used in this thesis.

The first wearable MEG recordings were made with 3D-printed personalised head casts (Boto et al., 2018), designed to fit a single participant using their individual MRI to generate a “perfect fit” solution (Figure 3.16). This allows OPMs to be placed as close to the scalp surface as is possible to maximise the measured signal amplitudes, while also providing accurate knowledge of sensor position and orientation (or coregistration – see Section 3.8.3). This method has since been used in a range of studies across multiple research groups (e.g., Seymour et al., 2021), however, its use is limited by the expense and time required to design an individual head cast for each participant and is therefore impractical for large study cohorts.

Generic helmets overcome this limitation, allowing data collection from multiple participants with a single system. Early generic systems adapted adult and child-sized bicycle helmets (Figure 3.16) and used 3D digitisation to determine sensor positions and orientations within the helmet (Hill et al., 2020). These helmets benefitted from a lightweight and affordable design, but the foam padding built inside the helmet prevented heat dissipation and was therefore impractical for large arrays where overheating can become a problem.

A more flexible solution used flexible “EEG-like” caps with sensor holders sewn onto an elasticated fabric that conforms to different head shapes and sizes (Corvilain et al., 2023; Feys et al., 2022), an example of which is shown on a new-born in Figure 3.16. While this provides an optimal on-scalp placement for maximum signal detection, motion between sensors produced vibrational artefacts, and coregistration of each individual sensor location and orientation relative to one another and anatomy causes random error in sensor localisation, which is problematic in source localisation (Hill et al., 2020).



Figure 3.16. OPM-MEG helmet design. *From the top left, personalised 3D printed head cast (Seymour et al., 2022), adapted bicycle helmets (Hill et al., 2020), and flexible caps (Corvilain et al., 2023). Bottom row from left, prototype rigid helmet (Hill et al., 2020), 3D printed rigid helmets in adult large and 4-year-old sizes.*

3D-printed helmets in a range of generic sizes overcome many of the issues presented by flexible cap solutions. They hold sensors rigid relative to one another, reducing artefact and simplifying coregistration (improving source localisation by making errors systematic rather than random, Hill et al., 2020), while offering a close-to-scalp placement with appropriate age-matched sizes (see Figure 3.16). The helmets have been developed from the first adult prototype in 2020 to multiple sizes (at the time of writing, there are 1-year-old, 2-year-old, 4-year-old, adult small and adult large sizes). The helmets are designed with a 3D-printed mesh structure to reduce weight and allow for air circulation to provide cooling to the sensors and head. Cable management is also incorporated to provide an ergonomic and neat design. It must be noted that there are limitations to this system. Sensors must be moved between different helmets, meaning different head sizes cannot be scanned sequentially without time for changing helmets. In addition, the generic fit means that there is inhomogeneous coverage, particularly in the temporal regions as the helmet does not allow for sensor placement further down the sides of the head.

3.9 Coregistration

Reconstructing the MEG signal in source space requires an accurate knowledge of sensor locations relative to brain anatomy. This process is called coregistration and is described for cryogenic MEG in Chapter 2. The rigid helmets in the system described and used in this thesis, simplify the process of coregistration by holding sensor positions and orientations rigid with respect to one another. Therefore, coregistration simply requires the ability to determine the position of the helmet with respect to the head, and therefore an anatomical MRI.

This is achieved by taking a 3D digitisation of the participant wearing the helmet either prior to or following MEG data acquisition. In this thesis, a structure-light scanner was used to obtain the digitisation (EinScan H, Shining Inc., China). The 3D digitisation is coregistered to a surface scalp mesh (created from the segmented anatomical MRI) by matching facial features. A 3D mesh of the helmet is then aligned to the digitisation mesh by matching equivalent points on the helmet. This results in a transformation matrix that describes the rotation and translation from the sensor location and orientations in “helmet-space” to “MRI-space”, and therefore the array position relative to the brain is known. A schematic of the process is shown in Figure 3.17. This method was used in the work described in Chapters 5,6 and 7, and a similar method with an additional step is used and described in Chapter 4.

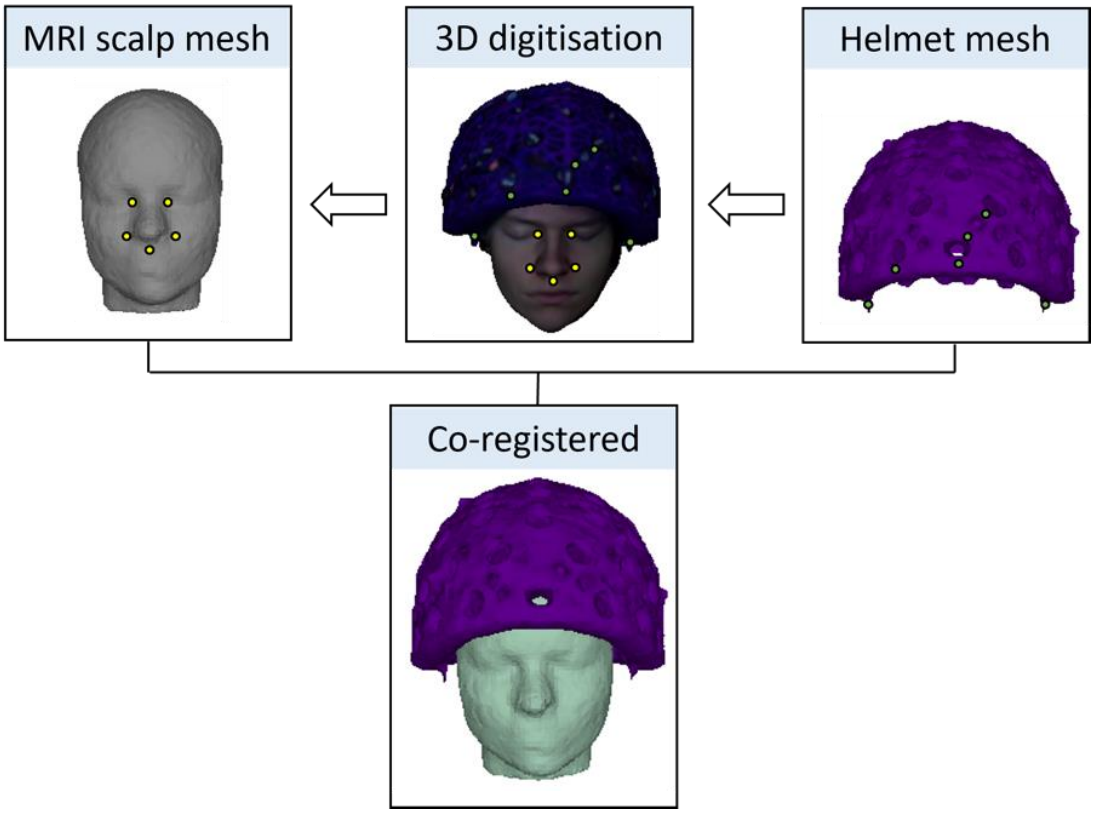


Figure 3.17. Optical coregistration for OPM-MEG. *The 3D digitisation is aligned to a mesh of the extracted scalp from the MRI by matching features, shown by yellow dots. The helmet mesh is then aligned to the 3D digitisation using feature matching demonstrated by the green dots. This results in the helmet mesh coregistered to the MRI scalp, and therefore sensor locations and orientations relative to brain anatomy.*

3.10 Chapter summary

In this chapter, we have discussed the elements that make up the OPM-MEG system, including the theory of optical pumping, triaxial measurement, and magnetic shielding. The next four chapters describe experimental studies using OPM-MEG.

4 Measuring theta band activity with OPM-MEG

4.1 Chapter overview

This chapter describes a study investigating low frequency, theta band (4 – 8 Hz), MEG signals during visual and working memory tasks using a whole-head OPM-MEG system in comparison to a cryogenic system. Detection of low frequency signals is particularly important when studying neurodevelopment, as oscillatory signals are lower frequency in early life (Hunt et al., 2019). In a wearable OPM-MEG system, low frequency signals may be more challenging to detect, as motion artefact typically manifests below 10 Hz, and the noise floor of an OPM at low frequency is typically higher than conventional SQUID sensors. We therefore aim to characterise the sensitivity of the OPM-MEG system to oscillations across the theta band range as a precursor to neurodevelopmental studies. We compare the source-space power during both tasks in both systems in healthy adult participants, finding no significant differences in the signal-to-noise across groups, and a high correlation between individuals in each system. We also conduct a 'neural fingerprinting' analysis, showing that individual signatures are preserved between systems. The work presented in this chapter was published in NeuroImage in 2023 (Rhodes et al., 2023).

4.2 Introduction

Despite significant promise, OPM-MEG remains a nascent technology and has some potential disadvantages over SQUID-based instrumentation. Arguably the biggest limitation is diminished sensitivity to low frequency oscillations. Low frequency neural oscillations are extremely important neurophysiological markers; oscillations in the theta band are associated with a range of cognitive processes, including spatial navigation (Hasselmo et al., 2002), emotional regulation (Lesting et al., 2011) and memory. A connection between theta and memory processes was first made in local field potential (LFP) recordings from rats in the 1970s (Landfield et al., 1972), and has since been demonstrated non-invasively in humans with EEG and MEG (Inanaga, 1998; Jensen and Tesche, 2002; Onton et al., 2005). In clinical research and practice, an excess of low frequency neural oscillations at rest in adults (also termed cortical slowing) is a well-established marker of disease with examples including Alzheimer's

(Jeong, 2004) and Parkinson's disease (Stoffers et al., 2007). Critically for the work described in this thesis, low frequency signals are particularly important for studying development. There is a general shift of oscillatory activity towards lower frequencies at younger ages – for example, the alpha peak frequency is shifted to a lower frequency in children compared to middle-aged adults (Miskovic et al., 2015; Scally et al., 2018) and there is a trend of decreasing theta power and increasing alpha power with age from childhood to adulthood (Hunt et al., 2019; Miskovic et al., 2015). These examples show the importance of high-fidelity low frequency measurement. Consequently, any viable OPM-MEG system must be capable of accurately characterising such activity.

The challenge in detecting low frequency activity with OPM-MEG arises due to three separate effects. Firstly, the inherent noise level of an OPM increases at low frequencies (Boto et al., 2022). There are several reasons for this in the current generation of commercial OPMs, including the presence of magnetic impurities in the materials from which the sensor is made and crosstalk within feedback loops for the vapour cell and laser temperature stabilization, which in turn lead to fluctuations in the sensor output. Second, all MEG installations are housed inside a magnetically shielded room (MSR), typically constructed from multiple layers of high magnetic permeability and high electrical conductivity metal. The former reduces low frequency interference, and the latter attenuates high frequency magnetic fields (see Chapter 3.6 for more detail). Such shielding techniques are well established; however, the shielding of low frequency (< 10 Hz) variations in the magnetic field at the scale factors associated with MSRs designed for human measurements is challenging (Hill et al., 2022; Holmes et al., 2022), meaning higher interference at lower frequencies. Whilst this is also true for conventional MEG systems, SQUID-based sensors often measure magnetic field gradient, whereas OPMs measure the field itself, and the latter is influenced more by distant sources of interference. Finally, unlike SQUIDs, OPMs move with the head. Although this is a major advantage, if there is any remnant (temporally static) background field inside the MSR then sensors 'see' a changing magnetic field as they move. Since head movement is more likely to occur at low frequencies, this again disproportionately increases low frequency interference. In sum, the combined effect of inherent sensor noise, low frequency interference from the environment, and head movement make imaging low frequency effects with OPM-MEG a significant challenge.

Despite the difficulties, recent evidence suggests that it should be possible to measure low frequency effects using wearable OPM-MEG. For example, OPM measurements

in unconstrained subjects reliably detect neural oscillations in the theta band, which localise to the hippocampus (Barry et al., 2019; Tierney et al., 2021b) during a task involving the imagination of novel scenes. In addition, in a study on cortical tracking of speech in unconstrained subjects, the authors concluded that OPM-MEG is able to successfully measure brain activity at frequencies of 4 Hz and below (de Lange et al., 2021). However, there is yet to be a direct comparison of results from SQUID and OPM-MEG, when measuring low frequency neural oscillations.

In this chapter, we employ two tasks – a 4 – 8 Hz flashing visual stimulus, and an N-back working memory task (2-back condition), both of which elicit neural effects in the theta band. Both tasks were carried out by the same 14 participants using SQUID and OPM-based instrumentation and we make a quantitative comparison of the results. We test two hypotheses. First, despite the challenges, if the background magnetic field is controlled appropriately (Rea et al., 2021) and interference rejection methods are used effectively, the SNR of OPM-based measures of theta activity will be comparable to that of SQUID-based metrics. Second, we hypothesised that individual differences in the electrophysiological signature of frontal midline theta oscillations would be preserved between the two scanners.

4.3 Methods

4.3.1 Participants

Fourteen participants took part in the study (age range 27 ± 3; 8 identified as male, 6 as female). Each subject underwent two separate MEG recording sessions, with data collected by either OPM-MEG or SQUID-MEG[1]. The order of these sessions was alternated (eight participants underwent OPM-MEG scans first; six participants were scanned first in the SQUID-MEG). The average time between sessions was 19 ± 10 days (mean ± standard deviation). In addition to MEG data, volumetric anatomical magnetic resonance images were acquired for each participant using a Philips Ingenia 3T system running an MPRAGE sequence, with 1 mm isotropic spatial resolution. These anatomical images were used for subsequent coregistration between brain anatomy and sensor array geometries. All participants provided written informed consent prior to scanning, and the study was approved by the University of Nottingham's Faculty of Medicine and Health Sciences Research Ethics Committee.

[1] The author collected all the data described in this chapter.

4.3.2 Paradigms

A single scanning session comprised two experiments:

Visual task: Participants passively viewed a visual stimulus – a green square on a black background, flashing at either 4 Hz, 6 Hz or 8 Hz (adapted from Wittevrongel et al., 2021). The stimulus was presented in the lower right quadrant of the participant's field of view, subtending a visual angle of ~5°. Stimulation was presented for 2 s, followed by a 2 s rest period. This was repeated 120 times; with 40 trials for each frequency presented in pseudorandom order. The participant was asked to focus on a fixation cross at the centre of the screen throughout the recording, which lasted for 480 s.

2-back task: A single trial comprised 20 seconds of letter presentations on a screen (vertical visual angle ~3°). One letter was shown every 2 s and was visible for 1 s (i.e. the gap between letters was 1 s). Participants were asked to press a button using their right index finger when the current letter matched that presented two letters previously (i.e., for a sequence of letters running ‘F’ ‘H’ ‘E’ ‘F’ ‘E’ ‘D’ subjects should press the button at the presentation of the second ‘E’). 20 s of ‘2-back’ was followed by 20 s of rest, where participants were asked to focus on a central fixation dot on the screen. This was repeated for 25 trials, making the experiment duration 1000 s in total. 2-back tasks of this nature are known to elicit frontal midline theta activity (Brookes et al., 2011b; Missonnier et al., 2006; Owen et al., 2005).

Both paradigms were presented using back projection through a waveguide in the MSR onto a screen placed ~80 cm in front of the participant in the OPM-MEG system, and ~95 cm in the SQUID-MEG system. An Optoma HD39 Darbee projector with a refresh rate of 120 Hz was used to display the stimuli for both the OPM and SQUID recordings. A photodiode was attached to the screen at the location of the flashing square to monitor the timings of the visual task. Responses to the 2-back paradigm were recorded using a fORP 4-button fibre optic response pad (Cambridge Research Systems Ltd.). This enabled measurement of correct/incorrect responses as well as reaction times.

4.3.3 OPM-MEG data collection

The OPM-MEG system (See Figure 4.1) comprised 174 channels (58 triaxial OPM sensors [QuSpin Inc., Boulder, CO]). The sensors were uniformly distributed across a rigid additively manufactured adult helmet (Cerca Magnetics, Nottingham, UK)

providing approximately whole-head coverage. The outputs of each OPM channel were fed into a National Instruments digital acquisition system (DAQ) and were sampled at 1200 Hz. A further 4 OPMs (QZFM Gen-1 QuSpin Inc., Boulder, CO) were placed immediately behind the subject to sample the background magnetic field. The system was housed in an OPM-optimised magnetically shielded room (Cerca Magnetics Limited, Nottingham, UK) with four layers of mu-metal, 1 layer of copper and degaussing coils. The room was also equipped with a bi-planar coil, which surrounded the subject and was capable of active field control (Cerca Magnetics Limited, Nottingham, UK). A 6-camera motion tracking system (OptiTrack Flex 13, NaturalPoint Inc., Corvallis, Oregon, USA) was used to monitor subject movement for precision magnetic field control. OPM control, data acquisition, and coil outputs were controlled by a single ‘acquisition’ PC, whilst the stimuli and tracking cameras were controlled by a second ‘stimulus’ PC. Triggers delineating the timing of events throughout the experimental paradigms were sent from the stimulus PC to the DAQ and were recorded alongside the MEG data.

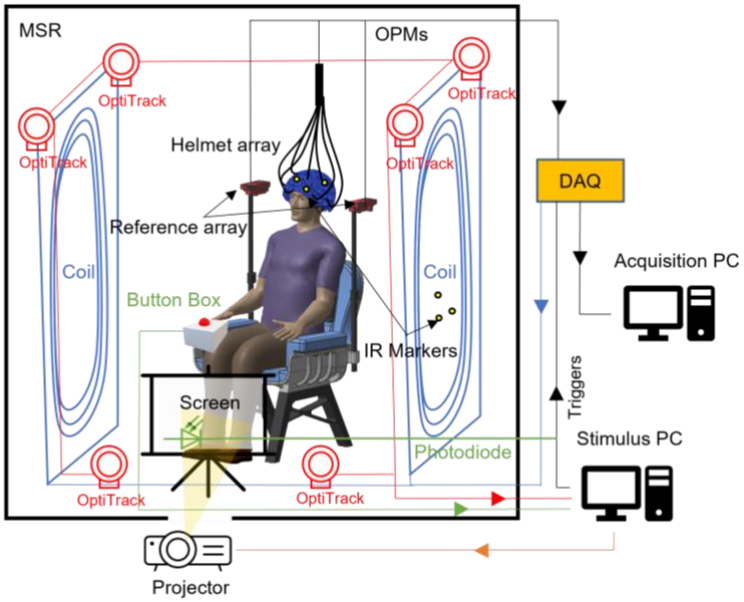


Figure 4.1. Schematic of the OPM-MEG system.

The 3D-printed helmet containing the OPMs was available in several sizes (Figure 4.2); prior to scanning, the subject's head circumference was measured, and the best-fitting helmet was selected and populated with OPMs. At the start of each scanning session, a 60 s “noise” recording was acquired with no subject present in the room, to assess levels of background interference and identify any problems with the system. Following this, subjects were seated comfortably on a patient support within the MSR, and the helmet was placed on their head. All subjects were completely free

to move during the scan (though they were not specifically asked to do so). Once seated, the degaussing and remnant magnetic field nulling procedures were carried out. Following this, MEG data were recorded during the two paradigms. In addition, the experiment was also run once with no subject present, to obtain an empty room noise recording with equivalent duration to subject data.

To spatially coregister the MEG data to the anatomical MRI, two 3D digitisations of each participant's head were acquired using an optical imaging system (Einscan H, SHINING 3D, Hangzhou, China), as described in Chapter 3.9. The first with the helmet on (to measure helmet position relative to the face) and the second with the helmet removed and a swimming cap used to flatten hair (to obtain an estimate of the whole head shape, including the scalp surface). A 3D surface representing the face and scalp was also extracted from the anatomical MRI scan. In contrast to the method described in Chapter 3.9, coregistration in this study was achieved via a 3-step process: 1) The two optical digitisations were segmented, leaving only points around the face, and were aligned to each other. 2) The second optical digitisation (with the helmet removed) was aligned to the surface extracted from the MRI. Combining steps 1 and 2 provided knowledge of the helmet position relative to the brain. 3) The locations and orientations of the OPMs relative to the helmet – known from the 3D printing process – were added, providing a complete coregistration of sensor position and orientation relative to the brain anatomy. This technique has been successfully used in previous work (Hill et al., 2020; Zetter et al., 2019). This final coregistration was subsequently used to enable forward modelling of the magnetic field generated by current dipoles in the brain.



Figure 4.2. Rigid 3D-printed generic helmet sizes. *From left to right: 2-year-old, 4-year-old, small adult, and large adult.*

4.3.3.1 Precision magnetic field control

Our system is housed inside an OPM-optimised MSR (Cerca Magnetics Limited, Nottingham, UK) equipped with a system for demagnetisation of the inner mu-metal layers. Demagnetisation typically leaves a magnetic field inside the MSR of ~ 3 nT – too high for effective OPM operation with unconstrained subjects. To further reduce this field, active magnetic field control was employed using the bi-planar coils. The bi-

planar coil system is capable of generating the three uniform field components, and the five independent linear gradient fields (due to Equations 3.25), within a volume of ~ 0.4 x 0.4 x 0.4 m^3 enclosing the participant's head (Holmes et al., 2019). Nulling the background field in this volume thus allows head movements from a seated position. Here, the coil was used in two ways – firstly, the reference array surrounding the helmet array was used to estimate the low frequency (< 3 Hz) temporal changes in the spatially uniform and gradient background magnetic fields (e.g. low frequency drifts caused by passing vehicles); such changes were fed back to the coil, which outputs an equal and opposite field to provide temporal stability (Holmes et al., 2019). Having stabilised the field in time, the remnant temporally static field was corrected via a nulling process first described by Rea et al (Rea et al., 2021). Briefly, a series of head movements was performed by the participant and the translation and rotation of 5 triaxial OPMs in the helmet were captured using optical tracking. The measured field changes generated by movements of the same sensors were simultaneously recorded, combined with the movement data, and fitted to a spherical harmonic model to determine the static background field and field gradients present in the vicinity of the head. The coil was then used to offset these fields. The entire process can be repeated to improve performance. This technique has been shown to cancel remnant fields to < 300 pT. Here, unlike previous demonstrations of this technique (Holmes et al., 2022; Rea et al., 2022, 2021), rather than starting with the raw field following demagnetisation, an initial estimate of the background magnetic field (based on past studies) was used, and estimated currents were applied to the coils before the nulling procedure took place. Thus, the starting field was expected to be lower than the ~3 nT typically observed. This procedure (outlined in Figure 4.3), which takes approximately 5 minutes, was carried out for all participants.

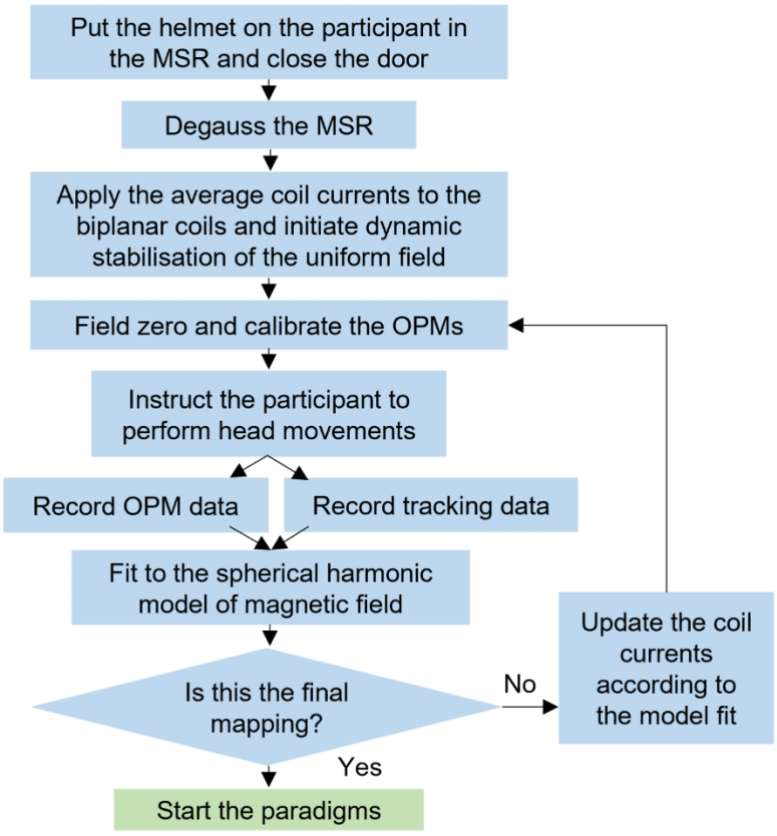


Figure 4.3. Precision magnetic field control. *A flowchart describing the field nulling process.*

4.3.4 SQUID-MEG data collection

SQUID-MEG data were acquired using a 275-channel CTF system (CTF, Canada) in third-order synthetic gradiometer configuration, with a sampling frequency of 1200 Hz for the visual task, and 600 Hz for the working memory task (see Figure 4.4). The SQUID-MEG system is housed in an MSR (Vacuumschmelze, Hanau, Germany) to reduce the effects of external interference. As with all conventional MEG recordings, the subjects were asked to remain still throughout data acquisition. Prior to entering the scanner, three head position indicator (HPI) coils were placed on the subject's head, and their locations inside the MEG helmet were tracked continuously throughout both experimental recordings. Motion greater than 5 mm was considered prohibitive, and data were discarded.

Following the experiment, a 3D digitiser (Polhemus, Colchester, Vermont, USA) was used to measure the location of the three HPI coils relative to the face and scalp surface. The digitised surface was then fitted by surface matching to the equivalent surface extracted from the anatomical MRI. This enabled complete coregistration of the MEG sensor geometry to brain anatomy (see Chapter 2.4.5). Note that this

technique was selected (over the optical approach used for OPMs) as it represents a “standard” means to enable coregistration with conventional MEG.

Following coregistration, the distance from all sensors to the closest point on the scalp surface was measured. This was carried out for both the SQUID and OPM systems.

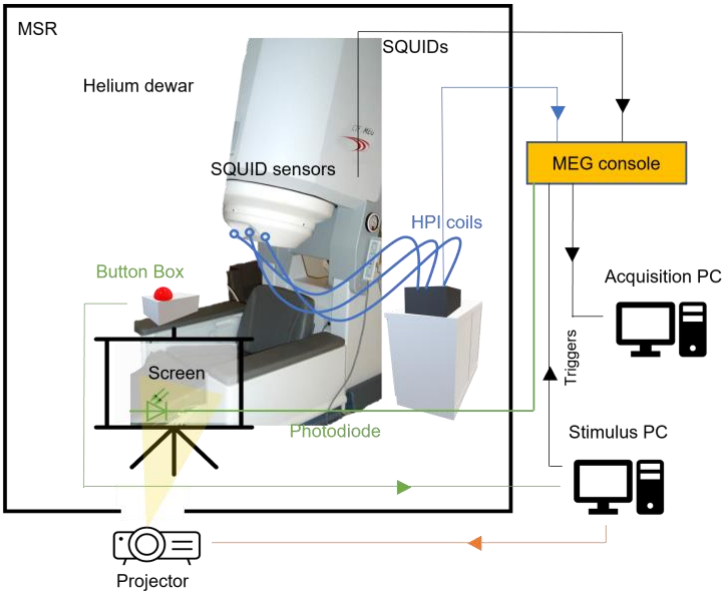


Figure 4.4. Schematic of the SQUID-MEG system.

4.3.5 Data analysis

4.3.5.1 Pre-processing

All OPM-MEG data were filtered from 1 – 40 Hz using a finite impulse response (FIR) non-causal bandpass filter. Data were then inspected visually and any channels or trials displaying excessive noise were identified and removed. Homogenous field correction (HFC) (Tierney et al., 2021a) was then applied to remove interference that manifests as a spatially uniform field. On average (across subjects) this resulted in the removal of 9 channels and 4 trials.

A synthetic third-order gradiometry approach was used to reduce the effects of external magnetic interference in the SQUID-MEG data. Following this, data were filtered from 1 – 40 Hz using the same FIR bandpass filter. Data were again inspected visually and any channels or trials displaying excessive noise were identified and removed. This resulted in the removal of an average of 4 channels and 1 trial.

4.3.5.2 Source localisation

Visual task: Data were narrowband filtered using a FIR bandpass filter within a 4 Hz range around each of the stimulation frequencies (4, 6 and 8 Hz). The broadband (1 – 40 Hz) and narrowband filtered data were then segmented into trials. Source localisation was performed using a linearly constrained minimum variance (LCMV) beamformer (Robinson and Vrba, 1998). The brain was divided into 4 mm cubic voxels. Forward solutions were computed using a single-shell head model and a dipole approximation of neural current (Nolte, 2003). Covariance matrices were generated using the 1 – 40 Hz filtered data in a time window spanning the whole experiment (excluding bad trials). The covariance matrix was regularised using the Tikhonov method with a regularisation parameter equal to 2 % of the maximum eigenvalue (Brookes et al., 2008). The optimised source orientation for each voxel was taken as that with the largest beamformer projected power (Sekihara et al., 2004). After generating the beamformer weights for each voxel, a pseudo-T statistical approach was used to contrast narrowband source power between the "on" window (0 – 2 s relative to stimulus onset) and "off" window (2 – 4 s) as described in Equation 2.41. Separate pseudo-T statistical images were constructed independently for the 4 Hz, 6 Hz and 8 Hz stimuli. In each case, we assessed the spatial signature of power changes at the fundamental frequency of stimulation. Voxels of interest were selected from the maximum of pseudo-T statistical images in a visual cortex mask, and a virtual electrode (VE) time course of the evolution of electrophysiological activity at these locations was reconstructed using the broadband data (see Chapter 2.5.2). The VE time course for each trial type was averaged across trials, and the Fourier Transform was computed (for the "on"- and "off"-windows separately). This enabled analysis of the spectral content. Note that this procedure was applied identically for the OPM- and the SQUID-MEG data.

2-back task: Data were filtered to the theta band (4 – 8 Hz) using a FIR bandpass filter and segmented into trials. Source localisation was performed using the same beamformer and forward model as described above. Covariance matrices were generated using theta band filtered data in a time window spanning the whole experiment (excluding bad trials) and were regularised again using the Tikhonov method with a regularisation parameter of 2 % of the maximum eigenvalue. A pseudo-T statistical approach, as described in Equation 2.41, was used to contrast theta band source power in the "on"- (5 – 20 s relative to trial onset) and "off" (24 – 39 s) contrast windows, producing volumetric images (again with 4 mm isotropic resolution) showing the spatial signature of the change in theta band power for each participant. A voxel

of interest was selected from the peak pseudo-T statistic in a frontal lobe mask for each participant, from which a VE time course was extracted using the broadband data (1 – 40 Hz). These were processed in 2 ways: first, the broadband data were theta band filtered using the same FIR filter and a Hilbert transform was generated, from which the absolute value of the resulting analytic signal was used to generate the amplitude envelope (or “Hilbert envelope”) of theta activity. This was then averaged across trials and baseline corrected (using the mean of the “off” period). The trial-averaged envelopes were then averaged across subjects. Second, the broadband VE data were segmented into task (0 – 20 s relative to trial onset) and rest (20 – 40 s) windows, and a spectral amplitude estimate was derived using Welch's overlapping segment averaging approach (with overlaps of 10 s). This method was applied to each trial separately, with results averaged over trials and participants. The empty room noise recording was also projected through the same beamformer weights that were derived for the 2-back data, and a spectral amplitude estimate was derived. This allowed for a comparison of spectral amplitude during task and rest, relative to sensor noise and background interference (excluding interference from the body [e.g. Magnetocardiogram] and movement artefact).

4.3.5.3 Statistical analyses

The SNR was quantified for both tasks. In the visual task, SNR was defined as the amplitude of the spectral peak at the frequency of interest (4 Hz, 6 Hz or 8 Hz) when the stimulus was on, divided by the average spectral amplitude in a 4 Hz window centred on the frequency of interest when the stimulus was off. For the 2-back task, SNR was defined as the difference in the mean Hilbert amplitude between task performance (0 – 20 s relative to trial onset) and rest (20 – 40 s), divided by the standard deviation of the signal at rest. In both cases, SNR calculations were carried out at the individual and group levels.

For the 2-back task, we expected significant inter-individual differences in both the amplitude and the spatial signature of the theta response (Inanaga, 1998; Meltzer et al., 2007), which would mask a traditional comparison of the two systems (involving group averaging) by increasing standard deviation between participants. However, we also expected that individual traits would be maintained between the two systems (i.e. a subject who had a high theta response in OPM-MEG would have a similarly high theta response in SQUID-MEG) (da Silva Castanheira et al., 2021). To test this, we carried out two separate analyses. First, we measured SNR at the individual subject level and plotted SNR in the SQUID system versus SNR in the OPM system. We expected a linear relationship, where the gradient would tell us which system had

the highest SNR (i.e. a gradient of 1 would indicate parity between the systems). Second, we compared the spatial signatures of the pseudo-T-statistical images. Specifically, we measured spatial correlation (a Pearson correlation coefficient between the vectorised functional images) between all possible functional image pairs. With 14 subjects scanned in OPM-MEG and SQUID-MEG there are 14^2 (= 196) possible combinations, of which 14 are within subject, and 182 are between-subject. We expected that the within-subject correlation values would be significantly higher than between-subject correlations. To test this statistically, we used a bootstrapping method. Of the 196 correlation values, we randomly switched which 14 values were chosen as the within-subject correlations; doing this for 100,000 iterations enabled the construction of an empirical null distribution and allowed us to estimate whether the real difference between within and between-subject correlations could have occurred by chance.

Finally, we were interested to see whether either the use of HFC (Tierney et al., 2021a) or the use of a triaxial array (Brookes et al., 2021) would affect the theta band signal-to-noise ratio. The above analysis was therefore repeated for 1) triaxial data with no HFC, 2) radial-only data with HFC and 3) radial-only data without HFC. Once again SNR was quantified (as above) and we explored the extent to which both the array design in our system and our post-processing techniques, impacted the performance of our OPM system.

4.4 Results

4.4.1 System comparison

We compared the scalp-to-sensor separation for each participant for each system, shown in Figure 4.5. On average, OPM sensors were 12 ± 3 mm closer to the scalp surface than SQUID sensors.

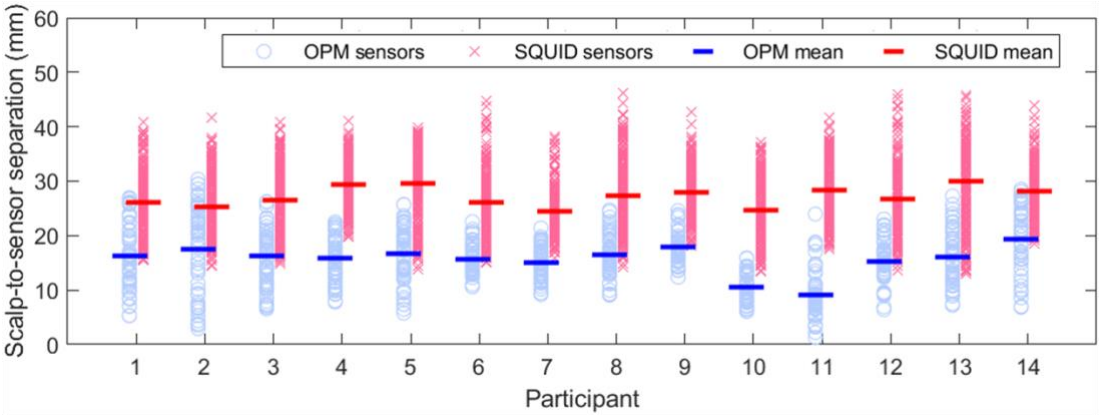


Figure 4.5. Scalp-to-sensor separation. *For OPM-MEG (blue) and SQUID-MEG (red). Data points show values for all sensors; lines show the mean.*

4.4.2 Magnetic field nulling

Figure 4.6 shows the effect of magnetic field nulling. The plot on the left shows the magnitude of the spatially homogeneous components of the magnetic field inside the MSR. The plot on the right shows the magnitude of the linear field gradients. Both are shown before (blue) and after (orange) application of the nulling procedure. The individual markers show the fields/gradients for 13 of the participants (individual participants are connected by the grey lines) – unfortunately, motion tracking data were unavailable for one participant. Here, in the case before nulling ("Null iteration 1") initial voltages had been applied to the coil currents to reduce the field in the room, based on measurements from previous studies (Rea et al., 2022). For this reason, the starting field magnitude (~0.9 nT) is lower than the typical ~3 nT that we would predict following degaussing. Nevertheless, optimisation via the nulling procedure reduced the field to an average of 0.31 $\pm$ 0.3 nT, highlighting the benefit of this process in data acquisition.

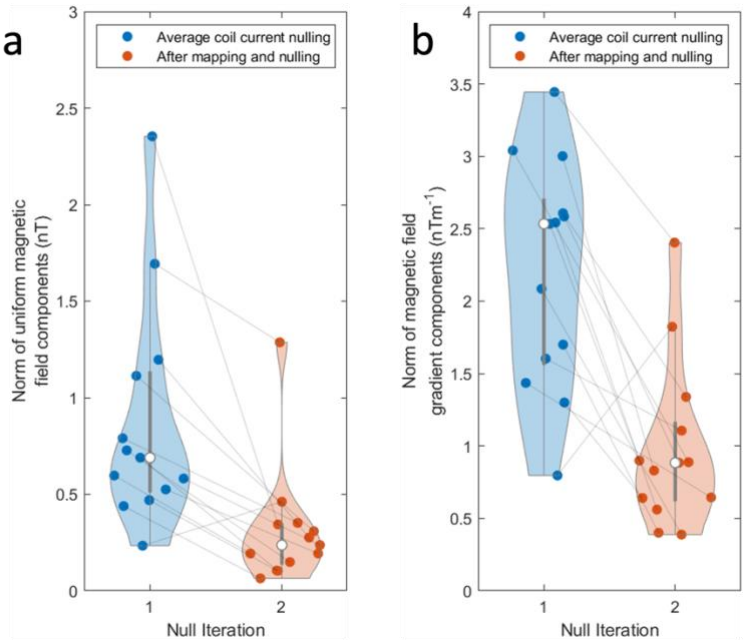


Figure 4.6. Precision magnetic field control results*. a) The magnitude of the homogeneous magnetic field and b) the linear field gradients before and after application of the nulling procedure. Solid circles show individual data points and lines show the field trajectories for 13 participants. The white circles show the mean values across subjects.*

4.4.3 Visual experiment

Figure 4.7 shows the results of the visual experiment. Panels a and b show the spatial signatures of changes in oscillatory power (all pseudo-T statistical images have been spatially coregistered to the MNI brain using FLIRT (Jenkinson et al., 2002) and averaged across participants and frequencies). The result is similar for both systems, with the largest effect localising to the left primary visual cortex. This was expected as the stimulus was presented in the lower right quadrant of the visual field and maps retinotopically to the cortex. Panels c-e show power spectral data of VEs extracted from the peaks in the pseudo-T statistical images. In all cases, the data during stimulation are shown. Panels c, d and e show 4 Hz, 6 Hz and 8 Hz, respectively. For all three stimulation types, peaks at the fundamental frequency and its harmonics are observed. Quantitatively, the peak oscillatory power changes for the two systems were separated by 12 mm with the OPM-MEG appearing slightly anterior. The Pearson correlation coefficient between the two (vectorised) pseudo-T statistical images was 0.89. The SNR values for OPM data were 2.0$\pm$0.8, 1.7$\pm$1.1 and 1.8$\pm$1.1 for 4 Hz, 6 Hz and 8 Hz, respectively. Equivalent values for the SQUID data were 2.3$\pm$1.2, 1.8$\pm$0.9 and 2.3$\pm$1.1. The SNR differences between the two systems were not significant ($p < 0.05$) according to a Wilcoxon sum-rank test.

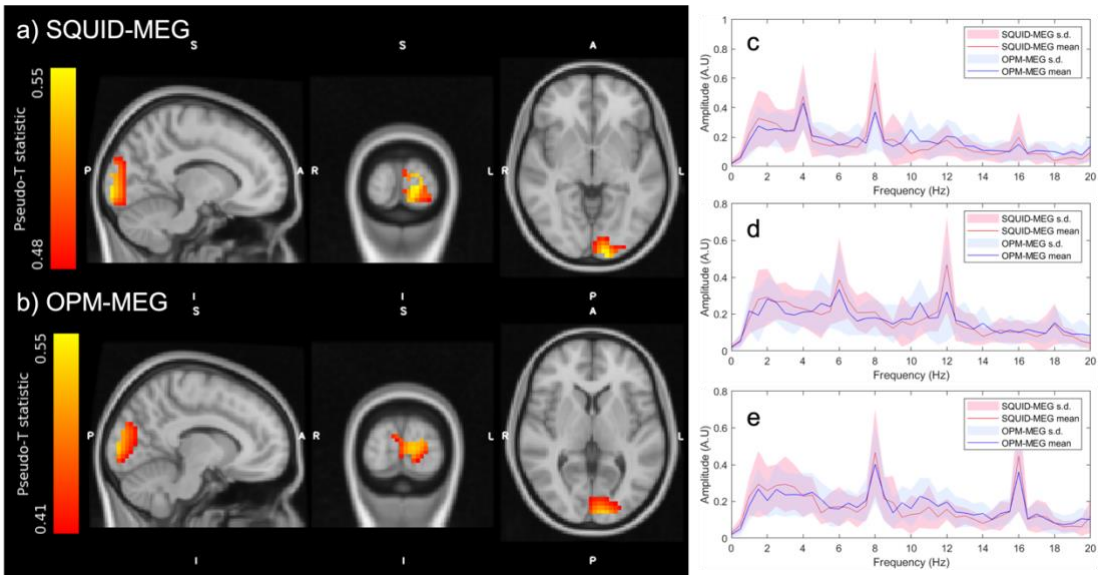


***Figure 4.7. Visual experiment results**. a-b) Show pseudo-~T statistical images of the spatial signature of changes in oscillatory power at the fundamental frequency of stimulation (note here that 4 Hz, 6 Hz and 8 Hz have been combined). a) shows the case for SQUID-MEG and b) shows the case for OPM-MEG. The locations of maximum change are separated by 12 mm. c-e) show the subject averaged Fourier spectra from the VE from the voxel with peak pseudo-T statistic during stimulation for c) 4 Hz, d) 6 Hz and e) 8 Hz. In all three cases, SQUID data are shown in red and OPM data in blue. Shading represents standard deviation across participants.*

4.4.4 Working memory (2-back) experiment

All 14 participants performed well on the 2-back task. For the OPM data, participants responded correctly to 95±3% of the 2-back targets (mean ± standard deviation). The false positive rate (i.e., the percentage of non-target letters that were incorrectly identified as being a 2-back match) was 0.5±0.5%. The average reaction time for correct responses was 0.576±0.08 s. For the SQUID data, participants responded correctly to 95±5% of the targets, the false positive rate was 0.5±0.5% and the reaction time for correct responses was 0.585±0.10 s.

Figure 4.8a and b show the spatial signatures of the theta band response, averaged across participants, and overlaid on the MNI brain (using FLIRT). In agreement with expectation, we observe a significant increase in the amplitude of theta oscillations that peaks in the frontal midline. Panel a) shows the results for the SQUID measurements and panel b) shows the case for OPMs. In both systems, the result is spatially similar with peak voxels in SQUID and OPM measurements separated by 13 mm. The Pearson correlation between the two (vectorised) images was 0.73. Panel c) shows time courses of the Hilbert envelope, extracted from the peak locations in the frontal cortex (derived from the pseudo-T statistical images) and averaged over trials and participants. A clear increase in theta amplitude is observed during the task (0 – 20 s) with strong similarity between MEG systems. The correlation between the

SQUID and OPM envelope time courses was 0.76; the group level SNR of the SQUID and OPM systems was 5.14 and 5.02, respectively.

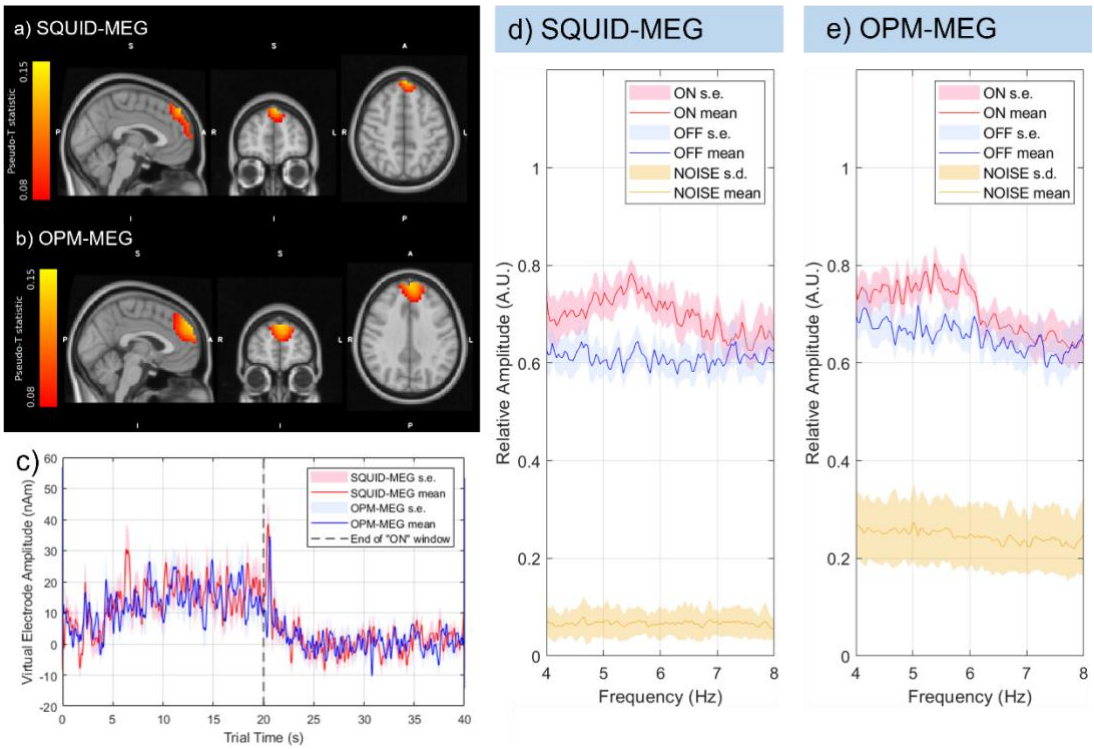


***Figure 4.8. Working memory task group source space results**. a-b) Pseudo-T statistical images showing the spatial signature of changes in theta band power. Images show the average across subjects for a) SQUID-MEG and b) OPM-MEG. The voxels with the highest theta change are separated by 13 mm between OPM and SQUID systems. c) shows the Hilbert envelopes showing the relative change in theta amplitude; the mean across subjects is shown and the shaded areas represent standard error for SQUID recordings (red) and OPM data (blue). Stimulus cessation is shown by the dashed grey line. d-e) show the subject averaged power spectral density from the virtual electrode during the task (red) and rest (blue) and from empty room noise recordings (yellow) for the SQUID (d) and OPM (e) measurements. The shaded areas for the task and rest windows show standard error across the 14 participants, and empty room noise recordings show standard deviation across the noise recording duration.*

Figure 4.8 d) and e) show the spectral amplitude of the SQUID- and OPM-derived virtual electrode data for the task period (red) and rest period (blue). Empty room recordings are also shown (yellow). Note the clear elevation in theta amplitude during the task, relative to rest. As expected, the spectral amplitude of the empty room OPM recordings increases with decreasing frequency; for example, the theta band baseline was 1.22 times higher than the beta band baseline (16.5 fT/$\sqrt{\text{Hz}}$ for theta compared to 13.6 fT/$\sqrt{\text{Hz}}$ for beta when averaged over all sensors and noise realisations). This increase can be seen in panel e). However, e) also shows that the beamformer projected empty room spectral amplitude for the OPM system was around 4 times lower than the spectral amplitude of theta measurements in subjects at rest, suggesting that it is not the dominant noise source for theta measurement – this will be addressed further in the discussion.

Figure 4.9 shows the results of our 2-back experiment at the individual participant level. a) shows SNR for the SQUID system plotted against SNR for the OPM system. Each data point represents an individual participant. Pearson correlation showed a significant (r = 0.86; p = 0.0001) relationship between the two measurements – i.e. those individuals who had a strong theta response in OPM-MEG data also tended to have a strong theta response in SQUID-based measurements. The slope of the line was 0.77±0.12, indicating that the SNR of the OPMs was marginally lower than that of the SQUIDs. However, this was driven to a degree by a single subject since removing one data point (circled) changed the slope of the line to 0.85 ± 0.22, while still resulting in a significant relationship (r = 0.76; p = 0.003).

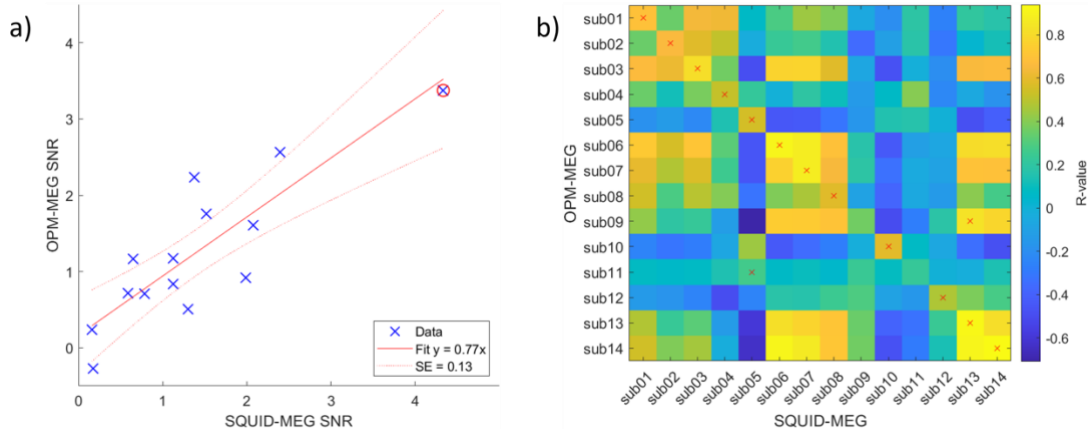


Figure 4.9. Working memory task individual results. *a) SNR of the theta band response measured in the OPM data, plotted against equivalent SNR measured for the SQUID data. Note the significant (p = 0.0001) linear relationship between the two systems. The red circled data highlights a single participant, whose strong theta response somewhat reduces the slope. b) shows the matrix of correlation values showing the spatial relationships between pseudo-T statistical images of task-induced theta change. Red crosses indicate the highest correlation value within each row. Note that crosses fall on the diagonal (i.e. within-subject correlation) for 12 out of 14 subjects.*

Panel b shows the correlation values between pseudo-T statistical images of change in theta power, for OPM-MEG and SQUID-MEG (i.e., each value shows how similar the two images are). The matrix elements show all 196 possible correlation values between all subjects; the diagonal values represent within-subject correlation, whereas the off-diagonal elements represent between-subject values. Note subjects are ordered according to the SNR of their theta response averaged across systems-i.e., subject 1 has the highest SNR; subject 14 has the lowest.

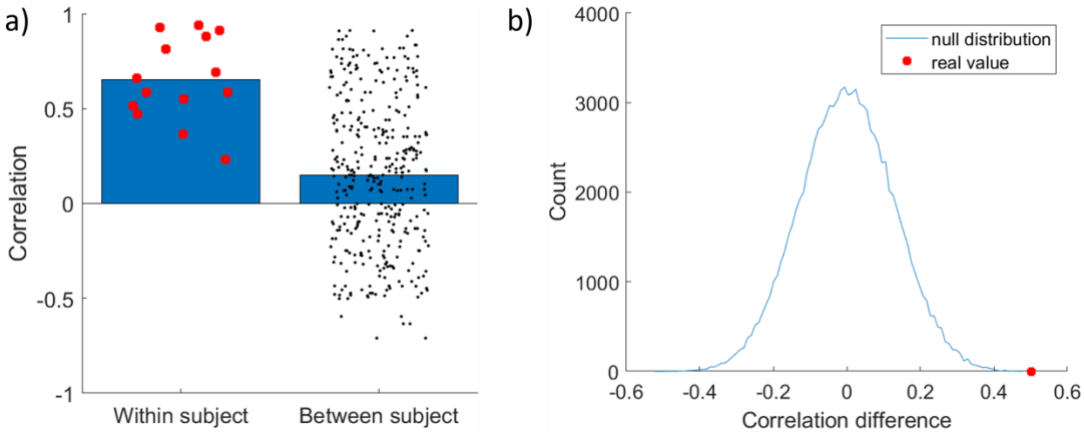


Figure 4.10. Bootstrapping statistical simulation. *a) The correlation values shown in Figure **4.9**b plotted as within and between subject correlations and b) Bootstrapping statistical test showing the null distribution and the real value for the average within-subject correlation.*

Figure 4.10 shows the results from the bootstrapping statistical tests on the pseudo-T statistical image correlations. Panel a) shows that the within-subject correlation (mean 0.65) is significantly higher than the between-subject correlation (mean 0.15), this is shown in the null distribution in panel b), where p = 0.00003. In support of this, in Figure 4.9b, the red crosses signify that for 12 out of 14 participants scanned, the highest correlation was within-subject between systems. This analysis is sometimes termed neural fingerprinting (da Silva Castanheira et al., 2021). These results demonstrate that individual variation, measured via both SNR of the theta band response and its spatial signature across the brain, is maintained across two independent MEG recordings using very different instrumentation.

4.4.5 OPM-MEG artefact reduction

Finally, we explored the extent to which the performance of OPM-MEG was influenced by both the use of a triaxial array (which is known to have good interference rejection properties (Brookes et al., 2021)) and homogeneous field correction (HFC). Figure 4.11a shows four realisations of the theta band subject-average response, formulated as instantaneous SNR (i.e., instantaneous oscillatory amplitude divided by the standard deviation of the signal in the rest [20 s to 40 s] window) and plotted against time. The far-left hand graph shows triaxial data with HFC, the centre-left graph shows triaxial data without HFC, the centre-right graph shows radial only data with HFC, and the far-right graph shows radial data without HFC. In all cases, the coloured line shows OPM-MEG SNR, and the black line shows SQUID-MEG SNR (identical for all four plots and shown only for comparison). Figure 4.11b shows the same data, but with the OPM SNR plotted against SQUID values. Here the slope of the line (which passes through the mean in the task and rest windows) is a representation of how

OPM SNR compares to SQUID SNR, at the group level. A slope of unity would indicate parity between the two systems. The four lines are overlaid in panel d. For triaxial data with HFC, the slope is 1.17, however, this drops to a value of 0.95 without HFC; 0.86 for radial-only with HFC and 0.85 when using radial recording and no HFC.

Figure 4.11c and e show similar analyses, performed at the individual subject level. Panel c shows individual subject SNR for OPM-MEG plotted against SQUID MEG. This is equivalent to Figure 4.9a but here four realisations are shown – from left to right: triaxial data with HFC, triaxial data without HFC, radial data with HFC, and radial data without HFC. Here the slope of the line indicates how OPM-MEG SNR compares to SQUID-MEG SNR at the individual level. The lines are overlaid in panel e. In agreement with the group average data, there is a marked effect on OPM-MEG performance, with a slope of 0.77 for triaxial data with HFC, falling to 0.67 with no HFC; 0.66 with radial-only recordings with HFC, and 0.59 with radial recordings and no HFC. These effects show that both the use of triaxial sensing and homogeneous field correction influence the quality of OPM-MEG reconstructions.

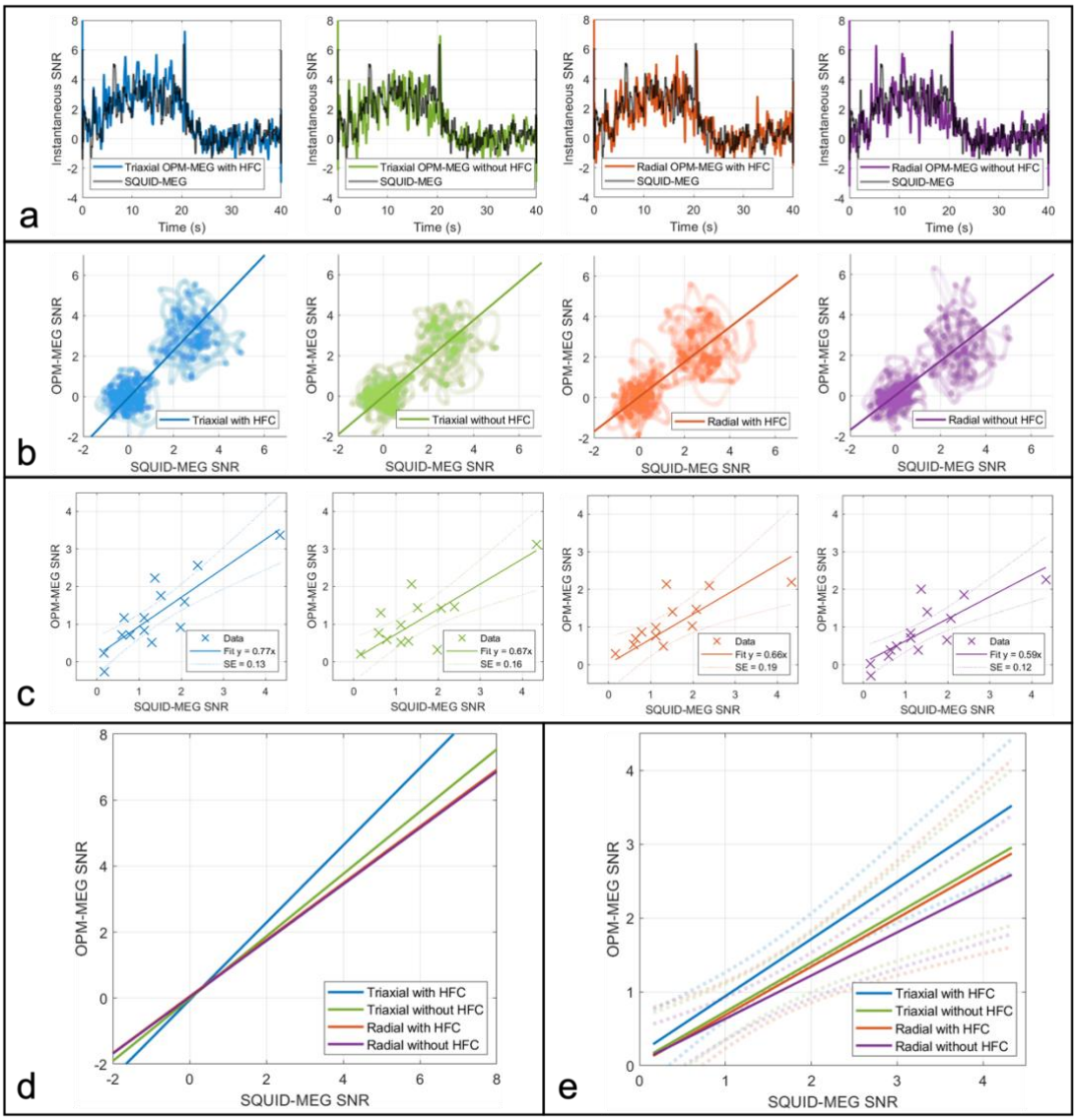


Figure 4.11. Artefact reduction with OPM-MEG*. a) Subject averaged instantaneous SNR of both the OPM (coloured) and SQUID (black) theta band responses plotted against time. b) OPM derived plotted against SQUID derived instantaneous SNR. In both a) and b) the 4 columns show triaxial data with HFC (far-left), triaxial data without HFC (centre-left), radial data with HFC (centre-right) and radial data without HFC (far-right). c) SNR values from individual subjects; SQUID plotted against OPMs. Order of columns as above. d) the line fits the mean for the task and rest windows from the data in b) overlaid. The slope of the line represents the relationship between SQUID and OPM instantaneous SNR values. e) the lines from c) overlaid. Notice in both d) and e) that the slope of the line is diminished by removing tangential axes, and by removing HFC.*

4.5 Discussion

The measurement of low frequency neural oscillations is a significant challenge for wearable OPM-MEG. Nevertheless, here we have shown that oscillations in the theta band can be measured reliably in unconstrained subjects using a 174-channel triaxial OPM-MEG system. We measured visual steady state evoked responses at 4 Hz, 6 Hz and 8 Hz, at a SNR that was not significantly different to a SQUID-based system (with 275 channels). Similarly, we measured task-induced increases in frontal midline

theta oscillations during a 2-back working memory task, again with comparable SNR at the group level (5.02 for OPM-MEG compared to 5.14 for SQUID-MEG). Analysis of our working memory task at the individual level showed striking relationships between results acquired using the two different systems. Specifically, we showed a linear relationship between individual SNR values. Further, when measuring the consistency of the spatial signature of task-induced theta increases, within-subject correlation (0.65) was significantly higher than between-subject correlation (0.15) – meaning that both the signal amplitude and spatial signature of theta change were maintained across the two independent recordings. Finally, we showed that—whilst OPM-MEG could be used to successfully characterise theta oscillations—SNR was dependent on both the array design (triaxial sensors) and on HFC.

We had hypothesised that characterisation of low frequency activity would be difficult in wearable MEG for several reasons. Firstly, the internally generated noise inherent to the OPM sensor increases with decreasing frequency. Secondly, whilst environmental fields are shielded by the MSR, such shielding becomes more difficult as frequency decreases. This second problem has been addressed in conventional MEG – for example via the use of 5 cm baseline axial gradiometers and a reference array with synthetic third-order gradiometry (Vrba and Robinson, 2001); both exploit the fact that whilst the signal from the brain decays quickly with distance from the scalp, distal interference sources decay more slowly and so, by measuring magnetic field gradients, interference can be minimised (other SQUID-based MEG systems employ similar [albeit radial, rather than axial] gradiometric techniques). The problem in wearable MEG is that commercial OPMs are formed as magnetometers, rather than gradiometers, and whilst gradiometers can be synthesised by digital signal subtraction, this results in an increase in random noise (by a factor of $\sim\sqrt{2}$). It is possible to construct inherent OPM-based gradiometers by allowing light to pass through two spatially separate vapour cells (Nardelli et al., 2020), however, this involves increasing the sensor size, which makes a wearable system cumbersome. It follows that for OPM-MEG, the use of gradiometry is challenging.

Here, both the inherent sensor noise and low frequency environmental interference were assessed using our empty room recordings. Spectral analysis showed that, as expected, the spectral amplitude increases with decreasing frequency; for example, the theta band baseline was 1.22 times higher than the beta band baseline (16.5 fT/$\sqrt{}$Hz for theta compared to 13.6 fT/$\sqrt{}$Hz for beta when averaged over all sensors and noise realisations). This increase can also be seen in the data in Figure 4.8e. However, Figure 4.8e also showed that the beamformer projected empty room

spectral amplitude was around 4 times lower when compared to the spectral amplitude of theta measurements in subjects at rest. It, therefore, follows that neither the low frequency interference nor the inherent sensor noise, both of which will be present in the empty room noise recording, is the dominant source of variance in the resting theta band signal. Nevertheless, comparing Figures d and e, the noise floor of a SQUID in the theta band remains much lower than that of an OPM – something that will be important for future OPM design.

A third source of low frequency interference is movement. Any motion of the OPM array within a static background field manifests as a dynamic signal; if the background field is large this will obfuscate neuromagnetic fields. Because movement is 'slow', such interference manifests at low frequency. Given the observation relating to empty room interference, it is tempting to speculate that the movement artefact is the dominant source of variance for low frequency wearable MEG measurements. Here, we attenuated the movement artefacts at the source by generating a background field as close to zero as possible. The background field was reduced to 0.31 ± 0.3 nT – a factor of ~10 better than we typically observe inside the MSR (with no field nulling applied) and ~160,000 times lower than the Earth's static field. This demonstrates the critical importance of field nulling; without the use of bi-planar coils the movement artefacts would have been 10 times larger – a rotation of just 1 degree would generate a field shift of 52 pT (much larger than brain activity), and a 90° rotation would be sufficient to render an OPM inoperable. Following our nulling procedure, even a full head rotation would maintain a total field shift of < 1 nT, meaning OPMs remain operational, and small rotations would generate artefacts of just a few pT. As an aside, we also assessed the effectiveness of the use of the bi-planar coil with pre-calculated currents based on past observations of the field in the MSR. This was sufficient to reduce the field to 0.9 nT, meaning that background fields are consistent over time (if they weren't, pre-calculated coil currents would be unlikely to reduce the field). However, the result was improved significantly by the nulling procedure, showing the importance of a bespoke field calculation per participant.

Despite the success of field nulling, there remains a residual movement artefact in the data due to the remnant (0.3 nT) field. There are also other sources of low frequency interference due to the presence of the participant, including magnetic fields from the heart, muscles, and eyes – all of which are larger than brain activity. In addition, fields from brain areas that are of no interest to the task (sometimes referred to as "brain noise") will also generate theta band interference. It follows that these sources, in some combination, provide the dominant source of variance in the theta band noise

floor. Here, we used a combination of HFC and beamforming to reduce the effects of such fields; HFC reduces fields that are uniform across the sensor array; meaning mainly fields from distant sources (Tierney et al., 2022). Beamforming is a spatial filtering technique that helps to remove fields that originate anywhere other than the brain region being probed (Brookes et al., 2021; Tierney et al., 2022). The performance of both techniques is known to be significantly enhanced using a triaxial array. The utility of these techniques is shown in Figure 4.11, where SNR was improved by HFC. In addition, the use of triaxial (rather than conventional radial) sensors also improved SNR. To a degree, this latter finding is confounded because the comparison also involves changing the total sensor count. Nevertheless, the raw measurements are affected by residual fields originating outside the brain, and likely caused by a combination of movement and biological fields of no interest. Thus, for future studies of low frequency oscillations in OPM-MEG, post-processing to attenuate such fields should be considered essential.

Despite the difficulties, our primary result showed that theta band oscillations were well characterised by both OPM and SQUID-based MEG systems, despite participants being unconstrained in the OPM device. The SNR of the two measurements was similar; plots of the OPM-MEG SNR versus the SNR of the SQUID measurements showed marginally higher SNR in OPMs at the group level (with a line gradient of 1.17) and marginally lower SNR in OPMs at the individual subject level (with a line gradient of 0.77). Individual differences between subjects (both signal amplitude and spatial specificity) were consistently captured across both systems, despite acquisitions being (on average) 19 days apart. This “neural fingerprinting” not only provides a validation of the OPM-MEG system but also of the robustness of electrophysiological measures of human brain activity. Variance between individuals is often treated as “noise” in neuroimaging studies. Nevertheless, these results add weight to an argument that between subject differences represent valuable sources of variance which should be properly modelled. Most importantly, the strength of theta oscillations is an important metric. Frontal midline theta is induced by tasks with high cognitive demand and therefore a useful marker of healthy brain function. Abnormally high theta oscillations can be a sign of cortical slowing – which itself denotes neurological problems – for example, dementia (Prichep et al., 2006; Vecchio et al., 2014), and concussion (Lee and Huang, 2014); higher amplitude theta waves are observed in children and their reduction with age is a marker of neurodevelopment (Hunt et al., 2019). For this reason, the ability to accurately measure and characterise theta waves is an important property of any MEG system.

Here we provide a benchmark showing that our 174-channel triaxial array design is, at minimum, capable of matching conventional SQUID-based instrumentation in characterising theta activity.

Finally, there are several limitations in the current study which should be addressed. We focussed on theta waves, with the lowest frequency at 4 Hz. This was for two reasons: first, the importance of theta waves in neuroscientific paediatric and clinical applications and second, the fact that theta oscillations are relatively easy to evoke in a repeatable (across systems) and well-controlled manner. Nevertheless, oscillations below 4 Hz, e.g., delta waves, exist and are important biological markers. They are challenging to evoke in a controlled manner, being most prevalent during sleep, and in patients with e.g., concussion (Lee and Huang, 2014). Nevertheless, future studies should aim to generate similar OPM/SQUID comparisons for these lower frequencies, though this would likely involve a redesign of the OPM helmet to facilitate comfortable sleep.

There are also technical limitations of our current implementation of OPM-MEG: Perhaps the most obvious is channel count – here we contrast 174 OPM channels to 275 SQUID channels. Channel count is important both for signal acquisition (at the simplest level, the more channels you can average over, the better the SNR you will get) and for differentiating between signals from different brain regions. Our OPM-MEG system allowed triaxial measurement – this offers significant advantages in terms of differentiating brain signal from external interference, but also some disadvantages because the measured tangential components of the magnetic field are smaller in amplitude than the radial components. The result is that the total signal (summed over channels) will be higher for the 275 SQUID-based radial channels compared to the 174 triaxial OPM channels. With this in mind, the fact that we approximately achieve parity between systems is compelling. Nevertheless, extension to higher channel counts, where one can reap the advantages of triaxial sensing whilst also optimising overall signal amplitude is an extremely important step forward. An additional advantage of a triaxial sensor array is that it is robust to cross-talk (Boto et al., 2022), so sensors can be placed in close proximity without interference. There is therefore no fundamental limit on how close sensors can be, and future work should aim to construct higher density arrays which would improve spatial resolution and decrease brain noise. Aside from channel count, our field nulling techniques, whilst successful, still left a residual field of 310 pT and even in this low field, small rotations of the head could cause artefacts which are similar in magnitude to neural signals. At the time of writing, it is not clear what the limit on field nulling is

– in principle it should be limited only by the extent to which we are able to prevent the field from changing during an experiment (around 0.13 nT (Holmes et al., 2019)), however small errors in head tracking, and potentially cable interactions between OPMs, are thought to affect the accuracy of modelling and therefore the extent to which we can null the background field. This said, there are no fundamental reasons why these techniques cannot be made more accurate, and thus the background field could be driven even lower. It is worth noting, however, that the precision nulling process requires participant involvement, and therefore may be unsuitable when scanning very young infants. Finally, the noise level of the OPMs themselves remains higher than that of a SQUID. As pointed out above, it is unlikely that this represents the dominant form of noise for the measurements shown. Nevertheless, further work to increase laser power and remove magnetic components from OPMs will be critical to driving the noise levels down closer to that of SQUIDs, which will help to improve SNR, particularly at low frequencies.

4.6 Conclusion

The accurate measurement and characterisation of theta band neural oscillations is a critical requirement for any viable MEG system, with applications ranging from neurodevelopment to dementia. However, such characterisation poses a significant challenge in wearable OPM-MEG systems due to higher levels of inherent sensor noise, magnetic interference (which is harder to shield at low frequency) and movement artefact in a static background magnetic field. Here we have shown that our 174-channel system can capture theta oscillations with similar accuracy to that of SQUID-based MEG. Further, we showed that individual differences between participants – including the amplitude and spatial signature of induced frontal-midline theta responses – are maintained across systems. Our results demonstrate the viability of a wearable OPM array to measure theta oscillations. Crucially, following this work, we can move forward with neurodevelopmental investigations, where low frequency signals are of particular interest and relevance.

5 MEG without MRI: a template warping method

5.1 Chapter overview

In this chapter, we address a second barrier in the development towards paediatric OPM-MEG. We propose and demonstrate a method of warping template anatomical MRI scans to 3D structure scans of the participant's head shape to generate "pseudo-MRIs", enabling the analysis of OPM-MEG data in source space without the acquisition of an individual's brain structure. We first describe the method by which the pseudo-MRIs are generated. We measure the geometric accuracy of the method by calculating the Euclidean distances between medoids of 78 AAL regions coregistered to either the individual or pseudo-MRIs. We evaluate the effectiveness of our method by analysing MEG data collected from 20 participants using forward models derived from both individual anatomy (from MRI) and pseudo-MRI anatomy. We quantify the spatial separation between locations of peak activity during a sensory task and correlate functional connectomes to investigate the impact of the pseudo-MRI forward model on two typical methods of MEG data analysis. We find a high correlation between pseudo-T statistical images generated using the pseudo-MRIs and individual anatomy, with peak locations separated by just 2.6 $\pm$ 5.4 mm (group average $\pm$ standard deviation). Finally, our connectivity analyses show highly correlated connectomes, with a clear bilateral sensorimotor network across the regions with the highest connectivity. Global connectivity was highly correlated at 0.98, suggesting that the pseudo-MRIs provide consistent results in comparison with individual anatomy.

5.2 Introduction

Magnetoencephalography (MEG) source reconstruction provides novel insight into the origin of electrophysiological signals. Usually, this requires an anatomical MRI scan alongside head localisation and digitisation to allow the generation of an accurate volume conductor model and subsequent calculation of the lead fields, as well as an anatomical structure on to which activity is overlaid (see Chapter 2.5). However, the acquisition of an MRI can be difficult due to: the cost of MRI scanning

(Holliday et al., 2003); remnant magnetisation (post-MRI) producing greater "magnetic noise" in subsequent MEG scans (Hutchinson et al., 2019; Kirschvink et al., 1992); and, perhaps most crucially, the unnatural MRI scanning environment, which can be challenging for a range of participant groups to endure, particularly children. This means that the development of methods that avoid the necessity of MRI is attractive. Indeed, wearable MEG systems comprising arrays of OPM sensors (see Brookes et al., 2022 for a review) enable the acquisition of data from an increased range of demographics, many of whom are unable to tolerate a "traditional" scanning environment (for example, OPM-MEG data has been acquired from young children (see Boto et al., 2022; Feys et al., 2023, 2022; Hill et al., 2019 and Chapters 6 and 7)). While these participants could in principle be sedated for a structural MRI, this is only ethical for patient groups and is not suitable for scanning healthy participants. There is a risk that, whilst we can collect data from challenging cohorts with OPM-MEG, we may be unable to process it due to the lack of MRI. It is therefore important that we develop source analysis for OPM-MEG data without the need for an MRI. However, OPMs also offer better data with higher SNR (Boto et al., 2016; Iivanainen et al., 2017) and better spatial resolution than conventional MEG due to the ability to place sensors closer to the scalp and the development of OPMs that can measure multiple axes of the neuromagnetic field (Boto et al., 2022). As SNR increases, source analyses become more susceptible to modelling errors and consequently to inaccuracies in the forward model. This means that any approach needs to be very accurate (more so than with conventional MEG analysis) to produce robust results.

Template MRIs offer a potential solution. Recent years have seen large databases of standard MRIs by age (Fillmore et al., 2015; Richards et al., 2016; Sanchez et al., 2012a, 2012b), which can be used as approximations for individual anatomy for subsequent MEG data analyses. Template MRIs are typically used in one of four methods: a single template is used for all participants (Douw et al., 2018); a template is selected via demographic matching (e.g., by age and/or sex); the best-fitting MRI is selected from a database using matching algorithms to 3D digitisations of the participant's head, typically using a Polhemus system (Holliday et al., 2003; Seymour, 2018); or a pseudo-MRI is designed for each participant by warping a template MRI to the 3D digitisation of the scalp geometry and location of fiducial markers (Tadel et al., 2011).

In this chapter, we describe a template warping method for use with OPM-MEG data. We use 3D structure light scanning, a recent development in 3D image acquisition that has been used previously with OPM data for coregistration (Zetter et al., 2019), to provide a higher resolution estimate of the head shape than a conventional Polhemus system. We warp an age-matched template anatomical MRI to the 3D head shape using a linear transformation algorithm to generate a personalised pseudo-MRI. We compare the geometry of the pseudo-MRIs to individual MRIs across a group of healthy participants. Further, we test the pseudo-MRIs using MEG data acquired during a sensorimotor task across the group of adult participants, comparing results from source analysis with individual anatomical MRIs and pseudo-MRIs from warping templates.

5.3 Methods

5.3.1 Template warping

Our method is inspired by the method used by the software tool Brainstorm and described in Tadel et al. (2011). The flowchart in Figure 5.1 describes how a 3D structure scan (a method of acquiring a 3D digitisation of the head shape, described in Chapter 3.9) and age-matched template MRI are processed and transformed to generate the pseudo-MRI. Briefly, a 3D structure scan is acquired while the participant is wearing an elastic cap to flatten the hair to provide an estimate of the head shape. A template anatomical MRI is selected from a database (Richards et al., 2016) and the scalp is extracted (using FieldTrip (Oostenveld et al., 2011)). Meshes representing the outer head surface from the structure scan and the template scalp are generated (using FieldTrip). A rough manual rigid body transformation is applied using MeshLab (Cignoni et al., 2008) to move the structure scan to the same space as the template MRI. This reduces the computational expense and guides how the structure scan is cropped to ensure the warping only fits the head and facial features. The two meshes (from the structure scan and scalp of the template MRI) are converted into binary 3D images, and “filled in” using a convex hull method. This results in images that have a value of one inside the head and zero outside the head. FSL’s FLIRT (Jenkinson et al., 2002) is then used to find the transformation matrix required to warp the binary images of the template scalp to the 3D head scan (parameters: X, Y, Z search from -90:90 degrees; correlation ratio cost function; 12 degrees of freedom; tri-linear interpolation) and then this transformation is applied to the template MRI, generating

a pseudo-MRI that has the same geometry as the outer head surface. A schematic showing the method on an example participant is shown in Figure 5.2.

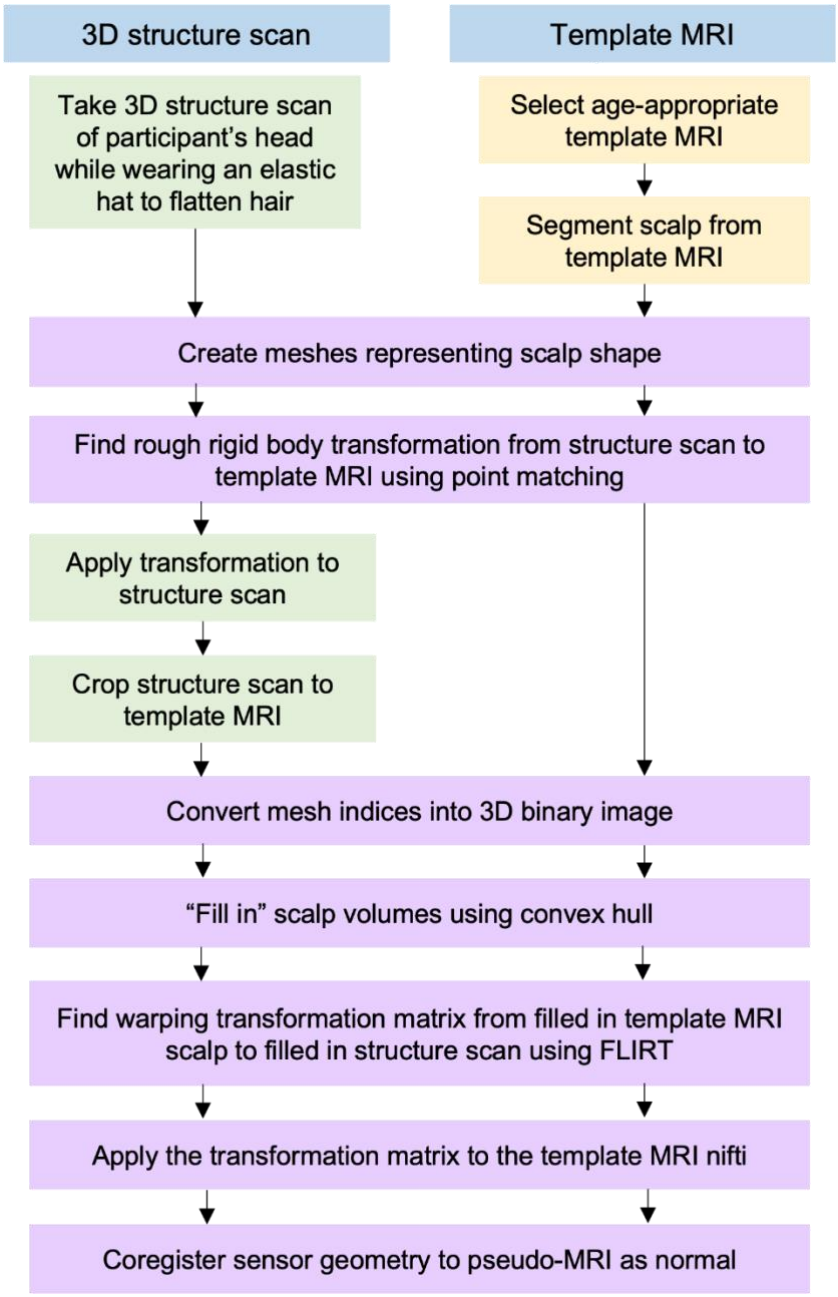


Figure 5.1. A flowchart of the template warping method. *A flowchart describing how the 3D structure scan and template MRI are processed to generate the pseudo-MRI.*

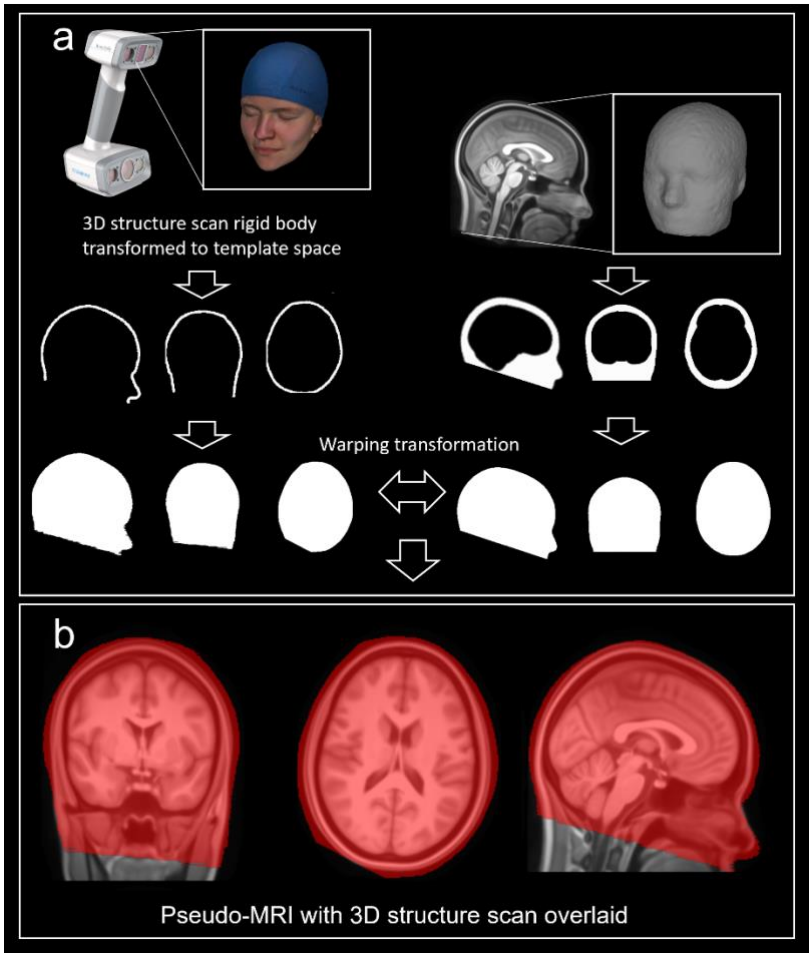


Figure 5.2. Template warping schematic. *An example is shown with a single participant: a) shows an image of the Einscan H device used to take the 3D structure scans, and an example head scan (left) and an example slice through a template MRI and the corresponding scalp mesh (right). Below are the binary images showing the scalp outlines for the 3D structure scan (left) and template MRI (right) and the equivalent scalp outlines "filled in" using a convex hull. b) shows the pseudo-MRI with the binary image from the 3D structure scan overlaid.*

5.3.2 MEG participants and paradigm

26 healthy adult participants took part in the study (age range 21 – 34; 12 identified as male), from which 20 participants had individual anatomical MRI scans (age range 23 – 34; 10 male) and were subsequently analysed[2]. All participants provided written informed consent prior to scanning and the study was approved by the University of Nottingham's Faculty of Medicine and Health Sciences Research Ethics Committee.

MEG data were recorded while participants received sensory stimulation via 'braille stimulators' and passively watched TV. The paradigm is described in Figure 5.3. Sensory stimulation involved tapping on the index finger (D2), followed by the little

[2] The author (and Dr. Lukas Rier) collected the data described in this chapter. This data is also described in Chapter 6 in combination with child participants.

finger (D5) of the right hand with 8 small plastic pins for 0.5 seconds (3 taps) followed by 3 s rest. This was repeated for 84 trials (42 per finger), throughout which, participants watched a television programme of their choice on a screen via projection onto a screen in the MSR.

Volumetric anatomical MRI scans were acquired using a Phillips Ingenia 3T system running an MPRAGE sequence with 1 mm isotropic resolution and T_1 contrast. Age-matched MRI templates were selected from the Neurodevelopmental MRI database (Richards et al., 2016).

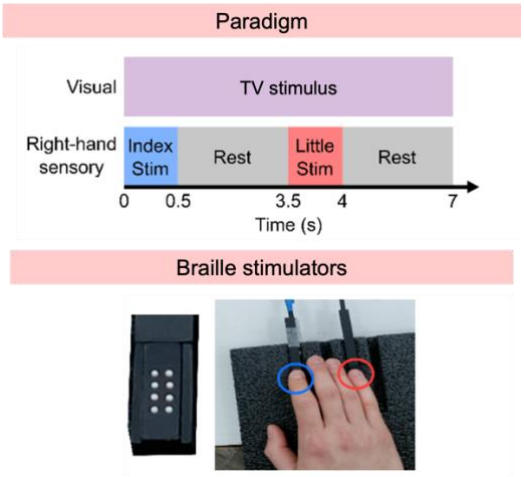


Figure 5.3. Braille Paradigm and stimulators. *A timeline describing a single trial of the braille task (top), an image of the pins of the braille stimulator (bottom left) and an example right-hand on the two braille stimulators (bottom right).*

5.3.3 OPM-MEG data acquisition

The OPM-MEG system is the same as that described in Chapter 4 but with more sensors. Here, the system comprised up to 64 tri-axial OPM sensors capable of measuring up to 192 channels of MEG data (QuSpin Inc., Boulder, CO, USA)). Sensors were uniformly distributed across rigid additively manufactured helmets in one of two sizes that were matched to the participant's head (Cerca Magnetics Limited, Nottingham, UK). OPM data were collected at 1200 Hz using a National Instruments (NI, Texas, US) data acquisition system interfaced with LabView (NI). The system was housed in an OPM-optimised MSR comprising 4 layers of mu-metal, a single layer of copper and equipped with degaussing coil. In contrast with Chapter 4, magnetic field control was instead provided by applying only the average computed coil currents from previous precision field control “mappings” to the bi-planar coils surrounding the participant (Rea et al., 2022, 2021; Rhodes et al., 2023). This provides compensation for the static magnetic field. Note that, although the bespoke field mapping (as carried out in Chapter 4) would result in a lower field (see Figure

4.6), the use of average currents was faster and therefore more practical for this paradigm that is later used with children (see Chapter 6).

Following the scan, two 3D digitisations were taken using an Einscan H (Shining 3D, China); one with the helmet on and one without. The 3D digitisation without the helmet was used for the template warping procedure (see Section 5.3.1) and the digitisation with the helmet was used for coregistration.

5.3.4 Coregistration

Coregistration was performed separately for pseudo-MRIs and individual MRIs following the method described in Chapter 3.9. Briefly, facial features were matched between the 3D scans taken of the participant wearing the helmet and the face of the scalp extracted from pseudo-MRI/MRI (using FieldTrip), transforming the helmet scan to the MRI space. A mesh of the helmet from 3D printing is then transformed via feature matching (see Figure 3.17 for typical features) to the scan of the participant wearing the helmet, thereby finding the complete transformation between MRI anatomy and sensor geometry (Hill et al., 2020; Zetter et al., 2019).

5.3.5 Geometric comparison

The anatomy of the individual MRI and pseudo-MRI were compared using an adaptation of the AAL atlas (Gong et al., 2009; Hillebrand et al., 2016; Tzourio-Mazoyer et al., 2002). The individual and pseudo-MRI brains were extracted using FieldTrip (Oostenveld et al., 2011) and divided into 78 cortical regions by coregistration to the MNI standard brain using FSL FLIRT (Jenkinson et al., 2002; Jenkinson and Smith, 2001). Due to the method of pseudo-MRI generation, the pseudo- and individual MRIs are in different spaces (I.e., the origin and orientations differ). To directly compare anatomy, we transformed the medoids from each AAL region from each MRI into a space that was defined by the OPM sensor array geometry. This provides a method of physical comparison of two brains (derived from individual and pseudo-MRI anatomy) that are in different spaces. Euclidean distance was calculated between corresponding regions from the individual and pseudo-MRIs.

5.3.6 Data pre-processing

We used a pre-processing pipeline described previously (Rier et al., 2023). Broken or excessively noisy channels were identified by manual visual inspection of channel power spectra and removed. Notch filters at the powerline frequency (50 Hz) and 2

harmonics, and a 1 – 150 Hz non-causal bandpass filter, were applied. Bad trials were defined as those with variance greater than 3 standard deviations from the mean trial variance, and automatically removed. A visual inspection was also carried out and any remaining trials with excess artifacts were removed. Finally, eye blink and cardiac artefacts were removed using ICA (implemented in FieldTrip (Oostenveld et al., 2011)) and homogeneous field correction (HFC) was applied to reduce interference (Tierney et al., 2021a). On average (across subjects) this resulted in 159 ± 9 available channels, and removal of 4 ± 2 trials.

5.3.7 MEG analysis

1.1.1.1 Beta modulation analysis

Here, only the index-finger trials were analysed to find the peak beta modulation. Data were filtered to the beta band (13 – 13 Hz) using a non-causal bandpass filter. Source localisation was performed using a linearly constrained minimum variance (LCMV) beamformer (Robinson and Vrba, 1998). We performed two separate analyses for beta modulation:

- A whole brain analysis in which we separated the brain into 4 mm isotropic voxels.
- A high-resolution analysis where we masked the sensorimotor cortices taking the precentral and postcentral left gyrus from the AAL atlas, dilating the volumes using a 5 mm sphere, and then dividing the resulting volume into 1 mm cubic voxels.

In both cases, forward solutions were computed using a single shell model (Nolte, 2003). Covariance matrices were generated using beta band filtered data across all trials (excluding bad trials) and were regularised using the Tichonov method with a regularisation parameter equal to 5 % of the maximum eigenvalue of the unregularized matrix (Brookes et al., 2008). The optimised source orientation for each voxel was taken as that with the largest projected power (Sekihara et al., 2004). Beamformer weights were generated for each voxel. A pseudo-T statistical approach was investigated, contrasting source power in the beta band during the active (0.3 – 0.8 s) window and control window (2.5 – 3 s) to generate source maps. The pseudo-T statistic was calculated as described in Chapter 2, Equation 2.41, where covariance matrices were generated using the beta band filtered data during the same active and control periods. This resulted in 2 separate pseudo-T statistical images: one for the whole brain (at 4 mm isotropic resolution) and one for the sensorimotor mask (at 1

mm isotropic resolution). A broadband (1 – 150 Hz) virtual electrode was extracted from the voxel within the sensorimotor mask with the peak beta modulation (the most negative pseudo-T statistic). The spectral content of the virtual electrode time course was examined using time-frequency spectrograms, as described in Chapter 2.3.3.

1.1.1.2 Connectivity

Whole-brain connectivity was investigated using amplitude envelope correlation (AEC) (Brookes et al., 2011c; Liu et al., 2010) as described in Chapter 2.5.3. Briefly, beta band filtered regional signals from the 78 AAL regions were extracted using the calculated beamformer weights. A time window from 0.1- 3.4 s after trial onset was selected to exclude edge artefacts and all trials were concatenated. Source leakage was corrected using pairwise orthogonalization (Brookes et al., 2012). The absolute value of the Hilbert transform was computed to generate the amplitude envelope from the oscillatory signal. This was then down sampled to 120 Hz and the Pearson correlation was computed between all possible AAL region pairs, generating a 78 x 78 matrix for each participant describing the beta band connectivity. The "Global Connectivity" in the beta band for each participant was calculated by summing all off-diagonal elements of the connectivity matrix. The connectomes from the pseudo and individual MRIs were compared across individuals, the group average, and regional averages using Pearson correlation.

1.1.1.3 Contribution of forward errors

We extracted lead fields (i.e., the solution to the forward model as described in Chapter 2.5.1) from the 78 AAL regions for the individual and pseudo-MRIs. The relationship between the difference in the geometry and the lead field correlation between the pseudo and individual MRIs and the difference between MEG analysis results were examined with Pearson correlation.

5.4 Results

5.4.1 Geometric comparison

A comparison between the individual MRI and pseudo-MRI is shown in Figure 5.4. The medoids from the 78 AAL cortical regions were compared between the individual and pseudo-MRIs, with an example for a single participant shown in Figure 5.4a. Across the 20 participants, the medoids were separated by an average of 9.7 ± 0.7 mm (mean $\pm$ standard error across participants). Figure 5.4b breaks this down across the 78 regions, where the standard deviation across regions is 2.42 mm. We can see

that regions towards the back of the head show a larger Euclidean distance than those at the front. This will be addressed in the discussion below.

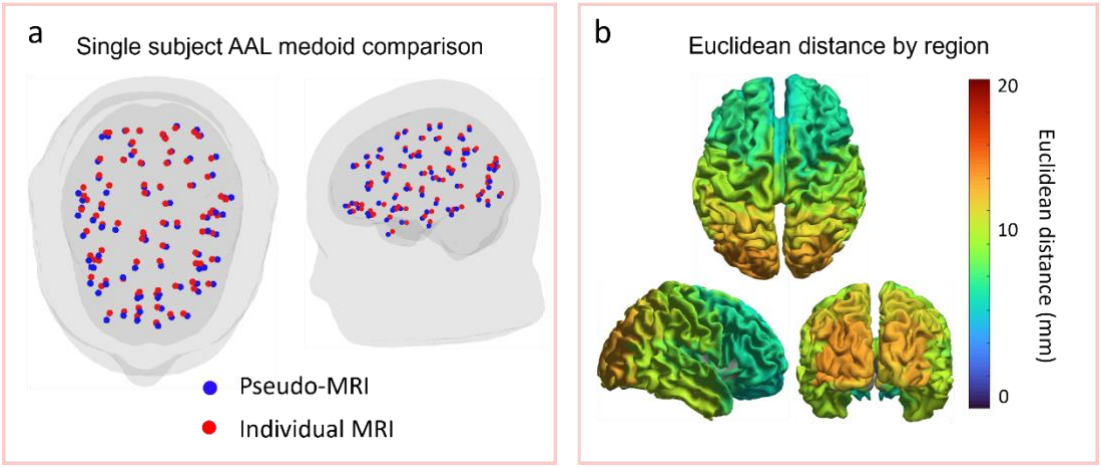


Figure 5.4. Geometric comparison. *a) Shows a mesh from a single participant's pseudo-MRI, with the 78 AAL region medoids from the pseudo-MRI (blue) and individual MRI (red) overlaid. b) shows the mean Euclidean distance between pseudo-MRI and individual MRI across participants for all regions.*

5.4.2 Peak beta modulation

Figure 5.5a and b show example data from a single participant. Panel a shows the pseudo-T statistical maps contrasting stimulation and rest periods from MEG analyses using the individual MRI (left) and pseudo-MRI (right) overlaid on the down-sampled anatomical brains, respectively. The peak beta modulation (shown by more negative pseudo-T values) localises to the left sensorimotor cortex using both models. The separation between the peak voxels from the sensorimotor mask for this participant was 5.84 mm. Panel b shows the time-frequency spectrograms (TFS) from a virtual electrode at the location of the peak beta modulation for the individual and pseudo-MRIs. The correlation coefficient between the individual MRI TFS and pseudo-MRI TFS for this participant is 0.99. Panel c shows a violin plot describing the distance between peak beta modulation for all twenty participants, with an average of 10 ± 5 mm (mean $\pm$ standard deviation). Figure 5.5d is a violin plot showing the correlation between each participant's pseudo-T statistical maps between pseudo and individual MRIs, where the average correlation is 0.84 ± 0.07 (mean $\pm$ standard deviation). Finally, panel e is a violin plot showing the correlation between TFS for all participants, with an average correlation of 0.91 ± 0.11 (mean $\pm$ standard deviation).

The peak beta modulation results across all 20 participants are shown in Figure 5.6. The group average pseudo-T statistical maps (a) and TFS (b) for the individual MRI and pseudo-MRI show highly similar results. The distance between the peaks from the group average images was 2.6 $\pm$ 5.4 mm (group average $\pm$ standard deviation).

The group average pseudo-T statistical maps have a Pearson correlation coefficient of 0.96. TFSs from the individual participant's peak voxels from the visual masks have a correlation of 0.98. Panel c describes the correlation across AAL regions for the average pseudo-T values. The top graph shows the relationship between the average pseudo-T statistic for each brain region, while the bottom shows the difference between the average pseudo-T statistic overlaid on a brain to highlight the locational bias of the difference in pseudo-T statistic. Overall, we see strong agreement between the pseudo-T statistic across regions, with a Pearson correlation of 0.97.

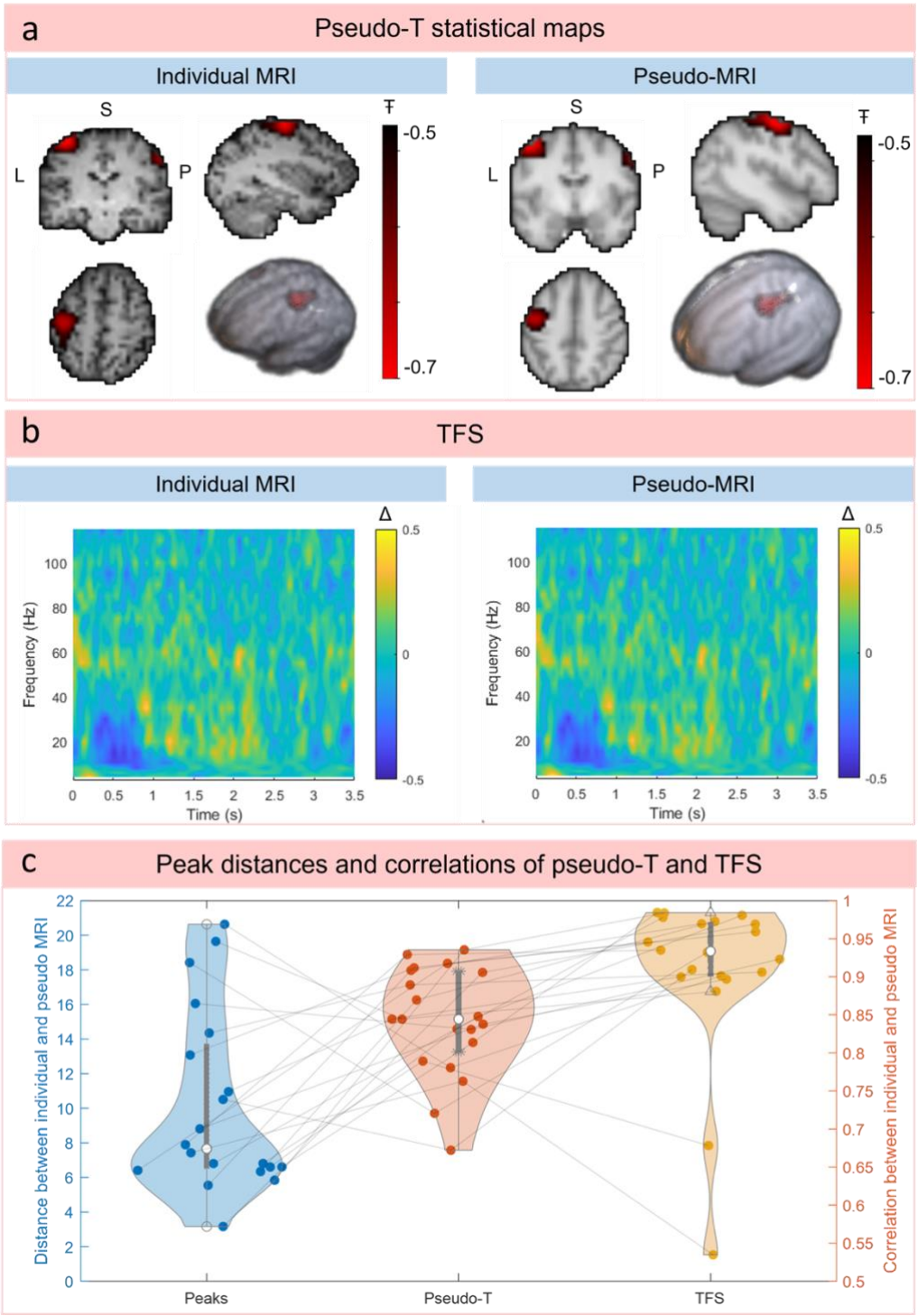


Figure 5.5. Individual beta modulation peaks. *a) The pseudo-T statistical map for the index finger trials with the individual MRI and pseudo-MRI and b) the corresponding TFS from the peak voxel in a sensorimotor mask for an example participant. Violin plots show c) the Euclidean separation between peak voxels across all participants, d) the correlation between pseudo-T statistical maps for each participant, and e) the correlation between TFS from the peak voxel in the sensorimotor mask for each participant.*

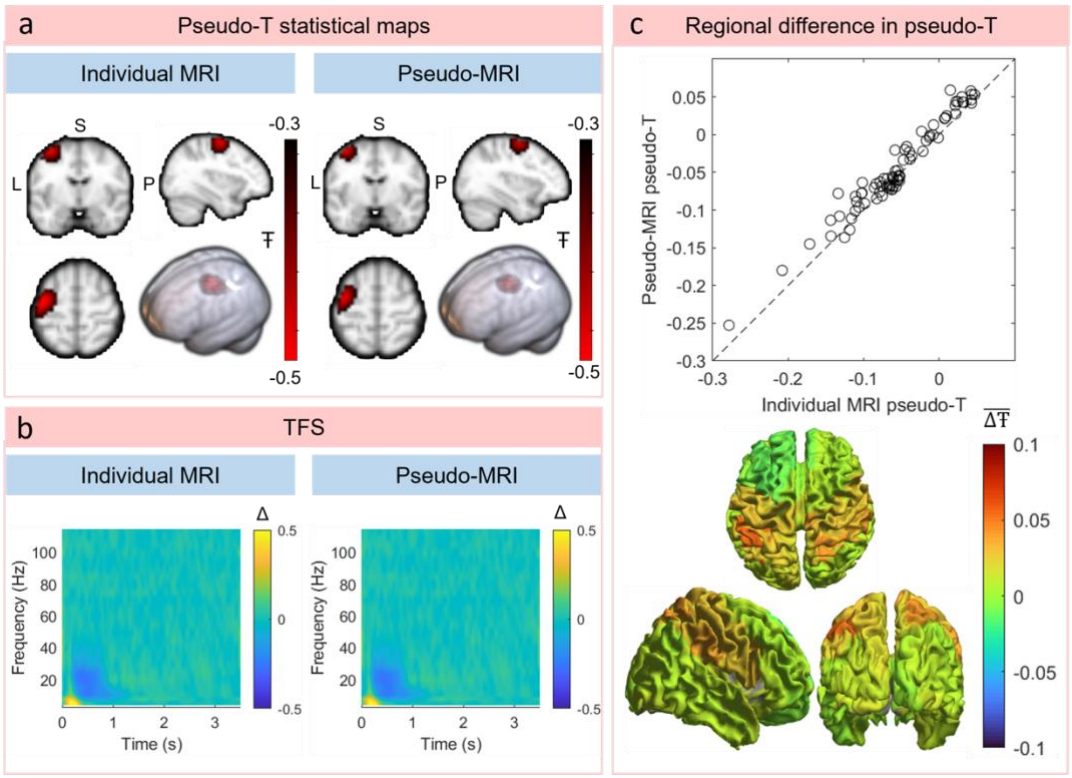


Figure 5.6. Group beta modulation*. a) Shows the group average pseudo-T statistical maps for the individual and pseudo-MRI and b) is the corresponding average TFS from the peak voxel in the sensorimotor cortex. Panel c describes the correlation between average pseudo-T values for each of the 78 AAL brain regions with the line of unity overlaid (top), and the group average difference between pseudo-T values for each region displayed on a brain plot (bottom).*

5.4.3 Connectivity

Figure 5.7 shows the results from the connectivity analysis across the group. The left panel shows the connectivity matrices and corresponding glass brain plots showing the 5% of connections with the highest connectivity values for the individual and pseudo-MRIs. The blue circles are scaled by connectivity strength (i.e. how connected each node is to all others). Both plots show a bilateral sensorimotor network, as expected. The relationship between all connections is explored in the top right plot, where a strong correlation (Pearson coefficient of 0.90) is seen between the connectivity for all AAL regions between the individual and pseudo-MRI. This relationship is broken down for each individual participant in Appendix A. The bottom right figure shows the relationship between the global connectivity (i.e., the sum of connectivity between all regions) for each participant with their individual and pseudo-MRI, with a correlation of 0.98.

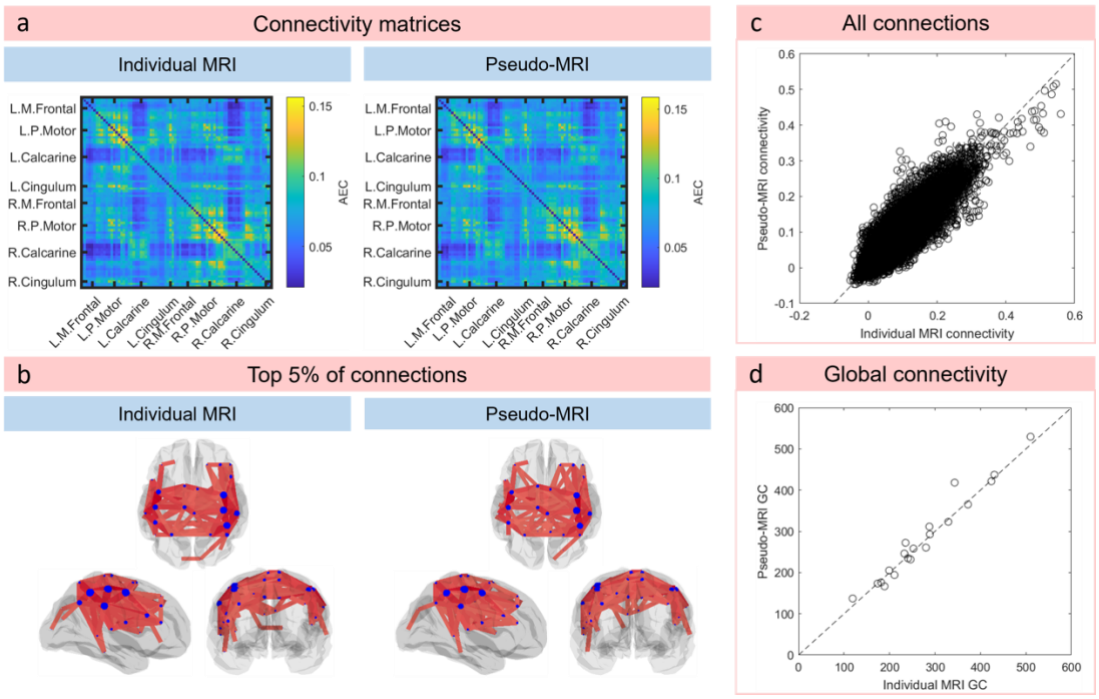


Figure 5.7 Group connectivity. *The left panel shows the connectivity matrices (top) and the corresponding top 5% of connections on a brain plot for the individual and pseudo-MRI. The top right panel correlates the connectivity between each region between MRIs. The bottom right shows the correlation between global connectivity for each participant.*

5.4.4 Contribution of forward errors

We investigated the relationship between the differences in both peak location and connectivity correlation with the structural separation across the AAL medoids and the lead field correlation, to consider the origin of the discrepancy between the MEG results from analysis with individual and pseudo-MRI anatomy. This is shown in Figure 5.8, with panel a describing the relationships to the location of peak beta modulation, and panel b showing the equivalent for connectivity. As expected, we find trends in all cases. The greater average structural separation between AAL regions produced a trend (that does not uphold after correcting for multiple comparisons) of greater distance between peaks ($R = 0.46, p = 0.04$) and a lower correlation in connectivity that was statistically significant ($R = -0.86, p = 1 \times 10^{-6}$). Almost equivalently, lower correlation in lead fields from the AAL regions resulted in a trend of greater distance between peaks ($R = -0.46, p = 0.04$) and lower correlation in connectivity ($R = 0.51, p = 0.02$) that again did not uphold correction for multiple comparisons.

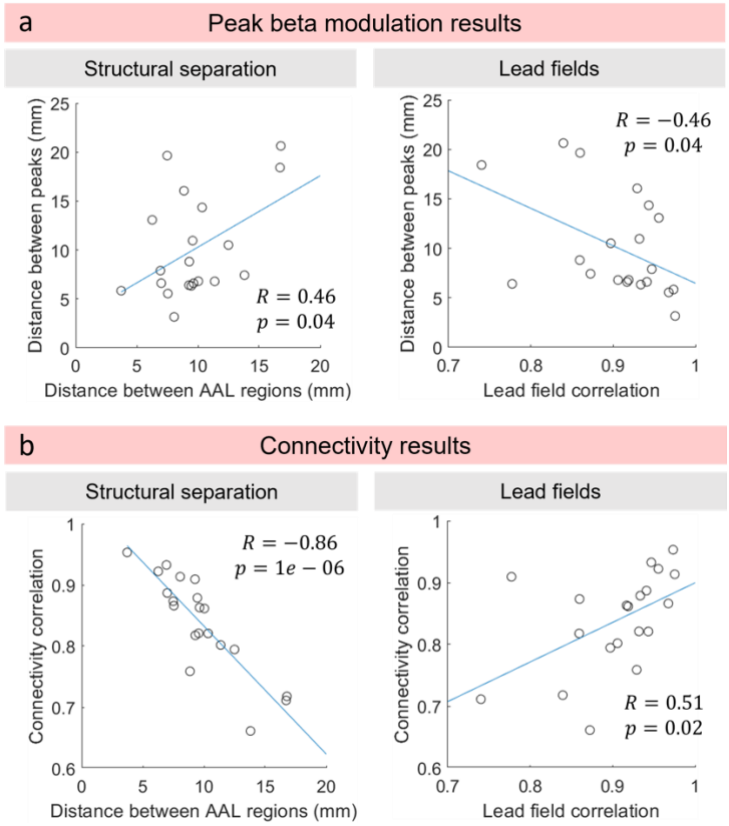


Figure 5.8. Contribution of forward errors. *a) The relationship between the distance between peaks in beta modulation from MEG analyses with individual and pseudo-MRIs and the mean distance between AAL regions (left,* $\boldsymbol{R = 0.46, p = 0.04}$*) and lead field correlation (right* $\boldsymbol{R = -0.46, p = 0.04}$*). b) the relationship between the correlation between connectivity matrices and the mean distance between AAL regions (left,* $\boldsymbol{R = -0.86, p = 1 \times 10^{-6}}$*) and lead field correlation (right,* $\boldsymbol{R = 0.51, p = 0.02}$*).*

5.5 Discussion

The ability to acquire wearable OPM-MEG data without individual MRI data opens new avenues for neuroscientific research, providing the potential to study participant groups that were previously not attainable. We have shown that a method of warping template MRI scans to 3D structure light scans of the head to generate pseudo-MRIs produces similar MEG results to individual anatomy. We tested the method on data collected across healthy adult participants, first examining the Euclidean distance between 78 cortical regions derived from individual anatomy and pseudo-MRI anatomy as a metric of structural differences. These showed a high overall agreement (Figure 5.4), with an average separation distance of 9.7 ± 0.7 mm. We found that the regions across the visual cortex had greater differences than those at the front of the head. There are a few factors that could contribute to this bias. Firstly, the 3D digitisation is typically less representative of the true head shape at the back of the head due to the volume of hair at the nape. This could be somewhat mitigated by using tighter-fit elastic caps or by accounting for hair thickness when generating the

pseudo-MRI. Secondly, the method used to make the geometric comparison (i.e., using the sensor array to define a mutual space) also encompassed coregistration errors from the coregistration that was completed separately for the individual and pseudo-MRI. These errors may have a bias towards the front of the head due to the necessity to use features at the front of the head (identifiable facial and helmet features – see Figure 3.17 for the coregistration procedure) to determine the transformation between anatomy and sensors. Small coregistration errors at the front of the head will therefore be amplified towards the back of the head. Feature matching points around the entire helmet would reduce this issue but is difficult due to cable management directing sensor cables to the back of the head, typically obscuring helmet features. This should be considered in future helmet and system designs.

We then examined the sensitivity of typical MEG analyses to the pseudo-MRI anatomy by analysing data during a sensory stimulation task using a recently developed whole-head OPM-MEG system. The equivalent analyses on MEG data using forward models generated from either individual or pseudo-MRI anatomy revealed beta modulation during a sensory task that localised to the left sensorimotor cortex, an example of which is shown in Figure 5.5. The distance between peak voxels during index-finger stimulation, shown by the violin plot in Figure 5.5c, had a median of 7.66 mm and a mean of 10 ± 5 mm (mean $\pm$ standard deviation), which shows improvement upon a comparable study by Douw et al. using unwarped template MRIs and conventional MEG, where their beta band peaks were separated by a median of approximately 12 mm (Douw et al., 2018).

The pseudo-T statistical maps showed a high correlation, with an average of 0.84 when considering individual participants, suggesting that the spatial patterns are highly similar despite using different anatomy for the forward model. The TFS from the peak location showed even greater similarity (Pearson correlation of 0.91), but had greater standard deviation, mostly due to two individual participants, whose TFS had a comparatively low correlation of 0.5343 and 0.6783. The difference in pseudo-T statistic for these two participants remained small (0.06 and 0.01), suggesting that the lower correlation in the TFS was potentially due to activity that was not just in the frequency band of interest (beta).

Group analyses shown in Figure 5.6 found that mean peak voxel locations were separated by only 2.6 mm, showing that individual discrepancies appear to largely average out across the group, meaning it is likely due to random error in individuals. As coregistration was calculated separately with the individual MRI and pseudo-MRIs,

and coregistration error is typically random and should average out across the group, this is to be expected. Using the same optical coregistration, Zetter et al. reported a mean error of 2.1 mm with localising phantom dipole (Zetter et al., 2019), which is in agreement with our average result. The group average TFS showed strongly correlated results, suggesting that source space analysis using pseudo-MRIs across a group of participants is robust.

We also evaluated the relationship in peak pseudo-T statistic across a parcellation of the whole brain between the individual and pseudo-MRI, shown in Figure 5.6c. The strong linear relationship (Pearson correlation of 0.9746) between the individual and pseudo-MRI shows little impact from the estimated anatomy on the resulting pseudo-T statistical values. The regional differences are highlighted in the brain plot, where the greatest difference in pseudo-T value (less than 0.1) appears in the sensorimotor cortex. This is to be expected as these regions saw the largest (most negative) pseudo-T, and so small differences due to template anatomy and coregistration will result in different regional values (it is not possible to compare these as percentages due to their proximity to zero). Only a single region saw an average pseudo-T statistical difference of over 0.05, suggesting that this method is suitable even for the measurement of small effect sizes (pseudo-T < 0.1).

We then analysed the impact of pseudo-MRIs on whole-brain functional connectivity. We calculated beta band connectivity between 78 cortical regions and found high consistency between connectomes derived from individual and pseudo-MRI forward models. Connectivity matrices were highly correlated ($R = 0.90$ and see Appendix A for individual participants) and the top 5% of connections showed a clear bilateral sensorimotor network with both methods. Individual global connectivity was consistent between individual and pseudo-MRI analyses, with the relationship tracking close to unity (i.e., those with higher global connectivity with their individual anatomy had near equally high global connectivity with the pseudo-MRI). This is to be expected (as the methods use equivalent MEG data) but confirms that there is minimal signal loss using approximated anatomy from our method.

Finally, we correlated the peak beta modulation and connectivity results to the geometric differences and the correlation between lead fields for the 78 cortical regions, shown in Figure 5.8. We expected this would show a significant correlation in all cases, as the difference in results should be largely explained by both the spatial separation between equivalent locations in individual and pseudo-MRI anatomy, and this should be equally reflected in the lead fields. We found trends in all cases,

although only the relationship between structural separation and connectivity correlation was significant when correcting for multiple comparisons. It must be noted that the structural separation and lead fields were derived only from the 78 AAL regions, and thus provide an estimate that does not represent the voxel-wise analysis that was used for determining the peak location. This likely explains why there was a lower correlation with the peak beta modulation than connectivity analyses.

There are a few notable limitations of the method described here. Firstly, the template MRIs we selected, while approximately age-matched (using 5-year windows), were not sex-matched. We know that there are structural differences in the brains of males and females (Giedd et al., 2012) beyond just head size, and so accounting for this could improve the resulting match. Secondly, we used a single shell forward model as this was suggested to be comparable to more complex BEM models (Stenroos et al., 2014). This model may be less susceptible to inaccuracies in anatomy than for example a three-shell BEM model. A pseudo-MRI approach may be less suited to more complex forward modelling. This should be investigated in future work. Similarly, we used beamforming for source localisation in this study; other methods of source analysis such as minimum-norm use cortical folds to constrain dipole orientations and as such may be more prone to anatomical differences. Future work should investigate how this method performs with such source localisation techniques. In addition, as mentioned above, it was not possible in this study to entirely separate errors associated with the pseudo-MRI and those associated with the coregistration procedure. Finally, we only studied index finger trials from our sensory paradigm for the peak location; analysing both finger trials would provide an additional measure of quality and increase statistical power, though it must be noted these must be analysed separately due to the expected difference in cortical signal origin.

5.6 Conclusion

Recently developed wearable OPM-MEG systems provide a more comfortable scanning environment than conventional neuroimaging techniques, enabling the study of typically less scan-compliant participants, including young children. However, MEG analyses typically require knowledge of structural information via anatomical MRI scans, which can be a challenge to acquire in those less compliant groups. Here, we suggest a method of warping template MRIs based upon that implemented in Brainstorm (Tadel et al., 2011), but instead using 3D structure scans to generate the pseudo-MRIs. We test this method on OPM-MEG data from a group of healthy adult participants with individual MRI scans for comparison. We conducted typical source

localisation and whole-head connectivity analyses and found highly correlated results between the individual and pseudo-MRIs. Our results demonstrate the feasibility of wearable MEG scanning without an individual MRI particularly for group studies, and through this, the ability to scan healthy typically developing children. This will be explored in Chapters 6 and 7.

Appendix A

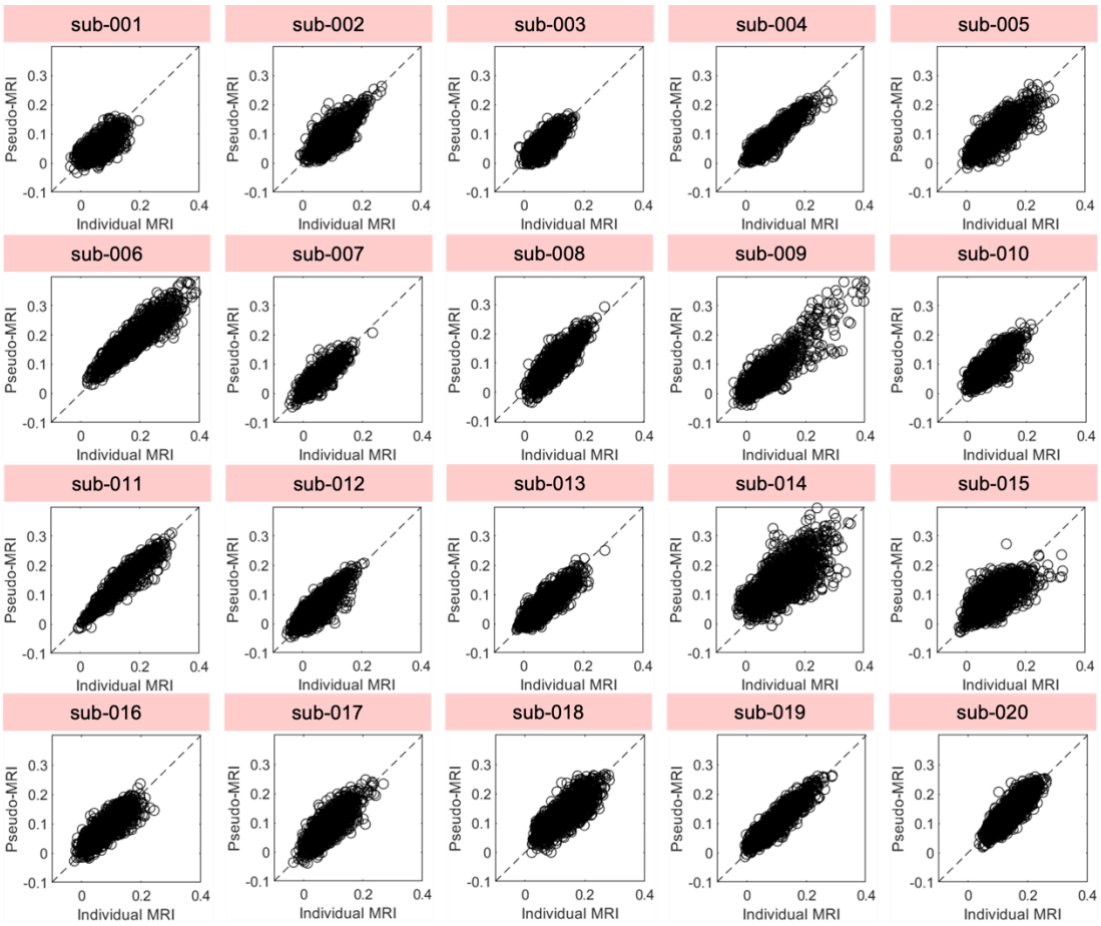


Figure 5.9 Connectivity correlation for all participants. *The relationship between the individual and pseudo-MRI connectivity matrices across the 78 AAL regions for each individual participant with a line of unity overlaid.*

6 The neurodevelopmental trajectory of beta band oscillations

6.1 Chapter overview

The experimental results in the previous two chapters address two of the significant hurdles in the path towards paediatric OPM-MEG: low frequency measurement (Chapter 4) and MRI acquisition (Chapter 5). Following this, here we describe our first neurodevelopmental study using OPM-MEG. We investigate the development of cortical beta band oscillations using a simple sensory task across a group of healthy children and adults. We detect the expected beta amplitude reduction during sensory stimulation across a wide age range (2 – 34 years) and find a significant relationship between age and task-related beta modulation. We conduct the first whole-head paediatric connectivity analyses with OPM-MEG, finding a significant increase in global connectivity with increasing age. We then use a Hidden Markov Model to determine that it is pan-spectral bursts that drive the modulation seen in the beta band and that the spectral content of these bursts changes significantly with age. In this way, we show that OPM-MEG is a valuable tool in the study of neurodevelopment. The results presented here are currently being considered for publication in Rier, Rhodes et al. 2024 (in submission at eLife).

6.2 Introduction

As described in Chapter 2, neural oscillations are a fundamental component of brain function. Oscillations in the beta range (canonically 13 – 30 Hz) are prominent in sensorimotor cortex (Barone and Rossiter, 2021) and measured in animal models in the cerebellum (Courtemanche et al., 2002) and basal ganglia (Courtemanche et al., 2003), associated with sensorimotor processes, although they are also seen across wider cortex (for example, Siegel et al., 2009). Across sensorimotor cortices, beta oscillations are diminished in amplitude during sensory stimulation or motor execution, and increased in amplitude (above a baseline level) following stimulus cessation, termed the post-movement beta rebound (PMBR) (Pfurtscheller and Lopes

da Silva, 1999). Beta oscillations and their modulation by tasks are robustly measured neuroscientific phenomena and their critical importance is highlighted by studies showing abnormalities across a range of disorders – e.g., autism (Ronconi et al., 2020), multiple sclerosis (Barratt et al., 2017), Parkinson's disease (Little and Brown, 2014) and Schizophrenia (Gascoyne et al., 2021). Despite this, little is known about the mechanistic role of beta oscillations; they are strongly associated with top-down processing, with theories suggesting their role is that of returning a 'status quo' state (Engel and Fries, 2010), or actively awakening (or re-activating) cognitive representations (Spitzer and Haegens, 2017). Evidence from in vitro animal research (Yamawaki et al., 2008), human drug studies (Hall et al., 2010; Muthukumaraswamy et al., 2013) and network-based models (Shaw et al., 2017) suggest a generating mechanism involving interconnected glutamatergic pyramidal cells and GABAergic inhibitory interneurons driven by activity in deep cortical layers. This proposes a relationship between beta oscillations and cortical inhibition and excitation, which is of particular interest in neurodevelopment. These studies highlighted employ invasive animal recordings or non-invasive neuroimaging techniques to adult populations. Whilst the sensorimotor system changes little in adulthood, there are marked changes in childhood and a complete characterisation of the neurodevelopmental trajectory of beta oscillations, particularly how they underpin behavioural milestones, might offer a new understanding of their role in healthy and abnormal brain function.

Several studies have investigated how neural oscillations change with age: Gaetz et al. (2010) measured beta modulation during index finger movement, showing that the PMBR was diminished in children compared to adults. Kurz et al (2016) reported a similar effect when studying 11–19-year-olds executing lower limb movement. Trevarrow et al. (2019) found an age-related increase in the PMBR amplitude in healthy 9–15-year-olds, and further that the decrease in beta power during movement execution did not modulate with age. Finally, Vakhtin et al. (2015) showed an increase in PMBR amplitude between adolescence and adulthood, and that this trajectory was abnormal in autism. A separate body of work has assessed neural oscillations in the absence of a task, demonstrating that there is a redistribution of oscillatory power across frequency bands as the brain matures. Specifically, low frequency activity tends to decrease, and high frequency activity increases with age (Candelaria-Cook et al., 2022; Clarke et al., 2001; Whitford et al., 2007). It is this redistribution of spectral power, shifting towards lower frequencies, that motivated the characterisation study described in Chapter 4. The changes in spectral content are spatially specific, with increasing beta power most prominent in posterior parietal and occipital regions (Hunt

et al., 2019; Ott et al., 2021). Beta oscillations are also implicated in long-range connectivity (Brookes et al., 2011c, 2011a) and previous studies have demonstrated increased connectivity strength with age (Schäfer et al., 2014), particularly in attentional networks (Brookes et al., 2018). In sum, there is an accord between studies that show increases in task-induced beta modulation and connectivity as well as redistribution of spectral power, with increasing age.

Despite this progress, neurodevelopmental studies remain hindered by instrumental limitations. OPM-MEG is ideal for children; for example, Hill et al. (2019) showed the validity of OPM-MEG in a 2-year-old and Feys et al. (2022) showed advantages for epileptic spike detection in school-aged children. However, there are no studies to date that have used OPM-MEG in large groups to measure neurodevelopment.

In addition to instrumental limitations, most neurodevelopmental studies have used an approach to data analysis where signals are averaged over trials. This has led to the idea that sensory-induced beta modulation comprises a drop in oscillatory amplitude during movement and a smooth increase upon movement cessation. However, recent studies (Jones, 2016; Sherman et al., 2016; Shin et al., 2017) investigating unaveraged signals show that rather than a smooth oscillation, the beta rhythm is, in part, driven by discrete punctate events, known as “bursts”. Bursts occur with a characteristic probability, which is altered by a task (Little et al., 2019; Seedat et al., 2020), and are not confined to the beta band but are pan-spectral, with components falling across many frequencies (Gascoyne et al., 2021; Seedat et al., 2020). There is also evidence that functional connectivity is driven by bursts that are coincident in time across spatially separate regions (Seedat et al., 2020). Recent work using EEG has found that, even in children as young as 12 months, beta band activity is driven by bursts (Rayson et al., 2022). These studies have changed the way the research community thinks about oscillations (van Ede et al., 2018) and a full understanding of beta dynamics, and their age dependence must be placed in the context of the burst model.

Here, we combine OPM-MEG with a burst analysis based on a Hidden Markov Model (HMM) (Baker et al., 2014; Seedat et al., 2020; Vidaurre et al., 2016) to investigate beta dynamics during a somatosensory task in a large range of children. Our study addresses two objectives. First, we test the viability of a novel 192-channel triaxial OPM-MEG system as described in Chapter 5 for use in a paediatric population, investigating its practicality in children (from age 2 years) and assessing whether previously observed age-related changes in task-induced beta modulation and

functional connectivity can be reliably measured using OPM-MEG. Second, we investigate how task-induced beta modulation in the sensorimotor cortices is related to the occurrence of pan-spectral bursts, and how the characteristics of those bursts change with age.

6.3 Methods

6.3.1 Participants and experiment

27 healthy, typically developing children (aged 2 – 13 years) and 26 healthy adults (aged 21 – 34 years) took part in the study[3]. All adult participants provided written informed consent prior to scanning, and a legal guardian provided written informed consent for participants under 18 years of age. The study was approved by the University of Nottingham's Faculty of Medicine and Health Sciences Research Ethics Committee.

The paradigm comprised tactile stimulation of the tips of the index and little fingers using two braille stimulators (METEC, Germany) (see Figure 5.3). Each stimulator comprised 8 independently controlled pins which could be raised or lowered to tap the participant's finger. A single trial comprised 0.5 s of stimulation (during which the finger was tapped 3 times using all 8 pins) followed by 3 s rest and the finger stimulated (index or little) was alternated between trials. There was a total of 42 trials for each finger, meaning the experiment lasted a total of 294 s. Throughout the experiment, participants watched a television program of their choice (presented via projection onto a screen in the MSR). All children were accompanied inside the MSR by a parent and one experimenter throughout their visit.

6.3.2 Data collection and coregistration

The sensor array comprised 64 triaxial OPMs (QuSpin Inc, Colorado, USA, QZFM-Gen-3 triaxial variant) which enabled a maximum of 192 measurements of the magnetic field around the scalp (192 channels). The OPMs were mounted in one of four 3D-printed helmets of different sizes (Cerca Magnetics Ltd., Nottingham, UK; see Figure 4.2); this affords (approximate) whole-head coverage and adaptation to the participant's head size. All participants wore a thin aerogel cap underneath the helmet to control heat from the sensors. The system is housed in an OPM-optimised

[3] The author (and Dr. Lukas Rier) collected the data described in this chapter. A portion of the adult data described here was also analysed in Chapter 5.

magnetically shielded room (MSR) that has 4 layers of mu-metal, a single layer of copper and is equipped with degaussing coils (Altarev et al., 2014) and active magnetic field control (Holmes et al., 2018) (Cerca Magnetics Ltd., Nottingham, UK). Prior to data collection, the MSR was demagnetised, and the magnetic field compensation coils were enabled (using currents based on previously obtained field maps, including those described in Chapter 4). The demagnetisation procedure ensures a repeatable background magnetic field and the magnetically quiet campus location of our MSR ensures field drifts < 0.05 nT/min (Rea et al., 2021; Rhodes et al., 2023)). This procedure, which results in a background magnetic field of ~ 0.6 nT (Rhodes et al., 2023, Chapter 4), is important to enable free head motion during a scan (Borna et al., 2022). All OPMs were equipped with on-board coils which were used for sensor calibration. MEG data were collected at a sampling rate of 1200 Hz using a National Instruments (NI, Texas, US) data acquisition system interfaced with LabView (NI).

Following data collection, two 3D digitisations of the participant's head, with and without the OPM helmet, were generated using a 3D structured light scanner (Einscan H, Shining 3D, Hangzhou, China). Participants wore a swimming cap to flatten hair during a "head-only" scan. The head-only digitisation was used to measure head size and shape, and an age-matched T1-weighted template MRI scan (Richards et al., 2016) was warped to the digitisation to generate a pseudo-MRI, as described in Chapter 5. Sensor locations and orientations relative to this anatomy were found by aligning it to the digitisation of the participant wearing the sensor helmet and adding the known geometry of the sensor locations and orientations within the helmet (Hill et al., 2020; Rier et al., 2023; Zetter et al., 2019) using MeshLab (Cignoni et al., 2008).

6.3.3 MEG data pre-processing

We used a pre-processing pipeline described previously (Rier et al., 2023) and outlined in Chapter 5. Briefly, broken or excessively noisy channels were identified by manual visual inspection of channel power spectra; any channels that were either excessively noisy or had zero amplitude were removed. Notch filters at the powerline frequency (50 Hz) and 2 harmonics, and a 1 – 150 Hz non-causal bandpass filter, were applied. Bad trials were defined as those with variance greater than 3 standard deviations from the mean trial variance, and automatically removed. A visual inspection was also carried out and any remaining trials with excess artifacts were removed. Finally, eye blink and cardiac artefacts were removed using ICA

(implemented in FieldTrip (Oostenveld et al., 2011)) and homogeneous field correction (HFC) was applied to reduce interference (Tierney et al., 2021a).

Following data pre-processing, high-fidelity data were available in 27 children and 24 adults. Two datasets were excluded as data quality was not sufficient to perform our Hidden Markov Model analysis. We removed 19 $\pm$ 12 % (mean $\pm$ standard deviation) of trials in children, and 9 $\pm$ 5 % of trials in adults due to excessive interference. On average we had 160 $\pm$ 10 channels with high-quality data available (note that not all sensors were available for every measurement – see also Discussion).

6.3.4 Source reconstruction and beta modulation

For source estimation, we used an LCMV beamformer spatial filter (Van Veen et al., 1997). For all analyses, covariance matrices were generated using data acquired throughout the whole experiment (excluding bad channels and trials). Covariance matrices were regularised using the Tikhonov method with a regularisation parameter equal to 5% of the maximum eigenvalue of the unregularized matrix. The optimised source orientation for each voxel was taken as that with the largest projected power (Sekihara et al., 2004). The forward model was based on a single-shell volumetric conductor (Nolte, 2003).

As described in Chapter 5, we constructed pseudo-T statistical images from data that were filtered to the beta band (13 – 30 Hz) and narrowband data covariance matrices were generated. Voxels were placed on both an isotropic 4-mm grid covering the whole brain and a 1-mm grid covering the contralateral sensorimotor regions identified by inflating a coregistered mask of the precentral and postcentral left gyrus from the AAL atlas (Hillebrand et al., 2016; Tzourio-Mazoyer et al., 2002). For each voxel, we contrasted power in active (0.3 – 0.8 s) and control (2.5 – 3 s) time windows as in Equation 2.41 to generate images showing the spatial signature of beta band modulation. Separate images were derived for index and little finger trials. To generate time-frequency spectra, we used broadband (1 – 150 Hz) filtered data and covariance matrices. The beamformer was used to produce a time course of neural activity (a “virtual electrode” as described in Chapter 2.5.2) at the voxel with maximum beta band modulation (the most negative pseudo-T statistic). The resulting projected broadband data were frequency-filtered into a set of overlapping bands, and a Hilbert transform was used to derive the analytic signal for each band.

To quantify the magnitude of beta-modulation, we filtered the virtual electrode to the beta band, calculated the Hilbert envelope and measured the mean difference in

amplitude between stimulation (0.3 – 0.8 s) and post-stimulus (1 – 1.5 s) time windows. These values (derived for every participant) were plotted against age and a relationship was assessed via Pearson correlation.

6.3.5 Functional connectivity analyses

To estimate connectivity, we first parcelled the brain into distinct regions. To this end, estimated brain anatomies were co-registered to the MNI standard brain using FSL FLIRT (Jenkinson et al., 2002; Jenkinson and Smith, 2001) and divided into 78 cortical regions according to the Automated Anatomical Labelling (AAL) atlas (Gong et al., 2009; Hillebrand et al., 2016; Tzourio-Mazoyer et al., 2002). Virtual electrode time courses were generated at the medoid of each of these 78 regions, and the beta band Hilbert envelope was derived. We then computed Amplitude Envelope Correlation (AEC) as an estimate of functional connectivity between all possible pairs of AAL regions (Brookes et al., 2011a; George C. O'Neill et al., 2015). Prior to AEC, we applied pairwise orthogonalisation to reduce source leakages (Brookes et al., 2011a; Hipp et al., 2012). This resulted in a single connectome matrix per participant. We estimated "Global Connectivity" as the mean connectivity across all elements in the connectome. This was plotted against age and the relationship was assessed using Pearson correlation. To visualise the spatial variation in age-related connectivity changes, we also estimated the correlation between node degree (i.e., the column-wise sum of connectome matrix elements) and age, for each of the 78 AAL regions.

6.3.6 Beta bursts and Hidden Markov Modelling

To estimate beta burst timings, we employed a three-state, time-delay embedded mass-univariate HMM (Vidaurre et al., 2016). This method has been described extensively in previous papers (Rier et al., 2021; Seedat et al., 2020). Briefly, virtual electrode time series were frequency-filtered between 1 – 48 Hz. The HMM was used to divide the time course into three "states", each depicting repeating patterns of activity with similar temporo-spectral signatures. The output was three time courses representing the likelihood of each state being active as a function of time. These were binarized (using a threshold of 2/3) and used to generate measures of the probability of state occurrence as a function of time in a single trial. The state whose probability of occurrence modulated most with the task was defined as the "burst state". We estimated age-related changes in burst probability modulation and the relationship between burst probability modulation and classical beta-modulation (see above) using Pearson correlation. Further, we investigated the spectral content of the

burst state and its modulation with age using multi-taper estimation of the power spectral density (PSD) (Vidaurre et al., 2016). Having derived the spectral content of the burst state we used Pearson correlation to measure how the PSD magnitude, for every frequency, changes with age.

6.4 Results

6.4.1 Beta modulation with age

Figure 6.1 shows beta band modulation during the task for a single representative child (7 years old). Panel a) shows the estimated brain anatomy (the pseudo-MRI generated by the method described in Chapter 5) with the locations of the largest beta desynchronisation – contrasted between a stimulus period (0.3 – 0.8 s relative to stimulus onset) and rest (2.5 – 3 s) – for index and little finger stimulation overlaid in blue and green, respectively. The largest effects fall in the sensorimotor cortices as expected. Panel b) shows time-frequency spectra depicting the temporal evolution of the amplitude of neural oscillations. Blue represents a decrease in oscillatory amplitude relative to baseline (2.5 – 3 s); yellow represents an increase. As expected, there is a reduction in beta amplitude during stimulation.

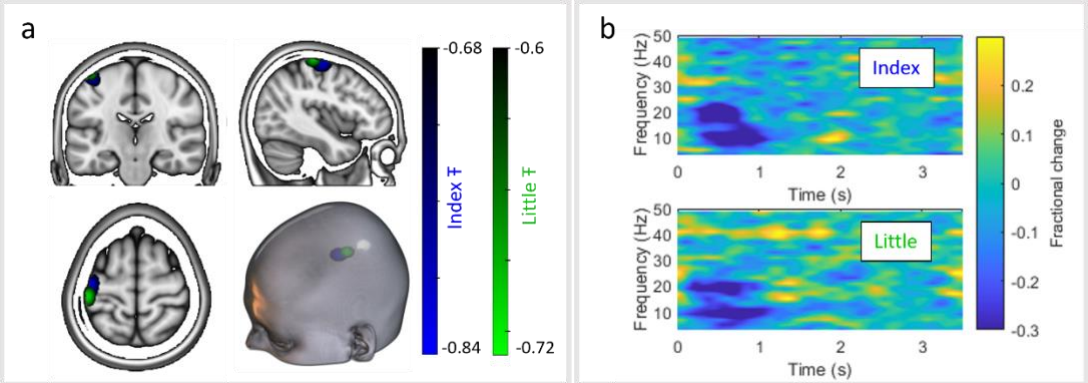


Figure 6.1. Data from a single participant. *a) Brain plots show slices through the left motor cortex, with a pseudo-T statistical map of beta modulation for a single 7-year-old participant. The blue peaks indicate locations of the largest beta amplitude during stimulation for index finger trials, while the green peaks show the little finger. b) time-frequency spectrograms showing neural oscillatory amplitude modulation (fractional change in spectral amplitude relative to baseline measured in the 2.5 – 3 s window) for both fingers, using data extracted from the location of peak beta modulation (left sensorimotor cortex). Note the beta amplitude reduction during stimulation, as expected.*

Group averaged beta dynamics are shown in Figure 6.2 for index finger stimulation and Figure 6.3 for little finger stimulation. Here, for visualisation, the children were split into three groups of 9: youngest (aged 2 – 6 years), middle (6 – 10 years), and oldest (10 to 13 years). Data were averaged within each group, and across all 24 adults (21 – 34 years) for comparison. The brain plots show group-averaged pseudo-

T statistical maps of stimulus-induced beta band modulation. In all groups, the peak modulation appeared in the left sensorimotor cortex. We observed no significant difference in the location of peak beta desynchronisation between index and little finger stimulation. The time-frequency spectrograms (TFSs) are also shown for each group. Here, we observe a drop in beta amplitude during stimulation for all three groups, however, this was most pronounced in adults and was weaker in younger children. For statistical analysis, we estimated the difference in beta band amplitude between the stimulation (0.3-0.8 s) and post-stimulation (1-1.5 s) windows and plotted this as a function of age (Figure 6.2b and Figure 6.3b) with Pearson correlation suggesting a significant relationship for both the index finger (R^2=0.29, p=0.00004) and little finger (R^2=0.23, p=0.00032). These data agree strongly with previous studies showing increased task-induced beta modulation with age. However, they are acquired using a new wearable technology, and in younger participants.

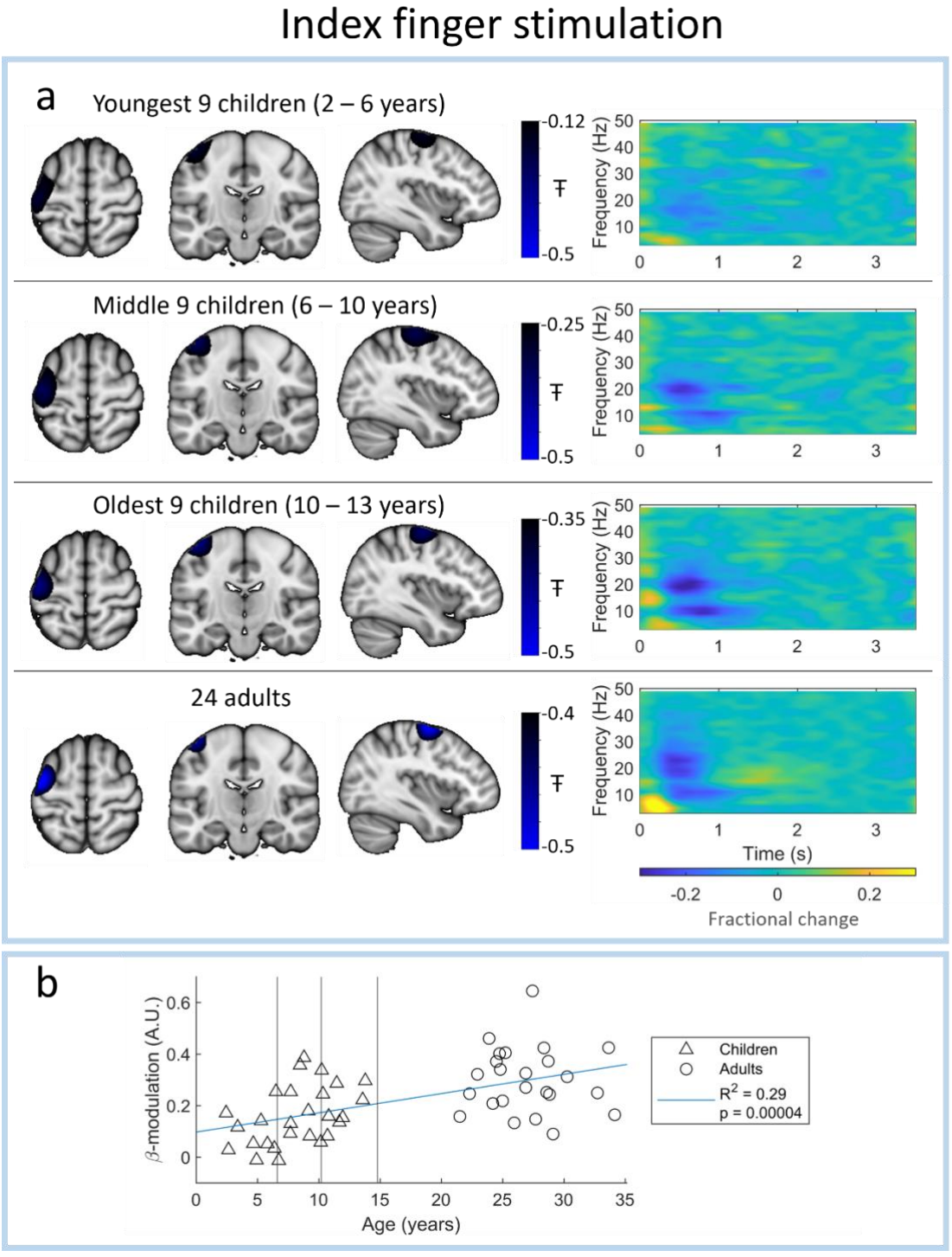


Figure 6.2. Beta modulation with age for index finger stimulation. *a) Brain plots showing slices through the left motor cortex, with a pseudo-T statistical map of beta modulation (blue/black) overlaid on the standard brain. Time-frequency spectrograms show modulation of the amplitude of neural oscillations (as in Figure 6.1). In all cases, results were extracted from the location of peak beta desynchronisation (in the left sensorimotor cortex). Note the clear beta amplitude reduction during stimulation. b) difference in beta band amplitude (0.3-0.8 s window vs 1-1.5 s window) plotted as a function of age (i.e., each data point shows a single participant; triangles represent children and circles represent adults). Note significant correlation (*R^2*=0.29, p=0.00004).*

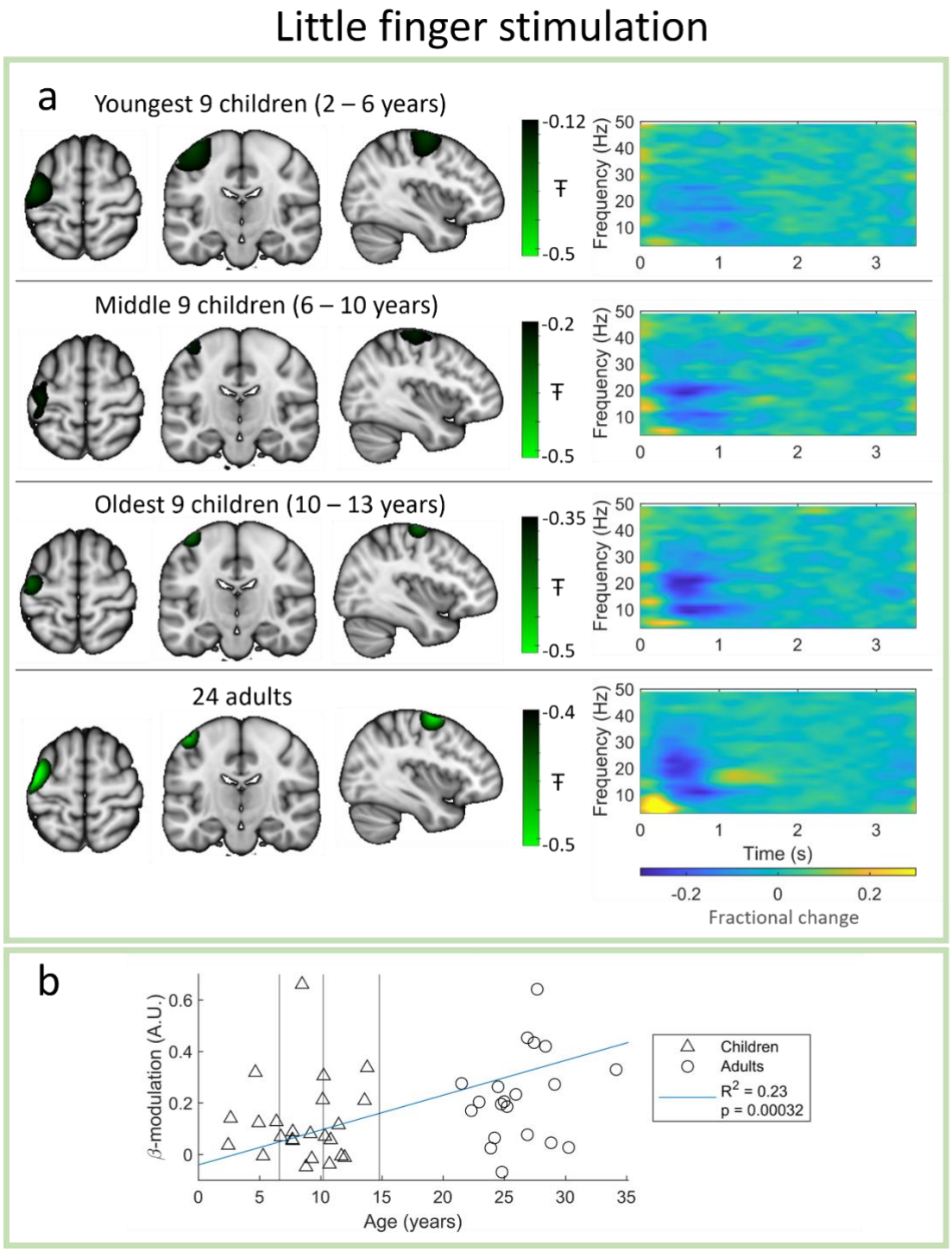


Figure 6.3. Beta modulation with age for little finger stimulation. *The equivalent of Figure 6.2 for the little finger stimulation, where a) are brain plots showing pseudo-T statistical maps of beta modulation (green/black) overlaid on the standard brain and time-frequency spectrograms showing modulation of the amplitude of neural oscillations from the location of peak beta desynchronisation in the left sensorimotor cortex. b) shows the difference in beta band amplitude (0.3-0.8 s window vs. 1-1.5 s window) plotted as a function of age (triangles represent individual children; circles for adults). Note significant correlation (($\boldsymbol{R^2}$=0.23, p=0.00032).*

6.4.2 Functional connectivity in the beta band

Figure 6.4 shows connectome matrices averaged across participants in each of the four groups; each matrix element represents the strength of a connection between two brain regions. In the “glass brains”, the red lines show the 150 pairs of regions with the highest connectivity, with the blue dots describing node strength. In adults, the connectome agrees with those from previous studies (Boto et al., 2021; Schäfer et al., 2014), with prominent sensorimotor, posterior-parietal- and frontoparietal connections. However, connectivity patterns in children differed in both strength and spatial signature, with the visual network showing the strongest connectivity. To statistically test the relationship between connectivity and age, we plotted global connectivity (i.e., the sum of all matrix elements) versus age (Figure 6.4b). Pearson correlation suggested a significant (R^2= 0.42, p = 2.67× 10^{-7}) relationship, with older participants showing increased global connectivity. We also probed how this relationship changes across brain regions: Figure 6.4d shows example scatter plots of node degree (i.e., how connected a specific region is to the rest of the brain) for two pairs of frontal and occipital regions from each hemisphere. Note that the gradient of the fit in the frontal regions (0.27 age^{-1}, R^2= 0.44, p = 1.2× 10^{-7} and 0.28 age^{-1}, R^2= 0.50, p = 5.8× 10^{-9}) is much larger than the occipital regions (0.10 age^{-1}, R^2= 0.18, p = 2× 10^{-3}, 0.12 age^{-1}, R^2= 0.29, p = 4.2× 10^{-5}). This is delineated for all brain regions in Figure 6.4c, where each region is coloured according to the gradient of the fit. The regions showing the largest change with age are the frontal and parietal areas, with the visual cortex demonstrating the smallest effect.

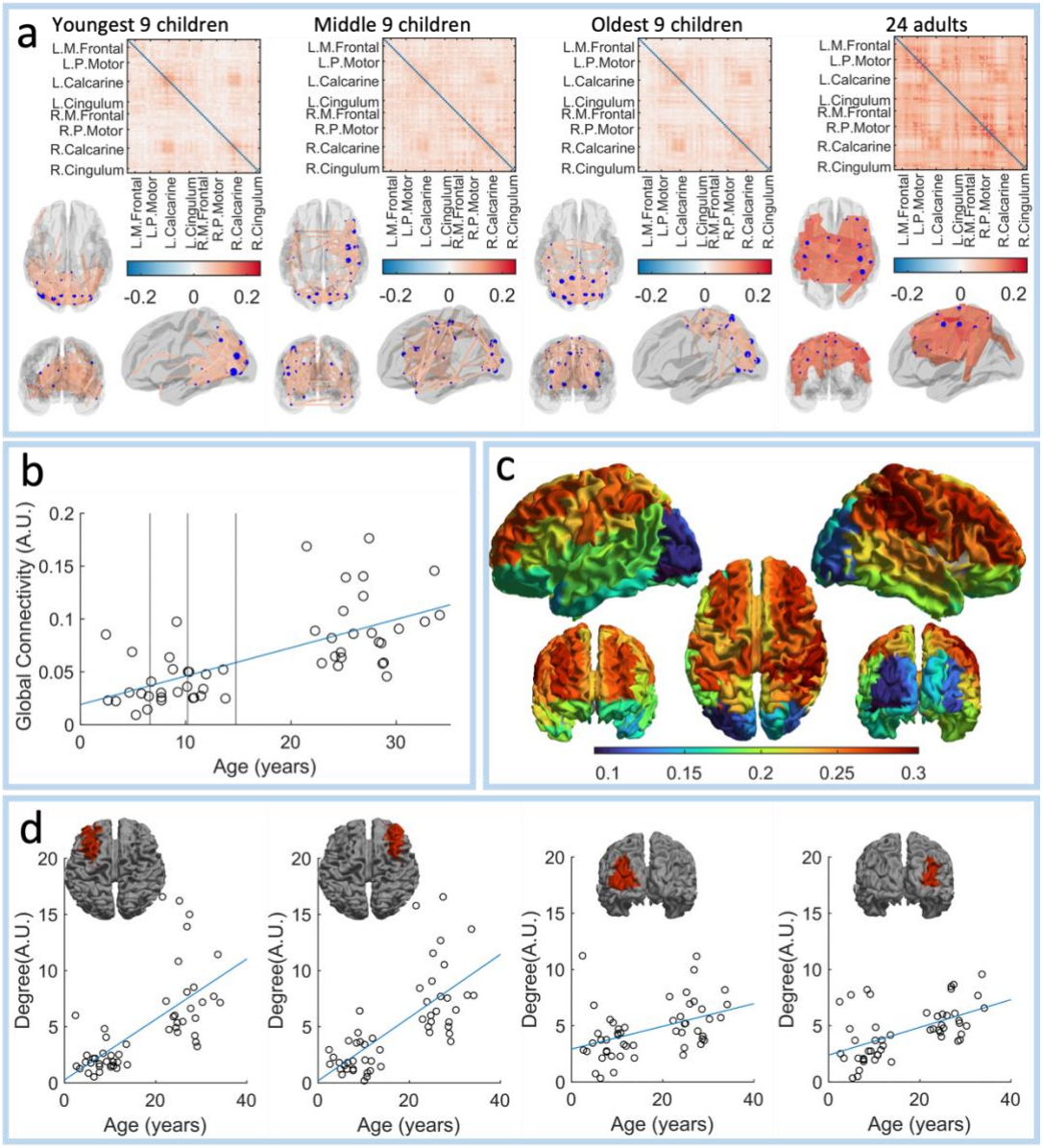


Figure 6.4 Functional connectivity – estimated using Amplitude Envelope Correlation (AEC) – varies with age. *a) Connectivity matrices constructed using 78 regions of the AAL atlas and glass brains showing average connectomes across groups and corresponding glass brains showing the strongest 150 connections. AEC was estimated across the entire task recording. b) global average connectivity increases significantly with age ($\boldsymbol{R^2}$= 0.42, p = 2.67 × $\mathbf{10^{-7}}$). c) age-related changes in connectivity vary spatially. Brain plot shows the linear fit gradient of node degree (the sum across the rows of the connectivity matrices against age) d) example plots show node degree against age for left and right frontal and occipital regions. Pearson correlation yielded (from left to right): ($\boldsymbol{R^2}$= 0.44, p = 1.2 × $\mathbf{10^{-7}}$, Degree = 0.27 · age + 0.26); ($\boldsymbol{R^2}$= 0.50, p = 5.8 × $\mathbf{10^{-9}}$, Degree = 0.28 · age + 0.17); ($\boldsymbol{R^2}$= 0.18, p = 2 × $\mathbf{10^{-3}}$, Degree = 0.10 · age + 2.92); ($\boldsymbol{R^2}$= 0.29, p = 4.2 × $\mathbf{10^{-5}}$, Degree = 0.12 · age + 2.38).*

6.4.3 Burst interpretation of beta dynamics

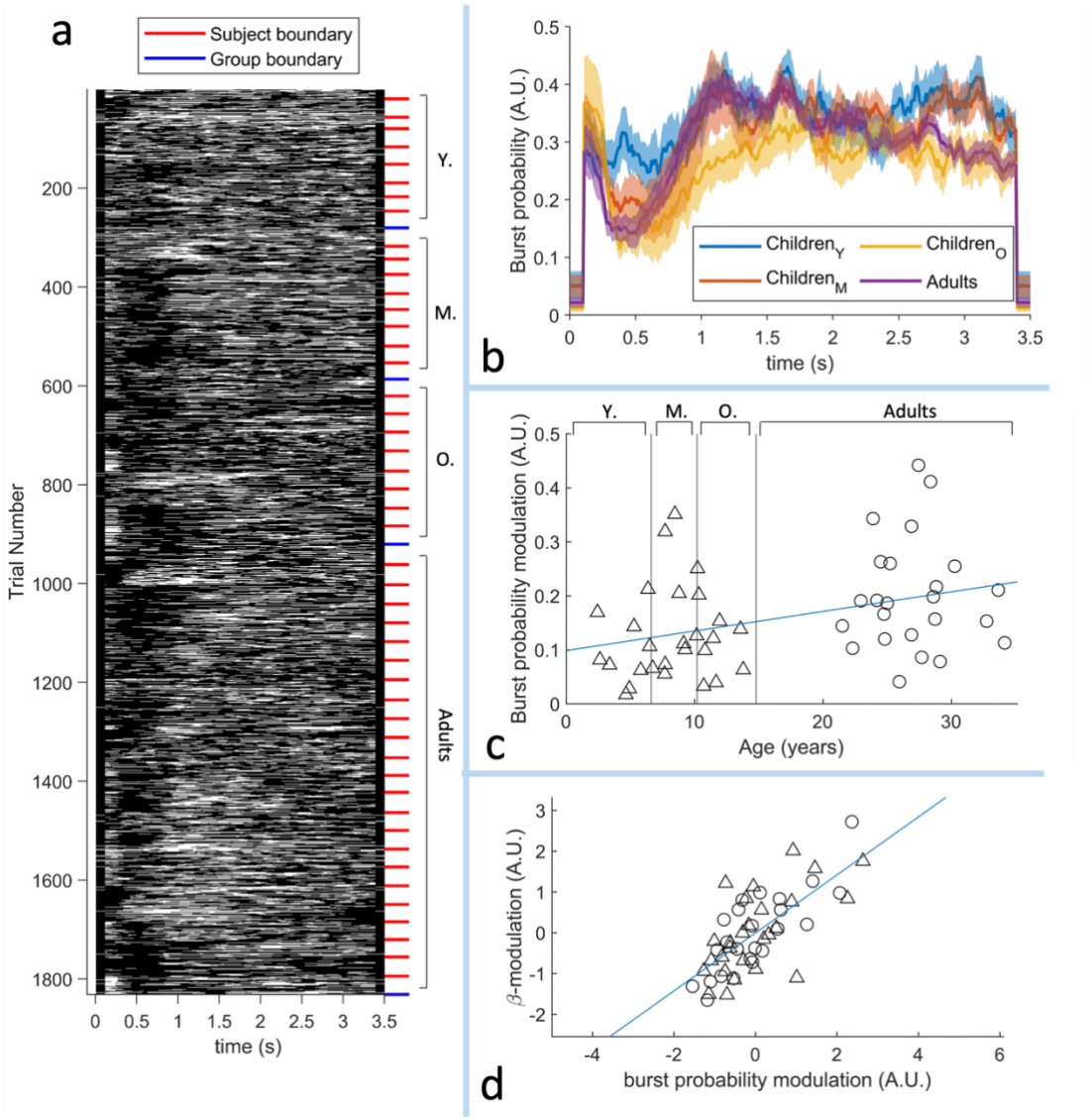


Figure 6.5. The relationship between beta band amplitude modulation and pan-spectral burst probability. *a) Raster plot showing burst occurrence (white) as a function of time for all trials and participants combined (participants sorted by increasing age). b) trial averaged burst probability time courses across the four participant groups. Shaded areas indicate the standard error within groups. c) stimulus- to post-stimulus modulation of burst probability (0.3-0.8 s vs 1-1.5 s) plotted against age. Note the significant (R^2= 0.13, p = 0.0089) positive correlation. d) beta amplitude modulation plotted against burst probability. Note again the significant correlation (R^2= 0.5, p = 5.2 × 10^{-9}). (values for both measured were z-transformed within the children and adult groups respectively to mitigate the age confound). Triangles and circles denote children and adults, respectively.*

Figure 6.5a shows a raster plot of (HMM-derived) burst occurrence for all individual task trials in all participants. White represents the time points and trials where bursts are occurring; black represents the absence of a burst. Participants are separated by the red lines and groups are separated by the blue lines. Burst absence is more likely in the 0.3 to 0.8 s time period (during stimulation), indicating a task-induced decrease in burst probability. Figure 6.5b shows group averaged burst probability as a function

of time. In all age groups, bursts were less likely during stimulation, though this modulation changes with age, with the younger group demonstrating the least pronounced effect. This is tested statistically in Figure 6.5c, which shows a significant (R^2= 0.13, p = 0.0089) positive Pearson correlation between the modulation of burst probability and age. Figure 6.5d shows the association between beta amplitude and burst probability modulation. Here the significant (R^2= 0.5, p = 5.2 $\times$ 10^{-9}) positive relationship supports a hypothesis that the observed change in task-induced beta modulation with age (shown in Figure 6.2) is driven by changes in the modulation of burst probability.

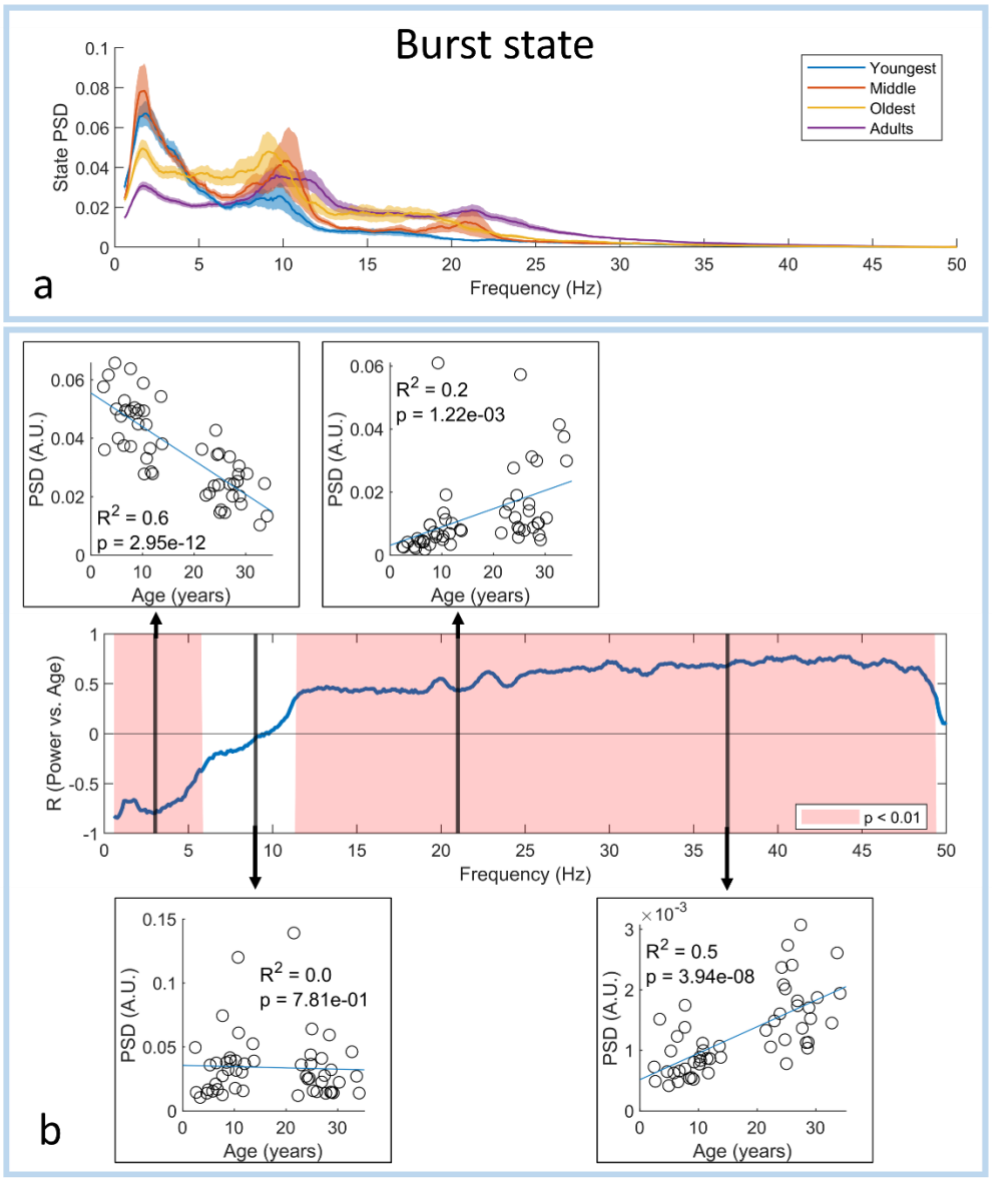


Figure 6.6. The spectral content of the burst state varies with age. *a) Average burst state spectra across groups. Shaded areas indicate standard error on the group mean. b) Pearson correlation coefficient for the PSD values in (a) against age across all frequency values. Red shaded areas indicate p < 0.01 (uncorrected). The four inset plots show example scatters of PSD values with age at select frequencies (3 Hz, 9 Hz, 21 Hz and 37 Hz). Low frequency spectral content decreases with age while high frequency content increases. No significant correlation was observed in the high theta and alpha bands.*

Finally, Figure 6.6a shows the burst spectra for all 4 participant groups. In adults, the spectral power diminishes with increasing frequency, with additional peaks in the alpha and beta bands. In children, high frequencies are diminished, and low frequencies are enhanced, compared to adults. This is also shown in Figure 6.6b where, for every frequency, we perform a linear fit to a scatter plot of spectral density versus age. Here, positive values indicate that spectral power increases with age, and negative power means it decreases. The insert scatter plots show example age relationships at 3 Hz, 9 Hz, 21 Hz and 37 Hz. We see a clear decrease in low-

frequency spectral content and increasing high-frequency content, with age. Interestingly, spectral content in the alpha band appeared stable with no significant correlation with age. Similar trends for changes in frequency content with age were found for the non-burst states (Figure 6.7).

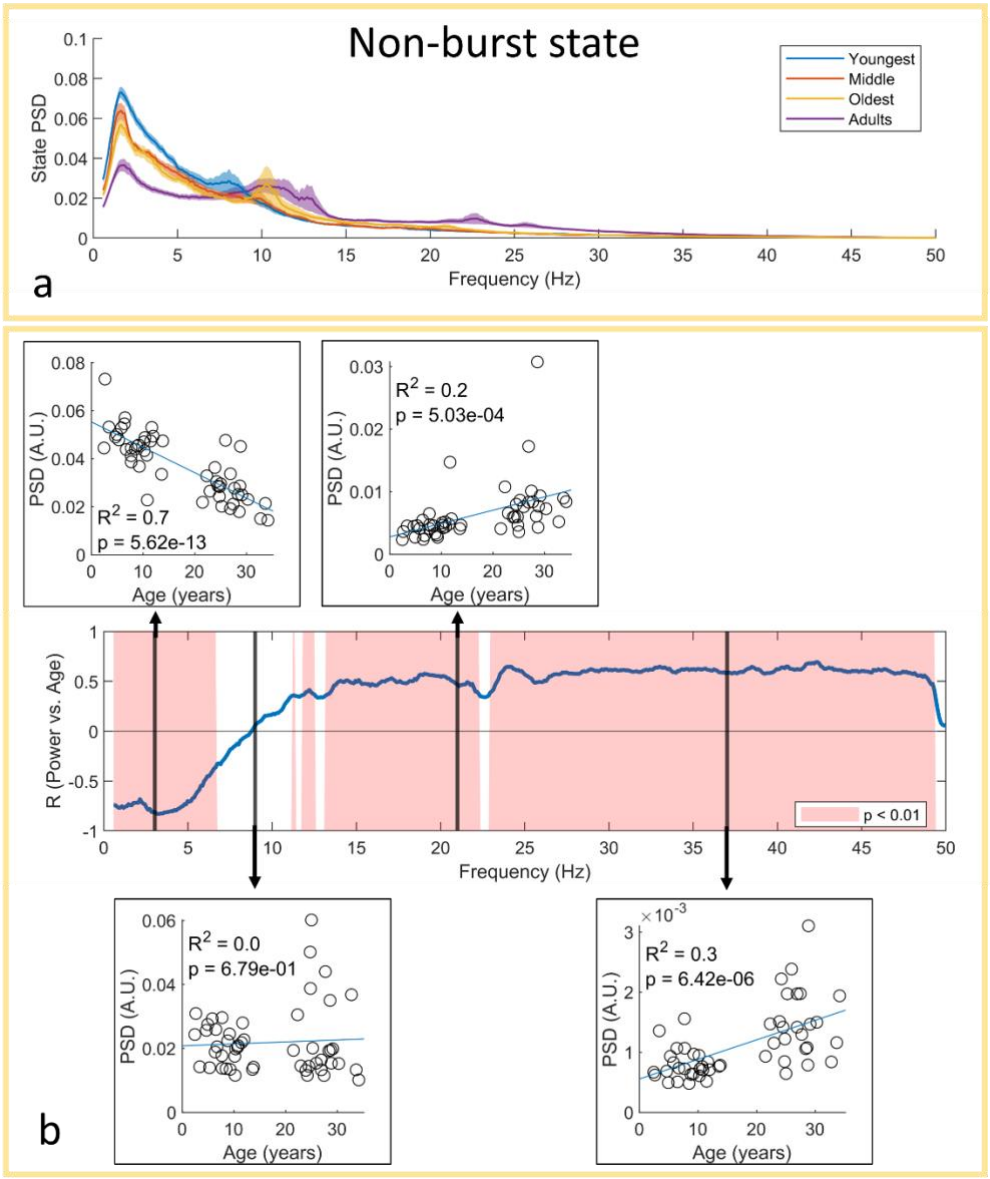


Figure 6.7. The spectral content of non-burst states. *a) Average non-burst state spectra across groups. Shaded areas indicate standard error on the group mean. b) Pearson correlation coefficient for the PSD values in (a) against age across all frequency values. Red shaded areas indicate p < 0.01 (uncorrected). The four inset plots show example scatters of PSD values with age at select frequencies (3 Hz, 9 Hz, 21 Hz and 37 Hz). Low-frequency spectral content decreases with age while high-frequency content increases. Results broadly mirror the frequency content and age relationships found in the burst state, however, features in the spectra corresponding to classical alpha and beta peaks are less prominent outside the burst state.*

6.5 Discussion

We designed our OPM-MEG system for lifespan compliance. The helmets were relatively lightweight, ranging from ~856 g (in the smallest case) to ~906 g (in the largest case). While this is heavier than, for example, a child's bicycle helmet (the average weight of which is ~300 – 350 g) they were well tolerated by our cohort, most likely due to the relatively short scanning duration of < 5 minutes. Multiple sizes of helmets meant we could select the best fitting size for any given participant, reducing the confounds of small head sizes which are associated with conventional MEG. Heat from sensors (which require elevated temperature to maintain operation in the SERF regime, see Chapter 3.3) was controlled via both convection cooling, with air able to flow through the helmet lattice, and an insulating material cap worn under the helmet by all participants. Together, these ensured that participants remained comfortable throughout data recording.

Whilst the helmet allows sensors to move with the head, sensors remain perturbed by background magnetic fields (e.g., any rotation/translation through static/gradient magnetic fields results in a measurement of changing field, which can obfuscate brain activity). Our system employed active field control (Holmes et al., 2018), which enabled us to reduce the ambient fields to a level where sensors worked reliably, even in the presence of head movements because our system was well tolerated and as a result of field control. We were able to obtain usable data in all 27 children and 24 of the 26 adults. Our findings of increased beta modulation and whole brain connectivity with age support previous studies (Gaetz et al., 2010; Kurz et al., 2016; Trevarrow et al., 2019), and in this way provide validation for this technology.

Importantly, most prior studies of neurodevelopmental trajectory were carried out in older children – for example, Kurz et al (Kurz et al., 2016) showed a similar effect in 11-19-year-olds; Trevarrow et al. (Trevarrow et al., 2019) employed a cohort of 9-15-year-olds and Brookes et al. scanned a cohort of 9 – 15-year-olds (Brookes et al., 2018). In the present study, we were able to successfully scan children from age 2 years. There are important reasons for moving to younger participants: from a neuroscientific viewpoint, many critical milestones in development occur in the first few years (even months) of life – such as learning to walk and talk. If we can use OPM-MEG technology to measure the brain activities that underpin these developmental milestones, this would offer not only a new understanding of brain function but also new avenues to explore in atypically developing children.

In addition to providing a new platform for neurodevelopmental investigation, our study also provides insights into coordinated brain activity and its maturation with age. Beta band oscillations are thought to mediate top-down influence on primary cortices, with regions of high beta amplitude likely being inhibited (for a review see Barone and Rossiter, 2021). Whilst most evidence is based on studies of movement, there is significant supporting evidence from somatosensory studies in adults; for example, Bauer et al. (Bauer et al., 2014) showed that, when one attends to events relating to the left hand, a relative decrease in beta amplitude is seen in the contralateral sensory cortex (right) and an increase in ipsilateral cortex- suggesting the brain is inhibiting the sensory representation of the non-relevant hand. Given this strong link to attentional mechanism and top-down processing, it is unsurprising that beta oscillations are not fully developed in children, and consequently change with age. Interestingly, Figure 6.2 implies that the well-known post-stimulus beta signal – the PMBR – appears to be absent in children but can be seen in adults. The rebound, as well as being linked to top-down inhibition of the sensorimotor cortex, is associated with long-range connectivity (Tewarie et al., 2019). The lack of rebound is therefore in agreement with the connectivity findings shown in Figure 6.4.

We failed to see a significant difference in the spatial location of the cortical representations of the index and little finger; there are three potential reasons for this. First, the system was not designed to look for such a difference – sensors were sparsely distributed to achieve whole-head coverage (rather than packed over the sensory cortex to achieve the best spatial resolution in one area). Second, our pseudo-MRI approach to head modelling is less accurate than the acquisition of participant-specific MRIs, and so may mask subtle spatial differences (see Chapter 5). Finally, previous work (Barratt et al., 2018) suggested that, for a motor paradigm in adults, only the beta rebound, and not the power reduction during stimulation, mapped motortopically. Nevertheless, it remains the case that by placing sensors closer to the scalp, OPM-MEG should offer improved spatial resolution in children and adults; this should be the topic of future work.

The burst model of beta dynamics is relatively new, yet significant evidence already shows that the neurophysiological signal in the beta band is driven by punctate bursts of activity, whose probability of occurrence changes depending on the task phase. Our study provides the first evidence that neurodevelopmental changes in the amplitude of task-induced beta modulation can also be explained by the burst model. Specifically, we showed that task-induced modulation of burst probability changes significantly as a function of age, suggesting bursts in the somatosensory cortex are

less likely to occur during stimulation of older participants compared to younger participants. We also showed that the “classical” beta modulation exhibited a significant linear relationship with burst-probability modulation. In addition, when bursts do occur, they tend to have different spectral properties in younger participants. Specifically, younger participants have increased low frequency activity, and decreased high frequency activity, compared to adults. It is likely that a combination of the change in burst probability with age, and the change in dominant frequency (away from the canonical beta band) drives the observation from previous studies of changing beta modulation with age.

Our connectivity finding is also of note, showing a significant increase in global functional connectivity with age. This is in good agreement with previous literature – for example, Schäfer et al. (Schäfer et al., 2014) showed quantitively similar data in conventional MEG, albeit again by scanning older children (ages 6 and up). Here we also showed that connectivity changes with age are most prominent in the frontal and parietal areas, and weakest in the visual cortex. It makes intuitive sense that the largest changes in connectivity over the age range studied should occur in the parietal and frontal regions, these regions are typically associated with both cognitive and attentional networks and are implicated in the networks that develop most between childhood and adulthood. Here, we observed a relative lack of age-related change in the visual regions; this could relate to the nature of the task – recall that all volunteers watched their favourite TV show and so the visual regions were being stimulated throughout, driving coordinated network activity in the occipital cortex. The visual system is also early to mature compared to the frontal cortex.

There are four limitations of our system that warrant discussion. Firstly, the range of available helmet sizes was limited, and future studies may aim to use more sizes, or a semi-flexible solution, to better accommodate variation in head size and shape. Also, even the lightweight helmet design used here may be too heavy for younger participants; whilst it was generally well tolerated, anecdotally, some of the very young participants commented that it was heavy. This indicates further optimisation of helmet design is needed if we want to move towards younger (< 2 years) participants; in babies, a fundamentally different solution must be found. Further optimisation is possible since, while the total weight is approximately 900 g, the combined sensor head weight is just 250 g. Similarly, the warmth generated by sensors was controlled by a combination of convection and insulation. However, for systems with a higher channel count, where more heat may be generated, active cooling (e.g., air forced through the helmet) may be required.

Second, the number of sensors available varies across participants – this was mainly for pragmatic purposes (the system was experimental and not all OPMs were available for every recording). Whilst we always ensured good coverage of the sensorimotor cortex and tried to optimise for whole brain coverage, the system is likely to have diminished sensitivity around the temporal cortex due to the helmet design, and this may explain why there was relatively little change in connectivity with age in those regions. In future, the inclusion of more sensors, particularly around the cheekbone would be a natural extension. Thirdly, magnetic field control was only available over a region encompassing the head, whilst participants were seated (i.e., participants had to be sat in a chair for the scanner to work). This was key to ensuring participants were unconstrained. However, in future studies, particularly in younger participants, it may be desirable to accommodate different positions (e.g., participants seated on the floor) and a greater range of motion (e.g., children crawling or walking). This may be possible with newly developing coil technology (Holmes et al., 2023b). Finally, here we chose to study sensory stimulation. There are many other systems to choose from – and whether the findings here regarding beta bursts and the changes with age also extend to other brain networks remains an open question that could be explored in future studies.

It is worth mentioning that our statistical analyses were based on a linear model with the relationship between our measured metrics (e.g. beta modulation, global connectivity and burst probability) and age assumed to vary linearly. This may not be the case; in conventional a large conventional MEG study, age relationships with oscillatory frequencies were found to vary quadratically in multiple frequency bands (Hunt et al., 2019). However, as our adult cohort only spanned 21-34 years, we are unable to study such patterns. This should be an area of future research, with OPM-MEG enabling the investigation of spectral trajectories across the entire lifetime.

6.6 Conclusion

Characterising how neural oscillations change with age is a key step towards understanding the developmental trajectory of coordinated brain function, and the deviation of that trajectory in disorders. However, limitations of conventional, non-invasive approaches to measuring electrophysiology have led to confounds when scanning children. Here, we have demonstrated a new platform for neurodevelopmental assessment. Using OPM-MEG, we have been able to provide evidence – supported by previous studies – that shows both task-induced beta modulation and whole-brain functional connectivity increase with age. In addition, we

have shown that the classically observed beta power drop during stimulation can be explained by a lower burst probability, and that modulation of burst probability changes with age. We further showed that the frequency content of bursts changes with age. Our results offer new insights into the developmental trajectory of beta oscillations and provide the first clear evidence that OPM-MEG is an ideal platform to study developing electrophysiology.

7 The development of visual gamma oscillations: a cross-site collaborative study

7.1 Chapter overview

The work presented in the previous chapters contributes to a wealth of evidence on the validity of OPM-MEG, particularly in the study of neurodevelopment. However, many previous studies were “proof-of-concept”, with limited numbers of participants. To address a wider range of neuroscientific questions, larger samples are needed to provide more statistical power, particularly in populations with high heterogeneity, such as those with neurodevelopmental disorders. This chapter describes the first OPM-MEG collaborative study with data collected at two sites (the University of Nottingham (UoN) and The Hospital for Sick Children (SickKids) in Toronto, Canada). We first perform an equivalent visual task using OPM-MEG systems at both sites, in two groups of 26 healthy adults, investigating cross-site consistency. We show that we can expect very similar performance across systems when investigating gamma band activity, finding no significant difference between groups. We then use the same paradigm with both adults and children from each site. This forms the largest (to date) OPM-MEG study of 102 participants, with 51 children aged 2 – 13 years and 51 adults aged 21 – 34 years. We investigate spectral changes relating to age in the visual cortex. We found a significant positive linear relationship between age and gamma amplitude but did not find a clear relationship between the frequency of the gamma response and age.

7.2 Introduction

Rhythmic neural activity in the gamma frequency range (canonically > 30 Hz) plays a pivotal role in the processing of information in the human brain. There is a broad consensus from *in vitro* models (Whittington et al., 1995) and animal local field potential (LFP) recordings (Gray et al., 1989; Gray and Singer, 1989), that gamma oscillations arise due to interactions between neuronal excitation and inhibition (Bartos et al., 2007; Vinck et al., 2013). More specifically, they are thought to depend

on inhibitory $GABA_A$ (γ-aminobutyric acid type A) receptor-mediated inhibition pathways and fast-spiking parvalbumin-expressing basket cell interneurons (Sohal et al., 2009). It therefore follows that gamma band synchronisation may provide a metric of cortical excitation-inhibition balance (E-I), and so measurement of such oscillations is of neuroscientific interest.

Gamma oscillations are of particular interest in neurodevelopment since one of the leading theories on the neural mechanisms behind autism spectrum disorder (ASD- one of the most prevalent neurodevelopmental conditions) is that of excitatory-inhibitory imbalance (Nelson and Valakh, 2015; Rubenstein and Merzenich, 2003; Sohal and Rubenstein, 2019). The relationship between gamma oscillations and ASD has therefore been investigated using EEG (Brown et al., 2005; Bruining et al., 2020; Dickinson et al., 2016a, 2016b, 2015; Orekhova et al., 2007) and MEG (An et al., 2018; Port et al., 2017; Rojas et al., 2008; Seymour et al., 2019; Sun et al., 2012). For example, excess induced gamma oscillations have been attributed to ASD participants (Orekhova et al., 2007) and their first-degree relatives (Rojas et al., 2008) during auditory or visual attention tasks. Peak gamma frequency was also suggested as an important metric for E-I imbalance in autism (Dickinson et al., 2016b). Two studies have found the peak gamma frequency to be higher in participants with ASD than typically developing participants (Dickinson et al., 2016a; Orekhova et al., 2023), and higher with autistic-like traits in the general population (Dickinson et al., 2015).

While gamma oscillations can be investigated during resting state (e.g., in autism Datko et al., 2016; Takesaki et al., 2016; van Diessen et al., 2015), this study focuses on task-induced gamma. One method of eliciting an increase in gamma oscillatory power is through the visual system. Visual stimuli of increasing intensity (e.g., contrast or temporal frequency) are known to induce a monotonically increasing frequency of gamma oscillations (Orekhova et al., 2018). Visual gamma has been associated with visual feature integration (Eckhorn et al., 1988; Gray et al., 1989), object representation (Tallon-Baudry and Bertrand, 1999), and selective attention (Fell et al., 2003), and appears to be altered in childhood (Gaetz et al., 2011; Orekhova et al., 2018) and in children with ASD (Orekhova et al., 2023). In addition, twin studies suggest the response is highly heritable, therefore having a strong genetic component (Pelt et al., 2012). The generation of visual gamma is thought to occur in the superficial layers (V1) of the visual cortex, and has been related by circuitry to inhibitory beta oscillations in deep layers, such that gamma (and theta) oscillations provide feedforward influence, while beta provides feedback (Bastos et al., 2015; Michalareas et al., 2016).

Visual gamma oscillations typically have a lower signal-to-noise ratio when measured using EEG compared to MEG (Muthukumaraswamy and Singh, 2013; Schofield et al., 2024). This is likely because high frequency artefacts have a greater effect on EEG signals than MEG (Boto et al., 2019; Muthukumaraswamy, 2013; Whitham et al., 2007), including across occipital channels due to the proximity of electrodes to neck muscles. Multiple studies have therefore employed MEG as the ideal tool to non-invasively investigate this brain response (Gaetz et al., 2011; Hall et al., 2005; Muthukumaraswamy et al., 2010, 2009; Orekhova et al., 2015; Tan et al., 2016). However, most MEG studies have been limited to adult or adolescent participants, mostly due to the scanning limitations (i.e., head size and movement restrictions) posed by conventional MEG systems. This is particularly detrimental for the study of neurodevelopmental disorders like ASD, which has a typical diagnostic age from 3 years, and where little is known of neuronal correlates or biomarkers. Further, as functional neuroimaging in the first few years of life is challenging, the normative trajectories of such oscillatory signals are undetermined. OPM-MEG offers a practical solution to this data gap, providing a brain imaging system with lifespan compliance (Hill et al., 2019).

To date, most OPM-MEG studies have been limited by small numbers of participants in 'proof-of-concept' studies. However as more research centres begin to access OPM-MEG technology to study the brain, collaboration becomes possible, which could lead to larger datasets. However, with the rapid nature of the development of such technology, systems typically vary in design (i.e., sensor type, channel count, array design, sampling noise floor, passive magnetic shielding, and active magnetic field control). Further, OPM-MEG systems are highly dependent on their magnetic environment, and so data quality may vary between sites. It is therefore crucial that we investigate the viability of combining data across sites, as we do not yet know if cross-site studies are feasible. An initial study on a single participant across two OPM-MEG sites with contrasting environments showed that, when two OPM-MEG systems are built to the same design, data are comparable within an individual (Hill et al., 2022), but this has not yet been extended to groups.

In this chapter, we conduct a cross-site comparison of two OPM-MEG systems; one system at the University of Nottingham, Nottingham, UK (UoN) and one at the Hospital for Sick Children Toronto, Canada (SickKids). We combine developmental data from both sites to investigate electrophysiological responses during a visual paradigm. Our dataset is the largest OPM-MEG study to date, comprising 102 participants aged from 2 to 34 years old. We investigate the development of visual gamma oscillations from

the early years up to adulthood, considering the spectral content of MEG signals extracted from the visual cortex during an inward drifting circular visual grating, known to induce an increase in power across the gamma band in adults. We will address two questions. Firstly, we assess whether OPM-MEG data from different sites can be collated to create large datasets that can address neuroscientific questions with sufficient statistical power. Second, we use our neurodevelopmental dataset to investigate how the spectral content of visual gamma oscillations develops from the early years to adulthood.

7.3 Methods

7.3.1 Paradigm

Efforts were made to ensure the paradigm was consistent between sites. At both sites, participants viewed a visual paradigm presented on a screen (placed approximately 1 m away at eye level) by back projection. Each trial started with a white fixation cross located centrally on a black screen, presented for an interstimulus interval (ISI) randomly jittered between 1050 – 1450 ms. Following this, either an emotional face image was presented for 500 ms, or an inward drifting circular grating (drifting at 1.2 $°s^{-1}$, subtending a visual angle of 7.6°) was presented for 1 s. This grating stimulus was chosen to compare results to similar developmental gamma work using cryogenic MEG by Orekova et al. (2018). This was repeated up to a total of 60 circles trials (there were between 120 – 160 faces trials due to UoN running a version of the paradigm that included an additional emotion, but these data were not analysed in this work). The total experiment lasted between 5-8 minutes (due to the varying number of face trials). Figure 7.1 provides an example of the visual stimuli and timeline of the paradigm.

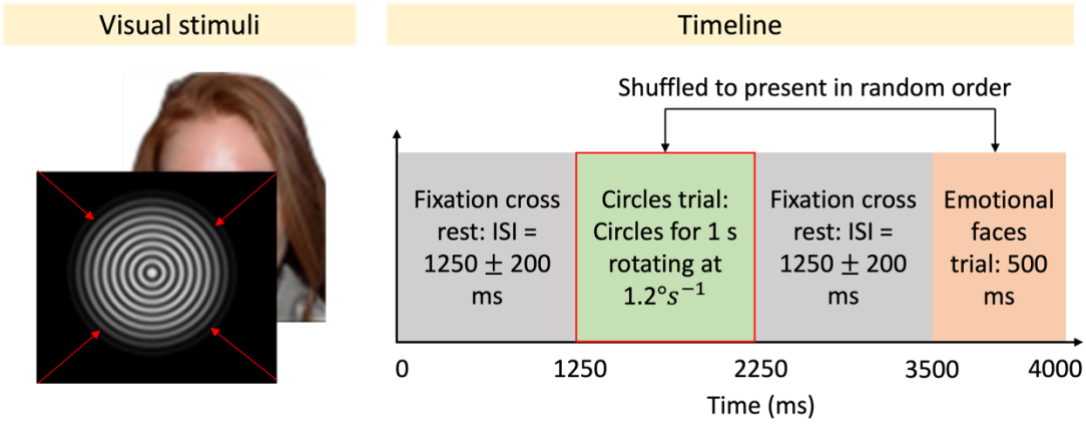


***Figure 7.1. The "Faces Circles" paradigm**. Left shows the circles stimulus, which is presented interspersed within emotional faces, with fixation cross trials between. The red arrows show the direction of drifting. The timeline of the stimulus presentation is shown on the right. The circles trials are highlighted in red, as it is only these trials that are used in subsequent analyses.*

7.3.2 Participants

Data were collected from 102 typically developing participants across the two sites[4]. Adult data were sex- and age-matched across the two sites and included one repeat measurement on a single participant in both systems. Children were always accompanied by a parent and at least one experimenter inside the MSR. Some of the youngest children (2-year-olds) were seated on a parent's lap during data acquisition. A description of the demographics in these data is provided in Figure 7.2. All adult participants provided written informed consent. A legal guardian for all participants under 18 years provided the written informed consent and the child gave verbal assent. This study was approved by the local research ethics board committee at both sites.

[4] The author collected data at both sites, operating or assisting in the operation of the system for 93 of the scanning sessions. 10 datasets from the SickKids children cohort were collected by the technical team at SickKids in the authors absence.

a) Demographics

	No. scans	Age (years, mean +/- standard deviation)	Age range (years)	No. males	No. females
UoN Children	27	7.67 ± 3.09	2 – 13	10	17
UoN Adults	26	26.35 ± 3.29	21 – 34	12	14
SickKids Children	24	3.79 ± 0.76	3 – 5	10	14
SickKids Adults	26	26.27 ± 3.26	21 – 34	12	14
Total	103	16.17 ± 10.71	2 – 34	44	59

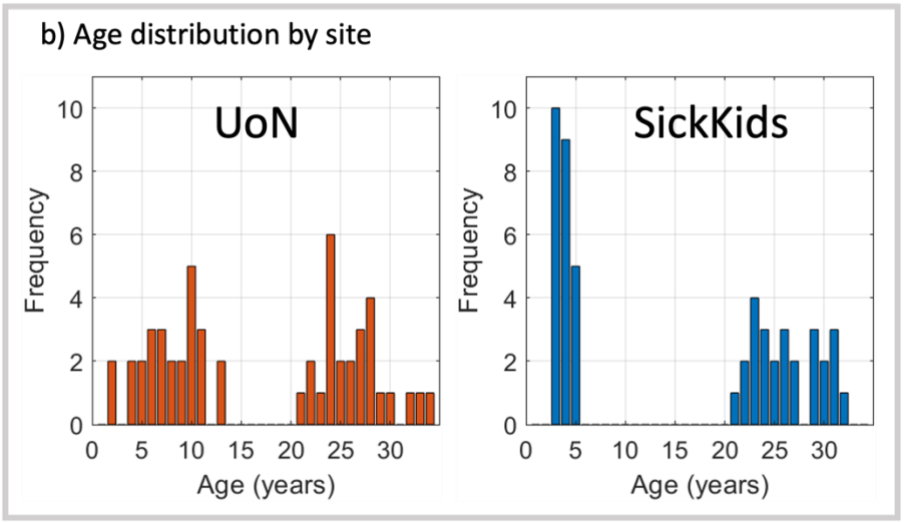


Figure 7.2. Participant demographics. *Table (a) and histograms (b) describe the age distribution of the participants recruited for this study from both sites.*

7.3.3 UoN system

The UoN array is described in Chapters 5 and 6 and shown again for reference in Figure 7.3. Briefly, the system comprised 64 QuSpin Gen-3 triaxial QZFM sensors, enabling up to 192 channels of magnetic field measurement. MEG data were collected at a sampling rate of 1200 Hz using a National Instruments (NI, Texas, US) data acquisition system interfaced with LabView (NI). Sensors were mounted in rigid 3D-printed helmets in one of three sizes (4–year–old, adult small and adult large, see Figure 4.2). Participants wore a thin aerogel cap under the helmet for thermal insulation. Participants were seated in a patient support at the centre of the OPM-optimised magnetically shielded room (which comprises of 4 layers of mu-metal, one layer of copper and is equipped with degaussing coils). Surrounding the participant

was a pair of bi-planar coils, through which average coil currents were applied (see Chapters 4 and 5), as such the static magnetic fields were compensated, but dynamic field changes were not. Participants were free to move throughout data acquisition (but were not specifically asked to do so). Two 3D digitisations of the participant's head (with and without the helmet) were acquired using a structured light camera (Einscan H, SHINING 3D, Hangzhou, China) for generation of pseudo-MRIs (Chapter 5) and coregistration (see Chapter 3.9).

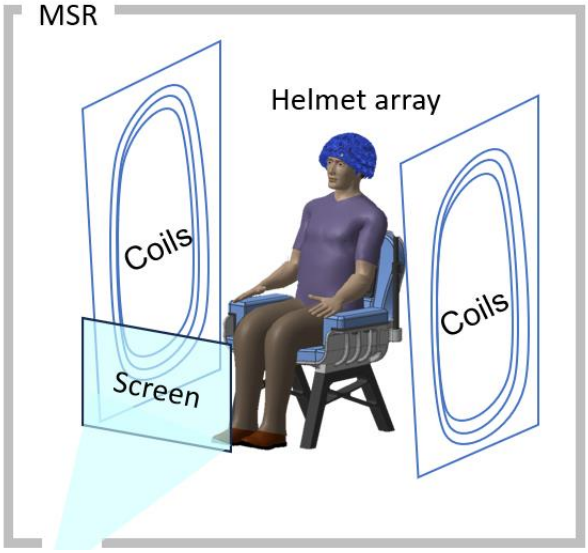


Figure 7.3. The UoN OPM-MEG system. *A diagram of the OPM-MEG system at UoN.*

7.3.4 SickKids system

The SickKids system comprised 40 QuSpin Gen-3 dual-axis QZFM sensors, enabling up to 80 channels of magnetic field measurement. MEG data were sampled at 1200 Hz using the same data acquisition system as mentioned above. Sensors were mounted in identical rigid 3D printed helmets (Cerca Magnetics Ltd., UK), albeit in one of only two sizes (4–year–old and adult large). Insulating padding was attached to the inside of the helmet for thermal management. Participants were seated in the same patient support at the centre of the shielded room (see Figure 7.4). The shielded room was repurposed from a cryogenic-MEG system and consisted of two layers of mu-metal and one layer of aluminium (Vacuumschmelze, Hanau, Germany), without the ability to degauss the inner mu-metal. The same bi-planar coils surrounded the participant, but at this site, they received magnetic field measurement from a pair of reference OPM sensors (QuSpin Gen-3 triaxial QZFM) that have been adapted to increase their dynamic range to enable measurement of the environmental magnetic fields (over $\pm$20 nT across 10-minutes, see Figure 3.15). The bi-planar coils therefore compensate for both static and dynamic magnetic fields. This was necessary to

compensate for the increased field drift of the SickKids site (caused by the busy city centre location and poorer shielding). Again, participants were free to move throughout data acquisition but were not specifically encouraged to do so. 3D structure scans (Einscan H, SHINING 3D, Hangzhou, China) were acquired with the helmet on and off the head (with some of the young children, the head scan without the helmet was not acquired due to their difficulty remaining still).

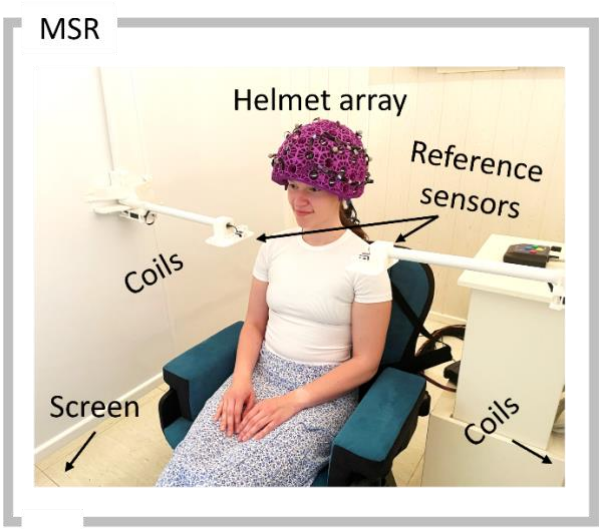


Figure 7.4. The SickKids OPM-MEG system. *A labelled photograph of an adult participant in the system at SickKids.*

A table comparing features of the system at each site is shown in Figure 7.5.

OPM-MEG site comparison		
	UoN	SickKids
No. sensors	64 triaxial	40 dual axis
No. channels	192	80
Helmet	Rigid 3D printed helmet in one of three sizes (adult S, adult L, 4-year-old)	Rigid 3D printed helmet in one of two sizes (adult L, 4-year-old)
Magnetic environment	Quiet campus location outside of the city centre	Downtown location, above a busy car park, near construction sites, main roads and underground transport lines
Passive shielding	OPM-optimised shielded room with four layers of mu-metal and one layer of copper	Repurposed Vacuumschmeltz room with two layers of mu-metal and one layer of aluminium
Degaussing coils	Yes	No
Magnetic environment with passive shielding	~2 nT static magnetic field with drifts of +/- 1 nT across 10 minutes (Rea et al., 2021)	~30 nT static magnetic field with drifts of +/- 20 nT across 10 minutes (Hill et al., 2022 and Figure 3.15)
Active shielding (static)	Via average coil currents through biplanar coils	Via reference array through biplanar coils
Active shielding (dynamic)	Not used (due to minimal dynamic drift)	Via reference array through biplanar coils

Figure 7.5. Site comparison. *A table describing the features of the OPM-MEG systems at each site.*

7.3.5 Pseudo-MRI generation

Individual anatomical MRIs were not available for all participants in this study, meaning pseudo-MRIs were generated for all source analyses. This was done using the process outlined in Chapter 5. Briefly, the scalp from an age-matched template MRI (Richards et al., 2016) was extracted using FieldTrip and warped to the individual participant's head digitisation using FSL FLIRT (Jenkinson et al., 2002). For some of the youngest participants, there was no available head digitisation, so the age-matched templates were used as the pseudo-MRI without warping.

7.3.6 Pre-processing

Data were pre-processed identically at both sites, with pre-processing steps described in Chapters 5 and 6. Broken or noisy channels channels were identified by manual inspection of the channel power spectra and removed. Data were notch filtered at the powerline frequency (50 Hz for UoN data and 60 Hz for SickKids) and

2 harmonics. A 1 – 150 Hz bandpass filter was applied, following which, data were epoched to 3 s trials encompassing 1 s prior to the onset of the “circles” trials and 2 s after. Bad trials were identified as those with trial variance greater than 3 standard deviations from the mean and were removed. Visual inspection was carried out and any further trials with noticeable artefacts were removed. ICA was used to remove eye blink and cardiac artefacts (implemented in FieldTrip (Oostenveld et al., 2011)) and homogeneous field correction (HFC) was applied to reduce interference (Tierney et al., 2021a).

Following pre-processing, data were available in 102 scans across 101 participants (there was one repeat measure, and one child participant was excluded due to failure to acquire digitisation before helmet removal). We removed 13 ± 9 (mean $\pm$ standard deviation) trials in children and 7 ± 4 trials in adults due to excessive interference. On average we had 159 ± 11 (mean $\pm$ standard deviation) channels of data in UoN, and 78 ± 3 channels in SickKids.

7.3.7 Source reconstruction

We used an LCMV beamformer spatial filter, as in Chapters 4-6 (and described in Chapter 2.5). Covariance matrices were generated using data spanning all “circles” trials (excluding bad trials) and were regularised using the Tikhonov method with a regularisation parameter of 5% of the maximum eigenvalue of the unregularized matrix (Brookes et al., 2008). As in previous chapters, the forward model was constructed from the pseudo-MRIs using a single shell model (Nolte, 2003) implemented in FieldTrip (Oostenveld et al., 2011).

Pseudo-T statistical images were constructed using Equation 2.41 with data filtered to the gamma band (30 – 80 Hz). Voxels were placed on:

- An isotropic 4-mm grid covering the whole brain
- The medoid of 78 AAL regions (Hillebrand et al., 2016; Tzourio-Mazoyer et al., 2002)
- A 1-mm isotropic grid covering the bilateral visual cortex (identified by dilating a mask of the left and right cuneus from the AAL atlas with a 5 mm spherical structuring element)

For each voxel, we contrasted power in active (0.3 – 1 s) and control (-0.8 – -0.1 s) windows relative to stimulus onset. A virtual electrode was extracted from the voxel from the 1-mm visual cortex mask with the largest pseudo-T statistic for subsequent

analyses. Beamformer weights were calculated using unfiltered data to enable the assessment of time-frequency dynamics across a broad bandwidth. We separate our participants into six age groups (3 for children and 3 for adults) for visualisation purposes but perform statistical analyses on individual data. As such, the 4-mm pseudo-T statistical maps are averaged across age groups to examine the location of peak activity across the whole brain.

7.3.8 Spectral analyses

We computed time-frequency spectrograms (TFS) to investigate the change in relative power across frequencies from 1 – 100 Hz. We used overlapping windows every 2 Hz, spanning 4 Hz bandwidth, from 2 Hz to 100 Hz to provide a high spectral resolution. The Hilbert envelope was computed from filtered unaveraged data and then averaged across trials to produce images that show the change in spectral amplitude across the trial duration, as described in Chapter 2.3.3. We plot the TFS from each age group and plot the mean change in spectral content across the stimulus time window for each group for comparison. We investigate the statistical relationship between age and amplitude modulation for individual participants across a range of frequencies using Pearson correlation.

For comparison with similar studies, we determined the peak gamma frequency and amplitude modulation to assess the relationship between the peak frequency and amplitude with age. This was done by calculating the average change in amplitude relative to baseline across the stimulus period from the TFS for each individual and taking the greatest amplitude between 30 – 80 Hz. How the frequency and amplitude changed with age was assessed using Pearson correlation.

7.4 Results

7.4.1 Cross-site comparison in a single adult

One adult participant was scanned in both systems, with approximately 5 months between scans. The location of the peak voxels in the visual mask (overlaid on the MNI brain) and the TFS from the two scans are shown in Figure 7.6. The peak voxels were separated by a Euclidean distance of 40 mm. The relative change across a period during the stimulus (0.3 – 1 s) relative to baseline (-0.8 – -0.1 s) in the gamma band (30 – 80 Hz) amplitude was 5.8% in UoN and 14.2% in SickKids. This relatively large discrepancy between scans conducted at the two sites will be addressed below in our discussion.

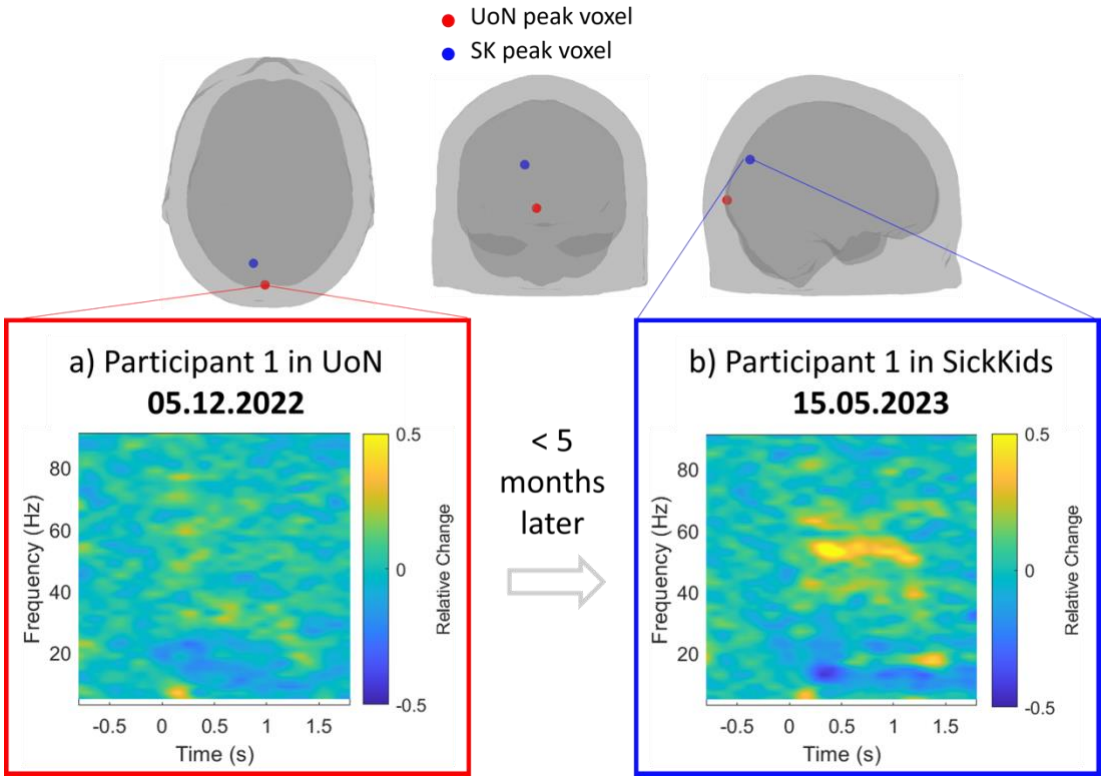


Figure 7.6. Single participant comparison. *TFS from the VE with the maximum contrast in the visual cortex for UoN (left) and SickKids (right).*

7.4.2 Cross-site comparison in a group of adults

Figure 7.7 shows the group cross-site comparison with results averaged across 26 adults at each site. Figure 7.7a shows the mean and standard deviation peak location plotted as ellipsoids overlaid on a mesh of the MNI brain (i.e., the axes of the ellipsoid represent the standard deviation of the peak location coordinates in x, y and z). Figure 7.7b shows the average TFS for participants scanned at UoN (left) and SickKids (right). Here, the UoN system has been reduced to an equivalent channel count as that used at SickKids. Figure 7.7c shows the envelope of 30 – 80 Hz oscillatory amplitude for the UoN system with full channel count (up to 192 channels) in red, UoN reduced channel count in green and SickKids system in blue. There were no significant differences found between the systems when computing an unpaired t-test between the relative change in the active (0.3 – 1 s) period for each participant across the two sites ($t = 1.01$, $p = 0.32$, for the reduced UoN channel count, $t = -0.26$, $p = 0.80$).

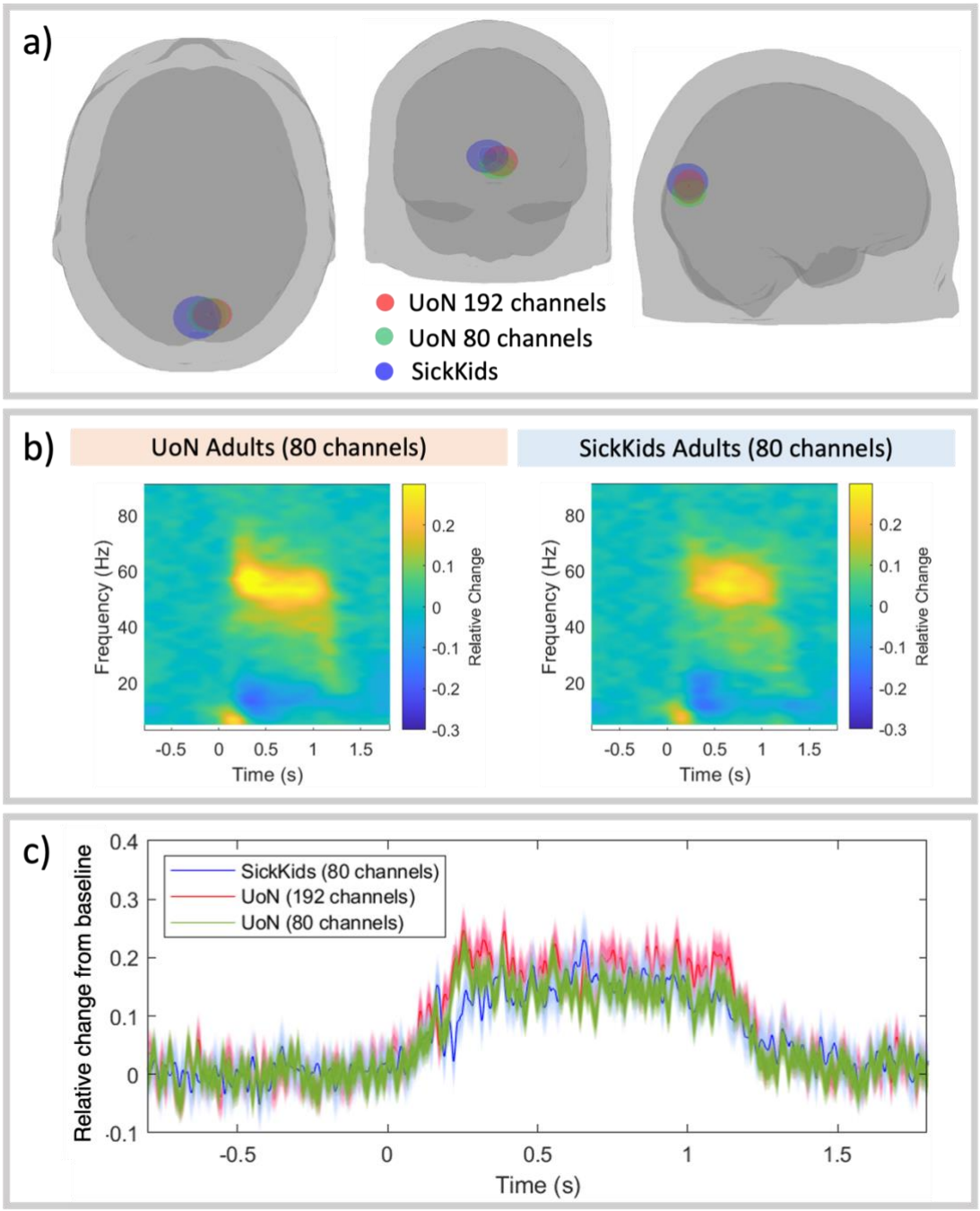


***Figure 7.7. Cross-site comparison**. a) Images showing mean and standard deviation of peak locations for gamma modulation. b) the time-frequency spectrograms and c) gamma band envelopes across groups at SickKids and UoN, with the UoN analyses performed for both the full channel count and reduced channel count.*

7.4.3 Developmental analyses

Section 7.4.2 showed comparative results between two age-matched groups of adults from each site. This demonstrates the validity of combining data across multiple OPM-MEG sites. In this section, we analyse results from all 101 participants (removing the repeat measurement in the single participant and the single participant without a helmet digitisation). Figure 7.8a shows the grand average pseudo-T statistical map

from all 101 participants overlaid on the MNI brain, showing a peak in the visual cortex, as expected. Figure 7.8b shows the location of the voxel with the peak pseudo-T statistic within the visual mask for all participants overlaid on a mesh of the MNI brain. The colour of the points relates to the age of the participant, with red signifying the youngest (2-year-olds) and blue the oldest (34-year-olds).

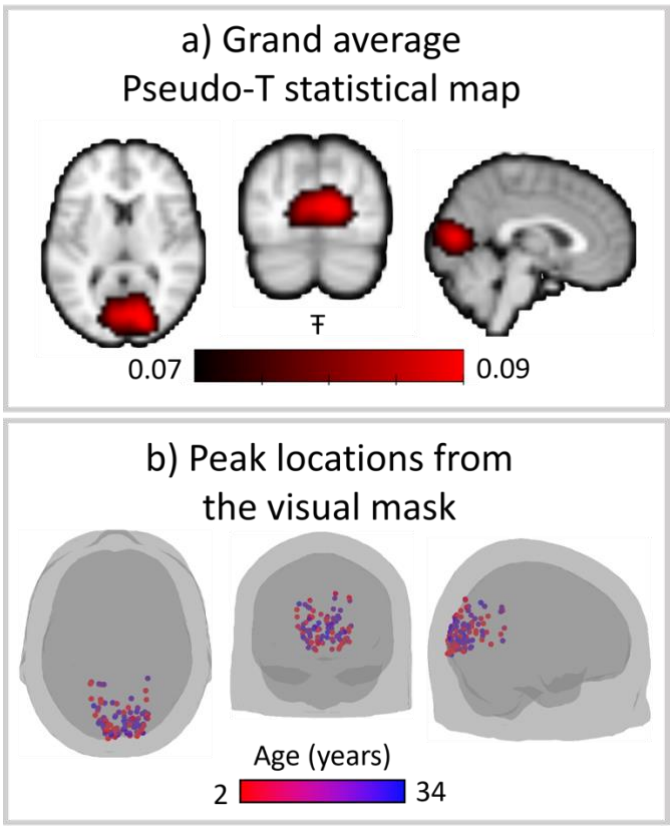


***Figure 7.8. Source localisation**. a) Grand average pseudo-T statistical maps (left) and b) individual peak locations for all participants overlaid on the MNI brain (right).*

Figure 7.9 shows the grand average TFS from the right cuneus (a primary visual region expected to show gamma activity in response to the visual stimuli) taken from the medoid of the region from the AAL atlas, compared to a control region of the pre-central gyrus in the left hemisphere (an area where we would not expect to see gamma activity from this stimulus). The brain plots highlight the region from which the TFS were extracted.

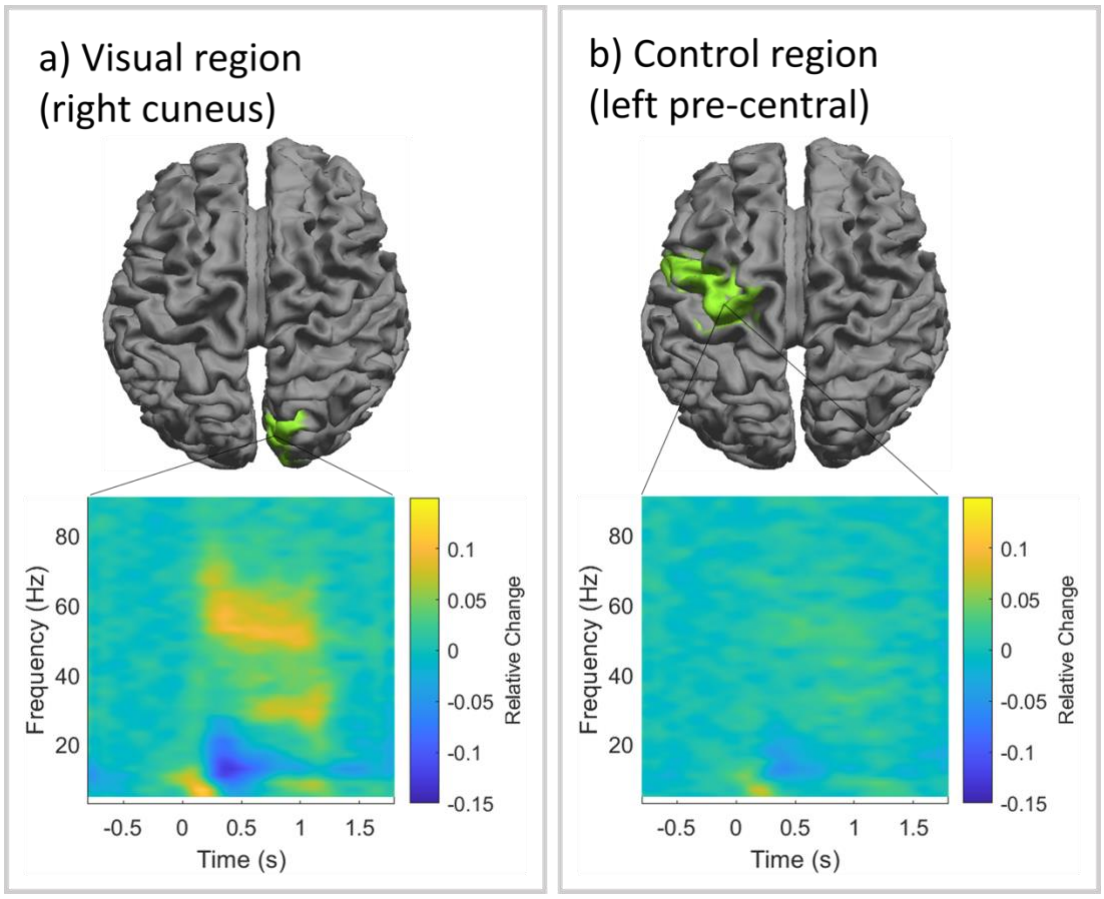


Figure 7.9. Control region comparison. *a) The grand average TFS from the right cuneus (highlighted in green) in the visual cortex for all participants, b) the equivalent TFS from a control region in the left pre-central cortex (highlighted in green).*

Figure 7.10 shows the average pseudo-T statistical maps and the average TFS from the peak in the visual mask, averaged across groups divided by age. The data from children were separated into three groups: 2 – 4 years, 5 – 8 years and 9 – 13 years, inclusive. The adult data were also separated by age (making the group sizes more comparable) to 21 – 24 years, 25 – 28 years and 29 – 34 years, inclusive. We see a change in relative spectral amplitude across the different age groups, particularly between the children and adults. In the group average pseudo-T statistic maps, we see a peak in the visual cortex for all groups. Figure 7.10g shows ellipsoids describing the average and standard deviation of the peak locations from the visual mask, separated by age groups. We see no significant difference in the location of the visual response with age in any axis ($p=0.36$, $p=0.92$ and $p=0.52$ for lateral, anterior-posterior, and inferior-superior), as measured across individuals.

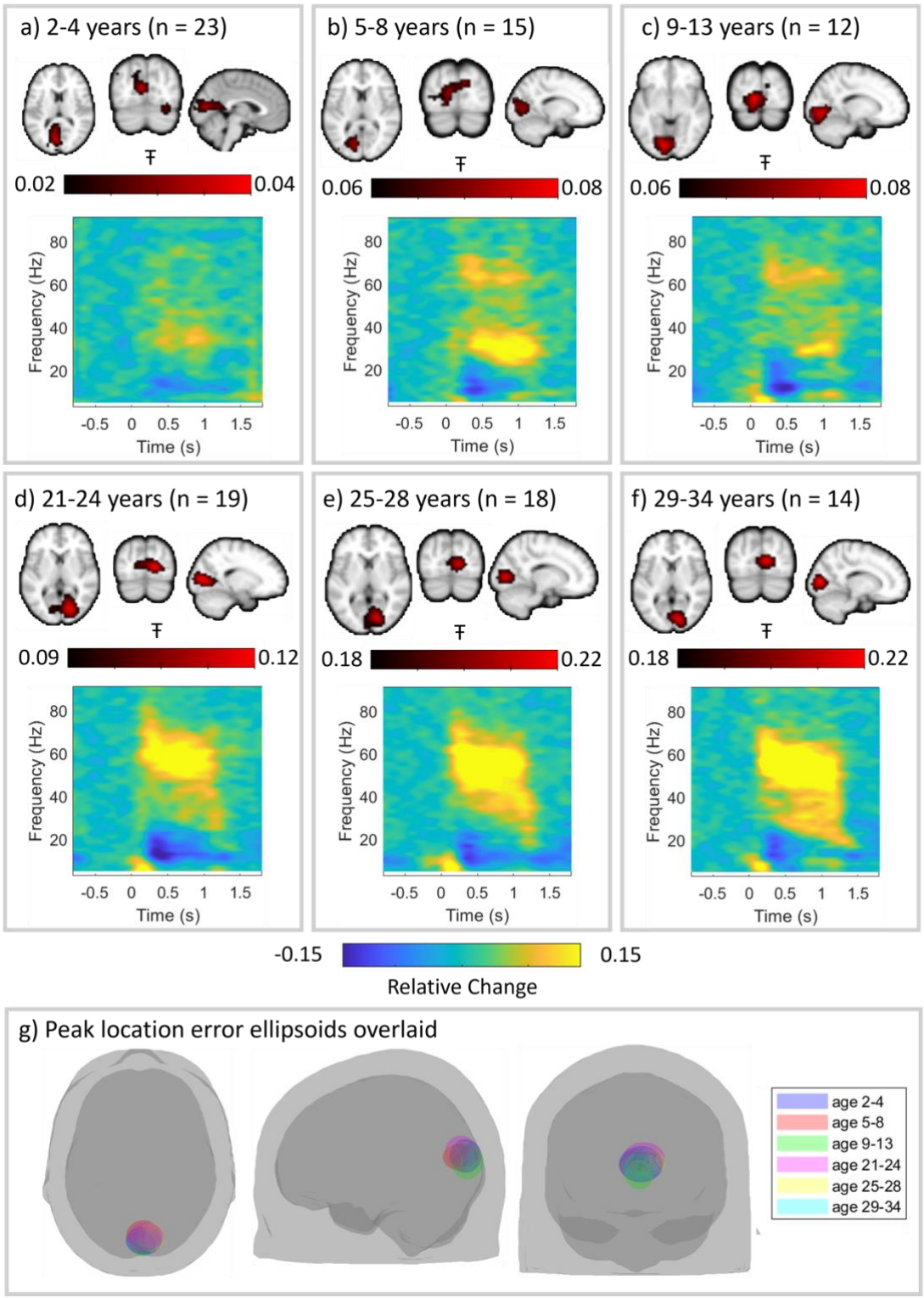


Figure 7.10. Age-related time-frequency spectrograms. *Participant averaged pseudo-T statical images (4mm brain) and average TFS (from the peak in the 1 mm visual cortex mask) for a) 2–4-year-olds (n=23), b) 5–8-year-olds (n=15), c) 9–13-year-olds (n=12), d) 21–24-year-olds (n=19), e) 25–28-year-olds (n=18) and f) 29–34-year-olds (n=14) (ages are inclusive). g) shows ellipsoids centred on the average (size determined by standard deviation) of the peak locations by age group, with no significant relationship in any axis (p=0.36, p=0.92 and p=0.52).*

7.4.4 Age-related spectral content changes

Figure 7.11 shows the stimulus-induced change in spectral content for each age group overlaid. This was calculated by taking the average relative change in oscillatory amplitude in the 0.3 – 1 s time window (Campbell et al., 2014). The inset plots show the individual participants for frequency bands 11-15 Hz, 29-33 Hz and 51-55 Hz. Pearson correlation suggested a significant ($\mathrm{R} = 0.55, p = 3.76 \times 10^{-9}$) relationship between age and change in spectral amplitude due to the stimulus between 51-55 Hz, with older participants showing a greater change in amplitude due to the stimulus than younger participants. This is in agreement with similar studies, that suggest that gamma power is positively correlated with age in school-aged children (Orekhova et al., 2018). Pearson correlation suggested no significant effect at 11-15 Hz and 29-33 Hz ($\mathrm{R} = -0.09, p = 0.39$ and $\mathrm{R} = -0.07, \mathrm{p} = 0.46$, respectively), suggesting no relationship between age and stimulus-induced amplitude change at the alpha/beta band and the low gamma band. This indicates that the data quality is not affected by participant age, suggesting quality data is obtainable across all ages scanned with OPM-MEG.

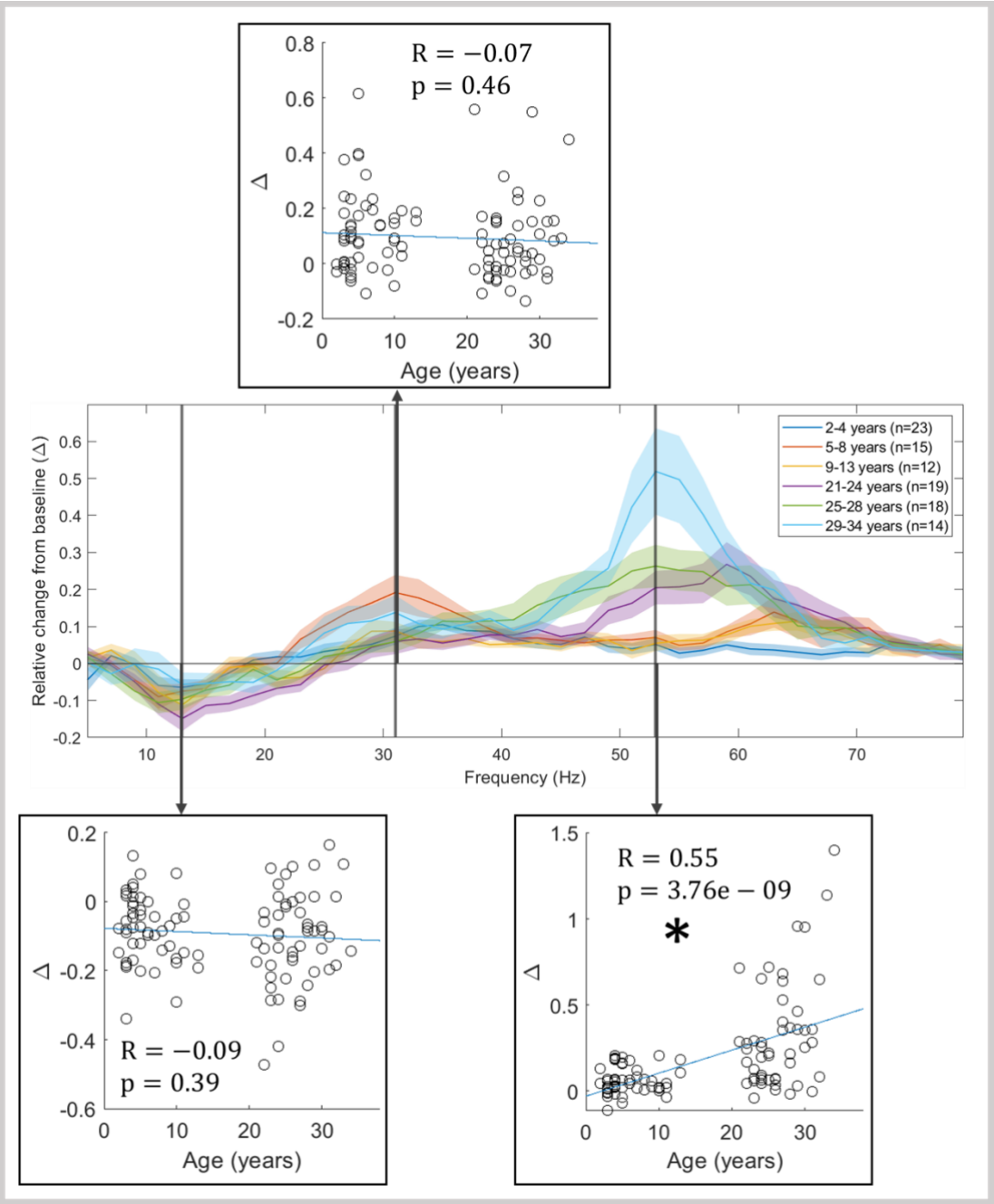


***Figure 7.11. Age-related spectra**. The relative change in amplitude from baseline is plotted against frequency. The relative change was averaged during the stimulus window (0.3 – 1 s post-stimulus, essentially showing a slice in the y-axis across the TFS plot). Each line shows the mean across the age group with shading representing standard error on the mean. The insets show the individual values in change from baseline relative to age, with lines fit to the data. At 11-15 Hz, $\boldsymbol{R = -0.09, p = 0.39}$, at 29-33 Hz, **R**=-0.07, p = 0.46 and at 51-55 Hz, $\boldsymbol{R = 0.55, p = 3.76 \times 10^{-9}}$, where the star indicates significance.*

We also investigated the relations between peak gamma frequency and amplitude at the peak frequency with age. We obtained the peak frequency by taking the maximum amplitude of the relative change from baseline (the spectra shown in Figure 7.11) between 30 – 80 Hz for each participant (see Figure 7.12a). The relationship was analysed by computing the Pearson correlation, which suggested that there was no

significant relationship between age and peak frequency ($\mathrm{R} = 0.14, p = 0.16$). Figure 7.12b shows the relationship between the amplitude at the peak frequency and age. The Pearson correlation suggested a significant positive relationship ($\mathrm{R} = 0.48, p = 4.42 \times 10^{-7}$). However, the gamma response across individuals was highly heterogeneous, with inter-subject variability beyond that explained by age. This is shown in Figure 7.12c and d, where Figure 7.12c shows three example participants who showed a strong gamma response, and Figure 7.12d shows three example participants with a weak gamma response. Note that the heterogeneity was evident across ages.

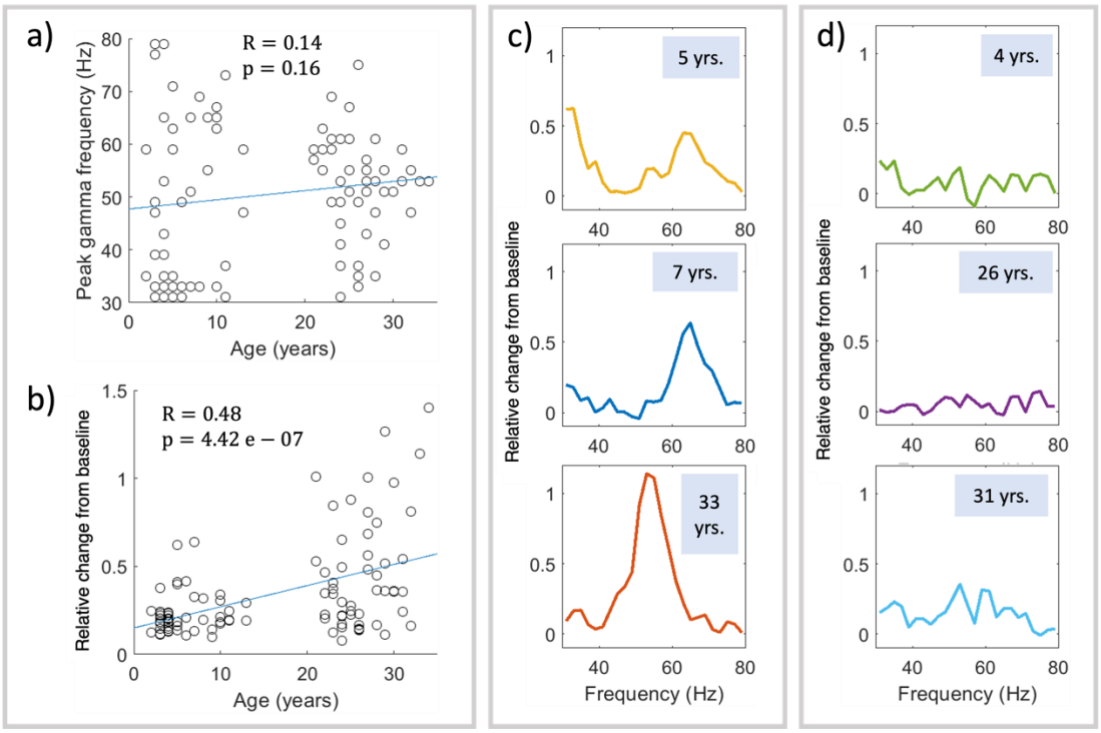


Figure 7.12. Peak gamma frequency and amplitude with age. *The left panel shows a) the peak gamma frequency and b) the relative amplitude at the peak frequency with age for all participants. The lines demonstrate the fit of the data with a)* $\boldsymbol{R = 0.14, p = 0.16}$*, and b)* $\boldsymbol{R = 0.48, p = 4.42 \times 10^{-7}}$*. The right two panels demonstrate the heterogeneity across the group with example participants showing c) a strong gamma response and d) minimal gamma response. Note that the 5-year-old example participant in c) shows two large peaks in the gamma range- one at 33 Hz and a second at 63 Hz.*

7.5 Discussion

The next stage in the development of OPM-MEG towards both research and clinical utility is the acquisition of large normative datasets across the lifespan. In this chapter, we have shown that this is possible through the integration of data from multiple OPM-MEG sites. We measured an induced change in gamma band amplitude elicited by a visual grating paradigm in a group of 102 participants aged from 2 years to 34 years.

7.5.1 Cross-site comparison

Our data included a single adult participant who was scanned twice, once in each system. This participant did not show a consistent spatial nor spectral gamma response between systems. It is important to note that the time between the two scans was long (~ 5 months), and while other studies have shown the reliability of the visual gamma response between scans (Hill et al., 2022; Muthukumaraswamy et al., 2010; Tan et al., 2016), they have typically used short time periods between sessions. Our result is instead consistent with one study that showed that visual gamma oscillations are the least reliable (in comparison to a range of other induced responses) across long time periods (scans that are 1 year apart) (McCusker et al., 2020). This may contribute to the discrepancy between scans. In addition, the individual participant was female, and one study found significant changes in gamma band activity across the menstrual cycle (Sumner et al., 2018). While they focused on peak gamma frequency, some participants had vastly different gamma amplitudes between scans. Despite this, they found consistent gamma amplitude when averaged across the entire group. In sum, it is unlikely that the difference in gamma amplitude is due to the different systems, particularly as the reduced response was seen in the system with greater potential sensitivity (UoN).

It is important to note the difference between the two systems used here, summarised in Figure 7.5. UoN benefits from a greater number of channels due to both more sensors and triaxial measurement; is located in an area with minimal magnetic noise and is housed within an OPM-optimised MSR. Whereas, SickKids has fewer channels of data, is in a magnetically noisy urban environment, and is housed within a re-purposed cryogenic MEG shielded room. Despite these differences, results between the two sites were very consistent across the age-matched adult participant groups, with no significant differences as measured by a two-sample t-test. This may in part be due to the signals we are measuring. In this study, we are measuring relatively high frequency signals, with the gamma band canonically described as frequencies above 30 Hz. Typically, motion artefacts, which would likely be greater in the SickKids system, are below 10 Hz, and so would have less impact at the frequencies of interest in this study. However, for studies investigating lower frequency oscillations, the variation in the background magnetic field environment between OPM-MEG systems must be considered.

It is important to note that visual gamma responses are highly dependent on stimuli parameters (Muthukumaraswamy and Singh, 2013). As such, the impact of site could

not only be OPM-MEG system related but may also be affected by the presentation of the paradigm. Despite this sensitivity, our results from the age-matched adult groups suggest that the stimuli were well-matched.

Reducing the channel count at UoN reduced the difference between systems, as expected; a greater density of sensors, particularly over the visual cortex, would give greater coverage over the active region, and therefore more likely to pick up maximal signal. Further, a greater number of channels of data improves the artefact rejection methods used here (homogeneous field correction and beamforming), leading to a greater reduction in noise.

To summarise, despite differences between the two OPM-MEG sites and systems, we found no significant differences in visual gamma response between our age- and sex-matched groups of healthy adults. This builds upon the result from a previous study with an individual participant (Hill et al., 2022), extending the comparison to consider group analyses.

7.5.2 Development of visual gamma

Across our entire neurodevelopmental dataset, we found the peak gamma response localised to the primary visual cortex, as expected. A virtual electrode at the right cuneus (in the primary visual cortex) showed the expected gamma response, shown by the TFS in Figure 7.9a, that was not clearly visible in other brain regions (for example a control region in the left motor cortex Figure 7.9b). We also see evoked activity at the onset of the visual stimulus and a decrease in amplitude across the alpha/beta band. This is comparable to studies using the same stimulus (Orekhova et al., 2018; Tan et al., 2016). However, selecting the medoid of the AAL atlas region ignores heterogeneity in peak location and may mask the true peak amplitude. We therefore computed the pseudo-T statistic for 1 mm voxels in a visual mask (to reduce computational expense and ensure we were selecting the peak from the visual cortex). From this, we extracted the location of the peak pseudo-T statistic for subsequent virtual electrode analysis. The peak location in the visual mask from all participants is plotted in Figure 7.8b, showing a distribution around the mask. This is likely due to the large number of participants who showed a very weak gamma response, which will be discussed below. We find no age-related locational bias from the colour grading of the points.

The participants were separated into six groups by age to visualise the changes in spectral content across the trial. Group average TFS plots show clear differences

between age groups, particularly between the child groups (Figure 7.10a-c) and adult groups (Figure 7.10d-f). This is shown further in the plot in Figure 7.11, which shows the change in relative amplitude across a range of frequencies, with each age group average plotted on the same axes. The inset plots highlight the individual values, from which the statistics were computed. We found no significant relationship between spectral amplitude and age at two of the clear features of the signal (the decrease in amplitude at 11-15 Hz and increase at 29-33 Hz) but did find a significant relationship between age and the amplitude at 51-55 Hz. The lack of correlation between the alpha desynchronisation and age suggests not only consistent data quality across age, but may support a hypothesis that in the very young children, generative circuitry (Shaw et al., 2020) is dominated by alpha/beta from deep cortical layers (feedback), and development sees a maturation in gamma oscillations (feedforward), resulting in the relative amplitude increase of gamma with age.

Finally, we considered the peak gamma frequency and the amplitude at the peak frequency, in accordance with similar studies. We found a significant positive relationship between the amplitude at the peak gamma frequency and age, replicating results from Orekhova et al. (2018). However, we were unable to replicate the peak frequency results, where multiple studies have suggested that there is a significant negative relationship between peak frequency and age (Gaetz et al., 2011; Orekhova et al., 2015, 2018). However, these studies only included participants down to 6 years of age. As such, little is known about the gamma response below this age. Further, it is unclear whether these studies excluded participants due to weak gamma response. One study found a relationship between the peak gamma frequency and the size of the primary visual cortex, suggesting that a larger cortical volume corresponded to a higher gamma frequency (Schwarzkopf et al., 2012). This would suggest that younger participants, for whom the primary visual cortex would be smaller, would show a lower gamma frequency. This discrepancy in hypotheses about the frequency of visual gamma warrants further investigation in future work.

7.5.3 Heterogeneity in the gamma response

A key finding from our results is that the visual gamma response is highly heterogeneous from early childhood up to adulthood. Similar studies have suggested that there are large inter-individual differences (Muthukumaraswamy et al., 2010) but have not investigated this with respect to age. We found that there was a large variation in both amplitude and spectral content that was not explained by age. This is evident from the scatter in our data shown in both Figure 7.11 and Figure 7.12. One

element of this is the two-peak vs. single-peak gamma response. We found that some participants had a gamma response that manifested as two peak frequencies, typically one low gamma and one in a higher gamma range (also seen in some of the plots in Figure 7.10). This phenomenon has been observed in previous studies (Hoogenboom et al., 2006; Tan et al., 2016) but makes the selection of a single peak gamma frequency complicated. The studies mentioned chose to take only the peak with the highest amplitude, which we followed here. However, this ignores some of the gamma response, and again the heterogeneity in the signal.

Finally, while some studies exclude participants who did not show a strong gamma response, we have chosen to include all data in our analyses. This allows us to highlight the variability in this signal, which we believe is an important feature of the response.

We believe that the result from this data suggests that visual gamma oscillations may not be a viable diagnostic marker for neurodevelopmental disorders such as ASD, due to the heterogeneity within the typically developing population. As shown, the response lacks sensitivity for individual participants. This agrees with previous conventional MEG results [for example, by Muthukumaraswamy et al. (2010) for an adult population], but we find that the inter-participant variability extends to the early years. However, the response may still have utility in the broader study of neurodevelopmental disorders on a group level and could provide a means to better understand the role of E/I balance in ASD, given large enough sample sizes.

7.5.4 Limitations

This study uses the same system (at UoN, although similar at SickKids) as described in the previous chapters so as such, many of the same limitations apply here. We only had a limited range of helmet sizes available, so there remains some separation between the sensors and the head surface, although this typically affects the temporal and frontal regions more than visual and was still greatly improved from cryogenic MEG. The helmet remains heavy with a full array of sensors, although this problem has been alleviated at SickKids with the use of a strap that holds the helmet from above to take some weight off the participant. The warmth remains an issue, although insulating inners designed for rigid helmets keep the heat away from the head surface. In addition, the scan duration is kept short to reduce the risk of overheating.

The number of sensors available for each participant varied significantly even within sites. We could have chosen to only analyse data from equivalent numbers of

sensors, but as we found no significant differences between our adult groups, we chose to analyse data from all channels at UoN. Similarly, we found a significant difference in the number of trials between the children and adult participants. We could therefore have analysed data without all trials, but we found this did not significantly impact the results (our significant results remained significant).

A further confound that may contribute to a difference between site systems is the operational mode of the QZFM sensors. As described in Chapter 3, QZFM sensors suffer from a poor dynamic range. In noisy environments, such as at SickKids, it is possible to operate sensors with a reduced gain, allowing for measurement of larger magnetic fields (up to $\pm$4.5 nT rather than $\pm$1.5 nT). However, this may come at the cost of gain errors due to a deviation from the linear regime of the voltage output (see Figure 3.9). At SickKids, all data were taken in the greater dynamic range operational mode. While this may be a concern, it does not seem to have caused noticeable differences across the adult group comparison.

It is worth mentioning the limitations posed by the choice of participants in this study. As these data were combined from multiple separate studies, we have an asymmetric range of ages, with many 3–5-year-olds from the SickKids database, a spread of 2–13-year-olds from UoN and a lack of data from adolescents from 13–21 years. While we can conclude that the visual gamma response is age-dependent, and we have shown this down to younger ages than measured before with MEG, more investigation is required to better understand the relationship between age and visual gamma oscillations. Finally, we performed linear fits to our data here, which may obscure more nuanced relationships between age and gamma oscillations. A more complex analysis may include higher order relationships or use a decoding method to better understand the relation between such signals and age.

7.6 Conclusion

OPM-MEG remains a new technology with considerable potential for neuroscientific impact, particularly in the study of early life and neurodevelopment. To date, OPM-MEG studies have been hindered by low participant numbers, most likely due to limited access to systems due to the recent development of the technology. Here, we have demonstrated that data can be collaborated across two systems at different sites. We have collected (to our knowledge) the largest known OPM-MEG dataset, including 102 participants aged 2 – 34 years, with a visual grating paradigm. We observed the expected increase in amplitude across the gamma band during the

visual task, which localised to the primary visual cortex. Time-frequency spectrogram analysis showed changes in the spectral content of the response that are related to age. We found a significant positive relationship between the amplitude of the response and age, with older participants showing a larger amplitude gamma response. Our results agree with previous studies suggesting that the visual gamma response has some age dependency. However, this response is highly heterogeneous, particularly in younger participants, which limits the utility of such measures as a clinical diagnostic tool.

8 Concluding remarks

8.1 Summary

This thesis aimed to **develop and test the first whole-head paediatric OPM-MEG system**. We addressed this aim in four experimental chapters. In Chapter 4, we evaluated the performance of an OPM-MEG system against a conventional MEG system for detecting low frequency oscillatory signals, which are of particular interest in neurodevelopment. We found comparable results between systems, with individual "neural fingerprints" in the theta band identifiable between MEG instrumentation, supplying evidence that OPMs are sensitive to such signals. Chapter 5 described a method of warping template MRIs to 3D digitisations of participants' head shapes to generate pseudo-MRIs. By analysing equivalent MEG data with individual and pseudo-MRI anatomy, we showed that results from our method are highly correlated with those from individual anatomy, negating the requirement for individuals to endure MRI scans, particularly in group studies. These two chapters (4 and 5) addressed two of the potential barriers for paediatric OPM-MEG, forming a foundation for the neurodevelopmental studies described in chapters 6 and 7. Chapter 6 investigated the development of cortical beta band oscillations during a sensory task, showing that OPM-MEG could be used to measure signals from children as young as 2 years old. We demonstrated that activity in the beta band can be explained by the 'beta burst' model, even in children; we showed that the spectral content of such bursts changes with age, with significantly more low frequency in younger children. Finally, chapter 7 explored the development of visual gamma oscillations in a multi-centre cohort of healthy child and adult participants. We found that the amplitude of gamma response varied significantly with age, in agreement with previous studies, but found that heterogeneity in the response persists down to young ages. These two studies provide evidence that OPM-MEG is an ideal platform for studying neurodevelopment.

8.2 Future work

8.2.1 Technical development: towards integrated OPM-MEG systems

The development of OPM-MEG technology has been rapid. In only 8 years, we have moved from an idea and simulation, through multiple prototype systems, to now commercially viable products that are being globally distributed to research institutes.

The technology continues to move forward at pace and there have already been system developments since the work described in Chapters 4-7 was conducted. Perhaps the most significant advance has been in the sensor (and sensor electronics) hardware. Original QZFM sensors were designed as individual units with bulky separate electronics, however, arrays are now being designed with multi-sensor systems in mind where a single electronics system controls all of the sensor heads. An example of this comes from QuSpin Inc. and is shown in Figure 8.1 (although it is worth mentioning that the other commercial OPM-MEG companies are designing similar integrated systems).

The QuSpin 'Neuro-1' is compact and ergonomic, with a backpack of electronics that can be worn by the participant to enable full ambulatory motion, or that can be attached to a patient support. In addition, the system comes with a closed-loop operational mode, which (as mentioned in Chapters 3.4 and 3.5) may help with preventing errors due to CAPE and is therefore a step towards a system design that is more robust to noisy magnetic field environments. For paediatric OPM-MEG systems, this approach will allow for greater motion with less artefact, improving data quality. A future can also be envisioned where electronics could be sufficiently compact for a young child or toddler to wear, allowing data to be collected while they learn to crawl and walk.

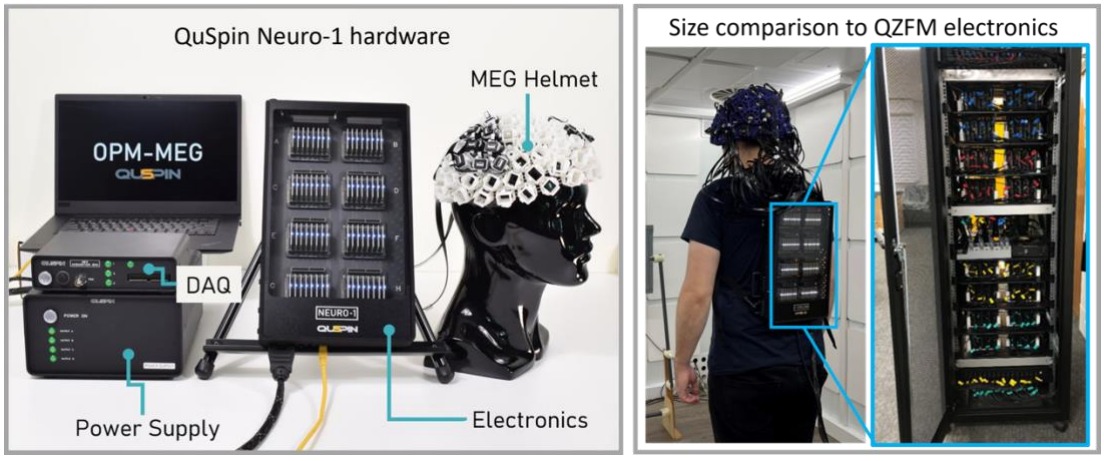


Figure 8.1. The QuSpin Neuro-1 system. *The system hardware is very compact (shown on the left, credit QuSpin Inc.), with the electronics reduced from a tall rack to a wearable backpack (right).*

8.2.2 Going younger: baby OPM-MEG

While the studies described in Chapters 6 and 7 included participants as young as 2 years old, the obvious next stage in paediatric OPM-MEG development is to develop a system suitable for scanning from birth. The flexibility afforded by lightweight OPM sensors makes this possible, and a baby scanning device has already been tested in

a small number of pilot studies. We conducted a brief project that investigated the feasibility of designing an OPM-MEG system for babies from 6 months to 18 months of age. In this project, we worked with a product design company to generate initial designs for a potential subject interface (or helmet) that afforded flexibility to different head sizes and a range of stages of development. We also did a series of pilot scans with four infants (aged between 9 – 18 months) using a flexible baby cap with sensor holders sewn on. Briefly, we collected MEG data from a small number of babies during a sensory task, in which an auditory signal instructed the parent/guardian (upon whom the infant was sat) to stroke the back of the right hand of the child. Upon averaging across a series of trials, this is predicted to cause a decrease in beta band amplitude (similar to Chapter 6). Results from one participant are shown in Figure 8.2.

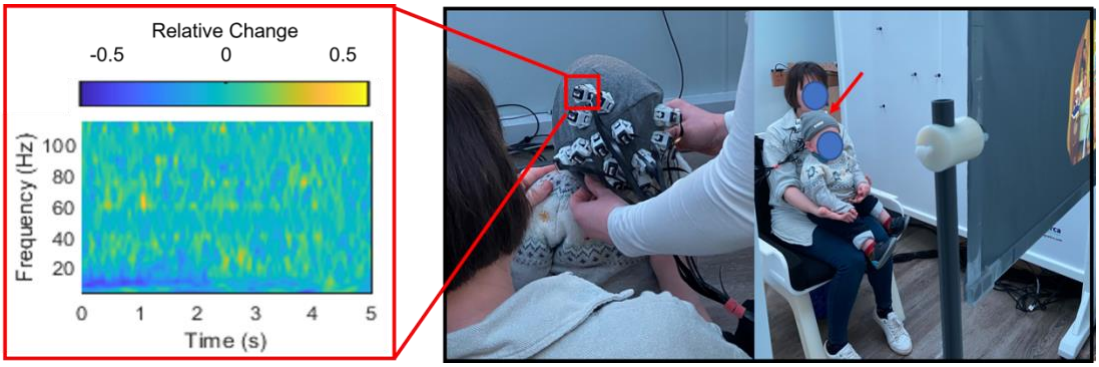


Figure 8.2. Baby OPM-MEG*. Images of a young participant wearing the flexible baby beanie hat, and the TFS from a single channel from a MEG pilot study using a maternal touch paradigm. The negative response at around 10-20 Hz from 0 – 2 s is potentially indicative of the beta modulation we describe in Chapter 6.*

More recently, a group in Belgium released a pre-print of their results collecting OPM-MEG data from a group of 20 newborn babies during a simple auditory task (Corvilain et al., 2023). The main challenge for the deployment of baby OPM-MEG it seems is the sensor array design; helmet weight and temperature control are challenging for very young participants. That said, these initial pilot results suggest that once a solution to this is achieved, OPM-MEG could be instrumental in studying very early development.

8.2.3 Paediatric OPM-MEG in the clinic

The work described in this thesis has focused on healthy, typically developing participants. But we hope that this system will allow us to study the brain not only in health but also in atypical development. The next step is to deploy this system for studying cohorts with atypically developing brains. The most obvious area to benefit from a paediatric OPM-MEG system is in the presurgical assessment and planning

for epilepsy. In cryogenic MEG, a recent study analysing 1000 epilepsy cases showed that those in whom MEG-identified regions were resected were significantly more likely to achieve seizure freedom (Rampp et al., 2019). Additionally, outcomes are improved when surgical treatment is administered as early as possible (Ryvlin et al., 2014). As such, it is hoped that OPM-MEG offers an exciting prospect for the future of epilepsy treatment, improving surgical outcomes even for very young patients (Pedersen et al., 2022).

Beyond epilepsy, there are other conditions that OPM-MEG may benefit, including neurodevelopmental disorders such as ASD and ADHD, two of the most prevalent neurodevelopmental disorders, affecting 1.5% and 5% of children, respectively (Polanczyk et al., 2014; Zeidan et al., 2022). Critically, our system provides the ability to scan participants at younger ages, before the typical diagnostic age of ~3 years. This provides an opportunity to better understand the progression of such disorders and may help discover diagnostic biomarkers, meaning interventions can begin at a younger age. This may improve future quality of life for children with such disorders.

8.3 Final thoughts

The brain undergoes massive changes within the first few years of life, forming the foundations of not only our sensory and cognitive abilities but also our personalities; indeed, who we are as individuals becomes apparent in these early years. Yet, we know so little about how such critical developmental milestones are supported by neural function. MEG arguably offers the greatest potential to unlock the trajectories of such function but has not previously been accessible to infant participants due to technical limitations.

OPM-MEG has already undergone rapid development and the work presented in this thesis represents a significant technical milestone, proving that the technology has unique potential to provide valuable insight into typical and atypical development. There remain system design and engineering challenges, and the coming years will undoubtedly see new innovations, which we have not yet conceived. However, what is clear is that how we, as humans, change from babies to adults remains a mystery. If we can use OPM-MEG technology to shine a new light on this, we will be helping to answer one of the oldest and most fundamental questions in science.

References

Alem, O., Hughes, K.J., Buard, I., Cheung, T.P., Maydew, T., Griesshammer, A., Holloway, K., Park, A., Lechuga, V., Coolidge, C., 2023. An integrated full-head OPM-MEG system based on 128 zero-field sensors. Front. Neurosci. 17, 1190310.

Allred, J., Lyman, R., Kornack, T., Romalis, M.V., 2002. High-sensitivity atomic magnetometer unaffected by spin-exchange relaxation. Phys. Rev. Lett. 89, Article Number: 130801.

Altarev, I., Babcock, E., Beck, D., Burghoff, M., Chesnevskaya, S., Chupp, T., Degenkolb, S., Fan, I., Fierlinger, P., Frei, A., Gutsmiedl, E., Knappe-Grüneberg, S., Kuchler, F., Lauer, T., Link, P., Lins, T., Marino, M., McAndrew, J., Niessen, B., Paul, S., Petzoldt, G., Schläpfer, U., Schnabel, A., Sharma, S., Singh, J., Stoepler, R., Stuiber, S., Sturm, M., Taubenheim, B., Trahms, L., Voigt, J., Zechlau, T., 2014. A magnetically shielded room with ultra low residual field and gradient. Rev. Sci. Instrum. 85, 075106. https://doi.org/10.1063/1.4886146

An, K., Ikeda, T., Yoshimura, Y., Hasegawa, C., Saito, D.N., Kumazaki, H., Hirosawa, T., Minabe, Y., Kikuchi, M., 2018. Altered Gamma Oscillations during Motor Control in Children with Autism Spectrum Disorder. J. Neurosci. 38, 7878–7886. https://doi.org/10.1523/JNEUROSCI.1229-18.2018

Appelt, S., Baranga, A.B.-A., Young, A., Happer, W., 1999. Light narrowing of rubidium magnetic-resonance lines in high-pressure optical-pumping cells. Phys. Rev. A 59, 2078.

Backus, G.E., Gilbert, F., 1968. The Resolving power of Gross Earth Data. Geophys. J. R. Astron. Soc. 16, 169–205.

Baker, A.P., Brookes, M.J., Rezek, I.A., Smith, S.M., Behrens, T., Probert Smith, P.J., Woolrich, M., 2014. Fast transient networks in spontaneous human brain activity. eLife 3, e01867. https://doi.org/10.7554/eLife.01867

Bardeen, J., Cooper, L.N., Schrieffer, J.R., 1957. Microscopic theory of superconductivity. Phys. Rev. 106, 162.

Barone, J., Rossiter, H.E., 2021. Understanding the Role of Sensorimotor Beta Oscillations. Front. Syst. Neurosci. 15, 655886. https://doi.org/10.3389/fnsys.2021.655886

Barratt, E.L., Francis, S.T., Morris, P.G., Brookes, M.J., 2018. Mapping the topological organisation of beta oscillations in motor cortex using MEG. NeuroImage 181, 831–844.

Barratt, E.L., Tewarie, P.K., Clarke, M.A., Hall, E.L., Gowland, P.A., Morris, P.G., Francis, S., Evangelou, N., Brookes, M.J., 2017. Abnormal task driven neural oscillations in multiple sclerosis: A visuomotor MEG study. Hum. Brain Mapp. 38, 2441–2453.

Barry, D.N., Tierney, T.M., Holmes, N., Boto, E., Roberts, G., Leggett, J., Bowtell, R., Brookes, M.J., Barnes, G.R., Maguire, E.A., 2019. Imaging the human hippocampus with optically-pumped magnetoencephalography. NeuroImage 203, 116192. https://doi.org/10.1016/j.neuroimage.2019.116192

Bartos, M., Vida, I., Jonas, P., 2007. Synaptic mechanisms of synchronized gamma oscillations in inhibitory interneuron networks. Nat. Rev. Neurosci. 8, 45–56. https://doi.org/10.1038/nrn2044

Başar, E., 2012. A review of alpha activity in integrative brain function: Fundamental physiology, sensory coding, cognition and pathology. Int. J. Psychophysiol. 86, 1–24. https://doi.org/10.1016/j.ijpsycho.2012.07.002

Bastos, A.M., Vezoli, J., Bosman, C.A., Schoffelen, J.-M., Oostenveld, R., Dowdall, J.R., De Weerd, P., Kennedy, H., Fries, P., 2015. Visual Areas Exert Feedforward and Feedback Influences through Distinct Frequency Channels. Neuron 85, 390–401. https://doi.org/10.1016/j.neuron.2014.12.018

Bauer, M., Stenner, M.-P., Friston, K.J., Dolan, R.J., 2014. Attentional Modulation of Alpha/Beta and Gamma Oscillations Reflect Functionally Distinct Processes. J. Neurosci. 34, 16117–16125. https://doi.org/10.1523/JNEUROSCI.3474-13.2014

Bell, W.E., Bloom, A.L., 1957. Optical Detection of Magnetic Resonance in Alkali Metal Vapor. Phys. Rev. 107, 1559–1565. https://doi.org/10.1103/PhysRev.107.1559

Berger, H., 1929. Über das Elektrenkephalogramm des Menschen. Arch. Für Psychiatr. Nervenkrankh. 87, 527–570.

Biswal, B., Yetkin, F.Z., Haughton, V.M., Hyde, J.S., 1995. Functional connectivity in the motor cortex of resting human brain using echo-planar MRI. Magn. Reson. Med. 34, 537–541. https://doi.org/10.1002/mrm.1910340409

Bloom, A.L., 1962. Principles of Operation of the Rubidium Vapor Magnetometer. Appl. Opt. 1, 61–68. https://doi.org/10.1364/AO.1.000061

Borna, A., Iivanainen, J., Carter, T.R., McKay, J., Taulu, S., Stephen, J., Schwindt, P.D., 2022. Cross-Axis projection error in optically pumped magnetometers and its implication for magnetoencephalography systems. NeuroImage 247, 118818.

Bosseler, A.N., Taulu, S., Pihko, E., Mäkelä, J.P., Imada, T., Ahonen, A., Kuhl, P.K., 2013. Theta brain rhythms index perceptual narrowing in infant speech perception. Front. Psychol. 4, 690. https://doi.org/10.3389/fpsyg.2013.00690

Boto, E., Bowtell, R.W., Krüger, P., Fromhold, M., Morris, P.G., Meyer, S., Barnes, G.R., Brookes, M.J., 2016. On the Potential of a New Generation of Magnetometers for MEG: A Beamformer Simulation Study. PLOS ONE 11(8), e0157655.

Boto, E., Hill, R.M., Rea, M., Holmes, N., Seedat, Z.A., Leggett, J., Shah, V., Osborne, J., Bowtell, R., Brookes, M.J., 2021. Measuring functional connectivity with wearable MEG. NeuroImage 230, 117815. https://doi.org/10.1016/j.neuroimage.2021.117815

Boto, E., Holmes, N., Leggett, J., Roberts, G., Shah, V., Meyer, S.S., Duque Muñoz, L., Mullinger, K.J., Tierney, T.M., Bestmann, S., Barnes, G.R., Bowtell, R., Brookes, M.J., 2018. Moving magnetoencephalography towards real-world applications with a wearable system. Nature 555, 657.

Boto, E., Meyer, S.S., Shah, V., Alem, O., Knappe, S., Kruger, P., Fromhold, M., Lim, M., Glover, P.M., Morris, P.G., Bowtell, R., Barnes, G.R., Brookes, M.J., 2017. A new generation of magnetoencephalography: Room temperature measurements using optically-pumped magnetometers. Neuroimage 149, 404–414.

Boto, E., Seedat, Z.A., Holmes, N., Leggett, J., Hill, R.M., Roberts, G., Shah, V., Fromhold, T.M., Mullinger, K.J., Tierney, T.M., Barnes, G.R., Bowtell, R., Brookes, M.J., 2019. Wearable neuroimaging: Combining and contrasting magnetoencephalography and electroencephalography. NeuroImage 201, 116099. https://doi.org/10.1016/j.neuroimage.2019.116099

Boto, E., Shah, V., Hill, R.M., Rhodes, N., Osborne, J., Doyle, C., Holmes, N., Rea, M., Leggett, J., Bowtell, R., Brookes, M.J., 2022. Triaxial detection of the neuromagnetic field using optically-pumped magnetometry: feasibility and application in children. NeuroImage 252, 119027. https://doi.org/10.1016/j.neuroimage.2022.119027

Broca, P., 1861. Remarks on the seat of the faculty of articulated language, following an observation of aphemia (loss of speech). Bull. Société Anat. 6, 330–357.

Brookes, M.J., Boto, E., Rea, M., Shah, V., Osborne, J., Holmes, N., Hill, R.M., Leggett, J., Rhodes, N., Bowtell, R., 2021. Theoretical advantages of a triaxial optically pumped magnetometer magnetoencephalography system. NeuroImage 236, 118025.

Brookes, M.J., Groom, M.J., Liuzzi, L., Hill, R.M., Smith, H.J.F., Briley, P.M., Hall, E.L., Hunt, B.A.E., Gascoyne, L.E., Taylor, M.J., Liddle, P.F., Morris, P.G., Woolrich, M.W., Liddle, E.B., 2018. Altered temporal stability in dynamic neural networks underlies connectivity changes in neurodevelopment. NeuroImage 174, 563–575. https://doi.org/10.1016/j.neuroimage.2018.03.008

Brookes, M.J., Hale, J.R., Zumer, J.M., Stevenson, C.M., Francis, S.T., Barnes, G.R., Owen, J.P., Morris, P.G., Nagarajan, S.S., 2011a. Measuring Functional Connectivity Using MEG: Methodology and Comparison With fcMRI. NeuroImage 56, 1082–104.

Brookes, M.J., Leggett, J., Rea, M., Hill, R.M., Holmes, N., Boto, E., Bowtell, R., 2022. Magnetoencephalography with optically pumped magnetometers (OPM-MEG): the next generation of functional neuroimaging. Trends Neurosci. 45, 621–634. https://doi.org/10.1016/j.tins.2022.05.008

Brookes, M.J., Vrba, J., Robinson, S.E., Stevenson, C.M., Peters, A.P., Barnes, G.R., Hillebrand, A., Morris, P.G., 2008. Optimising experimental design for MEG beamformer imaging. NeuroImage 39, 1788–1802.

Brookes, M.J., Wood, J.R., Stevenson, C.M., Zumer, J.M., White, T.P., Liddle, P.F., Morris, P.G., 2011b. Changes in brain network activity during working memory tasks: A magnetoencephalography study. NeuroImage 55, 1804–1815.

Brookes, M.J., Woolrich, M., Luckhoo, H., Price, D., Hale, J.R., Stephenson, M.C., Barnes, G.R., Smith, S.M., Morris, P.G., 2011c. Investigating the Electrophysiological Basis of Resting State Networks using Magnetoencephalography. Proc. Natl. Acad. Sci. USA 108, 16783–16788.

Brookes, M.J., Woolrich, M.W., Barnes, G.R., 2012. Measuring Functional Connectivity in MEG: a Multi-Variate Approach insensitive to linear Source Leakage. NeuroImage 63, 910–920.

Brossel, J., Margerie, J., Kastler, A., 1955. Augmenta-tion du taux dorientation atomique de la vapeur de sodium en presence dhydro-gene. CR Chim 241, 865.

Brown, C., Gruber, T., Boucher, J., Rippon, G., Brock, J., 2005. Gamma Abnormalities During Perception of Illusory Figures in Autism. Cortex 41, 364–376. https://doi.org/10.1016/S0010-9452(08)70273-9

Bruining, H., Hardstone, R., Juarez-Martinez, E.L., Sprengers, J., Avramiea, A.-E., Simpraga, S., Houtman, S.J., Poil, S.-S., Dallares, E., Palva, S., Oranje, B., Matias Palva, J., Mansvelder, H.D., Linkenkaer-Hansen, K., 2020. Measurement of excitation-inhibition ratio in autism spectrum disorder using critical brain dynamics. Sci. Rep. 10, 9195. https://doi.org/10.1038/s41598-020-65500-4

Cajochen, C., Foy, R., Dijk, D.-J., 1999. Frontal predominance of a relative increase in sleep delta and theta EEG activity after sleep loss in humans. Sleep Res. Online SRO 2, 65–9.

Campbell, A.E., Sumner, P., Singh, K.D., Muthukumaraswamy, S.D., 2014. Acute effects of alcohol on stimulus-induced gamma oscillations in human primary visual and motor cortices. Neuropsychopharmacol. Off. Publ. Am. Coll. Neuropsychopharmacol. 39, 2104–2113. https://doi.org/10.1038/npp.2014.58

Candelaria-Cook, F.T., Solis, I., Schendel, M.E., Wang, Y.-P., Wilson, T.W., Calhoun, V.D., Stephen, J.M., 2022. Developmental trajectory of MEG resting-state oscillatory activity in children and adolescents: a longitudinal

reliability study. Cereb. Cortex N. Y. N 1991 32, 5404–5419. https://doi.org/10.1093/cercor/bhac023
Cardy, J.E.O., Flagg, E.J., Roberts, W., Brian, J., Roberts, T.P., 2005. Magnetoencephalography identifies rapid temporal processing deficit in autism and language impairment. Neuroreport 16, 329–332.
Carlson, J.W., Derby, K.A., Hawryszko, K.C., Weideman, M., 1992. Design and evaluation of shielded gradient coils. Magn. Reson. Med. 26, 4349–4353.
Celozzi, S., Araneo, R., Lovat, G., 2008. Electromagnetic Shielding. IEEE Wiley.
Churchill, J.D., Tharp, J.A., Wellman, C.L., Sengelaub, D.R., Garraghty, P.E., 2004. Morphological correlates of injury-induced reorganization in primate somatosensory cortex. BMC Neurosci. 5, 43. https://doi.org/10.1186/1471-2202-5-43
Cignoni, P., Callieri, M., Corsini, M., Dellepiane, M., Ganovelli, F., Ranzuglia, G., 2008. MeshLab: an Open-Source Mesh Processing Tool. The Eurographics Association. https://doi.org/10.2312/LocalChapterEvents/ItalChap/ItalianChapConf2008/129-136
Clarke, A.R., Barry, R.J., McCarthy, R., Selikowitz, M., 2001. Age and sex effects in the EEG: Development of the normal child. Clin. Neurophysiol. 112, 806–814. https://doi.org/10.1016/S1388-2457(01)00488-6
Cohen, D., 1972. Magnetoencephalography: detection of the brain's electrical activity with a superconducting magnetometer. Science 175, 664–6.
Cohen, D., 1970. Large-volume conventional magnetic shields. Rev. Phys. Appliquée 5, 53–58. https://doi.org/10.1051/rphysap:019700050105300
Cohen, D., 1968. Magnetoencephalography: evidence of magnetic fields produced by alpha-rhythm currents. Science 161, 784–6.
Colclough, G.L., Brookes, M.J., Smith, S.M., Woolrich, M.W., 2015. A symmetric multivariate leakage correction for MEG connectomes. NeuroImage 117, 439–448. https://doi.org/10.1016/j.neuroimage.2015.03.071
Corvilain, P., Wens, V., Bourguignon, M., Capparini, C., Fourdin, L., Ferez, M., Feys, O., De Tiege, X., Bertels, J., 2023. Extending the applicability of optically pumped magnetoencephalography toward early human life (preprint). Neuroscience. https://doi.org/10.1101/2023.10.28.564455
Courtemanche, R., Fujii, N., Graybiel, A.M., 2003. Synchronous, Focally Modulated β-Band Oscillations Characterize Local Field Potential Activity in the Striatum of Awake Behaving Monkeys. J. Neurosci. 23, 11741–11752. https://doi.org/10.1523/JNEUROSCI.23-37-11741.2003
Courtemanche, R., Pellerin, J.-P., Lamarre, Y., 2002. Local Field Potential Oscillations in Primate Cerebellar Cortex: Modulation During Active and Passive Expectancy. J. Neurophysiol. 88, 771–782. https://doi.org/10.1152/jn.2002.88.2.771
da Silva Castanheira, J., Orozco Perez, H.D., Misic, B., Baillet, S., 2021. Brief segments of neurophysiological activity enable individual differentiation. Nat. Commun. 12, 1–11.
Dang, H., Maloof, A., Romalis, M., 2010. Ultrahigh sensitivity magnetic field and magnetization measurements with an atomic magnetometer. Appl Phys Lett 97, 151110.
Datko, M., Gougelet, R., Huang, M.-X., Pineda, J.A., 2016. Resting State Functional Connectivity MRI among Spectral MEG Current Sources in Children on the Autism Spectrum. Front. Neurosci. 10.
de Lange, P., Boto, E., Holmes, N., Hill, R.M., Bowtell, R., Wens, V., De Tiège, X., Brookes, M.J., Bourguignon, M., 2021. Measuring the cortical tracking of speech with optically-pumped magnetometers. NeuroImage 233, 117969. https://doi.org/10.1016/j.neuroimage.2021.117969

Dickinson, A., Bruyns-Haylett, M., Jones, M., Milne, E., 2015. Increased peak gamma frequency in individuals with higher levels of autistic traits. Eur. J. Neurosci. 41, 1095–1101. https://doi.org/10.1111/ejn.12881
Dickinson, A., Bruyns-Haylett, M., Smith, R., Jones, M., Milne, E., 2016a. Superior orientation discrimination and increased peak gamma frequency in autism spectrum conditions. J. Abnorm. Psychol. 125, 412–422. https://doi.org/10.1037/abn0000148
Dickinson, A., Jones, M., Milne, E., 2016b. Measuring neural excitation and inhibition in autism: Different approaches, different findings and different interpretations. Brain Res. 1648, 277–289. https://doi.org/10.1016/j.brainres.2016.07.011
Douw, L., Nieboer, D., Stam, C.J., Tewarie, P., Hillebrand, A., 2018. Consistency of magnetoencephalographic functional connectivity and network reconstruction using a template versus native MRI for co-registration. Hum. Brain Mapp. 39, 104–119. https://doi.org/10.1002/hbm.23827
Eckhorn, R., Bauer, R., Jordan, W., Brosch, M., Kruse, W., Munk, M., Reitboeck, H.J., 1988. Coherent oscillations: A mechanism of feature linking in the visual cortex? Biol. Cybern. 60, 121–130. https://doi.org/10.1007/BF00202899
Engel, A.K., Fries, P., 2010. Beta-band oscillations — signalling the status quo? Curr. Opin. Neurobiol., Cognitive neuroscience 20, 156–165. https://doi.org/10.1016/j.conb.2010.02.015
Engel, A.K., Gerloff, C., Hilgetag, C.C., Nolte, G., 2013. Intrinsic Coupling Modes: Multiscale Interactions in Ongoing Brain Activity. Neuron 80, 867–886.
Faley, M.I., Dammers, J., Maslennikov, Y.V., Schneiderman, J.F., Winkler, D., Koshelets, V.P., Shah, N.J., Dunin-Borkowski, R.E., 2017. High-Tc SQUID biomagnetometers. Supercond. Sci. Technol. 30, 083001. https://doi.org/10.1088/1361-6668/aa73ad
Fell, J., Fernández, G., Klaver, P., Elger, C.E., Fries, P., 2003. Is synchronized neuronal gamma activity relevant for selective attention? Brain Res. Rev. 42, 265–272. https://doi.org/10.1016/S0165-0173(03)00178-4
Feys, O., Corvilain, P., Aeby, A., Sculier, C., Holmes, N., Brookes, M., Goldman, S., Wens, V., De Tiège, X., 2022. On-Scalp Optically Pumped Magnetometers versus Cryogenic Magnetoencephalography for Diagnostic Evaluation of Epilepsy in School-aged Children. Radiology 304, 429–434. https://doi.org/10.1148/radiol.212453
Feys, O., Corvilain, P., Bertels, J., Sculier, C., Holmes, N., Brookes, M., Wens, V., De Tiège, X., 2023. On-scalp magnetoencephalography for the diagnostic evaluation of epilepsy during infancy. Clin. Neurophysiol. 155, 29–31. https://doi.org/10.1016/j.clinph.2023.08.010
Fillmore, P.T., Phillips-Meek, M.C., Richards, J.E., 2015. Age-specific MRI brain and head templates for healthy adults from 20 through 89 years of age. Front. Aging Neurosci. 7.
Fries, P., 2005. A mechanism for cognitive dynamics: neuronal communication through neuronal coherence. Trends Cogn. Sci. 9, 474–480. https://doi.org/10.1016/j.tics.2005.08.011
Gaetz, W., Macdonald, M., Cheyne, D., Snead, O., 2010. Neuromagnetic imaging of movement-related cortical oscillations in children and adults: Age predicts post-movement beta rebound. Neuroimage 51, 792–807.
Gaetz, W., Otsubo, H., Pang, E.W., 2008. Magnetoencephalography for clinical pediatrics: The effect of head positioning on measurement of somatosensory-evoked fields. Clin. Neurophysiol. 119, 1923–1933. https://doi.org/10.1016/j.clinph.2008.04.291
Gaetz, W., Roberts, T.P.L., Singh, K.D., Muthukumaraswamy, S.D., 2011. Functional and structural correlates of the aging brain: Relating visual cortex

(V1) gamma band responses to age-related structural change. Hum. Brain Mapp. 33, 2035–2046. https://doi.org/10.1002/hbm.21339
Gascoyne, L.E., Brookes, M.J., Rathnaiah, M., Katshu, M.Z.U.H., Koelewijn, L., Williams, G., Kumar, J., Walters, J.T.R., Seedat, Z.A., Palaniyappan, L., Deakin, J.F.W., Singh, K.D., Liddle, P.F., Morris, P.G., 2021. Motor-related oscillatory activity in schizophrenia according to phase of illness and clinical symptom severity. NeuroImage Clin. 29, 102524. https://doi.org/10.1016/j.nicl.2020.102524
Geselowitz, D., 1970. On the magnetic field generated outside an inhomogeneous volume conductor by internal current sources. IEEE Trans. Magn. 6, 346–347. https://doi.org/10.1109/TMAG.1970.1066765
Giedd, J.N., Raznahan, A., Mills, K.L., Lenroot, R.K., 2012. Review: magnetic resonance imaging of male/female differences in human adolescent brain anatomy. Biol. Sex Differ. 3, 19. https://doi.org/10.1186/2042-6410-3-19
Goldman, D.E., 1943. POTENTIAL, IMPEDANCE, AND RECTIFICATION IN MEMBRANES. J. Gen. Physiol. 27, 37–60. https://doi.org/10.1085/jgp.27.1.37
Gong, G., Rosa-Neto, P., Carbonell, F., Chen, Z.J., He, Y., Evans, A.C., 2009. Age- and Gender-Related Differences in the Cortical Anatomical Network. J. Neurosci. 29, 15684–15693. https://doi.org/10.1523/JNEUROSCI.2308-09.2009
Gray, C.M., König, P., Engel, A.K., Singer, W., 1989. Oscillatory responses in cat visual cortex exhibit inter-columnar synchronization which reflects global stimulus properties. Nature 338, 334–337. https://doi.org/10.1038/338334a0
Gray, C.M., Singer, W., 1989. Stimulus-specific neuronal oscillations in orientation columns of cat visual cortex. Proc. Natl. Acad. Sci. 86, 1698–1702. https://doi.org/10.1073/pnas.86.5.1698
Gutteling, T.P., Bonnefond, M., Clausner, T., Daligault, S., Romain, R., Mitryukovskiy, S., Fourcault, W., Josselin, V., Le Prado, M., Palacios-Laloy, A., Labyt, E., Jung, J., Schwartz, D., 2023. A New Generation of OPM for High Dynamic and Large Bandwidth MEG: The 4He OPMs—First Applications in Healthy Volunteers. Sensors 23, 2801. https://doi.org/10.3390/s23052801
Hadamard, J., 1902. Sur les problèmes aux dérivées partielles et leur signification physique. Princet. Univ. Bull. 49–52.
Hahl, F.A., Lindner, L., Vidal, X., Luo, T., Ohshima, T., Onoda, S., Ishii, S., Zaitsev, A.M., Capelli, M., Gibson, B.C., Greentree, A.D., Jeske, J., 2022. Magnetic-field-dependent stimulated emission from nitrogen-vacancy centers in diamond. Sci. Adv. 8, eabn7192. https://doi.org/10.1126/sciadv.abn7192
Hajizadeh, A., Matysiak, A., May, P.J.C., König, R., 2019. Explaining event-related fields by a mechanistic model encapsulating the anatomical structure of auditory cortex. Biol. Cybern. 113, 321–345. https://doi.org/10.1007/s00422-019-00795-9
Hall, S.D., Barnes, G.R., Furlong, P.L., Seri, S., Hillebrand, A., 2010. Neuronal network pharmacodynamics of GABAergic modulation in the human cortex determined using pharmaco-magnetoencephalography. Hum. Brain Mapp. 31, 581–594. https://doi.org/10.1002/hbm.20889
Hall, S.D., Holliday, I.E., Hillebrand, A., Singh, K.D., Furlong, P.L., Hadjipapas, A., Barnes, G.R., 2005. The missing link: analogous human and primate cortical gamma oscillations. NeuroImage 26, 13–17. https://doi.org/10.1016/j.neuroimage.2005.01.009
Hamalainen, M.S., Hari, R., Ilmoniemi, R.J., Knuutila, J., Lounasma, O.V., 1993. Magnetoencephalography: Theory, instrumentation, and applications to non-invasive studies of the working human brain. Rev. Mod. Phys. 65, 413–497.

Hämäläinen, M.S., Ilmoniemi, R.J., 1994. Interpreting magnetic fields of the brain: minimum norm estimates. Med. Biol. Eng. Comput. 32, 35–42. https://doi.org/10.1007/BF02512476
Hämäläinen, M.S., Sarvas, J., 1989. Realistic conductivity geometry model of the human head for interpretation of neuromagnetic data. IEEE Trans. Biomed. Eng. 36, 165–171. https://doi.org/10.1109/10.16463
Hanle, W., 1925. Die magnetische Beeinflussung der Resonanzfluoreszenz. Ergeb Exakt Naturw 4.
Happer, W., 1972. Optical Pumping. Rev. Mod. Phys. 44, 169–249. https://doi.org/10.1103/RevModPhys.44.169
Harlow, J.M., 1848. Passage of an iron rod through the head. Boston Med. Surg. J. 1828-1851 39, 0_1.
Harmony, T., 2013. The functional significance of delta oscillations in cognitive processing. Front. Integr. Neurosci. 7, 83. https://doi.org/10.3389/fnint.2013.00083
Hasselmo, M.E., Hay, J., Ilyn, M., Gorchetchnikov, A., 2002. Neuromodulation, theta rhythm and rat spatial navigation. Neural Netw. 15, 689–707.
Haueisen, J., Fleissig, K., Strohmeier, D., Elsarnagawy, T., Huonker, R., Liehr, M., Witte, O.W., 2012. Reconstruction of quasi-radial dipolar activity using three-component magnetic field measurements. Clin. Neurophysiol. 123, 1581–1585. https://doi.org/10.1016/j.clinph.2011.12.020
Hill, R.M., Boto, E., Holmes, N., Hartley, C., Seedat, Z.A., Leggett, J., Roberts, G., Shah, V., Tierney, T.M., Woolrich, M.W., Stagg, C.J., Barnes, G.R., Bowtell, R.R., Slater, R., Brookes, M.J., 2019. A tool for functional brain imaging with lifespan compliance. Nat. Commun. 10, 1–11. https://doi.org/10.1038/s41467-019-12486-x
Hill, R.M., Boto, E., Rea, M., Holmes, N., Leggett, J., Coles, L.A., Papastavrou, M., Everton, S.K., Hunt, B.A.E., Sims, D., Osborne, J., Shah, V., Bowtell, R., Brookes, M.J., 2020. Multi-channel whole-head OPM-MEG: Helmet design and a comparison with a conventional system. NeuroImage 219, 116995.
Hill, R.M., Devasagayam, J., Holmes, N., Boto, E., Shah, V., Osborne, J., Safar, K., Worcester, F., Mariani, C., Dawson, E., 2022. Using OPM-MEG in contrasting magnetic environments. NeuroImage 253, 119084.
Hillebrand, A., Tewarie, P., Van Dellen, E., Yu, M., Carbo, E.W., Douw, L., Gouw, A.A., Van Straaten, E.C., Stam, C.J., 2016. Direction of information flow in large-scale resting-state networks is frequency-dependent. Proc. Natl. Acad. Sci. 113, 3867–3872.
Hipp, J.F., Hawellek, D.J., Corbetta, M., Siegel, M., Engel, A.K., 2012. Large-scale cortical correlation structure of spontaneous oscillatory activity. Nat. Neurosci. 15, 884–890.
Hirata, M., Ikeda, T., Kikuchi, M., Kimura, T., Hiraishi, H., Yoshimura, Y., Asada, M., 2014. Hyperscanning MEG for understanding mother–child cerebral interactions. Front. Hum. Neurosci. 8.
Hoburg, J.F., 1995. Principles of quasistatic magnetic shielding with cylindrical and spherical shields. IEEE Trans. Electromagn. Compat. 37, 574–579. https://doi.org/10.1109/15.477342
Holliday, I.E., Barnes, G.R., Hillebrand, A., Singh, K.D., 2003. Accuracy and applications of group MEG studies using cortical source locations estimated from participants' scalp surfaces. Hum. Brain Mapp. 20, 142–147. https://doi.org/10.1002/hbm.10133
Holmes, M., Leggett, J., Boto, E., Roberts, G., Hill, R.M., Tierney, T.M., Shah, V., Barnes, G.R., Brookes, M.J., Bowtell R., 2018. A bi-planar coil system for nulling background magnetic fields in scalp mounted magnetoencephalography. NeuroImage 181, 760–774.

Holmes, N., Bowtell, R., Brookes, M.J., Taulu, S., 2023a. An Iterative Implementation of the Signal Space Separation Method for Magnetoencephalography Systems with Low Channel Counts. Sensors 23, 6537. https://doi.org/10.3390/s23146537
Holmes, N., Rea, M., Chalmers, J., Leggett, J., Edwards, L.J., Nell, P., Pink, S., Patel, P., Wood, J., Murby, N., Woolger, D., Dawson, E., Mariani, C., Tierney, T.M., Mellor, S., O'Neill, G.C., Boto, E., Hill, R.M., Shah, V., Osborne, J., Pardington, R., Fierlinger, P., Barnes, G.R., Glover, P., Brookes, M.J., Bowtell, R., 2022. A lightweight magnetically shielded room with active shielding. Sci. Rep. 12, 1–13.
Holmes, N., Rea, M., Hill, R.M., Leggett, J., Edwards, L.J., Hobson, P.J., Boto, E., Tierney, T.M., Rier, L., Rivero, G.R., Shah, V., Osborne, J., Fromhold, T.M., Glover, P., Brookes, M.J., Bowtell, R., 2023b. Enabling ambulatory movement in wearable magnetoencephalography with matrix coil active magnetic shielding. NeuroImage 274, 120157. https://doi.org/10.1016/j.neuroimage.2023.120157
Holmes, N., Tierney, T.M., Leggett, J., Boto, E., Mellor, S., Roberts, G., Hill, R.M., Shah, V., Barnes, G.R., Brookes, M.J., Bowtell, R., 2019. Balanced, bi-planar magnetic field and field gradient coils for field compensation in wearable magnetoencephalography. Sci. Rep. 9, 1–15.
Holst, M., Eswaran, H., Lowery, C., Murphy, P., Norton, J., Preissl, H., 2005. Development of auditory evoked fields in human fetuses and newborns: A longitudinal MEG study. Clin. Neurophysiol. 116, 1949–1955. https://doi.org/10.1016/j.clinph.2005.04.008
Hoogenboom, N., Schoffelen, J.-M., Oostenveld, R., Parkes, L.M., Fries, P., 2006. Localizing human visual gamma-band activity in frequency, time and space. NeuroImage 29, 764–773. https://doi.org/10.1016/j.neuroimage.2005.08.043
Hounsfield, G.N., 1973. Computerized transverse axial scanning (tomography). 1. Description of system. Br. J. Radiol. 46, 1016–1022. https://doi.org/10.1259/0007-1285-46-552-1016
Huang, M.X., Mosher, J.C., Leahy, R.M., 1999. A sensor-weighted overlapping-sphere head model and exhaustive head model comparison for MEG. Phys. Med. Biol. 44, 423–440. https://doi.org/10.1088/0031-9155/44/2/010
Huang, M.-X., Nichols, S., Baker, D.G., Robb, A., Angeles, A., Yurgil, K.A., Drake, A., Levy, M., Song, T., McLay, R., Theilmann, R.J., Diwakar, M., Risbrough, V.B., Ji, Z., Huang, C.W., Chang, D.G., Harrington, D.L., Muzzatti, L., Canive, J.M., Christopher Edgar, J., Chen, Y.-H., Lee, R.R., 2014. Single-subject-based whole-brain MEG slow-wave imaging approach for detecting abnormality in patients with mild traumatic brain injury. NeuroImage Clin. 5, 109–119. https://doi.org/10.1016/j.nicl.2014.06.004
Hunt, B.A.E., Wong, S.M., Vandewouw, M.M., Brookes, M.J., Dunkley, B.T., Taylor, M.J., 2019. Spatial and spectral trajectories in typical neurodevelopment from childhood to middle age. Netw. Neurosci. 3, 497–520. https://doi.org/10.1162/netn_a_00077
Hutchinson, G., Holmes, N., Brookes, M.J., Bowtell, R., 2019. Residual magnetization of human subjects after exposure to magnetic fields. Presented at the ISMRM.
Iivanainen, J., Stenroos, M., Parkkonen, L., 2017. Measuring MEG closer to the brain: Performance of on-scalp sensor arrays. Neuroimage 147, 542–553.
Iivanainen, J., Zetter, R., Grön, M., Hakkarainen, K., Parkkonen, L., 2019. On-scalp MEG system utilizing an actively shielded array of optically-pumped magnetometers. NeuroImage 194, 244–258. https://doi.org/10.1016/j.neuroimage.2019.03.022
Inanaga, K., 1998. Frontal midline theta rhythm and mental activity. Psychiatry Clin. Neurosci. 52, 555–566. https://doi.org/10.1046/j.1440-1819.1998.00452.x

Jenkinson, M., Bannister, P., Brady, M., Smith, S., 2002. Improved optimization for the robust and accurate linear registration and motion correction of brain images. Neuroimage 17, 825–841.
Jenkinson, M., Smith, S., 2001. A global optimisation method for robust affine registration of brain images. Med. Image Anal. 5, 143–156. https://doi.org/10.1016/S1361-8415(01)00036-6
Jensen, O., Mazaheri, A., 2010. Shaping Functional Architecture by Oscillatory Alpha Activity: Gating by Inhibition. Front. Hum. Neurosci. 4.
Jensen, O., Tesche, C.D., 2002. Frontal theta activity in humans increases with memory load in a working memory task. Eur. J. Neurosci. 15, 1395–1399. https://doi.org/10.1046/j.1460-9568.2002.01975.x
Jeong, J., 2004. EEG dynamics in patients with Alzheimer's disease. Clin. Neurophysiol. 115, 1490–1505. https://doi.org/10.1016/j.clinph.2004.01.001
Johnson, B.W., Crain, S., Thornton, R., Tesan, G., Reid, M., 2010. Measurement of brain function in pre-school children using a custom sized whole-head MEG sensor array. Clin. Neurophysiol. 121, 340–349. https://doi.org/10.1016/j.clinph.2009.10.017
Johnson, C.N., Schwindt, P.D., Weisend, M., 2013. Multi-sensor magnetoencephalography with atomic magnetometers. Phys. Med. Biol. 58, 6065–6077.
Jones, S.R., 2016. When brain rhythms aren't 'rhythmic': implication for their mechanisms and meaning. Curr. Opin. Neurobiol. 40, 72–80. https://doi.org/10.1016/j.conb.2016.06.010
Josephson, B.D., 1974. The discovery of tunnelling supercurrents. Rev Mod Phys 46, 251–254.
Josephson, B.D., 1962. Possible new effects in superconductive tunnelling. Phys Lett 1, 251–253.
Kamada, K., Sato, D., Ito, Y., Natsukawa, H., Okano, K., Mizutani, N., Kobayashi, T., 2015. Human magnetoencephalogram measurements using newly developed compact module of high-sensitivity atomic magnetometer. Jpn. J. Appl. Phys. 54, Article number 026601.
Kandel, E.R., Schwartz, J.H., Jessell, T.M., Siegelbaum, S., Hudspeth, A.J., Mack, S., 2000. Principles of neural science. McGraw-hill New York.
Karakaş, S., 2020. A review of theta oscillation and its functional correlates. Int. J. Psychophysiol. 157, 82–99. https://doi.org/10.1016/j.ijpsycho.2020.04.008
Kastler, A., 1951. Méthodes optiques d'étude de la résonance magnétique. Physica 17, 191–204. https://doi.org/10.1016/0031-8914(51)90058-4
Kikuchi, M., Yoshimura, Y., Mutou, K., Minabe, Y., 2016. Magnetoencephalography in the study of children with autism spectrum disorder. Psychiatry Clin. Neurosci. 70, 74–88. https://doi.org/10.1111/pcn.12338
Kirschvink, J.L., Kobayashi-Kirschvink, A., Woodford, B.J., 1992. Magnetite biomineralization in the human brain. Proc. Natl. Acad. Sci. 89, 7683–7687. https://doi.org/10.1073/pnas.89.16.7683
Knappe, S., Sander, T.H., Kosch, O., Wiekhorst, F., Kitching, J., Trahms, L., 2010. Cross-validation of microfabricated atomic magnetometers with superconducting quantum interference devices for biomagnetic applications. Appl. Phys. Lett. 97, 133703. https://doi.org/10.1063/1.3491548
Kominis, I.K., Kornack, T.W., Allred, J.C., Romalis, M.V., 2003. A subfemtotesla multichannel atomic magnetometer. Nature 422, 596–599.
Koshev, N., Butorina, A., Skidchenko, E., Kuzmichev, A., Ossadtchi, A., Ostras, M., Fedorov, M., Vetoshko, P., 2021. Evolution of MEG: A first MEG-feasible fluxgate magnetometer. Hum. Brain Mapp. 42, 4844–4856. https://doi.org/10.1002/hbm.25582

Kuhl, P.K., Ramírez, R.R., Bosseler, A., Lin, J.-F.L., Imada, T., 2014. Infants' brain responses to speech suggest Analysis by Synthesis. Proc. Natl. Acad. Sci. 111, 11238–11245. https://doi.org/10.1073/pnas.1410963111
Kuhnke, N., Schwind, J., Dümpelmann, M., Mader, M., Schulze-Bonhage, A., Jacobs, J., 2018. High Frequency Oscillations in the Ripple Band (80-250 Hz) in Scalp EEG: Higher Density of Electrodes Allows for Better Localization of the Seizure Onset Zone. Brain Topogr. 31, 1059–1072. https://doi.org/10.1007/s10548-018-0658-3
Kujala, A., Huotilainen, M., Hotakainen, M., Lennes, M., Parkkonen, L., Fellman, V., Näätänen, R., 2004. Speech-sound discrimination in neonates as measured with MEG. NeuroReport 15, 2089.
Kurz, M.J., Proskovec, A.L., Gehringer, J.E., Becker, K.M., Arpin, D.J., Heinrichs-Graham, E., Wilson, T.W., 2016. Developmental Trajectory of Beta Cortical Oscillatory Activity During a Knee Motor Task. Brain Topogr. 29, 824–833. https://doi.org/10.1007/s10548-016-0500-8
Kuschner, E.S., Kim, M., Bloy, L., Dipiero, M., Edgar, J.C., Roberts, T.P., 2021. MEG-PLAN: a clinical and technical protocol for obtaining magnetoencephalography data in minimally verbal or nonverbal children who have autism spectrum disorder. J. Neurodev. Disord. 13, 1–17.
Lalancette, M., Quraan, M., Cheyne, D., 2011. Evaluation of multiple-sphere head models for MEG source localization. Phys. Med. Biol. 56, 5621–5635. https://doi.org/10.1088/0031-9155/56/17/010
Landfield, P.W., McGaugh, J.L., Tusa, R.J., 1972. Theta Rhythm: A Temporal Correlate of Memory Storage Processes in the Rat. Science 175, 87–89. https://doi.org/10.1126/science.175.4017.87
Lauterbur, P.C., 1973. Image Formation by Induced Local Interactions: Examples Employing Nuclear Magnetic Resonance. Nature 242, 190–191. https://doi.org/10.1038/242190a0
Lee, R.R., Huang, M., 2014. Magnetoencephalography in the diagnosis of concussion. Concussion 28, 94–111.
Lesting, J., Narayanan, R.T., Kluge, C., Sangha, S., Seidenbecher, T., Pape, H.-C., 2011. Patterns of coupled theta activity in amygdala-hippocampal-prefrontal cortical circuits during fear extinction. PloS One 6, e21714.
Little, S., Bonaiuto, J., Barnes, G., Bestmann, S., 2019. Human motor cortical beta bursts relate to movement planning and response errors. PLOS Biol. 17, e3000479. https://doi.org/10.1371/journal.pbio.3000479
Little, S., Brown, P., 2014. The functional role of beta oscillations in Parkinson's disease. Parkinsonism Relat. Disord. 20 Suppl 1, S44-48. https://doi.org/10.1016/S1353-8020(13)70013-0
Liu, Z., Fukunaga, M., de Zwart, J.A., Duyn, J.H., 2010. Large-Scale Spontaneous Fluctuations and Correlations in Brain Electrical Activity Observed with Magnetoencephalography. NeuroImage 51, 102–111. https://doi.org/10.1016/j.neuroimage.2010.01.092
Mansfield, P., Grannell, P.K., 1973. NMR "diffraction" in solids? J. Phys. C Solid State Phys. 6, L422. https://doi.org/10.1088/0022-3719/6/22/007
Matsuzaki, J., Ku, M., Dipiero, M., Chiang, T., Saby, J., Blaskey, L., Kuschner, E.S., Kim, M., Berman, J.I., Bloy, L., 2020. Delayed auditory evoked responses in autism spectrum disorder across the life span. Dev. Neurosci. 41, 223–233.
McCusker, M.C., Lew, B.J., Wilson, T.W., 2020. Three-Year Reliability of MEG Visual and Somatosensory Responses. Cereb. Cortex N. Y. NY 31, 2534–2548. https://doi.org/10.1093/cercor/bhaa372
Meissner, W., Ochsenfeld, R., 1933. Ein neuer Effekt bei Eintritt der Supraleitfähigkeit. Naturwissenschaften 21, 787–788. https://doi.org/10.1007/BF01504252

Meltzer, J.A., Negishi, M., Mayes, L.C., Constable, R.T., 2007. Individual differences in EEG theta and alpha dynamics during working memory correlate with fMRI responses across subjects. Clin. Neurophysiol. 118, 2419–2436. https://doi.org/10.1016/j.clinph.2007.07.023

Messaritaki, E., Koelewijn, L., Dima, D.C., Williams, G.M., Perry, G., Singh, K.D., 2017. Assessment and elimination of the effects of head movement on MEG resting-state measures of oscillatory brain activity. Neuroimage 159, 302–324. https://doi.org/10.1016/j.neuroimage.2017.07.038

Mhaskar, R., Knappe, S., Kitching, J., 2012. A low-power, high-sensitivity micromachined optical magnetometer. Appl Phys Lett 101, 241105.

Michalareas, G., Vezoli, J., van Pelt, S., Schoffelen, J.-M., Kennedy, H., Fries, P., 2016. Alpha-Beta and Gamma Rhythms Subserve Feedback and Feedforward Influences among Human Visual Cortical Areas. Neuron 89, 384–397. https://doi.org/10.1016/j.neuron.2015.12.018

Miskovic, V., Ma, X., Chou, C.-A., Fan, M., Owens, M., Sayama, H., Gibb, B.E., 2015. Developmental changes in spontaneous electrocortical activity and network organization from early to late childhood. Neuroimage 118, 237–247.

Missonnier, P., Deiber, M.-P., Gold, G., Millet, P., Gex-Fabry Pun, M., Fazio-Costa, L., Giannakopoulos, P., Ibáñez, V., 2006. Frontal theta event-related synchronization: comparison of directed attention and working memory load effects. J. Neural Transm. Vienna Austria 1996 113, 1477–1486. https://doi.org/10.1007/s00702-005-0443-9

Muthukumaraswamy, S.D., 2013. High-frequency brain activity and muscle artifacts in MEG/EEG: a review and recommendations. Front. Hum. Neurosci. 7, 138.

Muthukumaraswamy, S.D., Edden, R.A.E., Jones, D.K., Swettenham, J.B., Singh, K.D., 2009. Resting GABA concentration predicts peak gamma frequency and fMRI amplitude in response to visual stimulation in humans. Proc. Natl. Acad. Sci. 106, 8356–8361. https://doi.org/10.1073/pnas.0900728106

Muthukumaraswamy, S.D., Myers, J.F.M., Wilson, S.J., Nutt, D.J., Lingford-Hughes, A., Singh, K.D., Hamandi, K., 2013. The effects of elevated endogenous GABA levels on movement-related network oscillations. NeuroImage 66, 36–41. https://doi.org/10.1016/j.neuroimage.2012.10.054

Muthukumaraswamy, S.D., Singh, K.D., 2013. Visual gamma oscillations: The effects of stimulus type, visual field coverage and stimulus motion on MEG and EEG recordings. NeuroImage 69, 223–230. https://doi.org/10.1016/j.neuroimage.2012.12.038

Muthukumaraswamy, S.D., Singh, K.D., Swettenham, J.B., Jones, D.K., 2010. Visual gamma oscillations and evoked responses: Variability, repeatability and structural MRI correlates. NeuroImage 49, 3349–3357. https://doi.org/10.1016/j.neuroimage.2009.11.045

Nardelli, N., Perry, A., Krzyzewski, S., Knappe, S., 2020. A conformal array of microfabricated optically-pumped first-order gradiometers for magnetoencephalography. EPJ Quantum Technol. 7, 11.

Nelson, S.B., Valakh, V., 2015. Excitatory/Inhibitory balance and circuit homeostasis in Autism Spectrum Disorders. Neuron 87, 684–698. https://doi.org/10.1016/j.neuron.2015.07.033

Nolte, G., 2003. The magnetic lead field theorem in the quasi-static approximation and its use for magnetoencephalography forward calculation in realistic volume conductors. Phys Med Biol 48, 3637–52. https://doi.org/10.1088/0031-9155/48/22/002

Nurminen, J., Taulu, S., Nenonen, J., Helle, L., Simola, J., Ahonen, A., 2013. Improving MEG performance with additional tangential sensors. IEEE Trans. Biomed. Eng. 60, 2559–2566. https://doi.org/10.1109/TBME.2013.2260541

Ogawa, S., Lee, T.M., Kay, A.R., Tank, D.W., 1990. Brain magnetic resonance imaging with contrast dependent on blood oxygenation. Proc. Natl. Acad. Sci. U. S. A. 87, 9868–9872.
Okada, Y., Hämäläinen, M., Pratt, K., Mascarenas, A., Miller, P., Han, M., Robles, J., Cavallini, A., Power, B., Sieng, K., Sun, L., Lew, S., Doshi, C., Ahtam, B., Dinh, C., Esch, L., Grant, E., Nummenmaa, A., Paulson, D., 2016. BabyMEG: A whole-head pediatric magnetoencephalography system for human brain development research. Rev. Sci. Instrum. 87, 094301. https://doi.org/10.1063/1.4962020
Okada, Y., Pratt, K., Atwood, C., Mascarenas, A., Reineman, R., Nurminen, J., Paulson, D., 2006. BabySQUID: A mobile, high-resolution multichannel magnetoencephalography system for neonatal brain assessment. Rev. Sci. Instrum. 77, Article number 024301.
O'Neill, George C., Barratt, E.L., Hunt, B.A.E., Tewarie, P.K., Brookes, M.J., 2015. Measuring electrophysiological connectivity by power envelope correlation: a technical review on MEG methods. Phys. Med. Biol. 60, R271-295. https://doi.org/10.1088/0031-9155/60/21/R271
O'Neill, G.C., Bauer, M., Woolrich, M.W., Morris, P.G., Barnes, G.R., Brookes, M.J., 2015. Dynamic recruitment of resting state sub-networks. NeuroImage 115, 85–95.
Onnes, H.K., 1911. The superconductivity of mercury. Comm Phys Lab Univ Leiden 122, 124.
Onton, J., Delorme, A., Makeig, S., 2005. Frontal midline EEG dynamics during working memory. NeuroImage 27, 341–356. https://doi.org/10.1016/j.neuroimage.2005.04.014
Oostenveld, R., Fries, P., Maris, E., Schoffelen, J.-M., 2011. FieldTrip: open source software for advanced analysis of MEG, EEG, and invasive electrophysiological data. Comput. Intell. Neurosci. 2011.
Orekhova, E., Butorina, A., Sysoeva, O., Prokofyev, A., Nikolaeva, A., Stroganova, T., 2015. Frequency of gamma oscillations in humans is modulated by velocity of visual motion. J. Neurophysiol. 114, jn.00232.2015. https://doi.org/10.1152/jn.00232.2015
Orekhova, E.V., Manyukhina, V.O., Galuta, I.A., Prokofyev, A.O., Goiaeva, D.E., Obukhova, T.S., Fadeev, K.A., Schneiderman, J.F., Stroganova, T.A., 2023. Gamma oscillations point to the role of primary visual cortex in atypical motion processing in autism. PLOS ONE 18, e0281531. https://doi.org/10.1371/journal.pone.0281531
Orekhova, E.V., Stroganova, T.A., Nygren, G., Tsetlin, M.M., Posikera, I.N., Gillberg, C., Elam, M., 2007. Excess of High Frequency Electroencephalogram Oscillations in Boys with Autism. Biol. Psychiatry, Autism and Attention Deficit Hyperactivity Disorder 62, 1022–1029. https://doi.org/10.1016/j.biopsych.2006.12.029
Orekhova, E.V., Sysoeva, O.V., Schneiderman, J.F., Lundström, S., Galuta, I.A., Goiaeva, D.E., Prokofyev, A.O., Riaz, B., Keeler, C., Hadjikhani, N., Gillberg, C., Stroganova, T.A., 2018. Input-dependent modulation of MEG gamma oscillations reflects gain control in the visual cortex. Sci. Rep. 8, 8451. https://doi.org/10.1038/s41598-018-26779-6
Osborne, J., Orton, J., Alem, O., Shah, V., 2018. Fully integrated standalone zero field optically pumped magnetometer for biomagnetism, in: Steep Dispersion Engineering and Opto-Atomic Precision Metrology XI. Presented at the Steep Dispersion Engineering and Opto-Atomic Precision Metrology XI, SPIE, pp. 89–95. https://doi.org/10.1117/12.2299197
Ott, L.R., Penhale, S.H., Taylor, B.K., Lew, B.J., Wang, Y.-P., Calhoun, V.D., Stephen, J.M., Wilson, T.W., 2021. Spontaneous cortical MEG activity undergoes unique age- and sex-related changes during the transition to

adolescence. NeuroImage 244, 118552. https://doi.org/10.1016/j.neuroimage.2021.118552
Owen, A.M., McMillan, K.M., Laird, A.R., Bullmore, E., 2005. N-back working memory paradigm: A meta-analysis of normative functional neuroimaging studies. Hum. Brain Mapp. 25, 46–59. https://doi.org/10.1002/hbm.20131
Parvizi, J., Kastner, S., 2018. Human Intracranial EEG: Promises and Limitations. Nat. Neurosci. 21, 474–483. https://doi.org/10.1038/s41593-018-0108-2
Pedersen, M., Abbott, D.F., Jackson, G.D., 2022. Wearable OPM-MEG: A changing landscape for epilepsy. Epilepsia 63, 2745–2753. https://doi.org/10.1111/epi.17368
Pelt, S. van, Boomsma, D.I., Fries, P., 2012. Magnetoencephalography in Twins Reveals a Strong Genetic Determination of the Peak Frequency of Visually Induced Gamma-Band Synchronization. J. Neurosci. 32, 3388–3392. https://doi.org/10.1523/JNEUROSCI.5592-11.2012
Pfurtscheller, G., Lopes da Silva, F., 1999. Event-related EEG/MEG synchronization and desynchronization: Basic principles. Clin Neurophysio 110, 1842–1857.
Pizzo, F., Frauscher, B., Ferrari-Marinho, T., Amiri, M., Dubeau, F., Gotman, J., 2016. Detectability of Fast Ripples (>250 Hz) on the Scalp EEG: A Proof-of-Principle Study with Subdermal Electrodes. Brain Topogr. 29, 358–367. https://doi.org/10.1007/s10548-016-0481-7
Polanczyk, G.V., Willcutt, E.G., Salum, G.A., Kieling, C., Rohde, L.A., 2014. ADHD prevalence estimates across three decades: an updated systematic review and meta-regression analysis. Int. J. Epidemiol. 43, 434–442. https://doi.org/10.1093/ije/dyt261
Port, R.G., Gaetz, W., Bloy, L., Wang, D.-J., Blaskey, L., Kuschner, E.S., Levy, S.E., Brodkin, E.S., Roberts, T.P.L., 2017. Exploring the relationship between cortical GABA concentrations, auditory gamma-band responses and development in ASD: Evidence for an altered maturational trajectory in ASD. Autism Res. 10, 593–607. https://doi.org/10.1002/aur.1686
Prichep, L.S., John, E.R., Ferris, S.H., Rausch, L., Fang, Z., Cancro, R., Torossian, C., Reisberg, B., 2006. Prediction of longitudinal cognitive decline in normal elderly with subjective complaints using electrophysiological imaging. Neurobiol. Aging 27, 471–481. https://doi.org/10.1016/j.neurobiolaging.2005.07.021
Purcell, E.M., Field, G.B., 1956. Influence of Collisions upon Population of Hyperfine States in Hydrogen. Astrophys. J. 124, 542. https://doi.org/10.1086/146259
Raichle, M.E., Martin, W.R., Herscovitch, P., Mintun, M.A., Markham, J., 1983. Brain blood flow measured with intravenous H2(15)O. II. Implementation and validation. J. Nucl. Med. Off. Publ. Soc. Nucl. Med. 24, 790–798.
Rampp, S., Stefan, H., Wu, X., Kaltenhäuser, M., Maess, M., Schmitt, F.C., Wolters, C., H.,., Hamer, H., Kasper, B.S., Schwab, S., Doerfler, A., Blümcke, I., Rössler, K., Buchfelder, M., 2019. Magnetoencephalography for epileptic focus localization in a series of 1000 cases. Brain 142, 3059–3071.
Rayson, H., Debnath, R., Alavizadeh, S., Fox, N., Ferrari, P.F., Bonaiuto, J.J., 2022. Detection and analysis of cortical beta bursts in developmental EEG data. Dev. Cogn. Neurosci. 54, 101069. https://doi.org/10.1016/j.dcn.2022.101069
Rea, M., Boto, E., Holmes, N., Hill, R., Osborne, J., Rhodes, N., Leggett, J., Rier, L., Bowtell, R., Shah, V., Brookes, M.J., 2022. A 90-channel triaxial magnetoencephalography system using optically pumped magnetometers. Ann. N. Y. Acad. Sci.
Rea, M., Holmes, N., Hill, R.M., Boto, E., Leggett, J., Edwards, L.J., Woolger, D., Dawson, E., Shah, V., Osborne, J., 2021. Precision magnetic field modelling and control for wearable magnetoencephalography. NeuroImage 118401.
Rempe, M.P., Ott, L.R., Picci, G., Penhale, S.H., Christopher-Hayes, N.J., Lew, B.J., Petro, N.M., Embury, C.M., Schantell, M., Johnson, H.J., Okelberry, H.J.,

Losh, K.L., Willett, M.P., Losh, R.A., Wang, Y.-P., Calhoun, V.D., Stephen, J.M., Heinrichs-Graham, E., Kurz, M.J., Wilson, T.W., 2023. Spontaneous cortical dynamics from the first years to the golden years. Proc. Natl. Acad. Sci. 120, e2212776120. https://doi.org/10.1073/pnas.2212776120

Renshaw, B., Forbes, A., Morison, B.R., 1940. Activity of isocortex and hippocampus: electrical studies with micro-electrodes. J. Neurophysiol. 3, 74–105. https://doi.org/10.1152/jn.1940.3.1.74

Rhodes, N., Holmes, N., Hill, R., Barnes, G., Bowtell, R., Brookes, M., Boto, E., 2022. Turning OPM-MEG into a Wearable Technology, in: Flexible High Performance Magnetic Field Sensors: On-Scalp Magnetoencephalography and Other Applications. Springer, pp. 195–223.

Rhodes, N., Rea, M., Boto, E., Rier, L., Shah, V., Hill, R.M., Osborne, J., Doyle, C., Holmes, N., Coleman, S.C., Mullinger, K., Bowtell, R., Brookes, M.J., 2023. Measurement of Frontal Midline Theta Oscillations using OPM-MEG. NeuroImage 271, 120024. https://doi.org/10.1016/j.neuroimage.2023.120024

Richards, J.E., Sanchez, C., Phillips-Meek, M., Xie, W., 2016. A database of age-appropriate average MRI templates. Neuroimage 124, 1254–1259.

Rier, L., Michelmann, S., Ritz, H., Shah, V., Hill, R.M., Osborne, J., Doyle, C., Holmes, N., Bowtell, R., Brookes, M.J., 2023. Test-retest reliability of the human connectome: An OPM-MEG study. Imaging Neurosci. 1, 1–20.

Rier, L., Zamyadi, R., Zhang, J., Emami, Z., Seedat, Z.A., Mocanu, S., Gascoyne, L.E., Allen, C.M., Scadding, J.W., Furlong, P.L., Gooding-Williams, G., Woolrich, M.W., Evangelou, N., Brookes, M.J., Dunkley, B.T., 2021. Mild traumatic brain injury impairs the coordination of intrinsic and motor-related neural dynamics. NeuroImage Clin. 32, 102841. https://doi.org/10.1016/j.nicl.2021.102841

Rjabinin, J.N., Shubnikow, L., 1935. Magnetic properties and critical currents of supra-conducting alloys. Nature 135, 581–582.

Roberts, G., Holmes, N., Alexander, N., Boto, E., Leggett, J., Hill, R.M., Shah, V., Rea, M., Vaughan, R., Maguire, E.A., 2019. Towards OPM-MEG in a virtual reality environment. NeuroImage 199, 408–417.

Roberts, T.P., Bloy, L., Ku, M., Blaskey, L., Jackel, C.R., Edgar, J.C., Berman, J.I., 2020. A multimodal study of the contributions of conduction velocity to the auditory evoked neuromagnetic response: anomalies in autism spectrum disorder. Autism Res. 13, 1730–1745.

Roberts, T.P., Cannon, K.M., Tavabi, K., Blaskey, L., Khan, S.Y., Monroe, J.F., Qasmieh, S., Levy, S.E., Edgar, J.C., 2011. Auditory magnetic mismatch field latency: a biomarker for language impairment in autism. Biol. Psychiatry 70, 263–269.

Roberts, T.P., Kuschner, E.S., Edgar, J.C., 2021. Biomarkers for autism spectrum disorder: opportunities for magnetoencephalography (MEG). J. Neurodev. Disord. 13, 1–9.

Roberts, T.P., Matsuzaki, J., Blaskey, L., Bloy, L., Edgar, J.C., Kim, M., Ku, M., Kuschner, E.S., Embick, D., 2019. Delayed M50/M100 evoked response component latency in minimally verbal/nonverbal children who have autism spectrum disorder. Mol. Autism 10, 1–10.

Roberts, T.P.L., Paulson, D.N., Hirschkoff, E., Pratt, K., Mascarenas, A., Miller, P., Han, M., Caffrey, J., Kincade, C., Power, B., Murray, R., Chow, V., Fisk, C., Ku, M., Chudnovskaya, D., Dell, J., Golembski, R., Lam, P., Blaskey, L., Kuschner, E., Bloy, L., Gaetz, W., Edgar, J.C., 2014. Artemis 123: development of a whole-head infant and young child MEG system. Front. Hum. Neurosci. 8, 99. https://doi.org/10.3389/fnhum.2014.00099

Robinson, H., Ensberg, E., Dehmelt, H., 1958. Preservation of spin state in free atom-inert surface collisions. Bull Am Phys Soc 3.

Robinson, S., Vrba, J., 1998. Functional Neuroimaging by synthetic Aperture Magnetometry. Recent Adv. Biomagn. Ed Yoshimoto T Kotani M Kuriki Karibe H Nakasato N Tohoku Univ Press Sendai Jpn. 302–305.
Rojas, D.C., Maharajh, K., Teale, P., Rogers, S.J., 2008. Reduced neural synchronization of gamma-band MEG oscillations in first-degree relatives of children with autism. BMC Psychiatry 8, 66. https://doi.org/10.1186/1471-244X-8-66
Ronconi, L., Vitale, A., Federici, A., Pini, E., Molteni, M., Casartelli, L., 2020. Altered neural oscillations and connectivity in the beta band underlie detail-oriented visual processing in autism. NeuroImage Clin. 28, 102484. https://doi.org/10.1016/j.nicl.2020.102484
Rondin, L., Tetienne, J.-P., Hingant, T., Roch, J.-F., Maletinsky, P., Jacques, V., 2014. Magnetometry with nitrogen-vacancy defects in diamond. Rep Prog Phys 77, 056503.
Rubenstein, J.L.R., Merzenich, M.M., 2003. Model of autism: increased ratio of excitation/inhibition in key neural systems. Genes Brain Behav. 2, 255–267. https://doi.org/10.1034/j.1601-183x.2003.00037.x
Ryvlin, P., Cross, J.H., Rheims, S., 2014. Epilepsy surgery in children and adults. Lancet Neurol. 13, 1114–1126. https://doi.org/10.1016/S1474-4422(14)70156-5
Sanchez, C.E., Richards, J.E., Almli, C.R., 2012a. Neurodevelopmental MRI brain templates for children from 2 weeks to 4 years of age. Dev. Psychobiol. 54, 77–91. https://doi.org/10.1002/dev.20579
Sanchez, C.E., Richards, J.E., Almli, C.R., 2012b. Age-Specific MRI Templates for Pediatric Neuroimaging. Dev. Neuropsychol. 37, 379–399. https://doi.org/10.1080/87565641.2012.688900
Sander, T., Jodko-Władzińska, A., Hartwig, S., Brühl, R., Middelmann, T., 2020. Optically pumped magnetometers enable a new level of biomagnetic measurements. Adv. Opt. Technol. 9, 247–251. https://doi.org/10.1515/aot-2020-0027
Sander, T.H., Preusser, J., Mhaskar, R., Kitching, J., Trahms, L., Knappe, S., 2012. Magnetoencephalography with a chip-scale atomic magnetometer. Biomed. Opt. Express 3, 981–990.
Sarvas, J., 1987. Basic mathematical and electromagnetic concepts of the biomagnetic inverse problem. Phys. Med. Biol. 32, 11–22.
Scally, B., Burke, M.R., Bunce, D., Delvenne, J.-F., 2018. Resting-state EEG power and connectivity are associated with alpha peak frequency slowing in healthy aging. Neurobiol. Aging 71, 149–155. https://doi.org/10.1016/j.neurobiolaging.2018.07.004
Schäfer, C.B., Morgan, B.R., Ye, A.X., Taylor, M.J., Doesburg, S.M., 2014. Oscillations, networks, and their development: MEG connectivity changes with age. Hum. Brain Mapp. 35, 5249–5261. https://doi.org/10.1002/hbm.22547
Schofield, H., Hill, R.M., Feys, O., Holmes, N., Osborne, J., Doyle, C., Bobela, D., Corvilian, P., Wens, V., Rier, L., Bowtell, R., Ferez, M., Mullinger, K.J., Coleman, S., Rhodes, N., Rea, M., Tanner, Z., Boto, E., Tiège, X. de, Shah, V., Brookes, M.J., 2024. A Novel, Robust, and Portable Platform for Magnetoencephalography using Optically Pumped Magnetometers. https://doi.org/10.1101/2024.03.06.583313
Schwarzkopf, D.S., Robertson, D.J., Song, C., Barnes, G.R., Rees, G., 2012. The Frequency of Visually Induced Gamma-Band Oscillations Depends on the Size of Early Human Visual Cortex. J. Neurosci. 32, 1507–1512. https://doi.org/10.1523/JNEUROSCI.4771-11.2012

Schwindt, P.D.D., Lindseth, B., Knappe, S., Shah, V., Kitching, J., Liew, L., 2007. Chip-Scale Atomic Magnetometer with Improved Sensitivity by Use of the Mx technique. Appl. Phys. Lett. 90, 081102-081102–3.
Seedat, Z.A., Quinn, A.J., Vidaurre, D., Liuzzi, L., Gascoyne, L.E., Hunt, B.A.E., O'Neill, G.C., Pakenham, D.O., Mullinger, K.J., Morris, P.G., Woolrich, M.W., Brookes, M.J., 2020. The role of transient spectral 'bursts' in functional connectivity: A magnetoencephalography study. NeuroImage 209, 116537. https://doi.org/10.1016/j.neuroimage.2020.116537
Sekihara, K., Nagarajan, S.S., 2008. Adaptive spatial filters for electromagnetic brain imaging. Springer Science & Business Media.
Sekihara, K., Nagarajan, S.S., Poeppel, D., Marantz, A., 2004. Performance of an MEG adaptive-beamformer source reconstruction technique in the presence of additive low-rank interference. IEEE Trans Biomed Eng 51, 90–99.
Seltzer, S.J., 2008. Developments in alkali-metal atomic magnetometry. Princeton University.
Seymour, R., 2018. Macquarie-MEG-Research/MEMES: For Zenodo. https://doi.org/10.5281/zenodo.1451031
Seymour, R.A., Alexander, N., Mellor, S., O'Neill, G.C., Tierney, T.M., Barnes, G.R., Maguire, E.A., 2022. Interference suppression techniques for OPM-based MEG: Opportunities and challenges. NeuroImage 247, 118834. https://doi.org/10.1016/j.neuroimage.2021.118834
Seymour, R.A., Alexander, N., Mellor, S., O'Neill, G.C., Tierney, T.M., Barnes, G.R., Maguire, E.A., 2021. Using OPMs to measure neural activity in standing, mobile participants. NeuroImage 244, 118604. https://doi.org/10.1016/j.neuroimage.2021.118604
Seymour, R.A., Rippon, G., Gooding-Williams, G., Schoffelen, J.M., Kessler, K., 2019. Dysregulated oscillatory connectivity in the visual system in autism spectrum disorder. Brain 142, 3294–3305. https://doi.org/10.1093/brain/awz214
Shah, V., Knappe, S., Schwindt, P.D., Kitching, J., 2007. Subpicotesla atomic magnetometry with a microfabricated vapour cell. Nat. Photonics 1, 649–652.
Shah, V., Romalis, M.V., 2009. Spin-Exchange-Relaxation-free Magnetometrty Using Elliptically Polarised Light. Phys. Rev. A 80, 013416.
Shah, V.K., Wakai, R.T., 2013. A compact, high performance atomic magnetometer for biomedical applications. Phys. Med. Biol. 58, 8153-8161.
Shaw, A.D., Moran, R.J., Muthukumaraswamy, S.D., Brealy, J., Linden, D.E., Friston, K.J., Singh, K.D., 2017. Neurophysiologically-informed markers of individual variability and pharmacological manipulation of human cortical gamma. NeuroImage 161, 19–31. https://doi.org/10.1016/j.neuroimage.2017.08.034
Shaw, A.D., Muthukumaraswamy, S.D., Saxena, N., Sumner, R.L., Adams, N.E., Moran, R.J., Singh, K.D., 2020. Generative modelling of the thalamo-cortical circuit mechanisms underlying the neurophysiological effects of ketamine. NeuroImage 221, 117189. https://doi.org/10.1016/j.neuroimage.2020.117189
Sheng, D., Perry, A.R., Krzyzewski, P., Geller, S., Kitching, J., Knappe, S., 2017. A microfabricated optically-pumped magnetic gradiometer. Appl Phys Lett 110, 031106.
Sherman, M.A., Lee, S., Law, R., Haegens, S., Thorn, C.A., Hämäläinen, M.S., Moore, C.I., Jones, S.R., 2016. Neural mechanisms of transient neocortical beta rhythms: Converging evidence from humans, computational modeling, monkeys, and mice. Proc. Natl. Acad. Sci. U. S. A. 113, E4885-4894. https://doi.org/10.1073/pnas.1604135113

Shin, H., Law, R., Tsutsui, S., Moore, C.I., Jones, S.R., 2017. The rate of transient beta frequency events predicts behavior across tasks and species. eLife 6, e29086. https://doi.org/10.7554/eLife.29086
Siegel, M., Warden, M.R., Miller, E.K., 2009. Phase-dependent neuronal coding of objects in short-term memory. Proc. Natl. Acad. Sci. 106, 21341–21346. https://doi.org/10.1073/pnas.0908193106
Silver, A.H., Zimmerman, J.E., 1965. Quantum Transitions and Loss in Multiply Connected Superconductors. Phys. Rev. Lett. 15, 888–891. https://doi.org/10.1103/PhysRevLett.15.888
Skidchenko, E., Butorina, A., Ostras, M., Vetoshko, P., Kuzmichev, A., Yavich, N., Malovichko, M., Koshev, N., 2023. Yttrium-Iron Garnet Magnetometer in MEG: Advance towards Multi-Channel Arrays. Sensors 23, 4256. https://doi.org/10.3390/s23094256
Sohal, V.S., Rubenstein, J.L.R., 2019. Excitation-inhibition balance as a framework for investigating mechanisms in neuropsychiatric disorders. Mol. Psychiatry 24, 1248–1257. https://doi.org/10.1038/s41380-019-0426-0
Sohal, V.S., Zhang, F., Yizhar, O., Deisseroth, K., 2009. Parvalbumin neurons and gamma rhythms enhance cortical circuit performance. Nature 459, 698–702. https://doi.org/10.1038/nature07991
Spitzer, B., Haegens, S., 2017. Beyond the Status Quo: A Role for Beta Oscillations in Endogenous Content (Re)Activation. eNeuro 4. https://doi.org/10.1523/ENEURO.0170-17.2017
Stenroos, M., Hunold, A., Haueisen, J., 2014. Comparison of three-shell and simplified volume conductor models in magnetoencephalography. NeuroImage 94, 337–348. https://doi.org/10.1016/j.neuroimage.2014.01.006
Steriade, M., Nunez, A., Amzica, F., 1993. A novel slow (< 1 Hz) oscillation of neocortical neurons in vivo: depolarizing and hyperpolarizing components. J. Neurosci. 13, 3252–3265. https://doi.org/10.1523/JNEUROSCI.13-08-03252.1993
Stoffers, D., Bosboom, J.L.W., Deijen, J.B., Wolters, E.C., Berendse, H.W., Stam, C.J., 2007. Slowing of oscillatory brain activity is a stable characteristic of Parkinson's disease without dementia. Brain 130, 1847–1860. https://doi.org/10.1093/brain/awm034
Sumner, R.L., McMillan, R.L., Shaw, A.D., Singh, K.D., Sundram, F., Muthukumaraswamy, S.D., 2018. Peak visual gamma frequency is modified across the healthy menstrual cycle. Hum. Brain Mapp. 39, 3187–3202. https://doi.org/10.1002/hbm.24069
Sun, L., Grützner, C., Bölte, S., Wibral, M., Tozman, T., Schlitt, S., Poustka, F., Singer, W., Freitag, C.M., Uhlhaas, P.J., 2012. Impaired Gamma-Band Activity during Perceptual Organization in Adults with Autism Spectrum Disorders: Evidence for Dysfunctional Network Activity in Frontal-Posterior Cortices. J. Neurosci. 32, 9563–9573. https://doi.org/10.1523/JNEUROSCI.1073-12.2012
Tadel, F., Baillet, S., Mosher, J., Pantazis, D., Leahy, R., 2011. Brainstorm: A User-friendly Application for MEG/EEG Analysis. Intell Neurosci. 2011, 8: 1–8: 13.
Takesaki, N., Kikuchi, M., Yoshimura, Y., Hiraishi, H., Hasegawa, C., Kaneda, R., Nakatani, H., Takahashi, T., Mottron, L., Minabe, Y., 2016. The Contribution of Increased Gamma Band Connectivity to Visual Non-Verbal Reasoning in Autistic Children: A MEG Study. PLOS ONE 11, e0163133. https://doi.org/10.1371/journal.pone.0163133
Tallon-Baudry, C., Bertrand, O., 1999. Oscillatory gamma activity in humans and its role in object representation. Trends Cogn. Sci. 3.
Tan, H.-R.M., Gross, J., Uhlhaas, P.J., 2016. MEG sensor and source measures of visually induced gamma-band oscillations are highly reliable. NeuroImage 137, 34–44. https://doi.org/10.1016/j.neuroimage.2016.05.006

Tewarie, P., Hunt, B.A.E., O'Neill, G.C., Byrne, A., Aquino, K., Bauer, M., Mullinger, K.J., Coombes, S., Brookes, M.J., 2019. Relationships Between Neuronal Oscillatory Amplitude and Dynamic Functional Connectivity. Cereb. Cortex 29, 2668–2681. https://doi.org/10.1093/cercor/bhy136

Tierney, T.M., Alexander, N., Mellor, S., Holmes, N., Seymour, R., O'Neill, G.C., Maguire, E.A., Barnes, G.R., 2021a. Modelling optically pumped magnetometer interference in MEG as a spatially homogeneous magnetic field. NeuroImage 244, 118484.

Tierney, T.M., Holmes, N., Mellor, S., López, J.D., Roberts, G., Hill, R.M., Boto, E., Leggett, J., Shah, V., Brookes, M.J., Bowtell, R., Barnes, G.R., 2019. Optically pumped magnetometers: From quantum origins to multi-channel magnetoencephalography. NeuroImage 199, 598–608. https://doi.org/10.1016/j.neuroimage.2019.05.063

Tierney, T.M., Levy, A., Barry, D.N., Meyer, S.S., Shigihara, Y., Everatt, M., Mellor, S., Lopez, J.D., Bestmann, S., Holmes, N., 2021b. Mouth magnetoencephalography: A unique perspective on the human hippocampus. NeuroImage 225, 117443.

Tierney, T.M., Mellor, S., O'Neill, G.C., Timms, R.C., Barnes, G.R., 2022. Spherical harmonic based noise rejection and neuronal sampling with multi-axis OPMs. NeuroImage 119338.

Trevarrow, M.P., Kurz, M.J., McDermott, T.J., Wiesman, A.I., Mills, M.S., Wang, Y.-P., Calhoun, V.D., Stephen, J.M., Wilson, T.W., 2019. The developmental trajectory of sensorimotor cortical oscillations. NeuroImage 184, 455–461. https://doi.org/10.1016/j.neuroimage.2018.09.018

Tzourio-Mazoyer, N., Landeau, B., Papathanassiou, D., Crivello, F., Etard, O., Delcroix, N., Mazoyer, B., Joliot, M., 2002. Automated anatomical labeling of activations in SPM using a macroscopic anatomical parcellation of the MNI MRI single-subject brain. Neuroimage 15, 273–289.

Vakhtin, A.A., Kodituwakku, P.W., Garcia, C.M., Tesche, C.D., 2015. Aberrant development of post-movement beta rebound in adolescents and young adults with fetal alcohol spectrum disorders. NeuroImage Clin. 9, 392–400. https://doi.org/10.1016/j.nicl.2015.09.005

van Diessen, E., Senders, J., Jansen, F.E., Boersma, M., Bruining, H., 2015. Increased power of resting-state gamma oscillations in autism spectrum disorder detected by routine electroencephalography. Eur. Arch. Psychiatry Clin. Neurosci. 265, 537–540. https://doi.org/10.1007/s00406-014-0527-3

van Ede, F., Quinn, A.J., Woolrich, M.W., Nobre, A.C., 2018. Neural Oscillations: Sustained Rhythms or Transient Burst-Events? Trends Neurosci. 41, 415–417. https://doi.org/10.1016/j.tins.2018.04.004

Van Veen, B.D., Buckley, K.M., 1988. Beamforming: a versatile approach to spatial filtering. IEEE ASSP Mag. 5, 4–24. https://doi.org/10.1109/53.665

Van Veen, B.D., van Drongelen, W., Yuchtman, M., Suzuki, A., 1997. Localization of brain electrical activity via linearly constrained minimum variance spatial filtering. IEEE Trans. Biomed. Eng. 44, 867–880. https://doi.org/10.1109/10.623056

Vasung, L., Abaci Turk, E., Ferradal, S.L., Sutin, J., Stout, J.N., Ahtam, B., Lin, P.-Y., Grant, P.E., 2019. Exploring early human brain development with structural and physiological neuroimaging. NeuroImage, Physiological and Quantitative MRI 187, 226–254. https://doi.org/10.1016/j.neuroimage.2018.07.041

Vecchio, F., Miraglia, F., Marra, C., Quaranta, D., Vita, M.G., Bramanti, P., Rossini, P.M., 2014. Human Brain Networks in Cognitive Decline: A Graph Theoretical Analysis of Cortical Connectivity from EEG Data. J. Alzheimers Dis. 41, 113–127. https://doi.org/10.3233/JAD-132087

Vidaurre, D., Quinn, A.J., Baker, A.P., Dupret, D., Tejero-Cantero, A., Woolrich, M.W., 2016. Spectrally resolved fast transient brain states in electrophysiological data. NeuroImage 126, 81–95. https://doi.org/10.1016/j.neuroimage.2015.11.047

Villringer, A., Planck, J., Hock, C., Schleinkofer, L., Dirnagl, U., 1993. Near infrared spectroscopy (NIRS): A new tool to study hemodynamic changes during activation of brain function in human adults. Neurosci. Lett. 154, 101–104. https://doi.org/10.1016/0304-3940(93)90181-J

Vinck, M., Womelsdorf, T., Fries, P., 2013. Gamma-band synchronization and information transmission, in: Quian Quiroga, R., Panzeri, S. (Eds.), Principles of Neural Coding. CRC Press Boca Raton, FL, pp. 449–469.

Vivekananda, U., Mellor, S., Tierney, T.M., Holmes, N., Boto, E., Leggett, J., Roberts, G., Hill, R.M., Litvak, V., Brookes, M.J., Bowtell, R., Barnes, G.R., Walker, M.C., 2020. Optically pumped magnetoencephalography in epilepsy. Ann. Clin. Transl. Neurol. 7, 397–401. https://doi.org/10.1002/acn3.50995

Vrba, J., 2002. Magnetoencephalography: the art of finding a needle in a haystack. Phys. C Supercond. 368, 1–9. https://doi.org/10.1016/S0921-4534(01)01131-5

Vrba, J., Robinson, S., 2001. Signal processing in magnetoencephalography. Methods 25, 249–271.

Whitford, T.J., Rennie, C.J., Grieve, S.M., Clark, C.R., Gordon, E., Williams, L.M., 2007. Brain maturation in adolescence: concurrent changes in neuroanatomy and neurophysiology. Hum. Brain Mapp. 28, 228–237. https://doi.org/10.1002/hbm.20273

Whitham, E.M., Pope, K.J., Fitzgibbon, S.P., Lewis, T., Clark, C.R., Loveless, S., Broberg, M., Wallace, A., DeLosAngeles, D., Lillie, P., Hardy, A., Fronsko, R., Pulbrook, A., Willoughby, J.O., 2007. Scalp electrical recording during paralysis: Quantitative evidence that EEG frequencies above 20Hz are contaminated by EMG. Clin. Neurophysiol. 118, 1877–1888. https://doi.org/10.1016/j.clinph.2007.04.027

Whittington, M.A., Traub, R.D., Jefferys, J.G.R., 1995. Synchronized oscillations in interneuron networks driven by metabotropic glutamate receptor activation. Nature 373, 612–615. https://doi.org/10.1038/373612a0

Wittevrongel, B., Holmes, N., Boto, E., Hill, R., Rea, M., Libert, A., Khachatryan, E., Van Hulle, M.M., Bowtell, R., Brookes, M.J., 2021. Practical real-time MEG-based neural interfacing with optically pumped magnetometers. BMC Biol. 19, 158. https://doi.org/10.1186/s12915-021-01073-6

Xia, H., Baranga, A.B.A., Hoffman, D., Romalis, M.V., 2006. Magnetoencephalography with an atomic magnetometer. Appl Phys Lett 89.

Yamawaki, N., Stanford, I.M., Hall, S.D., Woodhall, G.L., 2008. Pharmacologically induced and stimulus evoked rhythmic neuronal oscillatory activity in the primary motor cortex *in vitro*. Neuroscience 151, 386–395. https://doi.org/10.1016/j.neuroscience.2007.10.021

Yoshimura, Y., Kikuchi, M., Shitamichi, K., Ueno, S., Munesue, T., Ono, Y., Tsubokawa, T., Haruta, Y., Oi, M., Niida, Y., Remijn, G.B., Takahashi, T., Suzuki, M., Higashida, H., Minabe, Y., 2013. Atypical brain lateralisation in the auditory cortex and language performance in 3- to 7-year-old children with high-functioning autism spectrum disorder: a child-customised magnetoencephalography (MEG) study. Mol. Autism 4, 38. https://doi.org/10.1186/2040-2392-4-38

Yoshimura, Y., Kikuchi, M., Shitamichi, K., Ueno, S., Remijn, G.B., Haruta, Y., Oi, M., Munesue, T., Tsubokawa, T., Higashida, H., Minabe, Y., 2012. Language performance and auditory evoked fields in 2- to 5-year-old children. Eur. J. Neurosci. 35, 644–650. https://doi.org/10.1111/j.1460-9568.2012.07998.x

Zeidan, J., Fombonne, E., Scorah, J., Ibrahim, A., Durkin, M.S., Saxena, S., Yusuf, A., Shih, A., Elsabbagh, M., 2022. Global prevalence of autism: A systematic review update. Autism Res. 15, 778–790. https://doi.org/10.1002/aur.2696
Zetter, R., Iivanainen, J., Parkkonen, L., 2019. Optical Co-registration of MRI and On-scalp MEG. Sci. Rep. 9, 1–9.